AP-E 301167

ADA130932

(12)

DNA 6171F

DESIGN AND DEVELOPMENT OF A MULTIPIN SGEMP CURRENT INJECTION TEST TECHNIQUE

General Electric Company, Space Division
Valley Forge Space Center
P.O. Box 8555
Philadelphia, Pennsylvania 19101

1 June 1982

Final Report for Period 1 June 1978—1 June 1982

Contract No. DNA 001-78-C-0251

APPROVED FOR PUBLIC RELEASE;
DISTRIBUTION UNLIMITED.

THIS WORK WAS SPONSORED BY THE DEFENSE NUCLEAR AGENCY
UNDER RDT&E RMSS CODE B323079462 G37PAXYX95711 H2590D.

DTIC
ELECTE
AUG 1 1983
S
B

Prepared for
Director
Defense Nuclear Agency
Washington, D. C. 20305

83 00 00 000

Destroy this report when it is no longer
needed. Do not return to sender.

REPORT DOCUMENTATION PAGE		READ INSTRUCTIONS BEFORE COMPLETING FORM
1. REPORT NUMBER DNA 6171F	2. GOVT ACCESSION NO. AD-A130 932	3. RECIPIENT'S CATALOG NUMBER
4. TITLE *(and Subtitle)* DESIGN AND DEVELOPMENT OF A MULTIPIN SGEMP CURRENT INJECTION TEST TECHNIQUE		5. TYPE OF REPORT & PERIOD COVERED Final Report for Period 1 Jun 78 to 1 Jun 82
		6. PERFORMING ORG. REPORT NUMBER
7. AUTHOR(s) D. Tasca J. Peden J. Klisch B. Beers (Beers Associates, Inc.) H. O'Donnell J. Tigner (Science Applications,Inc.)		8. CONTRACT OR GRANT NUMBER(s) DNA 001-78-C-0251
9. PERFORMING ORGANIZATION NAME AND ADDRESS General Electric Company, Space Division Valley Forge Space Center P.O. Box 8555 Philadelphia, Pennsylvania 19101		10. PROGRAM ELEMENT, PROJECT, TASK AREA & WORK UNIT NUMBERS Subtask G37PAXYX957-11
11. CONTROLLING OFFICE NAME AND ADDRESS Director Defense Nuclear Agency Washington, D.C. 20305		12. REPORT DATE 1 June 1982
		13. NUMBER OF PAGES 212
14. MONITORING AGENCY NAME & ADDRESS*(if different from Controlling Office)*		15. SECURITY CLASS. *(of this report)* UNCLASSIFIED
		15a. DECLASSIFICATION DOWNGRADING SCHEDULE N/A since UNCLASSIFIED

16. DISTRIBUTION STATEMENT *(of this Report)*

Approved for public release, distribution unlimited

17. DISTRIBUTION STATEMENT *(of the abstract entered in Block 20, if different from Report)*

18. SUPPLEMENTARY NOTES

This work was sponsored by the Defense Nuclear Agency under RDT&E RMSS Code
B323079462 G37PAXYX95711 H2590D.

19. KEY WORDS *(Continue on reverse side if necessary and identify by block number)*

SGEMP
Satellite Survivability
Current Injection Test
Radiation Simulation Testing

20. ABSTRACT *(Continue on reverse side if necessary and identify by block number)*

Verification tests are imposed by satellite system survivability specifi-
cations which require that an SGEMP current injection test be performed on each
Qualification Level Component Box to demonstrate SGEMP hardness.

This report represents the results of an extensive analytical and computa-
tional evaluation of the response of termination loads to cable SGEMP signals
driven in multiwire cable bundles, and the design, development and experimental
verification of a Multipin Current Injection Test

DD ₁ FORM ₁JAN 73 1473   EDITION OF 1 NOV 65 IS OBSOLETE

20. ABSTRACT (Continued)

verification of a Multipin Current Injection Test (C.I.T.) Method for performing SGEMP hardness verification tests on electronic component boxes.

This C.I.T. method was developed to meet the technology needs for user-oriented current injection technique using realistic hardware to correctly perform these SGEMP electrical simulation tests at the individual component box level as well as at the subsystem and system levels. The purpose of the analytical development work was to quantify the dependence of the termination response on the manifold of parameters which specify the cable SGEMP threat in multiwire cables. This quantification is essential for making a rational choice of the drive levels, coupling factors, and cable characteristic impedances required in the implementation of this test technique.

SUMMARY

Verification tests are imposed by satellite system survivability specifications which require that an SGEMP current injection test be performed on each Qualification Level Component Box to demonstrate SGEMP hardness.

This report presents the results of an extensive analytical and computational evaluation of the response of termination loads to cable SGEMP signals driven in multiwire cable bundles, and the design, development and experimental verification of a Multipin Current Injection Test (C.I.T.) Method for performing SGEMP hardness verification tests on electronic component boxes.

This C.I.T. method was developed to meet the technology needs for user-oriented current injection technique using realistic hardware to correctly perform these SGEMP electrical simulation tests at the individual component box level as well as at the subsystem and system levels. The purpose of the analytical development work was to quantify the dependence of the termination response on the manifold of parameters which specify the cable SGEMP threat in multiwire cables. This quantification is essential for making a rational choice of the drive levels, coupling factors, and cable characteristic impedances required in the implementation of this test technique.

1

PREFACE

TABLE OF CONTENTS

3

TABLE OF CONTENTS (Continued)

LIST OF ILLUSTRATIONS

LIST OF ILLUSTRATIONS (Continued)

LIST OF TABLES

SECTION 1
INTRODUCTION

1-1 BACKGROUND

Systems generated electromagnetic pulse (SGEMP) is a transient radiation effect produced in the exposure of a hardware system to the pulsed x-radiation and γ-radiation from a nuclear burst. Electrons are driven from irradiated material surfaces which generate electromagnetic fields within and about system structure and drive currents on system surfaces. This electromagnetic environment couples energy into electrical systems; if sufficiently intense, this coupled energy can produce upset or damage in sensitive electronic components.

For satellite systems the SGEMP threat can be classified into four response regimes: external SGEMP, internal SGEMP, photon direct drive SGEMP, and black box SGEMP. These regimes are defined in the following paragraphs.

External SGEMP. Electron emission from irradiated external surfaces of the satellite produces a space current which drives electric and magnetic fields in the neighborhood of the satellite and currents on structural surfaces of the satellite. These currents and fields may couple directly to electrical systems through coupling into antennas and exposed electrical cabling, or indirectly through penetration into the satellite and along electrical cabling shields.

Internal SGEMP. Photons which penetrate into the satellite interior drive electrons from irradiated internal surface producing space current within enclosures. These cavity space currents drive electromagnetic fields and replacement currents which couple into electrical cabling.

Photon Direct Drive SGEMP. Photons which penetrate into electrically shielded cables drive electron emission from the interior surfaces of cable shields and external surfaces of cable conductors. This charge displacement drives replacement currents on the cable conductors which propogate to interfacing circuitry.

9

Black Box SGEMP. Photons which penetrate into electrical component boxes
drive electron emission from internal surfaces of the boxes and external surfaces
of conductors and bulk currents within dielectrics. The currents drive replacement
currents and fields which couple into wiring and printed circuitry. This effect is
particularly significant in component boxes such as RF amplifiers which utilize
high atomic number plating materials in their internal construction.

The net effect of the various SGEMP responses is to establish an electrical
threat to the interface circuits of component boxes which can be analytically repre-
sented as shown in Figure 1 by a number of separate invariant (independent of cable
and load impedances) distributed drive sources. The field coupled threat due to the
external and internal SGEMP can be represented by capacitive and inductive voltage
sources, E_C and E_L respectively. In the absence of space charge limiting, the wave-
shape of E_C follows the photon threat pulse shape $\dot{\gamma}$, while E_L follows the time de-
rivative of the photon pulse. The photon direct drive threat, on the other hand,
is represented by a current source whose waveshape also follows the photon pulse. It
is the distributed nature of the threat, the voltage or current source representation
and the specific placement in the transmission line circuit which gives rise to the
unique energy-time transmission line waveshape profile associated with each SGEMP
response regime, and the principal reason for this development program.
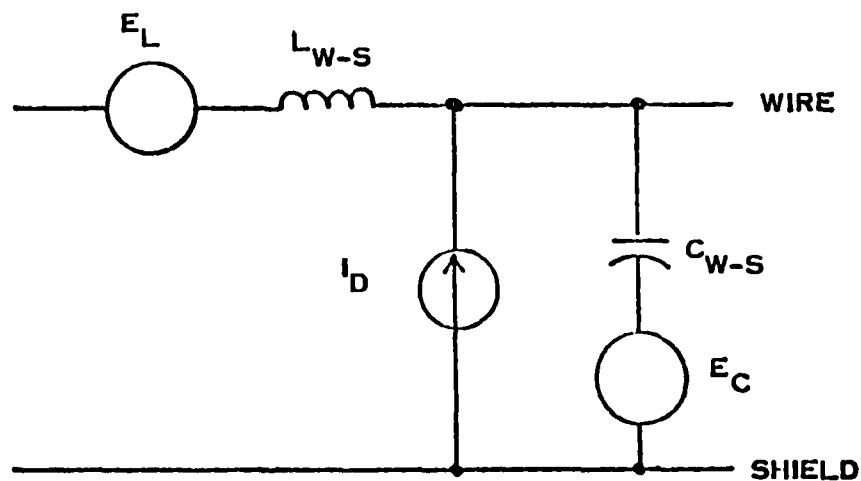
Figure 1. General SGEMP wire-to-shield drive source threats

It is possible through implementation of hardening techniques in the satellite design to strongly reduce the susceptibility of the system to the external SGEMP to a level small compared with the response to the internal SGEMP. Effective techniques are (1) the containment of all mission critical components in Faraday cage-design enclosures and (2) the routing of all cable runs between enclosures through conduits.

Similarly the system susceptibility to internal SGEMP can be strongly reduced through implementation of hardened design techniques to a level small compared with the photon direct drive SGEMP. Effective techniques here are (1) the use of RF-tight design for all mission critical component boxes, (2) the RF shielding of all cables and connectors interconnecting mission critical components, and (3) use of low Z coating on all internal surfaces. Therefore, with the exception of black box SGEMP where the above techniques cannot be applied, the primary concerns of the SGEMP survivability assessment are photon direct drive SGEMP.

1-2 PHOTON DIRECT DRIVE THREATS

The consequence of the photon direct drive being the primary SGEMP threat is that the threat presented to interface circuits shown in Figure 1 is altered such that the capacitive and inductive voltage sources become negligible. The basic invariant threat becomes a distributed current source (whose waveshape follows the photon pulse) driving a wire with transmission line characteristics.

Since satellite cables are comprised of many unshielded wires enclosed by a common bundle shield, the actual invariant threat presented to component boxes is as shown in Figure 2 for a general "N" wire cable. This threat consists of "N" individual distributed current sources; one for each wire, driving wire-to-shield. The physics of the photon direct drive interactions, though, are such that large differential mode current distributions are induced in the cable, that is, each wire has a different value current driver induced in it. This mechanism is such that the outer layer wires of the cable core on the X-ray incident side have high current levels induced in them. The source currents induced in the wires as the X-ray pulse travels through the core become progressively smaller, and even change polarity sign. Each wire in the cable represents a real wire-to-shield transmission line situation. The wires on the outer periphery of the core have the lowest characteristic impedance, while those on the inner layers have the highest. Each of the "N" wires on the bundles, however, are also tightly coupled to one another. Hence, the wires in the cable also represent a real wire-to-wire transmission line situation.

11
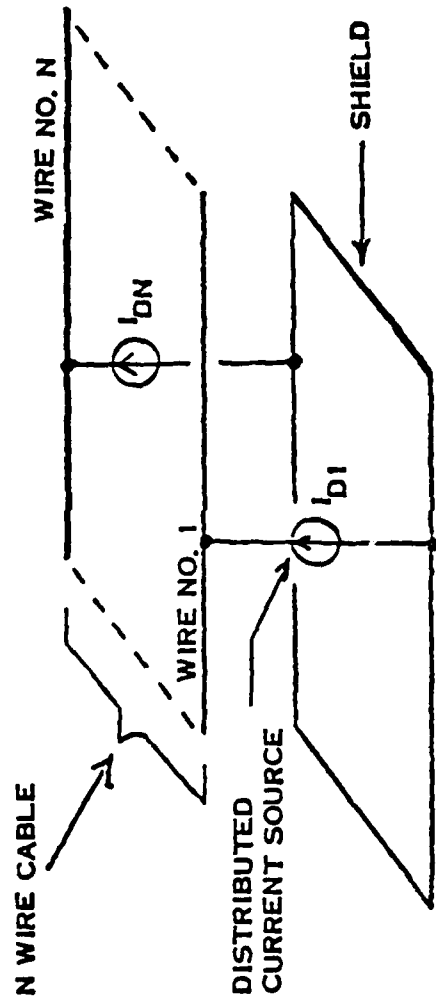
Figure 2. Photon direct drive threat in multiwire satellite cables

In spite of the apparent complexity of the electrical nature of the photon direct drive effects, the threat presented to each interface pin can be conceptually reduced to an equivalent wire-to-shield problem and represented as shown in Figure 3. The source term current, I_{DN}, shown here is an equivalent source term which represents the combination of the actual invariant source term induced in the wire and the amount of current coupled to or decoupled from the wire of interest to the other wires in the bundle. A quantatative representation such as this for each wire in the bundle reduces a very complex problem to a very simple task to identify which wire in the bundle represents the maximum energy threat to be used in a hardness verification test.

The above discussions have alluded to the importance of considering the transmission line nature of the photon direct drive threat. The significance of these characteristics, which will be discussed in full in Section 2, are implied in the typical behavior shown in Figure 4 and 5. This data shows the magnitude of the threat presented to component box interface pins in terms of the energy level and delivery time associated with a 1 ampere per meter direct drive threat in a single wire-to-shield system from a particular photon pulse shape.

It will be shown that as the interface impedance value increases, the threat energy delivered increases until, at large impedance values, the threat capability reaches a finite maximum. This maximum energy capability of the line increases linearly with line length. However, the impedance value at which the threat capability saturates decreases as line length increases until, the threat is essentially a constant energy value independent of impedance and is quite simply $Q^2/2C$ (i.e.: the equivalent charge, Q, produced by the X-ray threat divided by twice the cable capacitance, C).

It will also be shown in Section 2 that the time it takes to deliver the threat energy is also markedly effected by interface impedance . For an interface impedance which is matched to the wire-to-shield characteristic impedance, the threat energy is delivered in minimum times which are linearly related to line length. Higher and lower impedance values result in longer times for the threat energy delivery.

These response characteristics demonstrate the complex nature of the electrical pulse threat delivered to interface electronics from the photon direct drive threat. One of the most striking features of the response is that the load impedance value controls the amount of energy it receives for short line lengths,
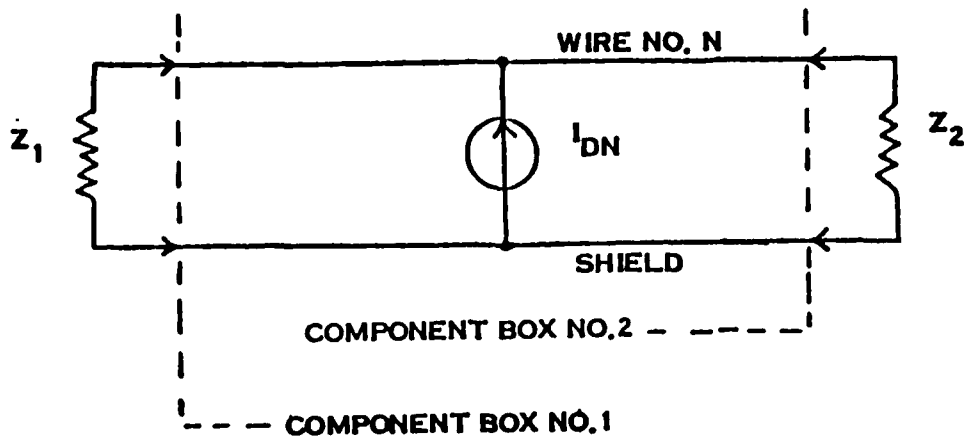
Figure 3. Equivalent single wire-to-shield photon direct
drive threat for component box interface pins.
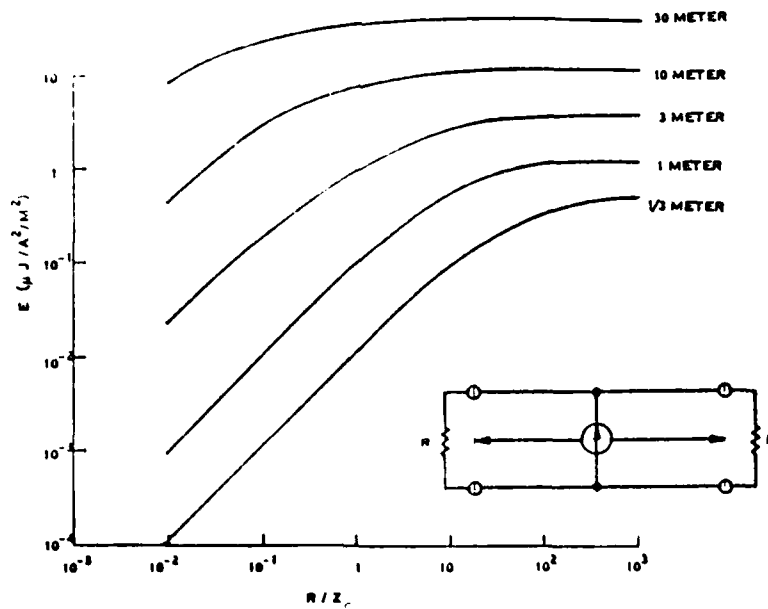
Figure 4. Transmission line dependence of the SGEMP energy delivered
to component box interfaces from a 1 ampere per meter
photon direct drive threat. The energy values shown are
50% of the final energy delivered.

14
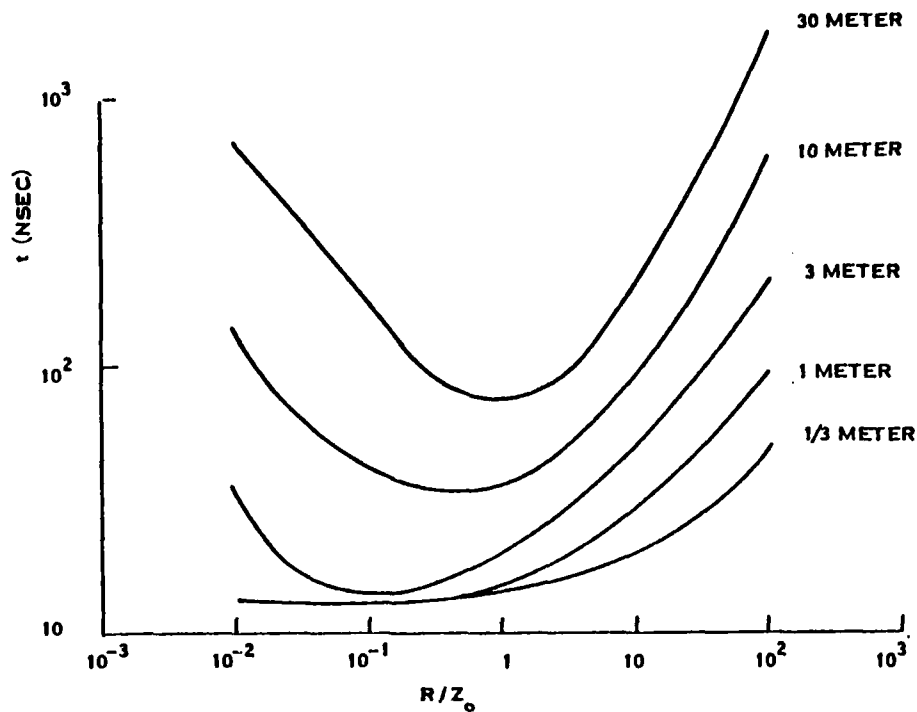
Figure 5. Transmission line dependence of the SGEMP energy rate
delivered to component box interfaces from a 1 ampere
per meter photon direct drive threat. The time value
shown is the time in which 50% of the final energy is
delivered.

while for the longer lengths the threat is essentially a constant energy one. The
energy-time characteristics and polarity of a pulsed electrical threat are of par-
ticular importance in determining piece part burnout vulnerability. Hence a correct
simulation test must duplicate the actual energy-time nature of threat. The purpose
of this work was to develop a technique and instrumentation to drive an interface
circuit with the actual waveshape of the invarient wire-to-shield source term which
follows the photon pulse, and with the actual cable length and characteristic
impedance of the cable going to the interface circuit.

1-3 MULTIWIRE CABLE CASE

The threat energy characteristics given in Figure 4 show that the maximum
energy capability of the photon direct drive is limited, as would be expected, to
finite values. It is actually the wire-to-shield characteristic impedance (which
is related to capacitance), dielectric constant, and wire length which control the
SGEMP threat from reaching physically unrealizeable values. The maximum energy
capability, in fact, is inversely proportional to dielectric constant and directly
proportional to characteristic impedance, line length and total charge associated
with the direct drive current source. This surfaces a significant, but somewhat
subtle, aspect of the photon direct drive threat.

15

Recall that the photon direct drive threat is essentially of a wire-to-shield transmission line nature with large differential mode source terms created in the cable bundle. Since the maximum energy capability of a particular wire is not only controlled by the magnitude of the wire's current source term but is also controlled by the wire-to-shield characteristic impedance, it does not necessarily follow that the wire with the largest source term represents the maximum threat condition, since this wire generally has the lowest wire-to-shield characteristic impedance.

In reality, each wire in the cable has it's own unique maximum energy capability associated with it. Conceptually, one could describe the variation in energy threat of the individual wires in the cable core as a function of wire characteristic impedance, as shown in Figure 6 along with the complete mathematical expressions for maximum wire-to-shield energy, short circuit current and open circuit voltage.

The development of such a display is, in fact, what would be required in order to define the maximum energy threat that the SGEMP direct drive poses to interface circuits. Furthermore, the definition of the wire-to-shield characteristic impedance associated with the maximum energy is essential to correctly simulate the threat, since the indiscriminate use of a lower or higher impedance value would result in an undertest or overtest respectively.

The correct threat specification situation is further complicated by the fact that since satellite cables are comprised of many unshielded wires enclosed by a common bundle shield, significant interwire coupling occurs which alters the equivalent electrical parameters (equivalent drive source level and wire-to-shield characteristic impedance) of the transmission line type threat. From a threat specification standpoint, one could adopt an approach based on defining the maximum threat posed to component box pins in terms of the total cable core current and some nominal or worst case characteristic impedance. This is an extremely conservative approach which is unrealistic but mathematically representative of an upper limit. This approach, however, is completely intolerable from a satellite system standpoint since it represents a significant hardware impact design solution to providing adequate hardening against a realistic threat level.

16

I_D MAX & Z_0 MIN

I_D MAX & Z_0 MAX

$< I_D$ MAX & Z_0 MAX

I_D MIN & Z_0 MIN

$\dot{\gamma}$

MAX. ENERGY WIRE

E_{MAX} PER WIRE

Z_0 PER WIRE

$$E_{MAX} = \sqrt{\frac{3\times10^8}{\mu_R \epsilon_R}} \; \frac{1}{2} \left[\int_0^{\tilde{\tau}} I_{D(t)} \right]^2 Z_0 \ell$$

$$I_{MAX} = \sqrt{\frac{3\times10^8}{\epsilon_R}} \int_0^{\tilde{\tau}} I_{D(t)}$$

$$V_{MAX} = \sqrt{\frac{3\times10^8}{\epsilon_R}} \; Z_0 \int_0^{\tilde{\tau}} I_{D(t)}$$

$$Q_\ell = \frac{N_i}{\sqrt{\epsilon_R}} Q_\ell = N_p Q_\ell = I_{peak} \frac{t_{peak}}{length} \frac{N}{p}$$
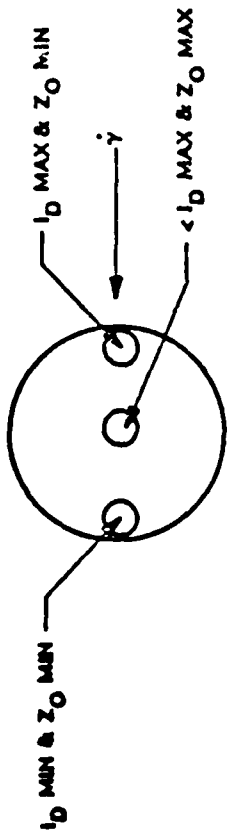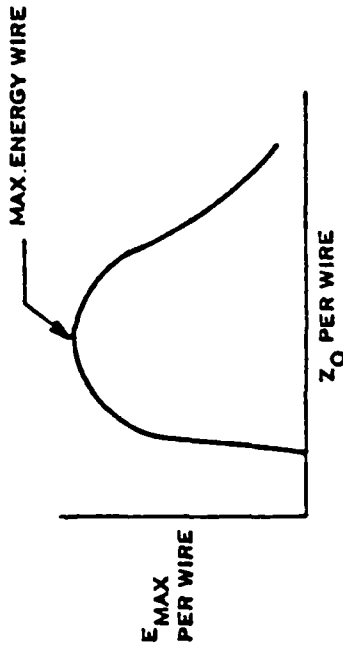
for square wave

$$= I_{peak} \frac{peak}{length}$$

ℓ electrical length of x-ray pulse in cable

Figure 6. Distribution of maximum photon direct drive energy threats for individual wires in a multiwire cable

17

Hence, to correctly specify and simulate the maximum threat induced by the photon direct drive response, Sections 3 and 4 develop analytical techniques which would allow one to define a realistic set of electrical parameters which are representative of the realistic maximum energy threat contained in a multiwire satellite cable.

1-4 REVIEW OF PRESENT SGEMP DIRECT DRIVE SIMULATION METHODS

Since operational testing of the survivability of a satellite is precluded by the nuclear test ban, simulation experiments must be employed to perform SGEMP hardness verification tests. Photon simulators with threat level fluences are not available, however, and recourse must be made to current injection test (C.I.T.) techniques are required by the present satellite system survivability specifications. The various C.I.T. techniques which are presently available under existing techno- logy for possible use in the hardness verification tests are as follows:

1. Direct pin injection from a commercial pulse generator
2. Inductive/Capacitive (L/C) coupling to cable shield
3. Direct injection on cable shield

An advanced development technique, which is described in Section 5 of this report could also be considered as "direct injection wire-to-shield".

The primary considerations in selecting any candidate C.I.T. technique are associated with the capability to reproduce the energy-time characteristics of the photon direct drive threat, the compatability with actual satellite equip- ments, and the degree of risk inherent with the approach. Detailed evaluations of each candidate approach have been performed by GE/SD to identify the optimum method which should be used to perform photon direct drive simulations. The essential results of these evaluations are shown in Table 1. Direct pin injection from a single, commercially available pulse generator is not included in the Table. This technique could conceivably be configured to provide positive current control at the high SGEMP required threat frequencies even for the high density type (large number of connector pins) connectors used in satellite systems. This technique, however, does not come anywhere near being capable of simulating the transmission line nature of the actual SGEMP threat. The conclusions from the C.I.T. evaluations are that the C.I.T. technology which has been developed to date does not provide the means to meet the SGEMP hardness verification specification in design hardened satellite systems where the SGEMP threat is due to photon direct drive effects.

18

Table 1. Evaluation of various current injection techniques for photon direct drive simulation

	L/C COUPLING	DIRECT INJECTION ON HARNESS SHIELD	DIRECT INJECTION FROM WIRE TO SHIELD
Basic Method	L/C coupling of current to outer surface of harness shield	Hard wire connection of pulse generator to harness shield	Hard wire connection of pulse generator from wire to shield
Advantages	No hard wire connection of pulser to any harness required. Currents on wires inside harness are distributed	Hard wire connection to only harness shield required	Positive control of current amplitude and waveshape for each wire tested Capable of testing for either common mode or worst case differential threats for any group of wires in harness No overstress levels produced in wires not being tested Test levels for different wire lengths can be produced through one standard interface by capacitively loading pulse generator to simulate various cable lengths Most efficient method of test with respect to pulse generator power required

Table 1. Continued

	L/C COUPLING	DIRECT INJECTION ON HARNESS SHIELD	DIRECT INJECTION FROM WIRE TO SHIELD
Disadvantages	Although the wire currents are produced from a distributed source the absolute current level on each wire is controlled by the shield effectiveness of the harness shield and position of the wire in the harness bundle		Interface "T" required to provide hardwire access of pulser to each wire tested and shield
	Current waveshape on wires is generally a complex frequency dependent function of the harness shield transfer characteristics		Special coupling techniques generally required for RF-Coax interfaces
	Generally have to overdrive outer wires in harness bundle to induce required test levels on inner wires		Limitations with respect to allowable wire-to-wire isolation/loading by the pulse generator interface
	For component harness bundles which have wires of various lengths in the S/C, the wires which have shorter length will have to be overdriven to induce the required test levels on wires which have long lengths in the S/C		Distributed current is approximated by single point or finite multipoint injection
	Can not test for worst case effects of differential drive in harness since the relative current distribution in the wires is controlled by the position of each wire in the test harness used		
	Least efficient method of test with respect to pulse generator power required due to inherent losses in the L/C coupler and shield attenuation characteristics	Inefficient method of test with respect to pulse generator power required	

20

Table 1. Concluded

	I/C COUPLING	DIRECT INJECTION ON HARNESS SHIELD	DIRECT INJECTION FROM WIRE TO SHIELD
Conclusions	This method is generally employed for the field coupled EMP type threat. The current amplitudes on individual wires are difficult to control and an overtest of some interfaces could occur. This method is not generally accepted as an adequate simulation of the SGEMP direct drive threat.		Most desirable method from standpoint of controlling amplitude on individual wires, eliminating unintentional overtest situations, and producing desired waveshapes to simulate the SGEMP direct drive threat.

Techniques such as those previously developed under EMP programs do not provide a correct simulation of the energy-time nature of the photon direct drive threat nor do they provide a practical, low risk approach which is compatable with photon direct drive hardened designs in satellite equipments. Capacitive and inductive coupling techniques, for example, do not correctly simulate the actual transmisson line nature of the photon direct drive source term. Furthermore, these techniques do not provide individual, positive control of currents delivered to component box pins when both long and short wire threats are required to be simultaneously injected at the same connector interface.

The most desirable approach identified is direct injection wire-to-shield. This approach is the most desirable from the standpoint of controlling amplitudes on individual wires, eliminating unintentional overstress situations, and producing the desired waveshapes to simulate the SGEMP direct drive threat. The technology development effort required to establish a realistic C.I.T. technique which is capable of both correctly simulating the electrical nature of the SGEMP photon direct drive threat with a multipin, simulataneous drive capability, as well as meeting the practical and hardened design constraints posed by actual satellite electronic and complex cable harness hardware is described in detail in Section 5.

1-5 THREAT SIMULATION HARDWARE CONSIDERATIONS

Since the severity of the SGEMP photon direct drive threat is controlled by energy-time transmission line characteristics and specific wire length, hardening requirements are imposed based on actual cable length in the satellite system for each interface circuit as well as the quantitatively defineable electrical loads, not only at the circuit of concern, but at the interfacing circuit at the opposite end of the wire. In many cases, for example, the presence of a particular low impedance electrical load or the addition of a single zener diode at one end of a short-to-medium length wire is sufficient to provide protection to the interfacing circuits at both ends of the line. For longer length lines, SGEMP hardening is implemented at both ends of the line consistent with the line length of the transmission line type threat. Hence, many interfacing circuits in a component box are only SGEMP hardened when all their respective interface component boxes are electrically connnected.

An additional design consideration for threat simulation is associated with the physical nature of the electrical systems (cables and connectors) in actual satellites. Satellite cables are unlike re-entry vehicle cables in that they are not generally straight, two connector cables. Instead, satellite cables are typically complex configurations comprised of large bundles of upwards of hundreds of unshielded wires contained within a common bundle shield with numerous branches and connector breakouts, with high density (large number of pins) connectors used for component box interfaces. Furthermore, the wiring in these cables consist of wires with short total lengths (low threat level wires which require minimal SGEMP hardening of their respective interface circuits) in a common bundle with wires of long total lengths (high threat level wires which require extensive interface circuit hardening).

The consequence of these design aspects are that an SGEMP simulation technique must not only provide high simulation fidelity of the energy-time transmission line nature of the SGEMP threat for multipin, simultaneous drive of component boxes, but must also be capable of correctly driving a component box whose SGEMP protection is contained in numerous other component boxes which are not in the test setup, as well as being capable of simultaneously driving some pins at high levels and others at low levels to accomodate various distributions of long and short wire threats at the same connector interface. This latter requirement also has a significant impact on the risk potential associated with any potential simulation technique.

Since the SGEMP hardness verification test is typically performed inline at the latter portion of the total Qualification Cycle (generally before thermal-vacuum qualification), a low risk simulation approach is required to avoid inadvertent overstress levels which could cause spacecraft equipment failures and impact system integration and, possibly, flight schedules In view of the typical SGEMP hardening designs employed in satellite systems, one cannot generally affort the luxury of overdriving some pins at higher levels in order to assure that the minimum required test levels are properly established in all pins. As such, the simulation method must also be capable of providing individual positive control of each of the currents delivered to each of the interface pins to eliminate high current (or voltage) hazards to both the equipment as well as the operating personnel. An obvious additional requirement, which is more practically oriented for user test evaluation, is that the simulation methods be capable of being configured into portable, in-house hardware readily adaptable to correctly interfacing (both electrically and mechanically) with actual satellite component boxes and their associated ground test equipments.

SECTION 2
TWO WIRE TRANSMISSION LINE CHARACTERISTICS

2-1 BACKGROUND AND APPROACH

This section describes a terminated two wire transmission line which has point current sources distributed along its length from return to signal line. A number of fundamental transmission line response equations are developed which provide useful tools for analyzing photon direct drive cable resopnses in a X-ray radiation environment.

The fundamental equations on which this work rests appear in Schelkunoff (Reference 1) where the waves produced on a transmission line by point sources are succinctly described. The work of King (Reference 2) and Weeks (Reference 3) provide additional development of transmission line theory and point sources which form the background theory to this section.

The response of a loaded two wire transmission line to distributed point sources is derived in Section 2-2. The point current sources along the length of line are assumed to be proporational to a defined waveshape, but with peak amplitude and start time arbitrarily varying along the length of line. The line is assumed to be linear, time invariant (Reference 4) and lossy. Loads are also assumed linear and time invariant. The equations for load currents and for current on the line are developed with reasonable generality in the frequency domain.

In Section 2-3, the transmission line response with current drivers is then studied for the corollary case of a cable illuminated by an X-ray with an arbitrary angle of incidence so that the induced point sources turn on as the X-ray moves along the cable. Section 2-4 applies the results of Sections 2-2 and 2-3 to specific applications of load impedance, pulse width and a current source amplitude.

2-2 TRANSMISSION LINE RESPONSE TO DISTRIBUTED CURRENT SOURCES

A two wire transmission line of length S is shown in Figure 7. The line is loaded by two loads: Z_0 at z=o and Z_s at z=s, where z is the distance on the line from its end. Both line and loads are linear and time-invariant. The

24

transmission line is driven by a distributed current source, assumed to be distributed point sources in the sense of Schelkunoff (reference 1). The point current source is described mathematically as:

$$i_0 (x,t) = A(x) \, g \, (t-t_x) \tag{2.1}$$

where $A(x)$ is an arbitary amplitude density function (Amp/m) of source location x, measured from the end of the line. The function $g(t)$ is assumed to be dimensionless, normalized and causal, i.e.,

$$|g(t)|_{max} = 1 \tag{2.2a}$$

and

$$g(t) = 0 \text{ for } t < 0 \tag{2.2b}$$

The parameter t_x is an arbitary function of source location x. Thus, the equation for $i_0(x,t)$ is a representation of a point source which exists along the length of the line with an arbitary amplitude $A(x)$ and with an arbitrary start time t_x, dependent on location x from the end of the line.

The Fourier transform of $i_0(x,t)$ can now be written as

$$I_0(x,\omega) = F \, (i(x,t)) = \rho(x,\omega) \, G(\omega) \tag{2.3}$$

where

$$G(\omega) = F \, (g(t)) = \int_0^\infty g(t) \, \exp \, (-j\omega t)dt$$

and

$$\rho(x,\omega) = A(x) \, \exp \, (-j\omega t_x).$$

For simplicity, the abbreviated notation $I_0(x,\omega) = I_0(x)$ and $\rho(x)$ is introduced.
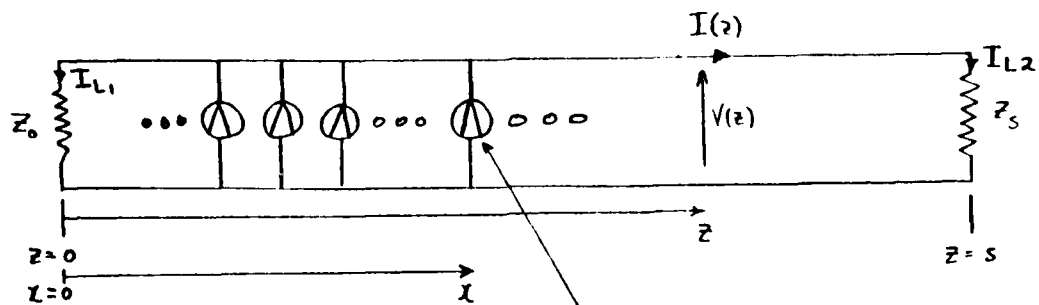
Point Current Source Density
$i_0(x,t)=A(x)g(t-t_x)$, Distributed
Along Line

$I(z)$ = Line Current Toward Z_s @ Location Z

$V(z)$ = Line Voltage @ Location Z

Figure 7. Transmission line with distributed
point current sources

The standard transmission line notations of reference 2 are introduced:

characteristic impedance

$$Z_c = \sqrt{\frac{R + j\omega L}{G + j\omega C}}$$ (2.4a)

line propogation constant

$$\gamma = \sqrt{(R + j\omega L)(G + j\omega C)}$$ (2.4b)

reflection coefficients

$$\Gamma_o = \frac{Z_0 - Z_c}{Z_0 + Z_c} \qquad \Gamma_s = \frac{Z_s - Z_c}{Z_s + Z_c}$$ (2.4c)

where   R = series line resistance Ω/M

L = series line inductance   H/M

G = shunt line conductance   S/M

C = shunt line capacitance   F/M

The extensions of Z_C and γ to include skin effects and other high frequency losses are covered in reference 2.

The objective of this derivation is to compute the current on the line I_z at location z. The current I_z can be thought of as the difference of two currents:

$$I_z = I_1(z) - I_2(z) \tag{2.5}$$

where $I_1(z)$ is the contribution to I_z of all sources to the left of z, i.e., $x<z$ and $I_2(z)$ is the contribution of all sources to the right of z, i.e., $x>z$.

Using Schelkunoff's development (reference 1), a point source driver at location x of Z_S to location x and where Z_L is the reflection of Z_0 to location x as indicated in Figure 8A. It is assumed that a differential source term driver $I_0(x)$ dx within a differential length of line dx launches a wave $dI_R(x)$ with the sign convention of Figure 8a indicating plus to the right. Thus, by current division,

$$dI_R(x) = \frac{Z_L(x)}{Z_L(x) + Z_R(x)} \tag{2.6a}$$

where

$$Z_L(x) = Z_C \; \frac{1 + \Gamma_0 \exp(-2\gamma x)}{1 - \Gamma_0 \exp(-2\gamma x)} \tag{2.6b}$$

$$Z_R(x) = Z_C \; \frac{1 + \Gamma_s \exp(-2\gamma(s-x))}{1 - \Gamma_s \exp(-2\gamma(s-x))} \tag{2.6c}$$

Reflecting $dI_R(x)$ to location Z gives:

$$dI_1 = \frac{\exp(-\gamma z) - \Gamma_s \exp[-\gamma(2s-z)]}{\exp(-\gamma x) - \Gamma_s \exp[-\gamma(2s-x)]} dI_R \tag{2.7}$$

$$= R_R(z,x)\, dI_R$$

where differential operator "d" is on x only.

Using the complementary model of Figure 8b for the left current (sources at $x>z$) yields

$$dI_L(x) = \frac{Z_R(x)}{Z_L(x) + Z_R(x)} \; I_0(x)\, dx \tag{2.8}$$

and

$$dI_2(z) = \frac{\exp(\gamma z) - \Gamma_0 \exp(-\gamma z)}{\exp(\gamma x) - \Gamma_0 \exp(-\gamma x)} \; dI_L \tag{2.9}$$

$$= R_L(z,x)\, dI_L$$

a) Location x<z.

Figure 8a.

b) Location x>z.
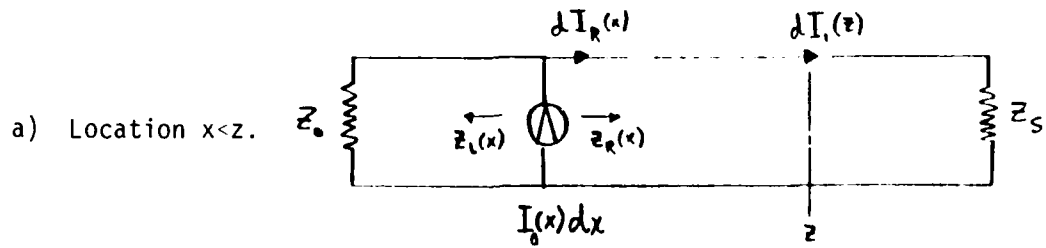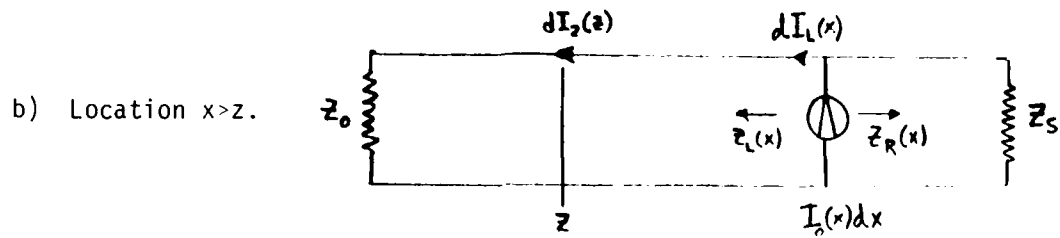
Figure 8b.

Then from Equation 2.5 I_Z is written as:

$$I_Z = \int_0^Z dI_1 - \int_Z^S dI_2 \qquad (2.10)$$

The integrals are of the form:

$$I_Z = \int_0^Z H_R(Z,X) \, I_0(X) \, dx - \int_Z^S H_L(Z,X) \, I_0(X) \, dx \qquad (2.11)$$

where

$$H_R = R_R(Z,X) \, \frac{Z_L(X)}{Z_L(X)+Z_R(X)} \qquad (2.11b)$$

$$H_L = R_L(Z,X) \, \frac{Z_R(X)}{Z_L(X)+Z_R(X)} \qquad (2.11c)$$

28

Contrary to the devastating appearance of these expressions, term cancellations occur throughout, so that Equation 2.12 is all that remains. One is careful to note that the direction of I_Z is assumed to be towards Z_S.

$$\frac{I_Z}{G(\omega)} = \frac{\left[e^{-\gamma z} - \Gamma_s e^{-\gamma(2s-z)}\right]}{2\left(1 - \Gamma_0 \Gamma_s e^{-2\gamma s}\right)} \int_0^Z \left(e^{\gamma x} + \Gamma_0 e^{-\gamma x}\right) \rho(X) dx$$

$$- \frac{\left[e^{\gamma z} - \Gamma_0 e^{-\gamma z}\right]}{2\left(1 - \Gamma_0 \Gamma_s e^{-2\gamma s}\right)} \int_Z^S \left(e^{-\gamma x} + \Gamma_s e^{-2\gamma s} e^{\gamma x}\right) \rho(X) dx \qquad (2.12)$$

Equation 2.12 is the desired transfer function $I_Z/G(\omega)$ which relates I_Z to the input source pulse shape $G(\omega)$. The integrands are of simple exponential formats, with $\rho(x) = A(x) \exp(-j\omega t_x)$. The Fourier spectrum for line current I_Z is thus easily computed, once $\rho(x)$ is defined. Time domain histories can be obtained via standard Fourier inversion for a specified $G(\omega)$.

The line voltage at location z can now be computed from the line current I_Z via superposition from the relation:

$$V(Z) = Z_R(Z) \int_0^Z dI_1 - Z_L(Z) \int_Z^S dI_2 \qquad (2.13)$$

where the functions Z_R and Z_L have been identified in Equations 2.6b and 2.6c. The integrals for I_1 and I_2 are easily identified from Equations 2.10 and 2.12.

The load current in Z_S, namely I_{L2}, is simply I_Z evaluated at $Z=S$, so:

$$\frac{I_{L_2}(\omega)}{G(\omega)} = \frac{e^{-\gamma s}(1 - \Gamma_s)}{2\left(1 - \Gamma_0 \Gamma_s e^{-2\gamma s}\right)} \int_0^S \left(e^{\gamma x} + \Gamma_0 e^{-\gamma x}\right) \rho(X) dx \qquad (2.14)$$

The load current into Z_0, namely I_{L1} with the sign convention of Figure 7 is $-I_Z$ evaluated at $z=0$.

$$\frac{I_{L_1}(\omega)}{G(\omega)} = \frac{(1 - \Gamma_0)}{2\left(1 - \Gamma_0 \Gamma_s e^{-2\gamma s}\right)} \int_0^S \left(e^{-\gamma x} + \Gamma_s e^{-2\gamma s} e^{\gamma x}\right) \rho(X) dx \qquad (2.15)$$

29

2-3 APPLICATION TO X-RAY DIRECT DRIVE RESPONSE

The application of Equation 2.12 to cable direct drive resulting from X-ray illumination is straight forward. The geometry of Figure 9 shows a cable with an X-ray illumination environment. The distributed current source is assumed to have the form of equation 2.1:

$$i_0(x,t) = i_0(t-t_x) = I_D \, g(t-t_x) \tag{2.16}$$

where, $A(x) = I_D$ = constant. If the angle of incident illumination is Θ, as shown in Figure 9, the point drivers turn on along the line at time $t_x = x \cos\Theta/V_0$ where V_0 is the speed of light in M/S and t_x is time relative to the time point when location x=o is illuminated.

By taking the Fourier transform of i_0, the function of $\rho(x)$ is identified as:

$$\rho(x) = I_D \exp(-j\omega x \cos\theta/v_0)$$
$$= I_D \exp(-j\beta_0 \cos\theta x) \tag{2.17}$$

Thus, for normal incidence, t_x=o and the entire cable is driven simultaneously, resulting in $\rho(x) = I_D$ = constant. For on line incidence, θ = o and $t_x = x/v_0$, resulting in $\rho(x) = I_D \exp(-j\omega x/v_0)$.
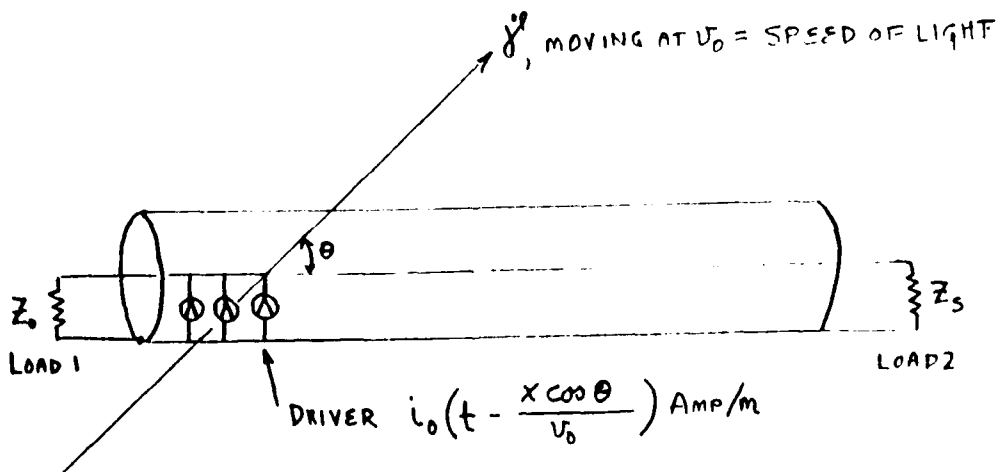
Figure 9. Cable geometry with radiation γ
incident at arbitrary angle $0 \cdot 0 \leq \frac{\pi}{2}$

30

In other words, when the fluence propagates along the length of cable, the X-ray illuminates the cable with sources that turn on at time x/v_0. The cable generates a wave which moves, generally speaking, slower than v_0. Equations 2.14 and 2.15 will now be studied to find out what effects these wave motions have on load currents.

Whereas, the equations for load currents I_{L1} and I_{L2} (2.14 and 2.15) are perfectly general and can be analyzed via numerical Fourier analysis for lossy cables, the consideration of lossless transmission lines is now taken up. This restriction is applicable for the analysis of many practical cable configurations. The lossless line also allows for the introduction of simple line parameters, in particular, the line's one way transit time τ, so as to provide a continuing physical insight to the meaning of the equations as they are developed. The following notation is introduced (R=G=0):

$$v_0 = 3 \times 10^8 \text{ M/S, speed of light} \tag{2.18a}$$

$$S = \text{length of line in meters} \tag{2.18b}$$

$$\tau_0 = S/v_0 = \text{time for light to traverse line length S.} \tag{2.18c}$$

$$\beta_0 = \omega/v_0 \tag{2.18d}$$

$$v_p = 1/\sqrt{LC} \tag{2.18e}$$

$$\tau = S/v_p \quad \text{(line delay or one-way cable transit time} \atop \text{of a wave on the line.)} \tag{2.18f}$$

$$\gamma = j\omega\sqrt{LC} = j\beta \tag{2.18g}$$

$$\tau_1 = \tau - \tau_0 \cos\theta \tag{2.18h}$$

$$\tau_2 = \tau + \tau_0 \cos\theta \tag{2.18i}$$

$$I_0(\omega) = F\left(i_0(t)\right) \tag{2.18j}$$

$$Q(\omega) = \frac{SI_0(\omega)}{j\omega} \tag{2.18k}$$

The result of substituting $\psi(x) = \exp(-j\beta_0 \cos\theta\, x)$ into the Equation 2.14 for I_{L2} yields Equation 2.19, which when factored in yields Equation 3.20. These equations are valid for $\tau > \tau_0 \cos\theta$.

31

$$I_{L2} = \frac{\left(1-\Gamma_s\right) Q(\omega)}{2[1-\Gamma_0\Gamma_s \exp(-2j\omega\tau)]} \left\{ \frac{1}{\tau_1} \exp(-j\omega\tau_0 \cos\theta) \right.$$

$$\left. - \frac{\Gamma_0}{\tau_2} \exp\left[-j\omega(2\tau+\tau_0 \cos\theta)\right] - \left(\frac{1}{\tau_1} - \frac{\Gamma_0}{\tau_2}\right)\exp(-j\omega\tau) \right\} \tag{2.19a}$$

$$\Delta = 1-\Gamma_0\Gamma_s \exp(-2j\omega\tau) \tag{2.19b}$$

$$I_{L2} = \frac{(1-\Gamma_s) Q(\omega)}{2\tau_1\Delta} e^{-j\omega\tau_0 \cos\theta} \left\{ 1-\Gamma_0\frac{\tau_1}{\tau_2} e^{-2j\omega\tau} \right.$$

$$\left. - \left(1-\frac{\Gamma_0\tau_1}{\tau_2}\right)e^{-j\omega\tau} \right\} \tag{2.20}$$

Considerable algebraic effort is saved in the integral evaluation for I_{L1} by using the solution for I_{L2} with Zo replaced by Z_s in Figure 9 and noting that in this geometry,

$$\beta(X) = \exp(-j\beta_0 (S-X) \cos\theta) \tag{2.21}$$

Thus, to obtain I_{L1} from Equation 2.20 for I_{L2}, β_0 is replaced by $-\beta_0$, Zo is interchanged with Zs (thereby Γ_0 is interchanged with Γ_s), τ_1 is interchanged with τ_2, τ_0 is replaced by $-\tau_0$ and the whole expression is then multiplied by $\exp(-j\beta_0 S \cos\theta) = \exp(-j\omega\tau_0 \cos\theta)$ to yield:

$$I_{L1} = \frac{(1-\Gamma_0)Q(\omega)}{2\tau_2\Delta} \left\{ 1-\frac{\Gamma_s\tau_2}{\tau_1} e^{-2j\omega\tau} - \left(1-\frac{\Gamma_s\tau_2}{\tau_1}\right)e^{-j\omega\tau_2} \right\} \tag{2.22}$$

with Δ defined in Equation 2.19b. The student of Fourier theory will immediately recognize that, for $\theta \neq 0$, I_{L1} will start responding before I_{L2}, because of the absence of the phase shift multiplier $\exp(-j\omega\tau_0 \cos\theta)$ which occurs in Equation 2.20. That is to say that the current in the load at z=s will be zero for time less than $(\tau_0 \cos\theta)$, the time at which the X-ray arrives at z=s, whereas, the current at z=o will commence upon the illumination of that end of the cable.

For the case of perpendicular incidence, where the line is instantaneously and uniformly illuminated, $\theta = \pi/2$ and $\tau=\tau_1=\tau_2$ to yield:

$$I_{L_1} = \frac{(1-\Gamma_0)Q(\omega)}{2\tau\Delta}\left\{1-\Gamma_s \ e^{-2j\omega\tau} -(1-\Gamma_s) \ e^{-j\omega\tau}\right\} \tag{2.23}$$

$$I_{L_2} = \frac{(1-\Gamma_s)Q(\omega)}{2\tau\Delta}\left\{1-\Gamma_0 \ e^{-2j\omega\tau} -(1-\Gamma_0) \ e^{-j\omega\tau}\right\} \tag{2.24}$$

where $\Delta = 1-\Gamma_0\Gamma_s \ \exp(-2j\omega\tau)$ as defined in Equation 2.19b.

The term $Q(\omega)$ has been defined in Equation 2.18k. This function is identified as the total charge accreted on the open circuited line.

$$Q(\omega) = F\left(q(t)\right) \tag{2.25}$$

where

$$q(t) = S\int_0^t i_0(\zeta)d\zeta \tag{2.26}$$

It is interesting to note that the load currents are proportional to line charge accretion, and that the cable in a sense tries to integrate the waveshape of the illuminating X-ray. A detailed exposition of the wave structure follows.

2-3.1 Time Domain Response of a Resistively Loaded Lossless Line

The frequency domain equations for I_{L1} and I_{L2} can be inverted to the time domain by Fourier theory. The equations for load currents are of the form:

$$I_L = \frac{Q'(\omega)}{\Delta} = \frac{Q'(\omega)}{1-\Gamma_0\Gamma_s \ \exp(-2j\omega\tau)} \tag{2.27}$$

Using the binomial series expansion for $1/\Delta$ (reference 2), I_L becomes:

$$I_L = Q'(\omega) \sum_{n=0}^{\infty} (\Gamma_0\Gamma_s)^n \ \exp(-2j\omega n\tau) \tag{2.28}$$

so that for resistive loads, i.e., Γ_0 and Γ_s both real,

$$i_L(t) = \sum_{n=0}^{\infty} (\Gamma_0\Gamma_s)^n \ f(t-2n\tau) \tag{2.29}$$

where f(t) is causal so that the upper limit of the summation of Equation 2.29 may be changed from ∞ to n, and the following definition is implied:

$$(\Gamma_0 \Gamma_S)^n = 1 \quad \text{for } n=0 \tag{2.30}$$

when either Γ_0 or Γ_S or both are zero.

Noting too, that

$$Q(\omega) \exp(-j\omega t_0) = F\left(q(t-t_0)\right) \tag{2.31}$$

enables one to write, for the lossless resistively terminated line:

$$i_{L_1}(t) = \frac{(1-\Gamma_0)}{2\tau_2} \left\{ \sum_{n=0}^{n=\infty} (\Gamma_0 \Gamma_S)^n q(t-2n\tau) \right.$$

$$- \sum_{n=0}^{n=\infty} (\Gamma_0 \Gamma_S)^n \left(1-\Gamma_S \frac{\tau_2}{\tau_1}\right) q\left(t-\tau_0 \cos\theta - (2n+1)\tau\right) \tag{2.32}$$

$$\left. - \sum_{n=0}^{n=\infty} (\Gamma_0 \Gamma_S)^n \left(\frac{\Gamma_S \tau_2}{\tau_1}\right) q\left(t-(2n+2)\tau\right) \right\}$$

$$i_{L_2}(t) = \frac{(1-\Gamma_S)}{2\tau_1} \left\{ \sum_{n=0}^{n=\infty} (\Gamma_0 \Gamma_S)^n q\left(t-\tau_0 \cos\theta - 2n\tau\right) \right.$$

$$- \sum_{n=0}^{n=\infty} (\Gamma_0 \Gamma_S)^n \left(1-\frac{\Gamma_0 \tau_1}{\tau_2}\right) q\left(t-(2n+1)\tau\right) \tag{2.33}$$

$$\left. - \sum_{n=0}^{n=\infty} (\Gamma_0 \Gamma_S)^n \left(\frac{\Gamma_0 \tau_1}{\tau_2}\right) q\left(t-\tau_0 \cos\theta - (2n+2)\tau\right) \right\}$$

where, τ has been defined in Equation 2.18:

These equations are valid only for $\tau > \tau_0 (\cos\theta)$. The case of an air line, i.e., $\tau=\tau_0$ is addressed separately below.

The currents in either resistive load are sums of the waveforms as given in Equation 2.26 for $t \geq 0$ and $g(t)=0$ for $t<0$ for the accreted charge.

These summations can be regrouped by introducing two functions, which are dimensionally currents:

$$i_a(t) \equiv \frac{1}{2\tau_2} \left\{ q(t) - q(t-\tau_0 \cos\theta-\tau) \right\} \qquad (2.34a)$$

$$i_b(t) \equiv \frac{1}{2\tau_1} \left\{ q(t-\tau_0 \cos\theta) - q(t-\tau) \right\} \qquad (2.34b)$$

The load currents become:

$$i_{L_1}(t) = (1-\Gamma_0) \sum_{n=0}^{n=\infty} (\Gamma_0\Gamma_S)^n i_a (t-2n\tau)$$

$$+ (1-\Gamma_0)\Gamma_S \sum_{n=0}^{n=\infty} (\Gamma_0\Gamma_S)^n i_b (t-\tau-2n\tau) \qquad (2.35)$$

$$i_{L_2}(t) = (1-\Gamma_S) \sum_{n=0}^{n=\infty} (\Gamma_0\Gamma_S)^n i_b (t-2n\tau)$$

$$+ (1-\Gamma_S)\Gamma_0 \sum_{n=0}^{n=\infty} (\Gamma_0\Gamma_S)^n i_a (t-\tau-2n\tau) \qquad (2.36)$$

The structure of Equation 2.35 allows one to see that the initially incident pulse on load Z_0 is i_a. This pulse is followed by re-reflectance of i_a off load Z_s, plus the reflection of i_b initially incident on load Z_s, plus its re-reflections.

2-3.2 Resistively Matched Line

Equations 2.35 and 2.36 are vastly simplified when the line is matched at both ends, i.e., when $\Gamma_0 = \Gamma_S = 0$. In this case, there is no reflection off either load, and the load currents are equal to the first incident pulse:

$$i_{L_1}(t) = i_a(t) = \frac{1}{2\tau_2} \left\{ q(t) - q(t-\tau_0 \cos\theta-\tau) \right\} \qquad (2.37)$$

$$i_{L_2}(t) = i_b(t) = \frac{1}{2\tau_1} \left\{ q(t-\tau_0 \cos\theta) - q(t-\tau) \right\} \qquad (2.38)$$

again subject to the restriction that $\tau > \tau_0 \cos\theta$.

35

2-3.3 The Electrically Short Cable

The case of a uniformly illuminated short cable provides some additional clarification of the meaning of Equations 2.35 and 2.36 for load currents. For simplicity, the case where $\theta = \pi/2$ is considered, for which (Equation 2.34) the incident pulses become:

$$i_a(t) = i_b(t) = \frac{1}{2\tau}\left\{ q(t) - q(t-\tau) \right\} \qquad (2.39)$$

where

$$q(t) = S \int_0^t i_0(\zeta)\, d\zeta \text{ with } A(x) = \text{constant}$$

From Equation 2.35, the current in load 1 becomes:

$$i_{L_1}(t) = (1-\Gamma_0) \sum_{n=0}^{n=\infty} (\Gamma_0 \Gamma_S)^n \left\{ i_a(t-2n\tau) + \Gamma_S i_a(t-\tau-2n\tau) \right\} \qquad (2.40)$$

The current in load 2 is also given by Equation 2.40 with Γ_0 interchanged with Γ_S, because the cable is assumed to be instaneously and uniformly illuminated.

Since the one way cable transit time is defined by Equation 2.18f, the pulse i_a strictly goes to zero as τ goes to zero, and therefore, i_{L_1} goes to zero too. However, if one writes for $i_a(t)$ the integral expression

$$i_a(t) = \frac{1}{2\tau}\left\{ q(t) - q(t-\tau) \right\} = \frac{S}{2\tau} \int_{t-\tau}^t i_0(\zeta)\, d\zeta \qquad (2.41)$$

one may approximate the integral by

$$\int_{t-\tau}^t i_0(\zeta)\, d\zeta \cong \tau\, i_0(t) \qquad (2.42)$$

if i_0 is slowly varying over the time interval τ. This relation provides a definition of what constitutes an electrically short cable with respect to a drive pulse $i_0(t)$. With this relation, $i_a(t)$ simply becomes:

$$i_a(t) = \frac{S}{2} i_0(t) \qquad (2.43)$$

36

Now if load 1 is matched so that $\Gamma_0 = 0$ and load 2 is open so that $\Gamma_S = 1$, then from Equation 2.40

$$i_{L_1}(t) = i_a(t) + i_a(t-\tau) \tag{2.44}$$

independent of cable length. When τ is small so that

$$i_a(t) = i_a(t-\tau) = \frac{S}{2} i_0(t) \tag{2.45}$$

then the well known result

$$i_{L_1}(t) = S i_0(t) \tag{2.46}$$

is obtained.

The case where load 1 and load 2 are equal and resistive is somewhat more complex, but tractable. In this case $\Gamma_0 = \Gamma_S = (\eta-1)/(\eta+1)$ where $\eta = R/Z_c$. Defining $r = \Gamma_0 = \Gamma_S$ allows one to write from equation 2.40.

$$i_{L_1}(t) = 2\left(\frac{1}{1+\eta}\right) \sum_{n=0}^{\infty} r^{2n}\left\{ i_a(t-2n\tau)+r \, i_a(t-\tau-2n\tau) \right\} \tag{2.47}$$

again independent of cable length. Now assuming, for any value of n, that τ is small enough so that

$$i_a(t-2n\tau) \stackrel{\circ}{=} i_a(t-\tau-2n\tau) \tag{2.48}$$

allows one to write

$$i_{L_1}(t) = 2 \frac{1}{1+\eta} \sum_{n=0}^{\infty}\left\{ r^{2n} (1+r) \, i_a(t-2n\tau) \right\} \tag{2.49}$$

One may, with suitable caution, go further and assume that

$$i_a(t-2n\tau) = i_a(t) \tag{2.50}$$

for all times of interest, and then by identifying the binomial expansion for $(1-r^2)^{-1}$ one obtains:

$$i_{L_1}(t) = 2\left(\frac{1}{1+\eta}\right)\left(\frac{1}{1-r}\right) i_a(t) = i_a(t) \tag{2.51}$$

With $i_a(t) = S/2\ i_0(t)$ one finally obtains for the short cable

$$i_{L_1}(t) = \frac{S}{2}\ i_0(t) \tag{2.52}$$

This result simply states that the cable source term divides equally between the two loads. However, the application of Equation 2.52 to any specific case depends on load resistance R and pulse shape i_0. Clearly, for a rapidly varying $i_0(t)$, or a bipolar $i_0(t)$, both 2.42 and 2.50 may be readily violated, and effects arising from cable energy storage may become important to the computation of load current rise time/fall time, as well as to the duration of the trailing edge of the load current pulse. The effects of r are also implicit in the use of 2.50. As r^{2N} approaches an acceptably small number so that Equation 2.50 need only be valid for n·N, then 2.52 is an acceptable approximation. Therefore, the closer r is to zero, the less terms will be necessary in 2.49 for convergence and the more accurate 2.52 will be for a given $i_0(t)$ and given ι small. But even for small ι, when $|r|\rightarrow 1$, Equation 2.52 is not valid. As $r \rightarrow +1$, the cable capacitance determines the load pulse shape, since the cable will begin to charge faster than charge can flow thru R. As $r \rightarrow -1$, the cable will ring, albeit at a high freuqency, because the energy absorbed per cycle is low, regardless of ι. Clearly, when $r = -1$, the cable is truly shorted and being lossless, will ring forever so that 2.52 is not valid at all.

Thus, the derivation of Equation 2.50 is offered as a heuristic indication that the more complex expression of Equation 2.40 is consistent with elementary Kirchoff's laws applied to lumped element representations of the cable source problem.

2-4 ILLUSTRATE GENERIC RESULTS

Because the load current pulse waveforms previously derived are quite complex summations of pulses, this section provides some numerical and graphical results which highlight the nature of cable direct drive.

In Section 2-4.1, important energy relations are provided which relate the absorbed load energy to load resistance, to time, and to cable length.

In Section 2-4.2, the effects of angle of incidence and cable length for a square pulse driver on a matched line are developed.

2-4.1 Energy-Time Relations in Various Resistive Loads

An important phenomenon in a cable with distributed current sources is that the energy which can be extracted from the cable is a strong function of the termination loads. This section provides some insight as to what these terminal effects are.

Equations 2.23 and 2.24 have been analyzed via a numerical Fourier inverse with a uniformly distributed critically damped current driver of the form:

$$i_o(t) = I_D\left(\frac{t}{t_m}\right)\exp\left(1-\frac{t}{t_m}\right)u(t) \tag{2.53}$$

where I_D = peak current source in amps per meter, t_m = time of peak amplitude, and $u(t)$ = Heaviside unit step function. The cable is assumed to be instantaneously illuminated, so that $\theta = \pi/2$. The cable is assumed to be loaded at either end with a resistor R so that $Z_o = Z_s = R$ and $\Gamma_o = \Gamma_s = r$. With I_D normalized to unity, the energy in each load has been obtained for study by a computation of the running integral

$$E_L(t) = R \int_0^t i_L^2(\tau)d\tau \tag{2.54}$$

where $i_L(t)$ is the load current as a function of time. The integration was performed via a simple Simpson's rule from the time trace obtained by the numerical Fourier inversion of the current spectrum.

The results of these computations are shown in Figure 10 where the normalized energy has been plotted as a function of $\zeta = R/Z_C$ with $t = \infty$. E_L has been arbitrarily normalized to indicate relative behavior of E_L versus ζ and cable length S. Since S is proportional to cable transit time τ (Equation 2.18f), S has been indicated by τ. The time T_{90} is a measure of driver pulse duration, and is equal to the time when the driver pulse delivers 90% of its total energy to a resistive load via the action integral relation:

$$0.9 \int_0^\infty i_0^2(t)dt = \int_0^{T_{90}} i_0^2(t)dt \qquad (2.55)$$

The results of Figure 10 show that, as cable length is increased, the total energy absorbed by the loads is increased. Furthermore, Figure 10 shows that as load impedance is increased, the energy the load absorbs is also increased. For the geometry analyzed, equal loads at either end, each load receives one-half the energy delivered by the cable. In the limit, for $R \gg Z_C$, the loads absorb all the energy in the cable when open circuited, namely:

$$E_{max} = \frac{1}{2} Q_D^2/C \qquad (2.56)$$

where Q_D is the total accreted charge and $C = \tau/Z_C$ is the total cable capacitance. For the pulse shape under consideration Q_D is given by:

$$Q_D = SI_D \text{ e tm} = \lim_{t \to \infty} q(t) \qquad (2.57)$$

where e is the Napierian base. Since Q_D is proportional to cable length, as is total cable capacitance, the maximum energy available from the cable is also proportional to cable length.

On the other hand, for $R \ll Z_C$, the energy absorbed is significantly less than the total energy available in an open circuited cable. The physical explanation of this phenomenon lies in the fact that low impedance loads suppress the line voltage as incident waves are reflected, thereby reducing the amount of energy the cable can provide. It is an important, as well as interesting observation to note that the current drivers are assumed independent of line voltage and that consequently, the conservation of charge flow is the controlling law, making

40
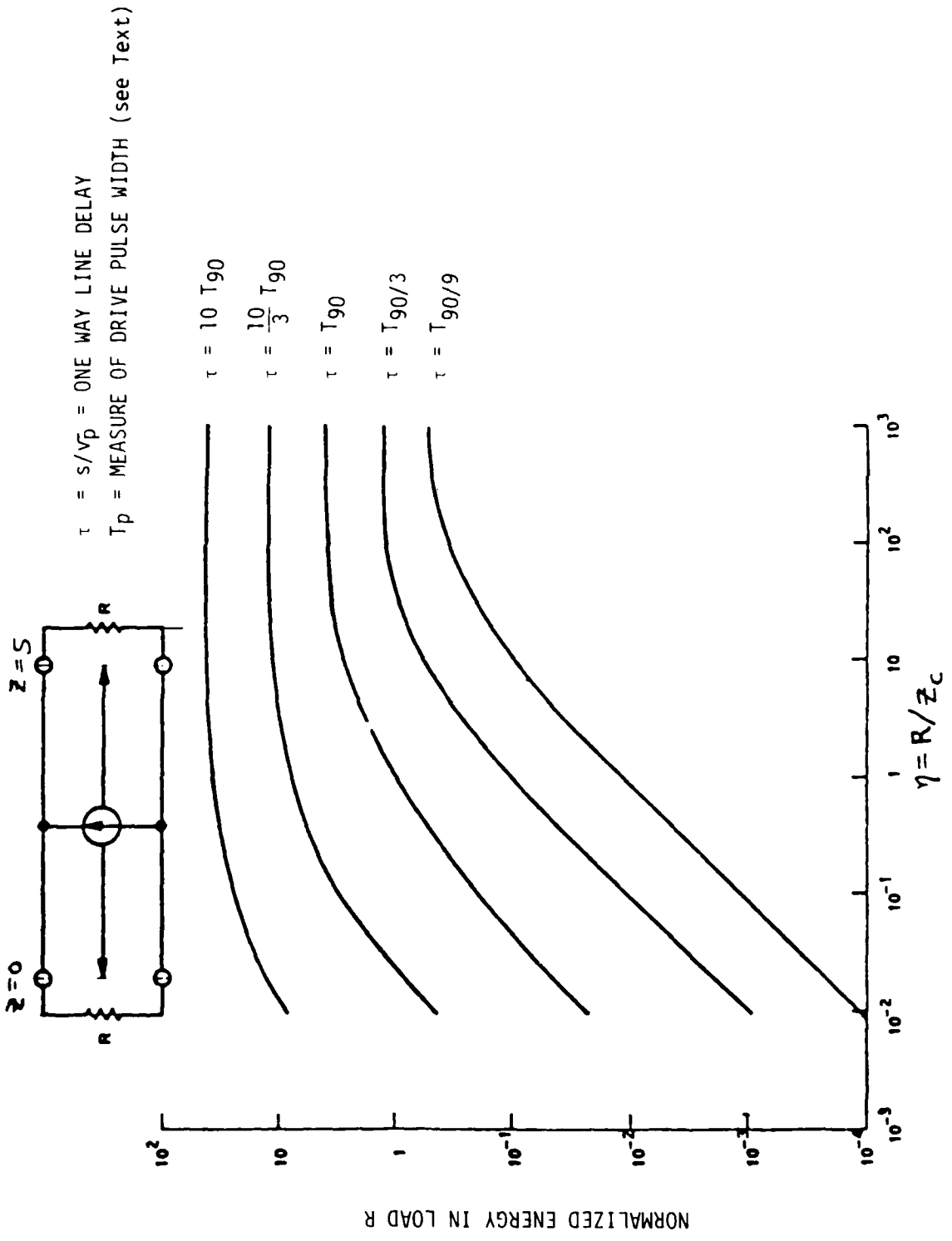
Figure 10. Normalized load energy versus normalized load resistance

the available cable energy strictly a function of the voltage level which the cable is allowed to build up to.

Of interest in Figure 10 is the knee in the energy curve, i.e., the value of (R/Z_c) below which energy falls off as (R/Z_c) is decreased. The location of the knee is a function of the electrical cable length, relative to drive pulse duration T_{90}. A cable possessing a one way transit time τ which is signficantly longer than the duration of the drive pulse i_0 will almost fully charge before *the effects of end terminations can act to reduce line voltage.* Thus, longer cables are capable of delivering higher energies regardless of termination.

Some specific examples have been plotted in Figures 11 through 15. The current driver has been taken as a square pulse with a constant $I_D \cdot T_P$ product of 30 Ans/m. For these figures the cable length has been held constant at 3m with a dielectric constant equal to 9. The curves were derived from Equation 2.54 using Equations 2.32 and 2.33 as the load currents through pure resistive loads. The five plots present a family of curves for loads between 0.05Ω to $50k\Omega$ and for pulse widths between 300ns to 3ns.

The effect of the dielectric constant on the rate of energy absorbed in the load resistance for values of Z_L between 0.05Ω to $50k\Omega$ is shown in Figures 16 through 19 for value of $\varepsilon=1$ (vacuum) to 81 (water). For values of most typical cable dielectric materials with ε_r between 1 and 3 the variation in energy for matched loads is relatively small and increase to nearly a factor of two between these limits for values of $\eta >> 1$ or $<< 1$.

The effect of the cable length on the temporal dependence of the energy absorbed in the load resistance is shown in Figures 20 through 23. As the cable length increases from 0.3m to 30m

$$E(t,\eta) \longrightarrow E(t,\eta^{-1})$$

and $\qquad E_{max}(\eta), \ E_{max}(\eta^{-1}) \longrightarrow E_{max}(Z_L=Z_c)$

That is the maximum energy in the load impedance becomes independent of the load impedance for long cables. Furthermore, the maximum energy limit increases as the cable length increases from $0.033\mu J$ for $S = 0.3m$ to $33\mu J$ for $S = 30m$.

42
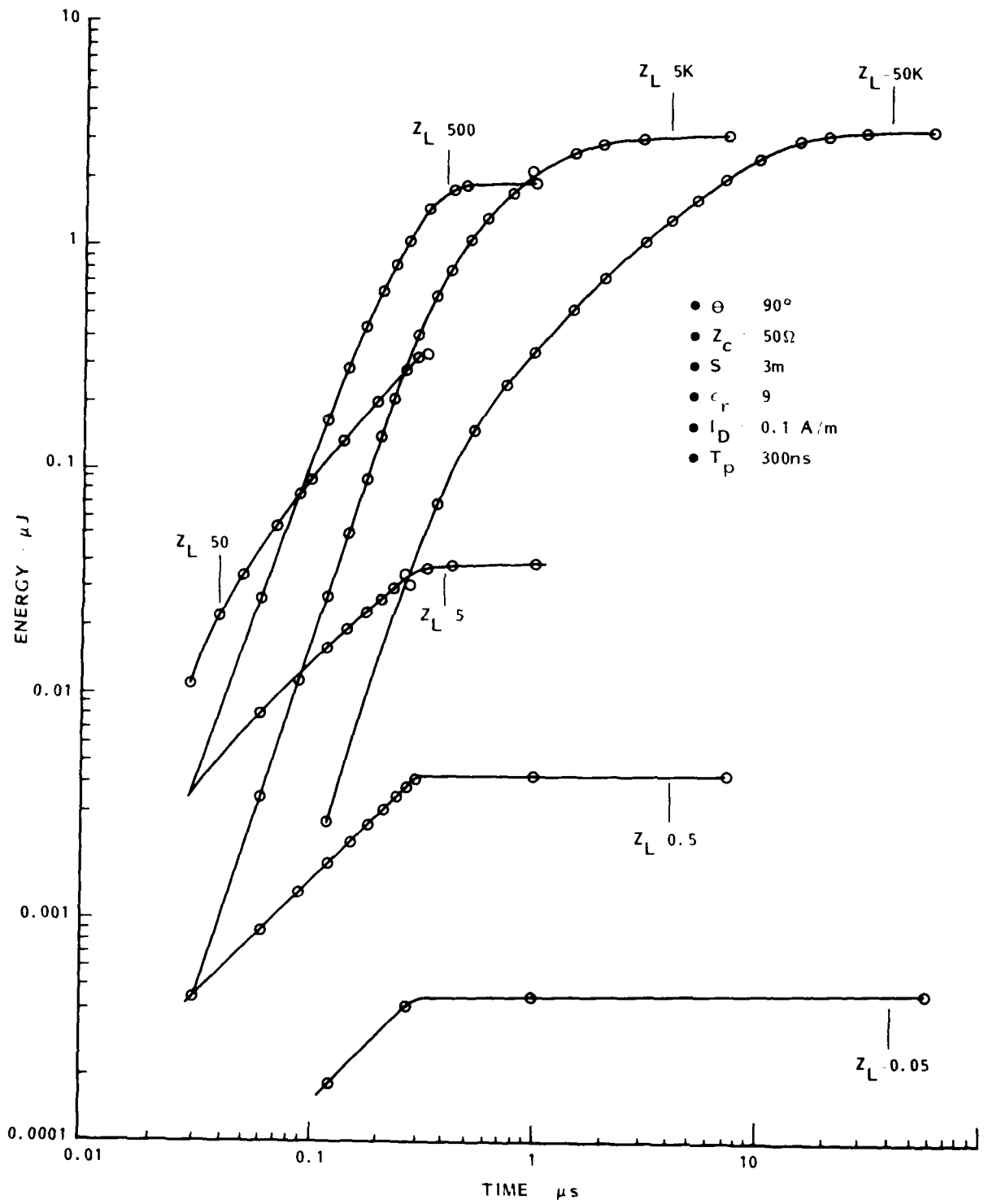
Figure 11.   Absorbed load energy versus time for I_D = 0.1A/m and ΔT_p=300ns (ϵ_r=9)

43
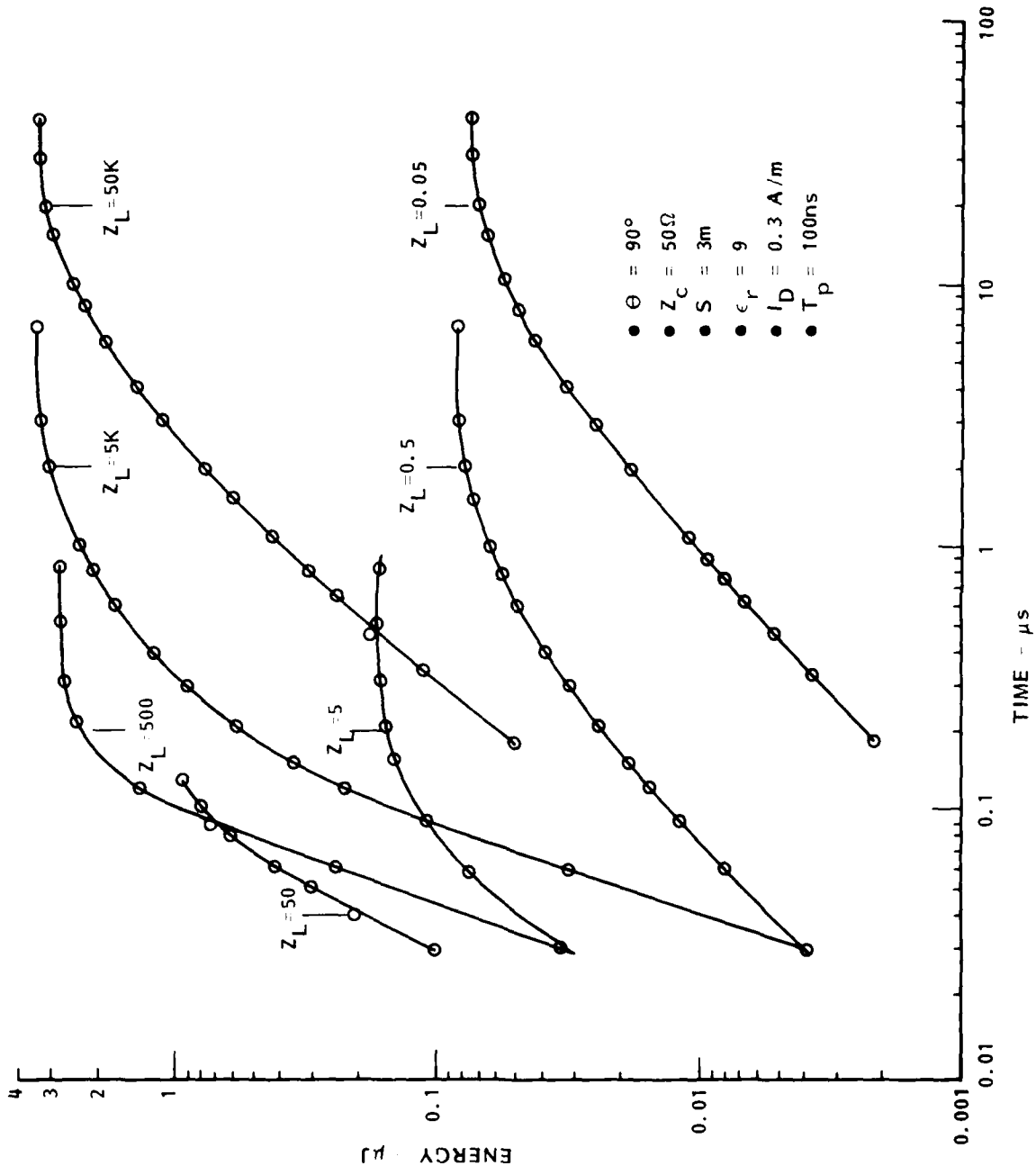
Figure 12. Absorbed load energy versus time for $I_D = 0.3 A/m$ and $T_p = 100ns$ ($\epsilon_r = 9$)

44
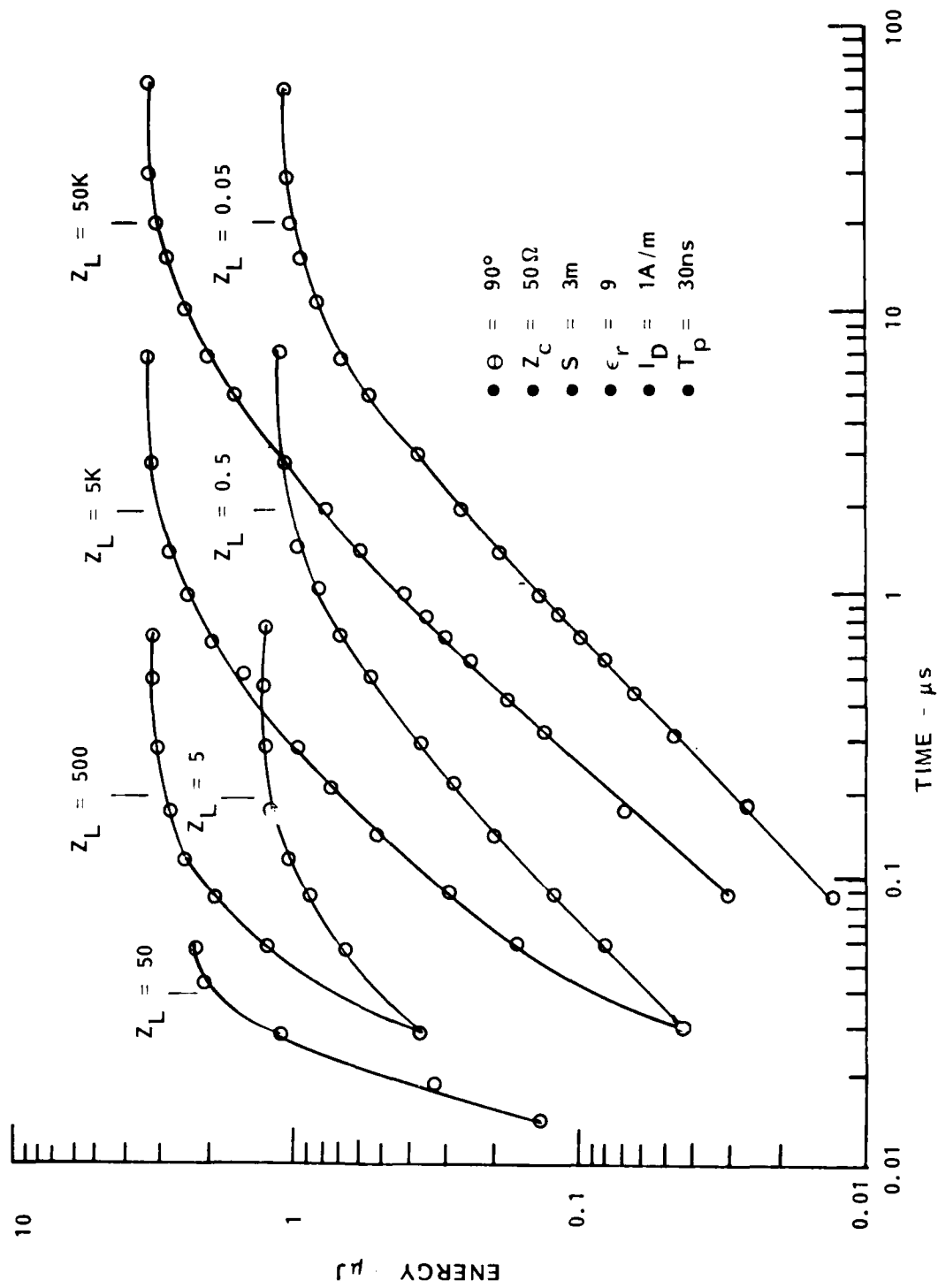
Figure 13. Absorbed load energy versus time for $I_D = 1nA/m$ and $T_p=30ns$ ($\epsilon_r=9$)

45
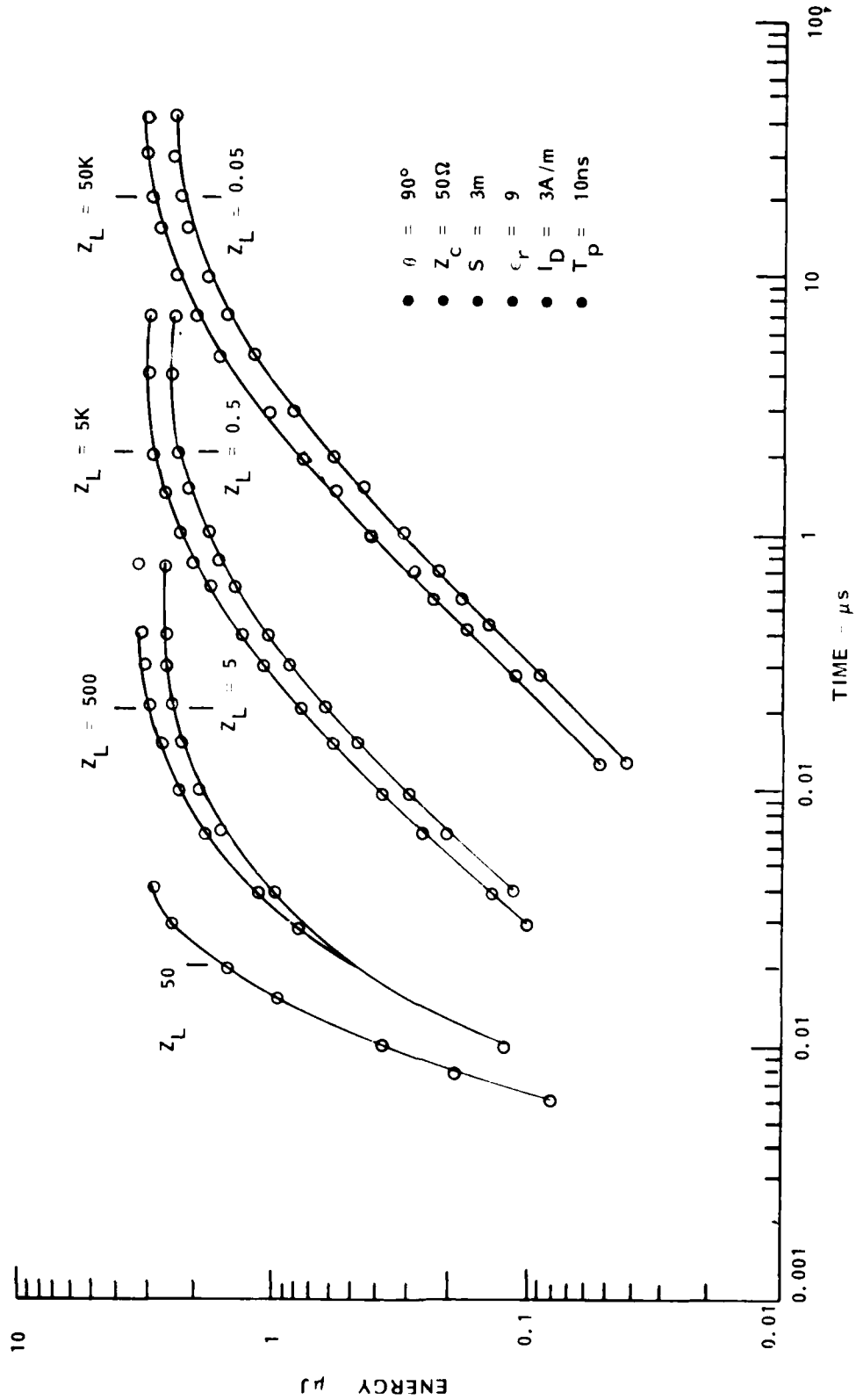
Figure 14. Absorbed load energy versus time for $I_D = 3A/m$ and $T_p = ns$ ($\epsilon_r = 9$)

46
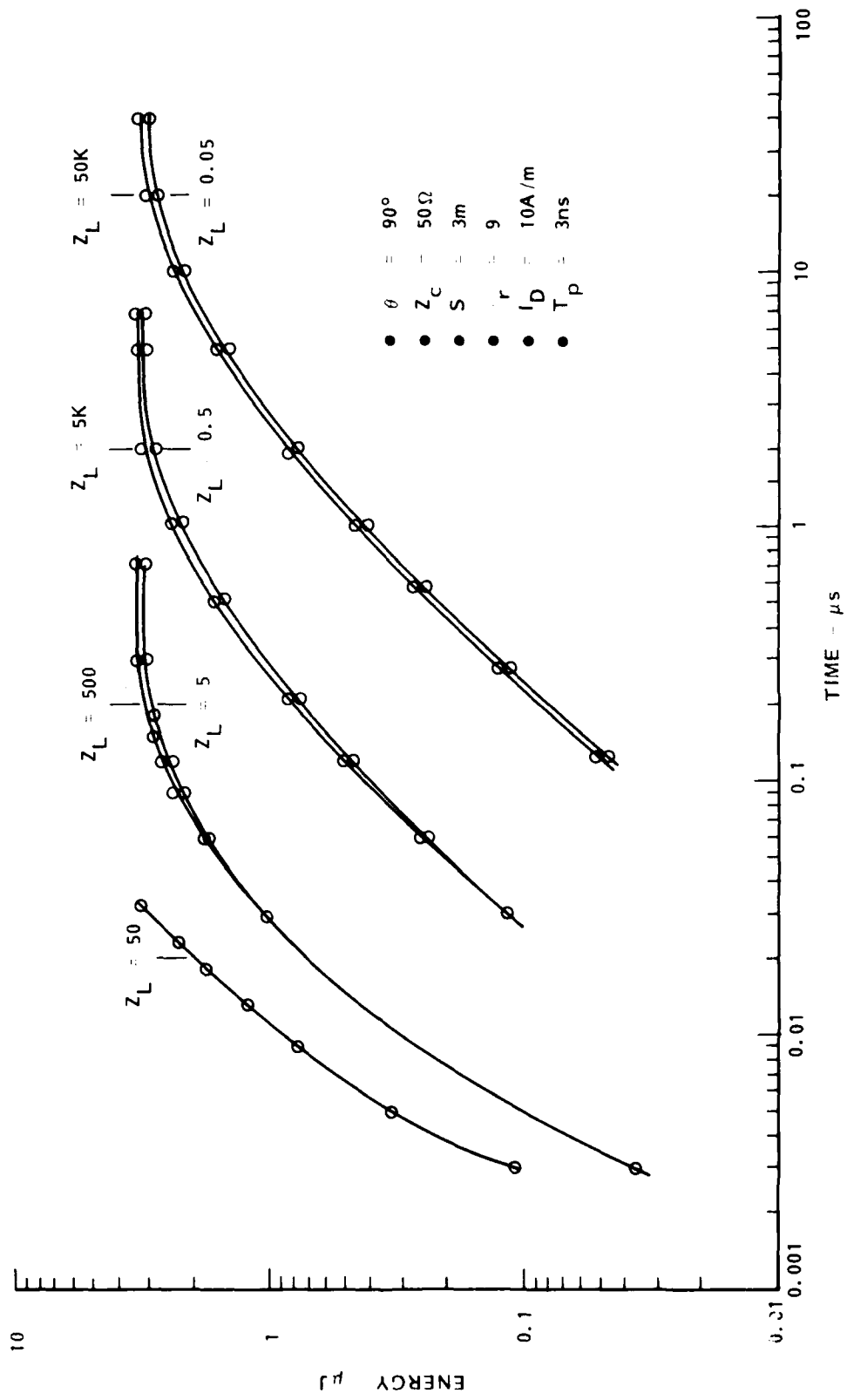
Figure 15. Absorbed load energy versus time for $I_D = 10A/m$ and $T_p = 3ns$ ($\epsilon_r = 9$)

47
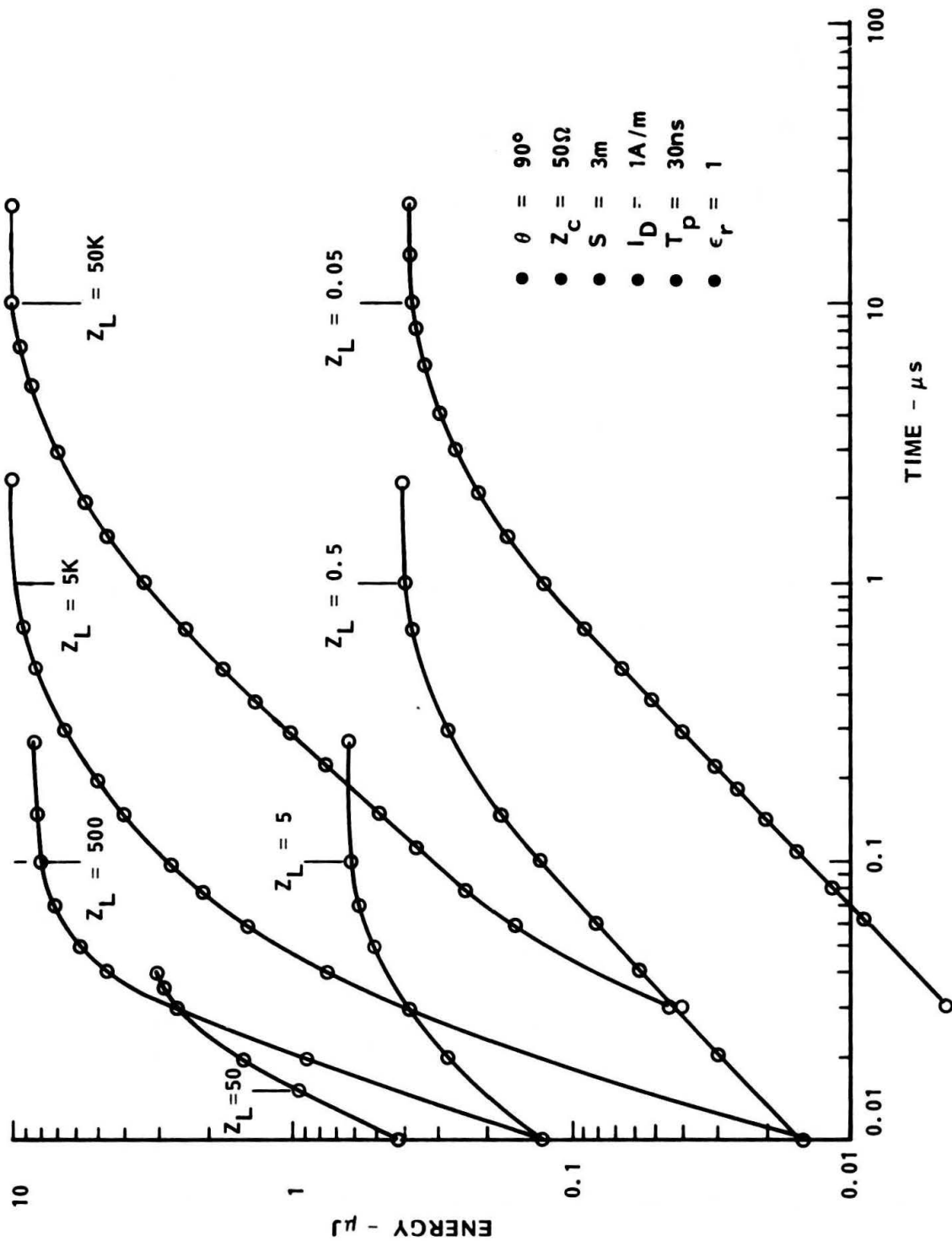
Figure 16. Absorbed load energy versus time for $\epsilon_r=1$ ($I_D = 1A/m$, $T_p=30ns$)

48
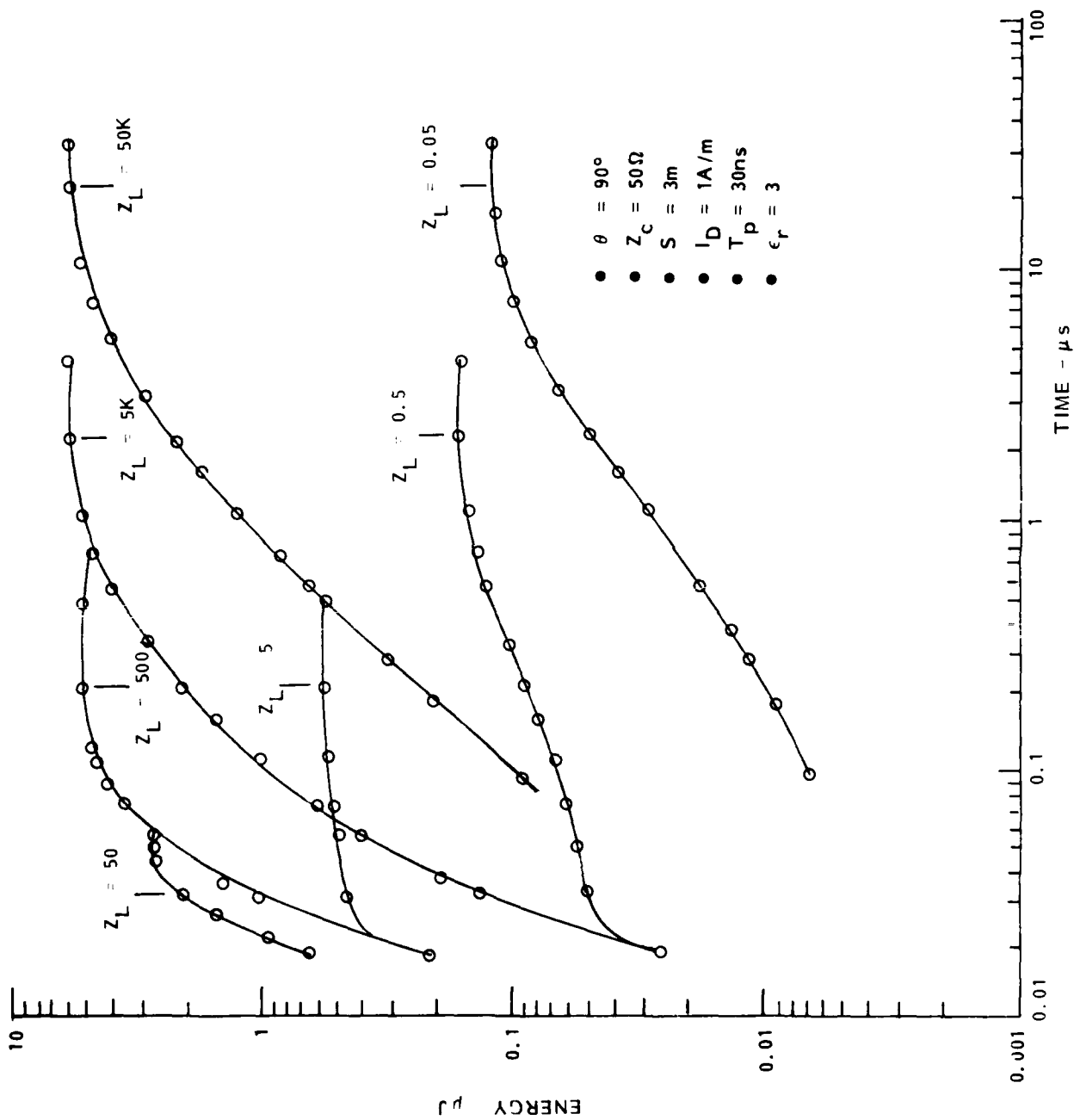
Figure 17. Absorbed load energy versus time for $\epsilon_r = 3$ ($I_D = 1A/m$, $T_p = 30ns$)

49
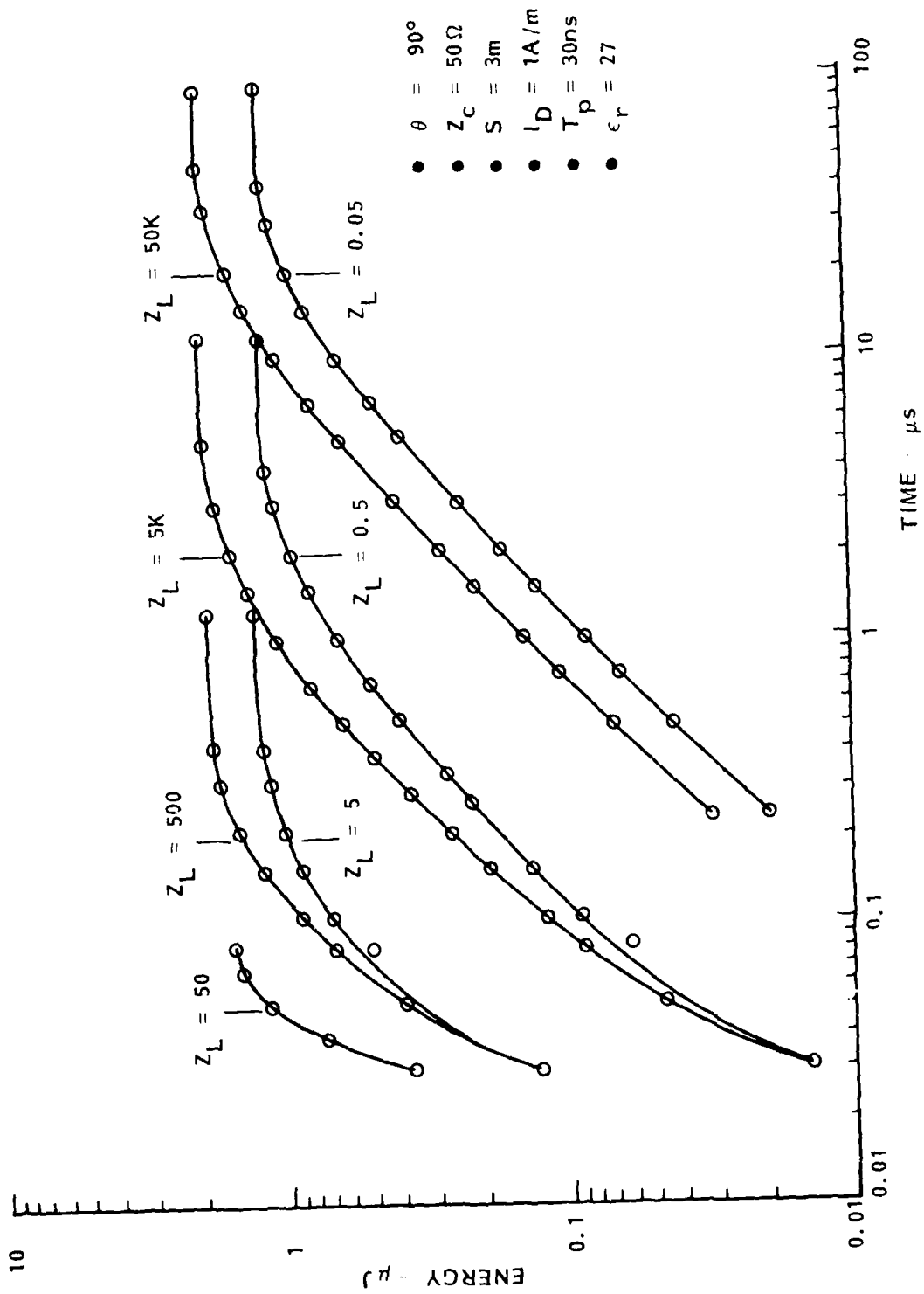
Figure 18. Absorbed load energy versus time for $\epsilon_r = 27$ ($I_D = 1/m$, $T_p = 30ns$)

$Z_L = 50K$

$Z_L = 0.05$

$Z_L = 5K$

$Z_L = 0.5$

$Z_L = 500$

$Z_L = 5$

$Z_L = 50$

- Θ = 90°
- Z_c = 50Ω
- S = 3m
- I_D = 1A/m
- T_p = 30ns
- ϵ_r = 81

TIME μs

ENERGY μJ

10

1

0.1

0.01

0.01   0.1   1   10   100   1000
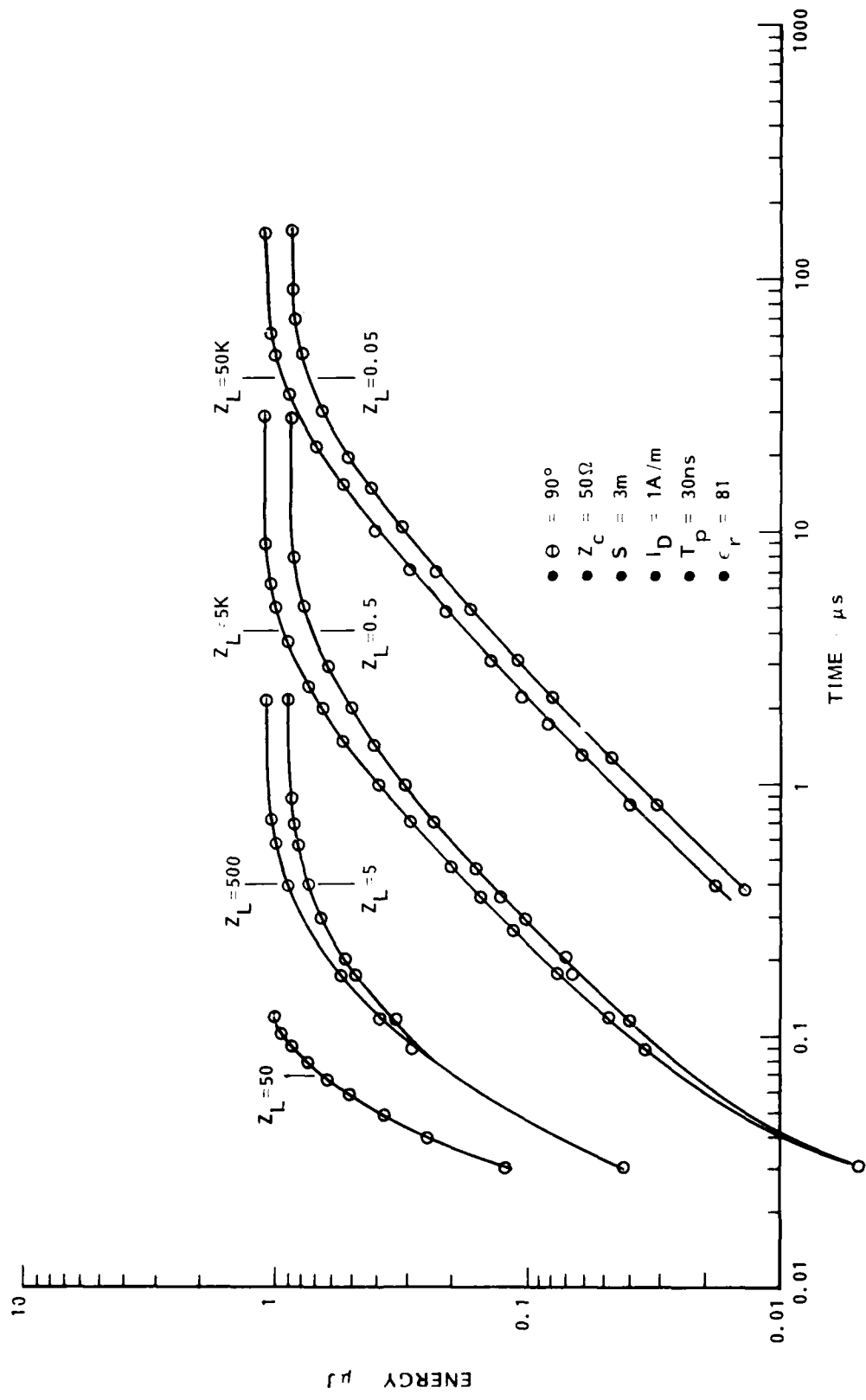
Figure 19. Absorbed load energy versus time for ϵ_r = 81 (I_D = 1A/m, T_p=30ns)
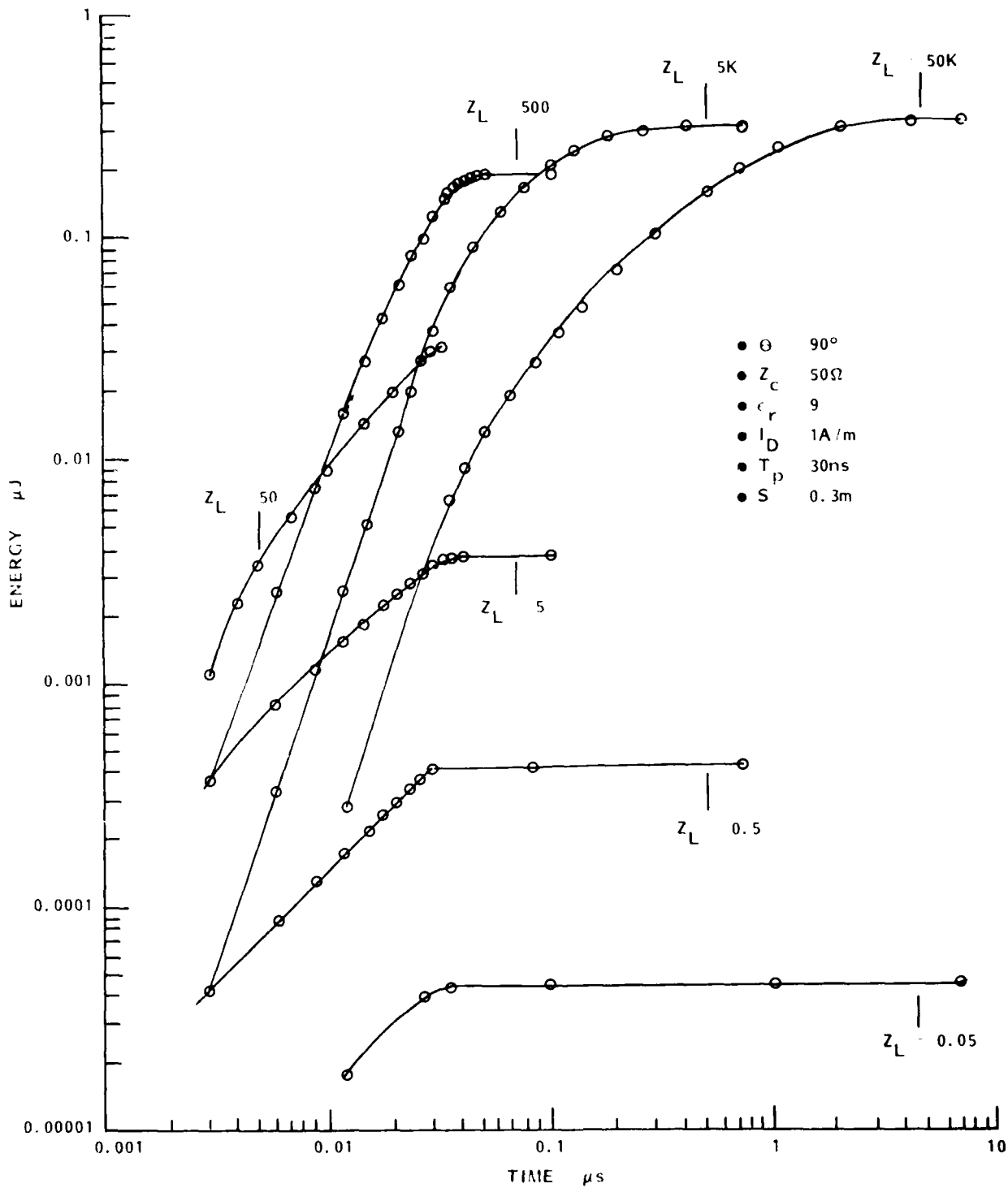
Figure 20. Absorbed load energy versus time for S=0.3m (I_D = 1A/m, T_p=30ns, ϵ_r=9)
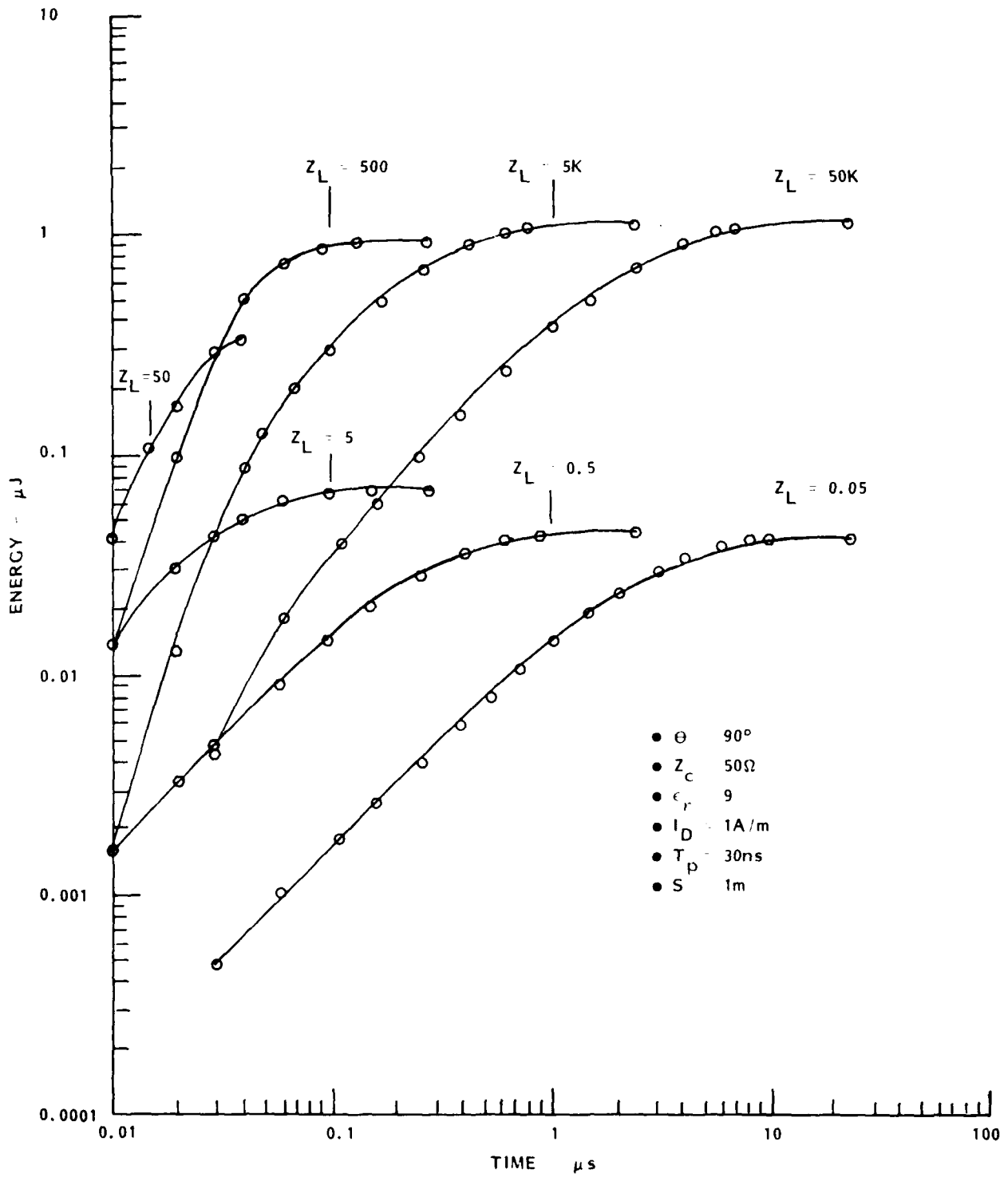
Figure 21.   Absorbed load energy versus time for S=1m (I_D = 1A/m, T_p=30ns, ϵ_r=9)
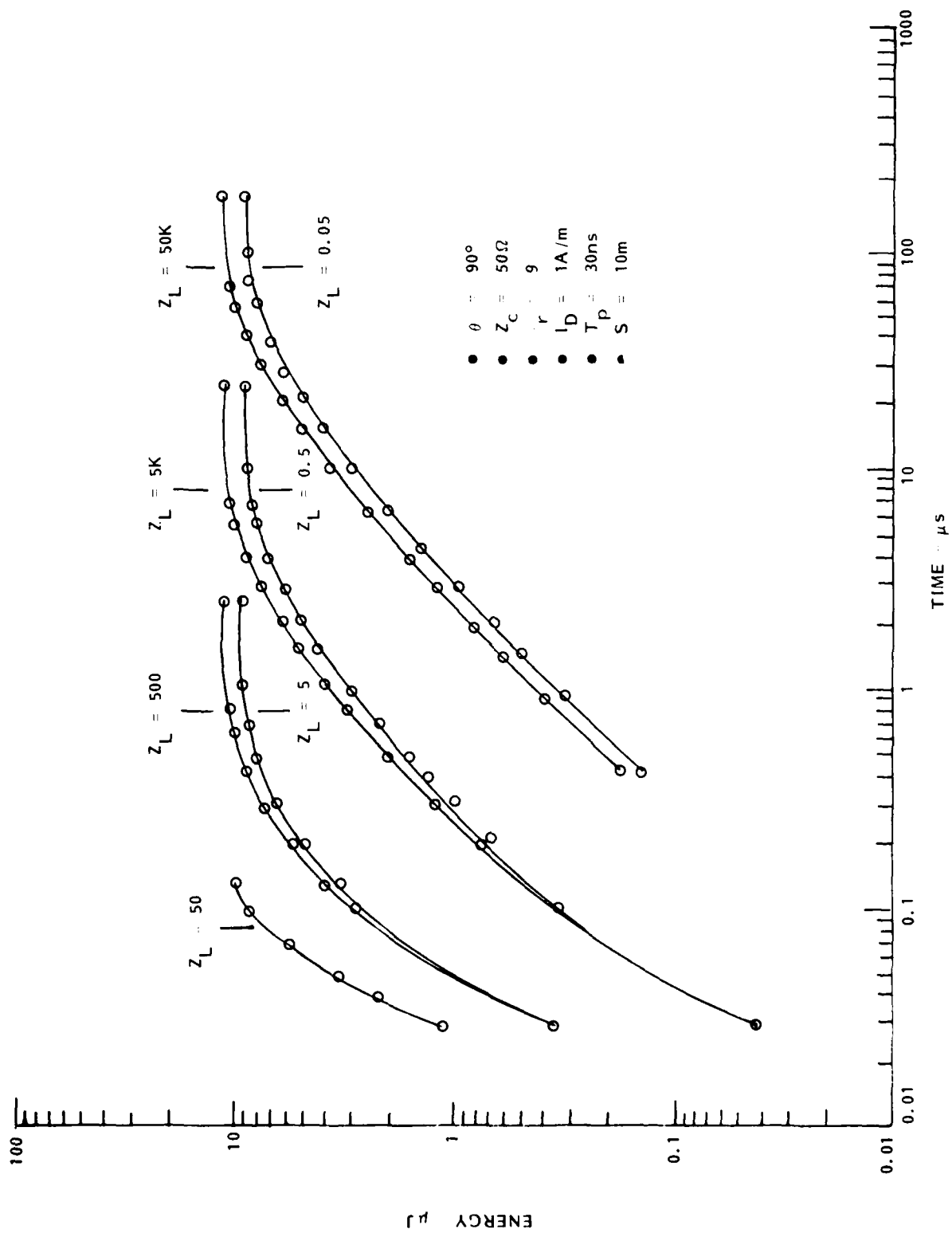
Figure 22. Absorbed load energy versus time for S=10m ($I_D = 1A/m$, $T_p=30ns$, $\epsilon_r=9$)
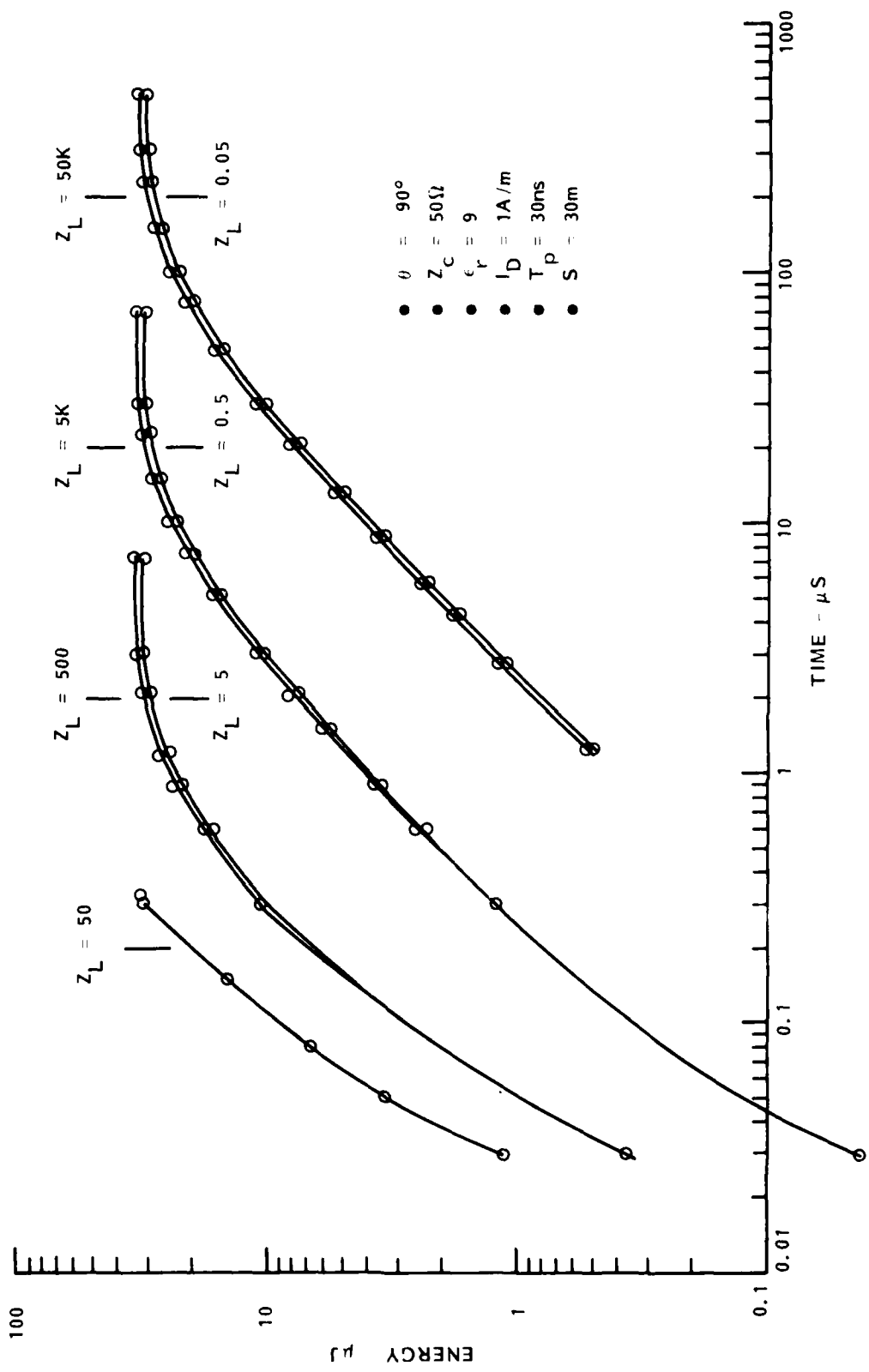
Figure 23. Absorbed load energy versus time for S=30m (I_D = 1A/m, T_p=30ns, ϵ_r=9)

55

The effect of the characteristic impedance on the absorbed energy is shown in Figure 24 for $Z_c = 5\Omega$ and 500Ω and a family of load resistances between 0.005Ω and $500k\Omega$.

The energy limit (E_{max}) which is absorbed in the load impedance is summarized in Figures 25 to 28 as a function of ζ, the load impedance normalized to the cable characteristic impedance. The summaries show the variation of E_{max} versus η in terms of a set of parametric curves. The parameter variables modeled are: 1) pulse width ($T_p=3$ to 300ns) with constant total charge, i.e., $I_0 \cdot T_p =$ constant ($30A \cdot ns/m$) in Figure 25, 2) dielectric constant ($\epsilon=1$ to 81) in Figure 26, 3) cable length (s=0.3 to 30m) for three values of ϵ_r (1,3,9) in Figure 27 and 4) cable impedance ($Z_c=5$ to 500Ω) in Figure 28.

Figures 29 and 30 summarize the maximum energy absorbed in the load as a function of the cable dielectric constant for a family of normalized load impedances. The two figures consider the special cases for cable characteristic impedance of 50Ω and free space (377.). Figure 31 shows the variation of absorbed energy with dielectric constant similar to Figure 29 but with the pulse width increased from 30ns to 90ns for the same I_0 (1A/m). In general the absorbed energy increases as the pulse width increases at a rate which is higher for larger η. An analogous situation is illustrated in Figure 32 where the cable length is shortened from 3m to 0.3m in comparison to the parameters in Figure 29 with the pulse width held at 30ns.

Equally important as the total energy into each load is the rate at which the energy is deposited, since energy rate is a measure of dissipated power. As indicated by the time expansion for $i_L(t)$ with $\eta=\cdot/2$ in Equation 2.40, the load current is a series of pulses whose shape depends on line delay τ and reflection coefficients Γ. Thus, the instantaneous power in each load can be expected to peak periodically. In a real system, the instantaneous power may not be as important as the total energy accrued in the load by N successive reflections. In order to measure the energy rate then, an arbitrary time reference is introduced, namely the time at which 90 percent of the total energy is absorbed by that load, denoted t_{90}. The underlying reason for this time reference lies in the fact that, theoretically, a mismatched cable will have finite, albiet vanishingly small currents for
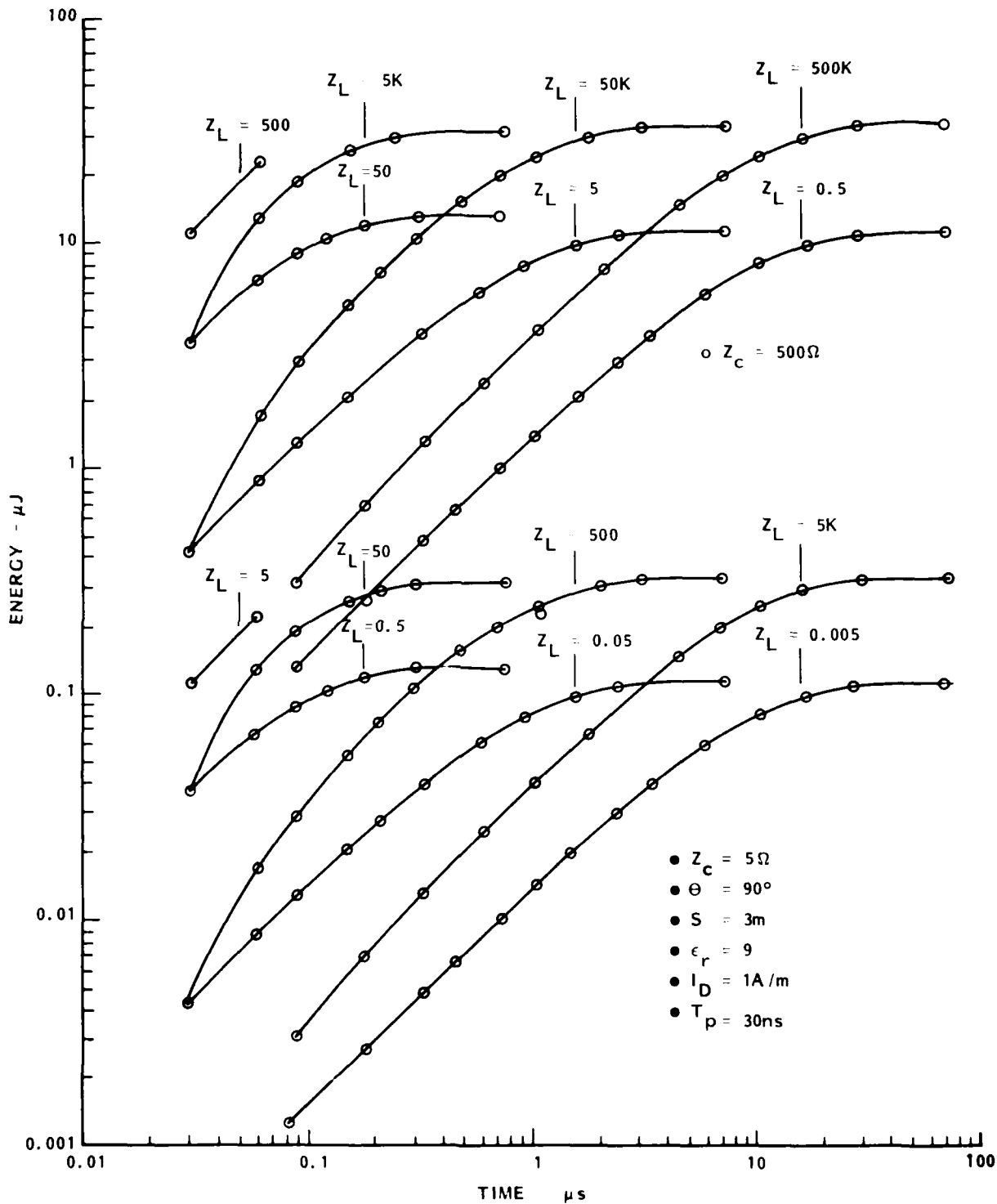
Figure 24. Absorbed load energy versus time for line impedance of 5Ω and 500Ω
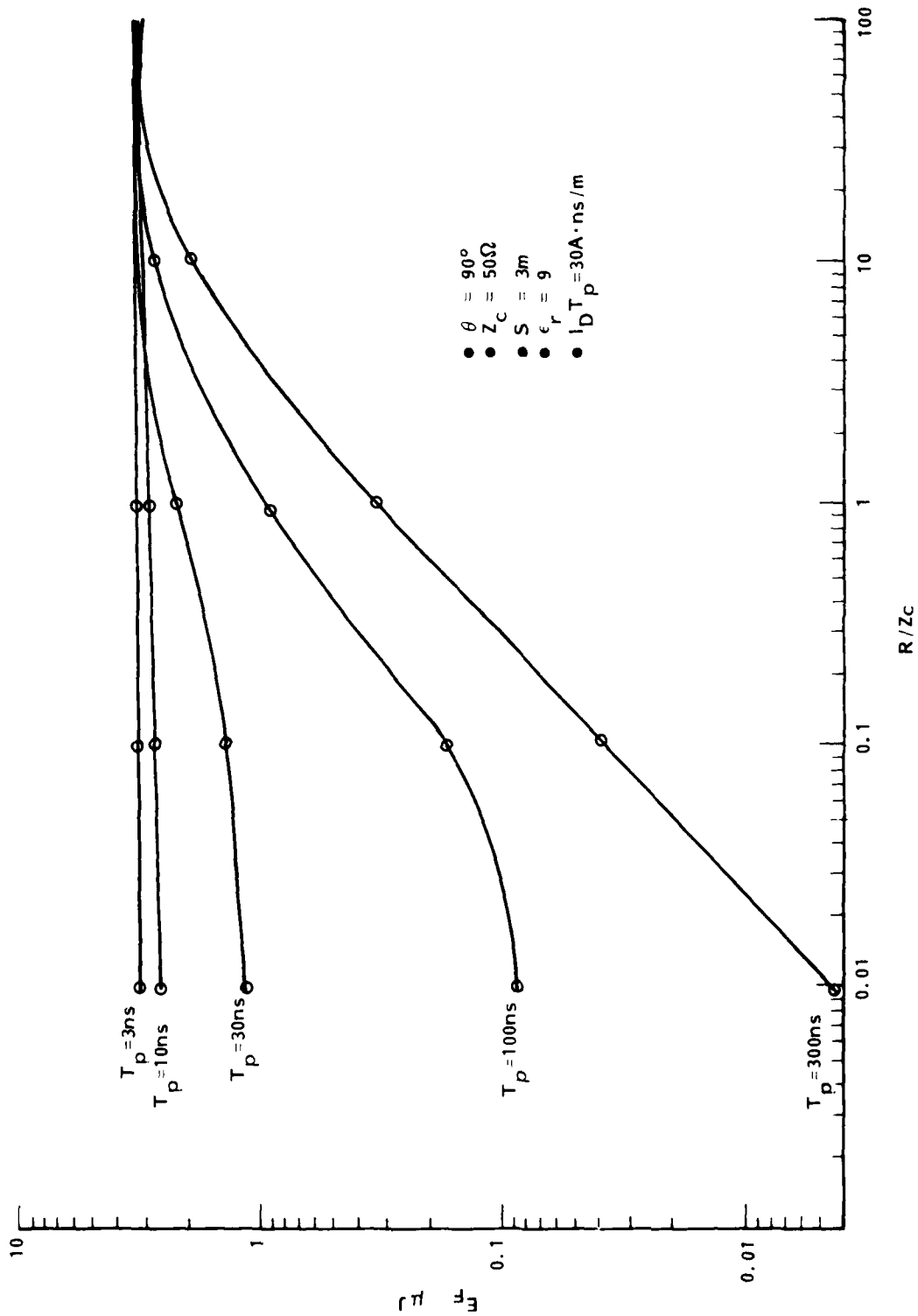
Figure 25. Maximum absorbed load energy versus normalized load impedance for $I_D T_p = 30A\cdot ns/m$

58
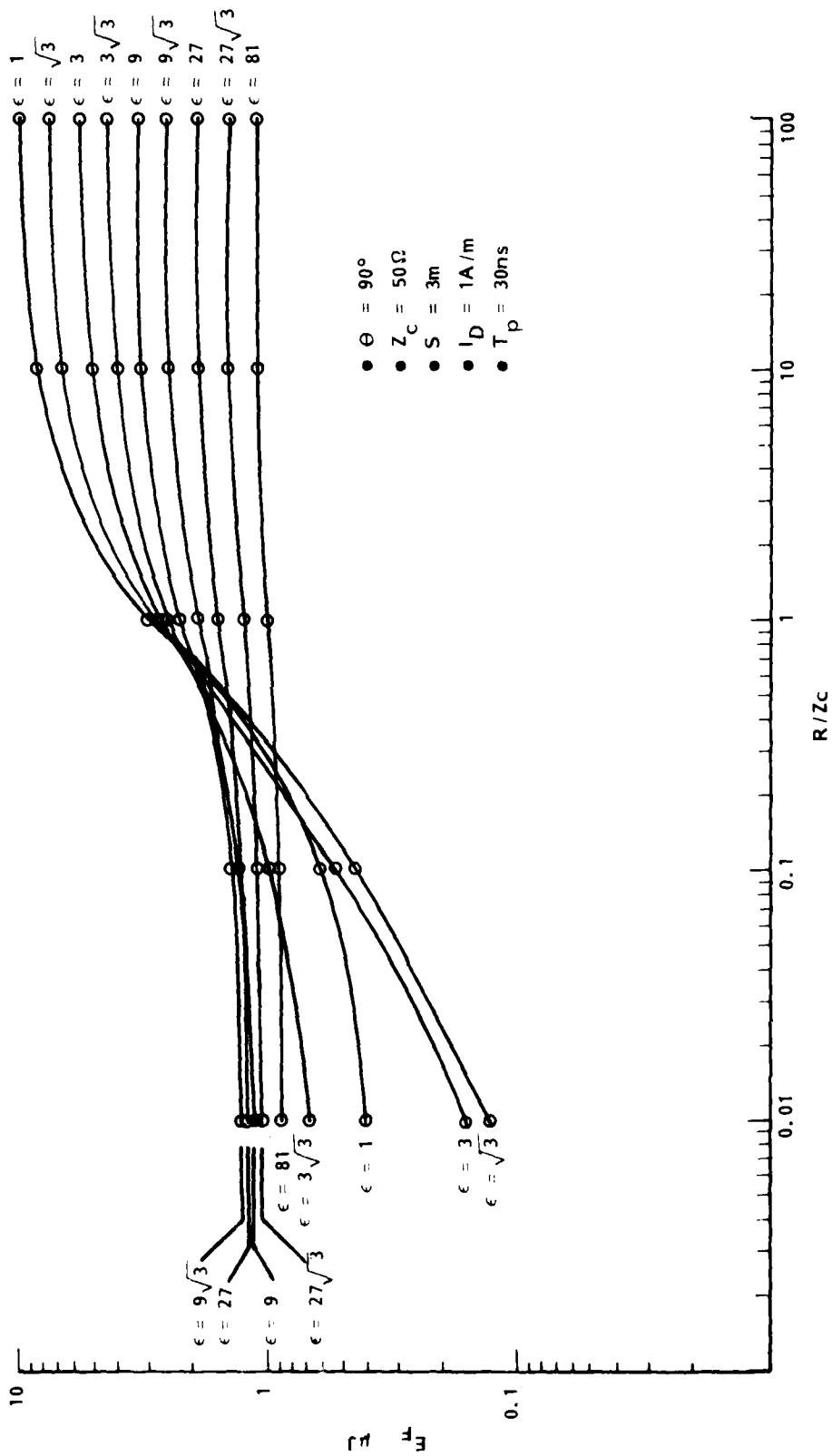
Figure 26. Maximum absorbed load energy versus normalized load impedance for various ϵ_r

10^{-4}

S = 30m

S = 10m

10^{-5}

E_F, JOULES

10^{-6}

S = 3m

10^{-7}

S = 1m

● Θ = 90°
● Z_c = 50Ω
● I_D = 1A/m
● T_p = 30ns

▽ ϵ_r = 1
△ ϵ_r 3
○ ϵ_r = 9

10^{-8}

10^{-9}

S = 0.3m

10^{-10}

0.01   0.1   1   10   100

R/Z_c
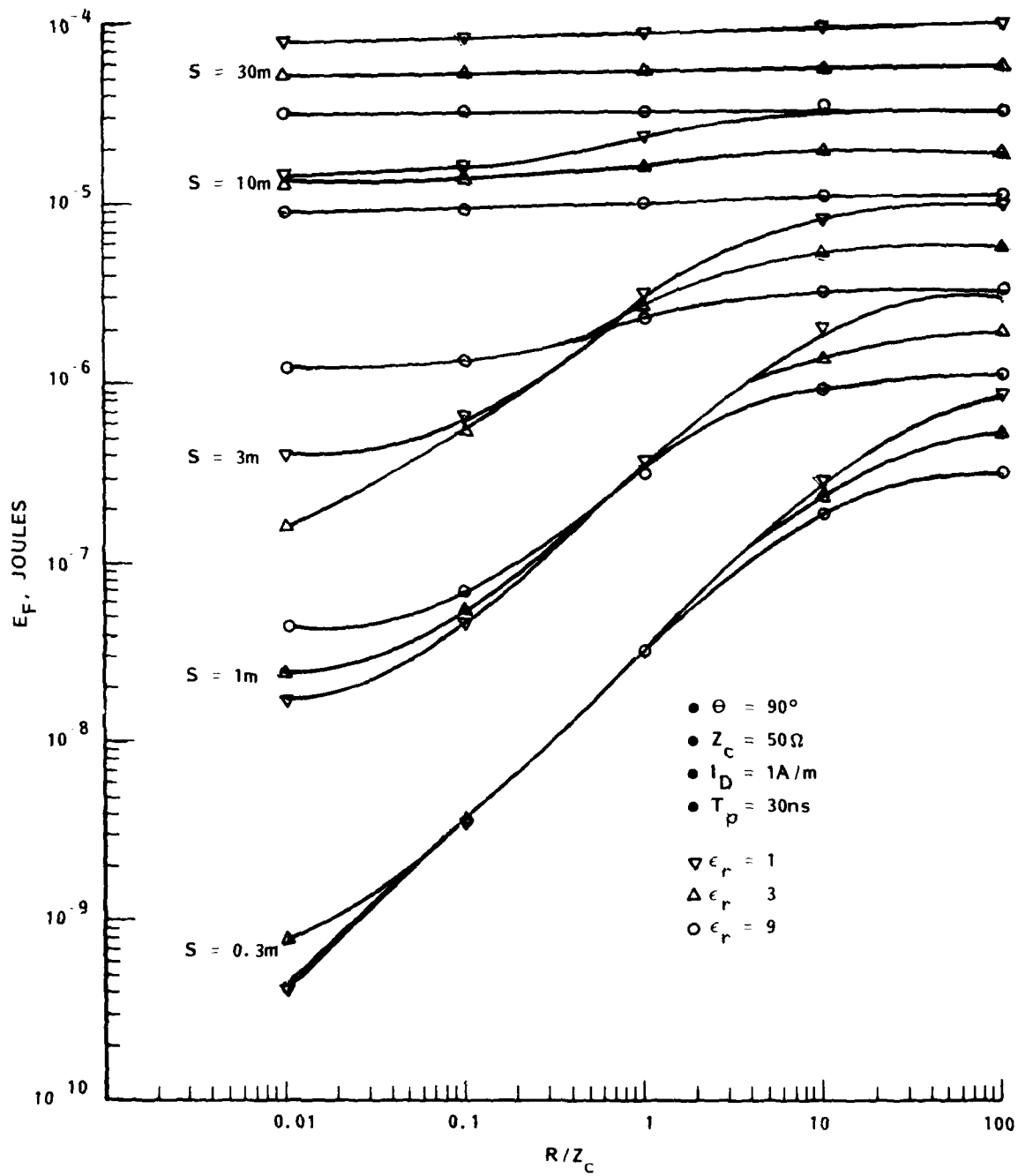
Figure 27.   Maximum absorbed load energy versus normalized load
impedance for various line lengths

60
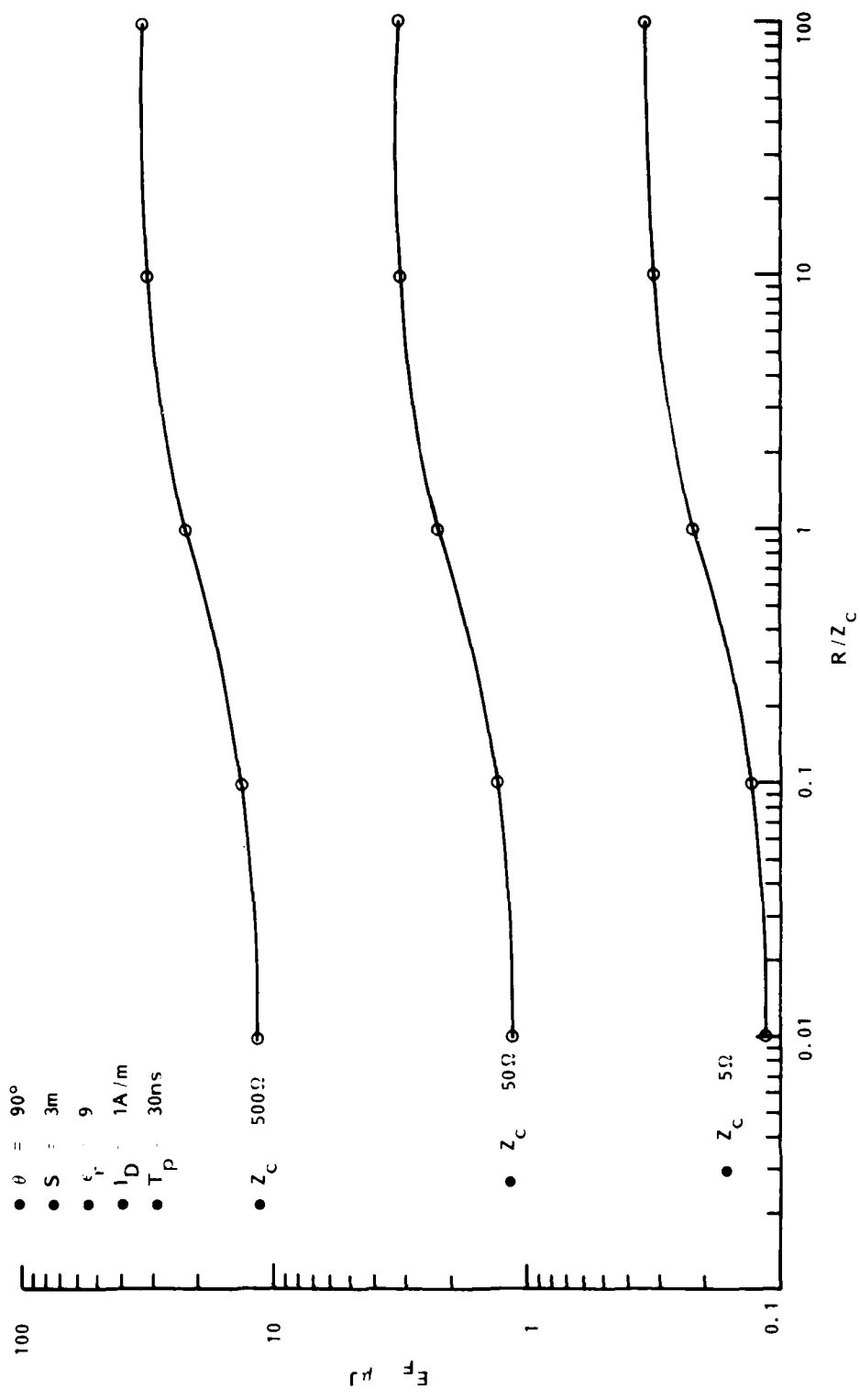
Figure 28. Maximum absorbed load energy versus normalized load impedance for various line impedances

61
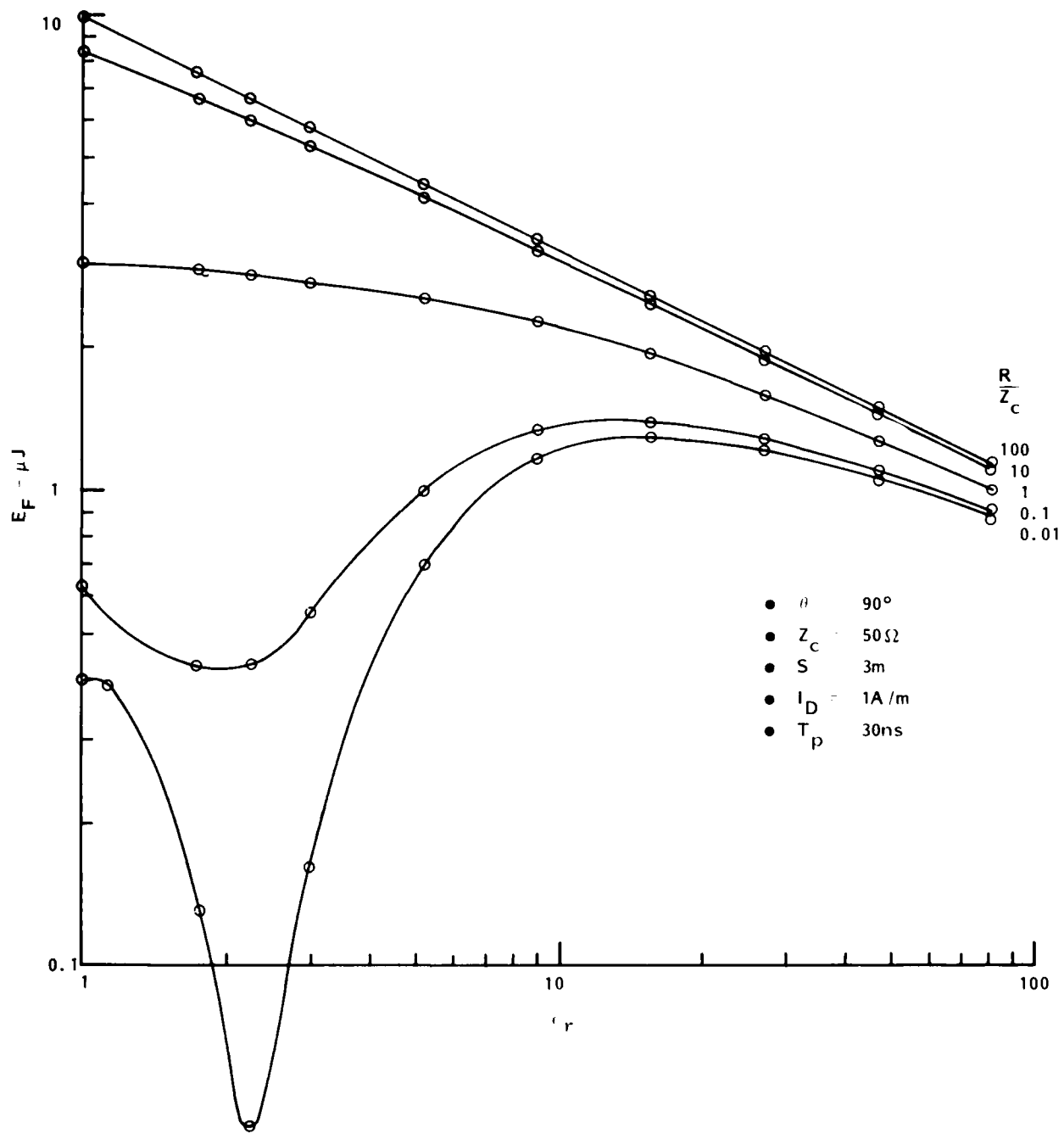
Figure 29. Maximum absorbed load energy versus ϵ_r for various normalized load impedances $(Z_c = 50\Omega)$ $T_p = 30ns$
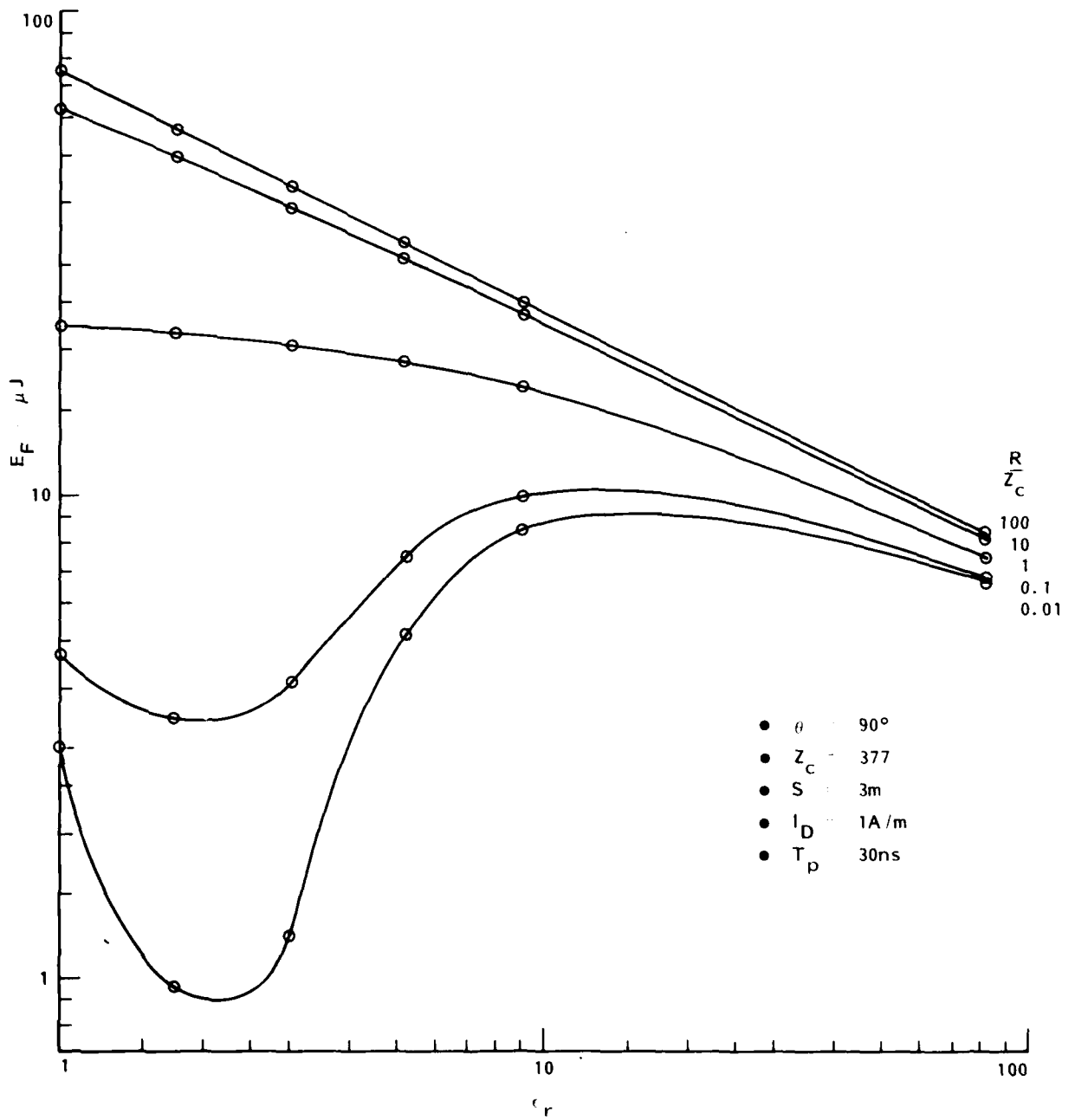
Figure 30. Maximum absorbed load energy versus ϵ_r for various normalized load impedances (Z_C=377Ω)

63
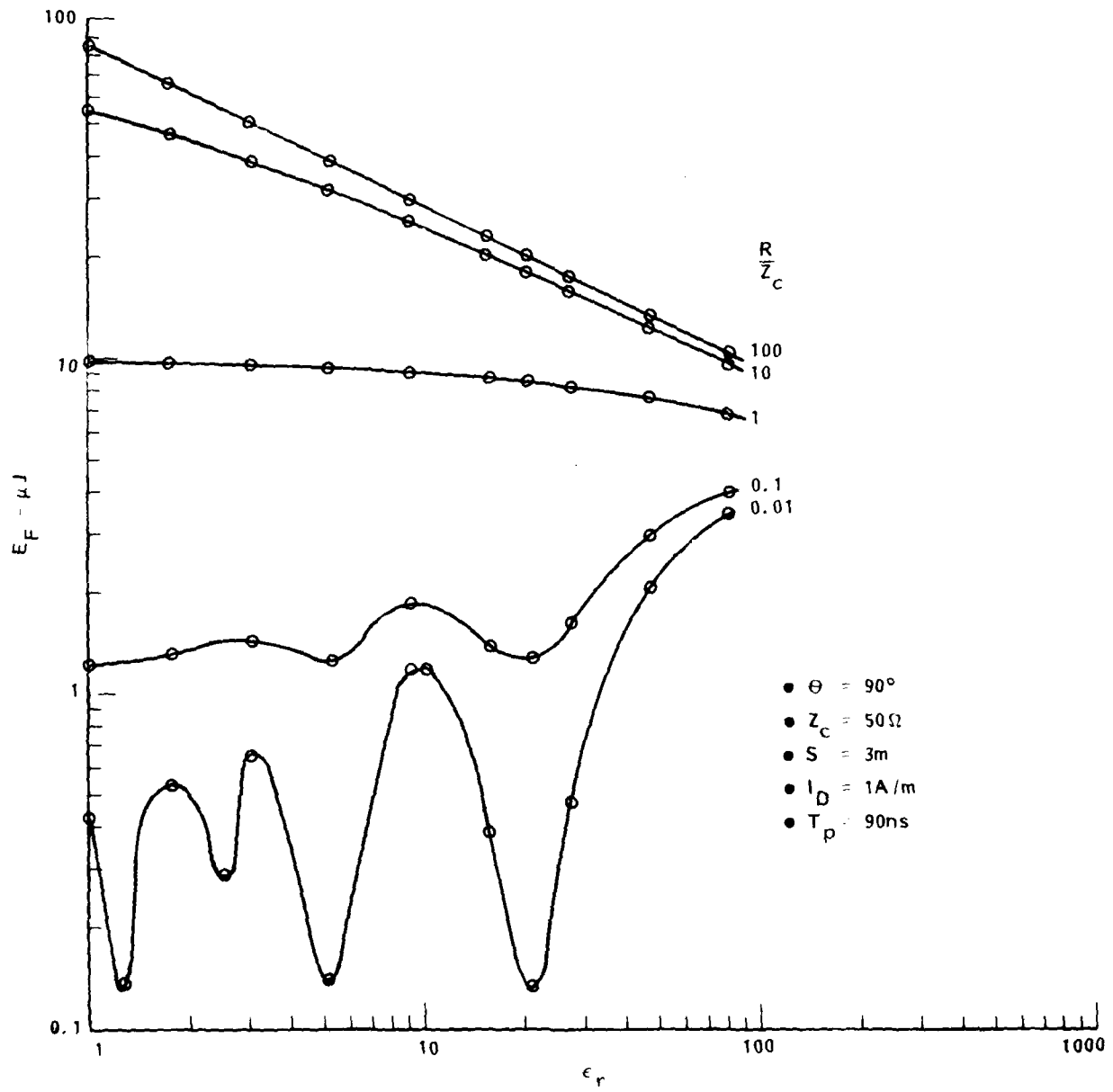
Figure 31. Maximum absorbed load energy versus ϵ_r for various normalized load impedances (Z_c=50, T_p=90ns)
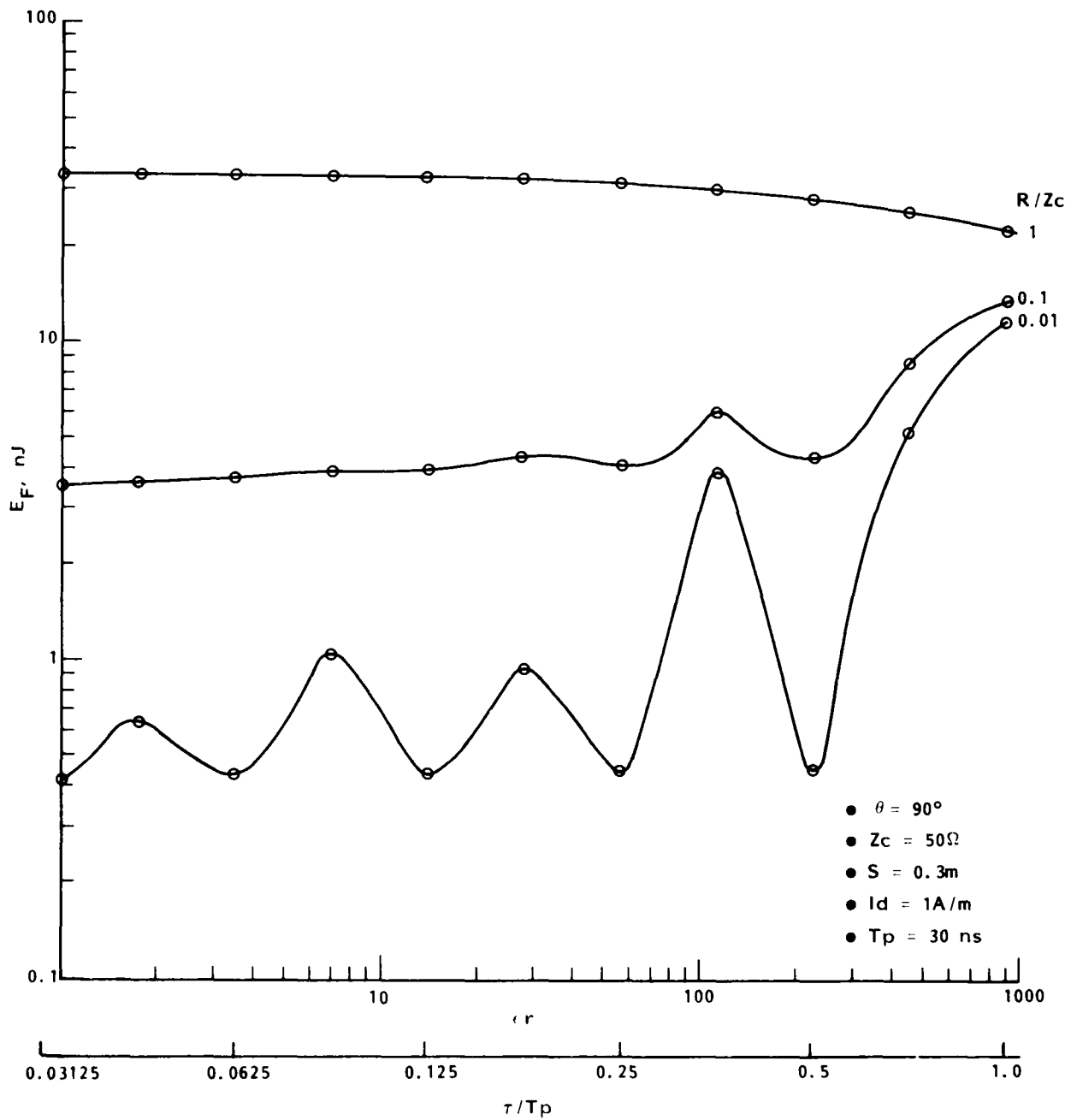
Figure 32. Maximum absorbed load energy versus ϵ_r for various normalized load impedances ($Z_C = 50\,\Omega$, S=.3m)

65

times much greater than t_{90}. Mathemetically, t_{90} is obtained from the relationship:

$$E_L(t_{90}) = 0.9E_L(\infty) \tag{2.58a}$$

or via the equivalent action integral relation

$$\int_0^{t_{90}} i_L^2(t)dt = 0.9 \int_0^\infty i_L^2(t)dt \tag{2.58b}$$

A plot of normalized t_{90} versus $\eta = R/Z_c$ is shown in Figure 33 for the same condition from which Figure 10 is obtained. For the longer cables, energy is deposited in the load most rapidly when the cable is nearly matched, as has been indicated by D. Tasca, et al (reference 5). When a longer cable is mismatched, the longer wave transit times induce lengthly oscillatory ringdowns in load currents so that each reflected wave spends significant time traveling betwen loads. Thus, the time for the load to absorb energy from the cable increases rapidly as η varies from the matched condition. Figure 34 shows a plot of normalized t_{50} (the time required for load to absorb 50% of the total energy) for a family of curves with the dielectric constant between 1 and 9 and for cable lengths between 0.3m to 30 meters. Figure 35 shows the normalized plot for a family of values of the drive pulse width.

For electrically short cables, the load current tends to converge to a wave shape proportional to the driver pulse

$$i_{L_1}(t) \to \frac{S}{2} i_0(t)$$

as indicated in Section 2-3.4 (Equation 2.52) so that t_{90} convertes to T_p. It is interesting to note that for the cable where τ is approximately equal to T_p, t_{90} increases as R gets small. This is exactly the point of caveat of the derivation of Section 2-3.3, namely, that when the cable delay is a significant fraction of pulse duration, mismatches produce significant ringdowns. The plots of t_{90} and t_{50} exhibit rather broad based minimums in Figures 33 to 35. These minima are a function of driver pulse shape, as well as the line parameters τ and η.
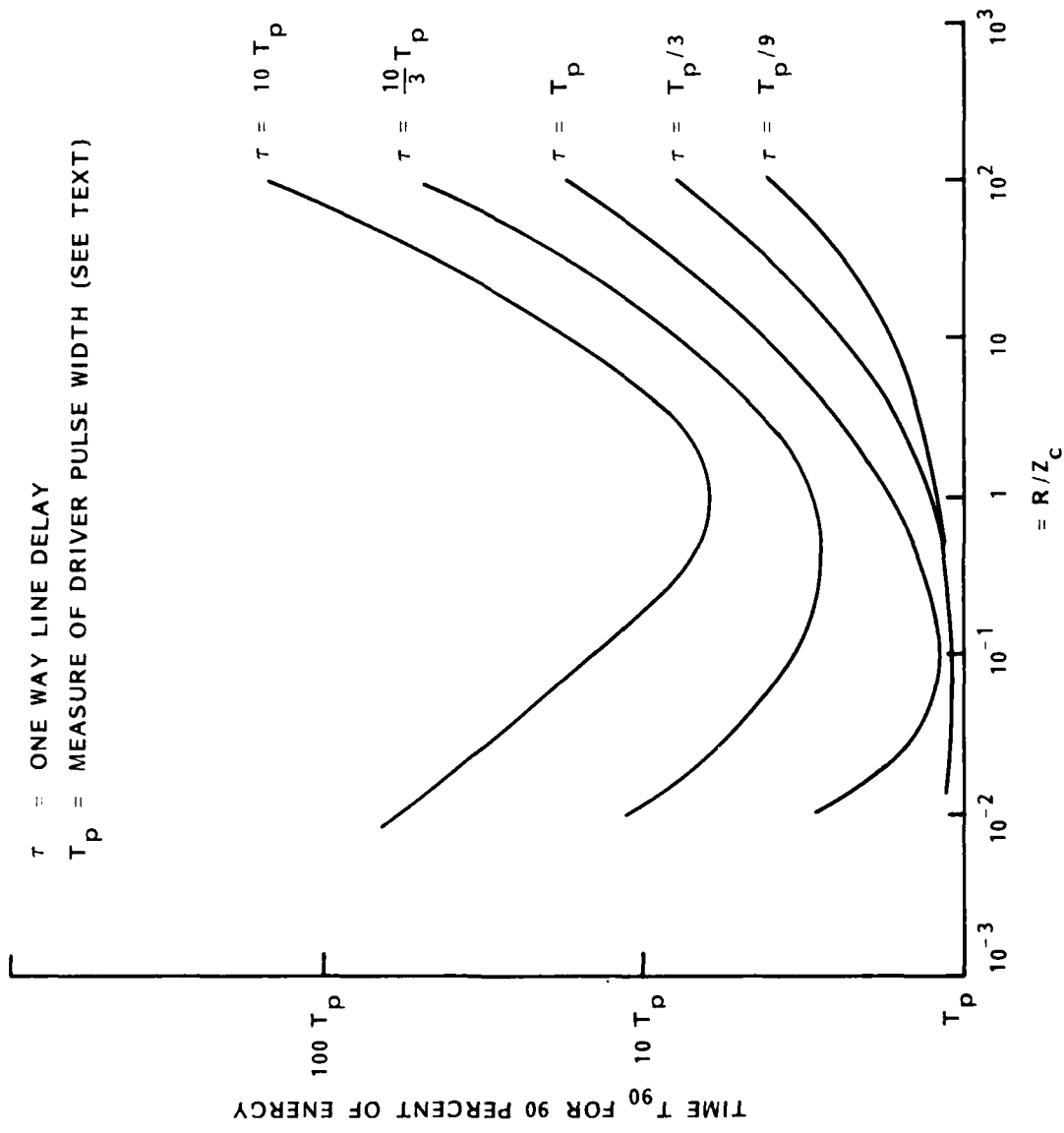
Figure 33. Plot of time for 90 percent of total energy to be delivered to load versus normalized load resistance

67
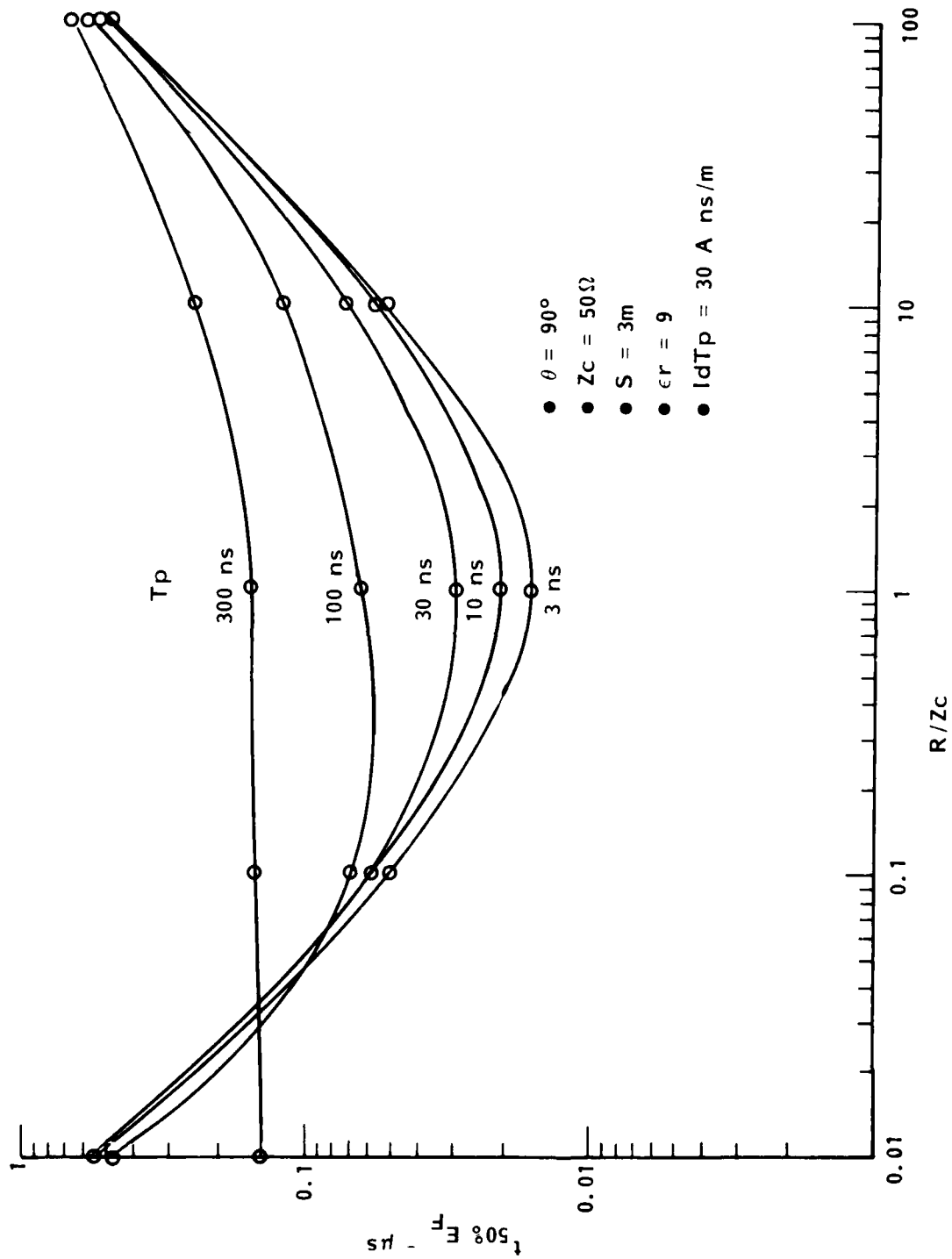
Figure 34. $\tau_{1/2}$ E_{max} versus normalized load impedance for various pulse widths
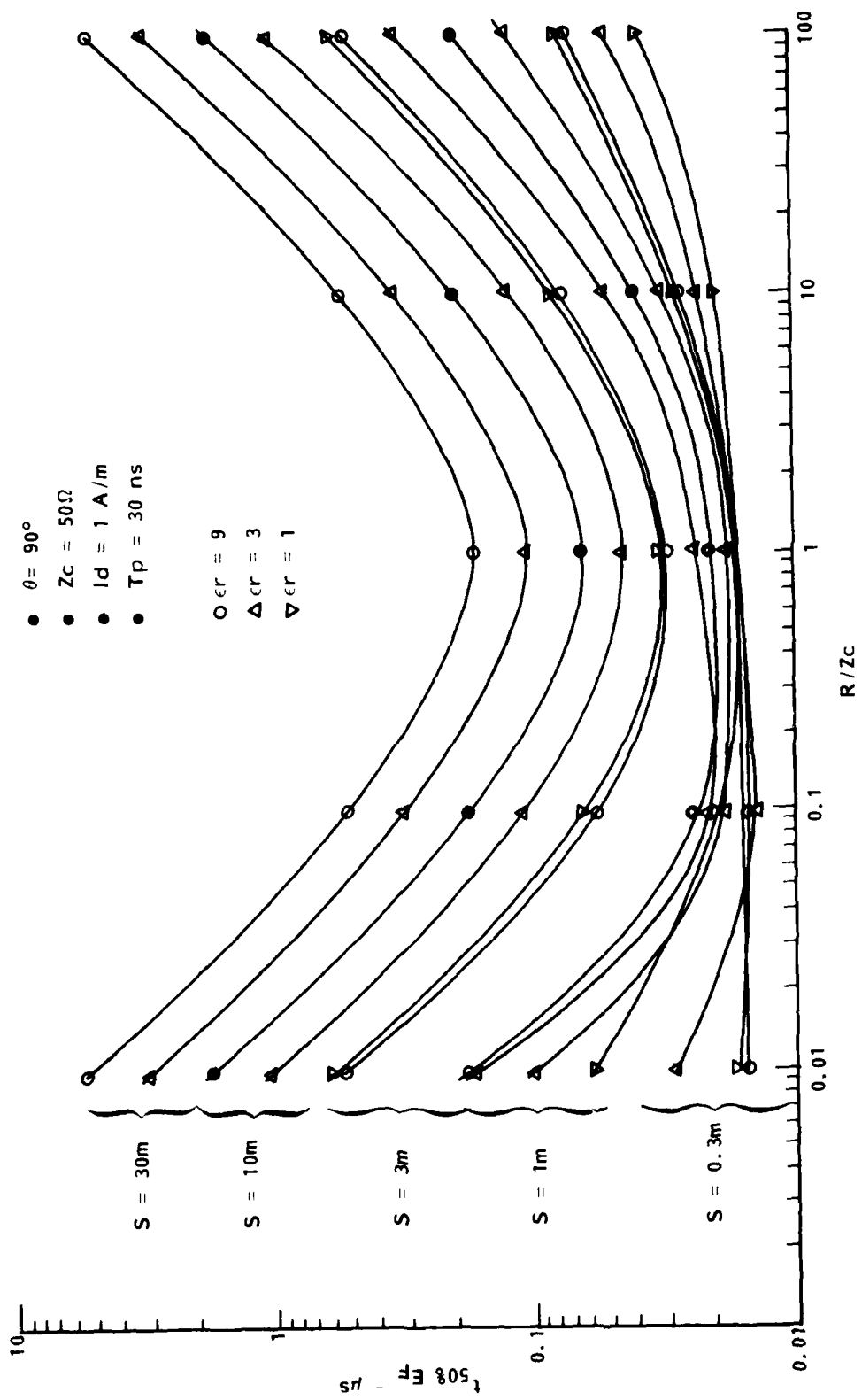
Figure 35. $\tau_{1/2}$ E_{max} versus normalized load impedances for various ϵ_r and line lengths

69

2-4.2 Square Pulse Drivers on a Matched Line

Equations 2.35 and 2.36 show that, for a resistively loaded lossless transmission line, the load currents consist of sums of fundamental incident pulses which are reflected and re-reflected off the mismatches. When the transmission line is matched, $\Gamma_0 = 0$ and $\Gamma_s = 0$ so that the load currents become simply:

$$i_{L_1}(t) = i_a(t) = \frac{1}{2\tau_2}\left\{q(t) - q(t-\tau_0 \cos\theta-\tau)\right\} \tag{2.59}$$

$$i_{L_2}(t) = i_b(t) = \frac{1}{2\tau_1}\left\{q(t-\tau_0 \cos\theta) - q(t-\tau)\right\} \tag{2.60}$$

These equations are useful to study the effects of angle of incidence θ, line delay τ, and X-ray propogation time τ_0. Important relationships between τ and τ_0 will emerge that help place the concept of an electrically short line on firmer footing.

For simplicity, assume $i_0(t)$ to be square pulse driver, of strength I_D and width T_p. Then, for an arbitrary angle of incidence θ, line delay τ, the load current waveforms are provided in Figures 36 and 37 by direct application of Equations 2.59 and 2.60. The peak load currents, rise times, full width-half maximum durations, and total energies of each waveform are provided in Tables 2 and 3 where the load resistances are equal to the line characteristics impedance because of the assumed matched condition. Except when $\tau=\tau_0$ and $\theta=0$ the waveforms are trapezoidal. In addition, the rise time of the load currents is, in general, a function of τ, T_p, and ($\tau_0 \cos\theta$). The distinction between what constitutes an electrically long line and a short line is very clearly defined*. Technically short and long line waveforms are dependent on the load location, since the load current rise times and pulse amplitudes are a function of where the load is with respect to illumination. Load 1 ($z=o$) is assumed to be illumined before Load 2 ($z=s$) as in the derivations of Section 2-3. However, the line can always be considered short (when the line is matched) for a square pulse if

$$T_p > \tau + \tau_0 \cos\theta$$

---

* for this special case, see Section 2-3.3 for the general case

70
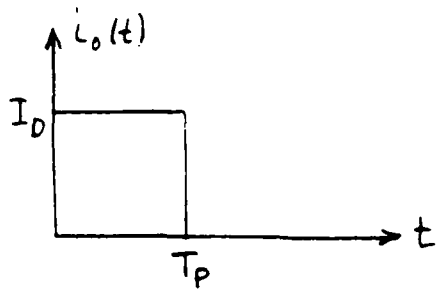
(a) SQUARE PULSE
    CURRENT DRIVER

(b) LINE CHARGE

$Q_D = s I_D T_P$
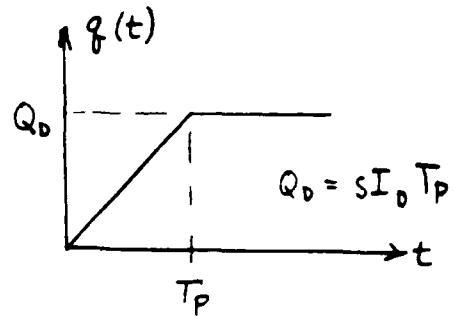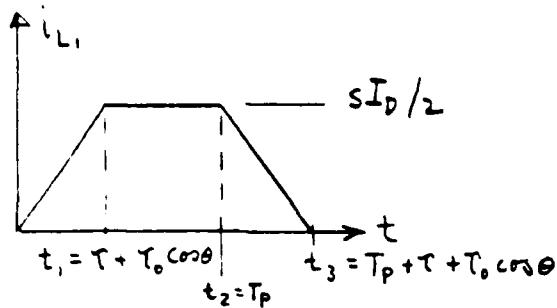
(c) LOAD 1 CURRENT WITH $(\tau + \tau_0 \cos\theta) < T_P$

$s I_D / 2$

$t_1 = \tau + \tau_0 \cos\theta$
$t_2 = T_P$
$t_3 = T_P + \tau + \tau_0 \cos\theta$
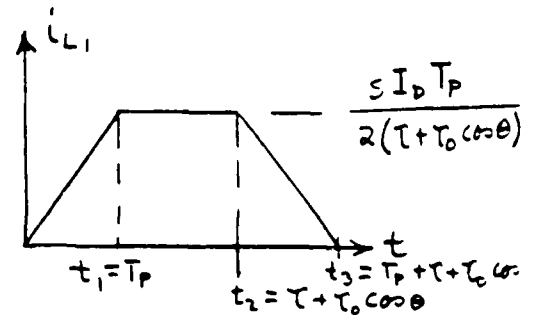
(d) LOAD 1 CURRENT WITH $(\tau + \tau_0 \cos\theta) \geqslant T_P$

$\dfrac{s I_D T_P}{2(\tau + \tau_0 \cos\theta)}$

$t_1 = T_P$
$t_2 = \tau + \tau_0 \cos\theta$
$t_3 = T_P + \tau + \tau_0 \cos\theta$

(e) LOAD 2 CURRENT
    WITH $(T_P + \tau_0 \cos\theta) > \tau$

$- s I_D / 2$

$t_1 = \tau_0 \cos\theta$
$t_2 = \tau$
$t_3 = T_P + \tau_0 \cos\theta$
$t_4 = \tau + T_P$
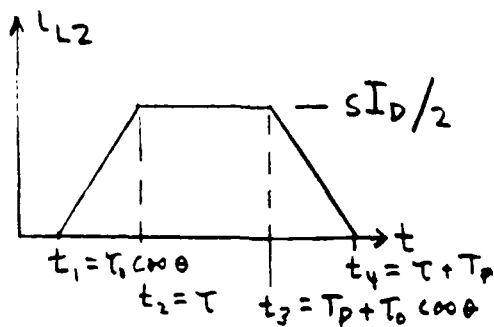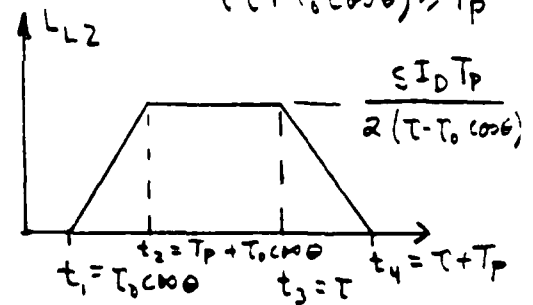
(f) LOAD 2 CURRENT
    WITH $(T_P + \tau_0 \cos\theta) \leq \tau$

$\dfrac{s I_D T_P}{2(\tau - \tau_0 \cos\theta)}$

$t_1 = \tau_0 \cos\theta$
$t_2 = T_P + \tau_0 \cos\theta$
$t_3 = \tau$
$t_4 = \tau + T_P$

Figure 36.   Load current waveforms for a square pulse driver;
matched line of delay τ and lengths
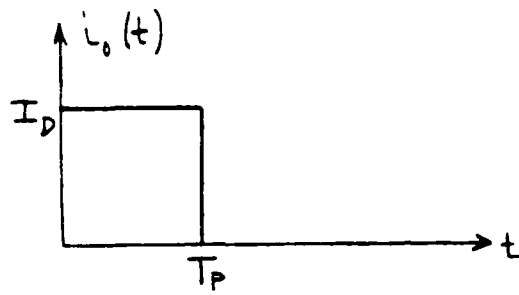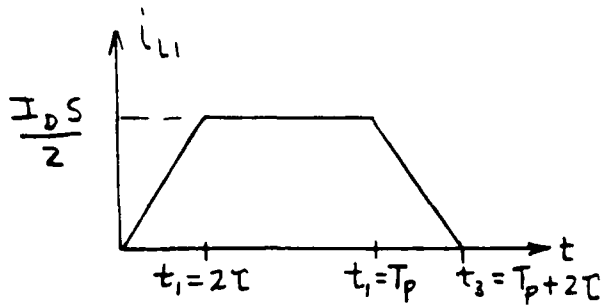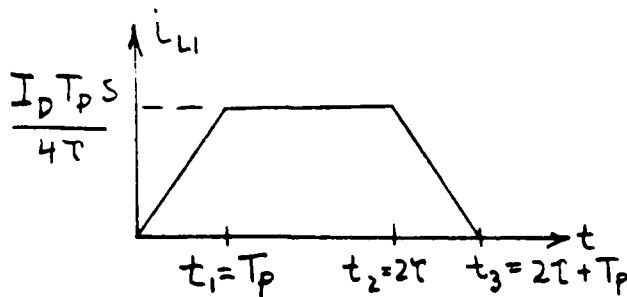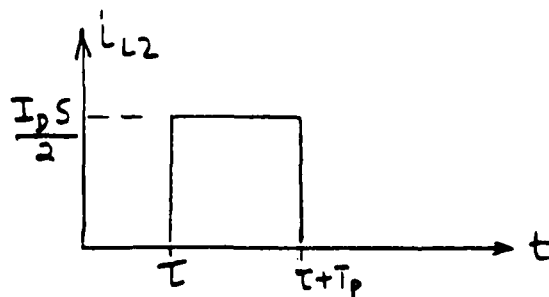
Figure 37. Load currents for a square pulse driver
on a matched lossless air line of delay
ι length S and ··=0

72

Table 2. Incident pulse parameters for a square pulse driver dielectric line (or air line with $\theta \neq 0$)

	SHORT LINE	LONG LINE
LOAD 1		
DRIVE PULSE RELATION	$T_P > (\tau+\tau_o \cos\theta)$	$T_P \leq (\tau+\tau_o \cos\theta)$
INCIDENT PULSE AMP (I_P)	$S\,I_D/2$	$\dfrac{S I_D T_P}{2(\tau+\tau_o \cos\theta)}$
RISE TIME	$\tau+\tau_o \cos\theta$	T_P
FWHM	T_P	$\tau+\tau_o \cos\theta$
INCIDENT PULSE ENERGY (normalized to peak power)	$\left\{ T_P - \dfrac{(\tau+\tau_o \cos\theta)}{3} \right\}$	$\left\{ (\tau+\tau_o \cos\theta) - \dfrac{T_P}{3} \right\}$
LOAD 2		
DRIVE PULSE RELATION	$T_P > (\tau-\tau_o \cos\theta)$	$T_P \leq (\tau-\tau_o \cos\theta)$
INCIDENT PULSE AMP (I_P)	$S I_D/2$	$\dfrac{S I_D T_P}{2(\tau-\tau_o \cos\theta)}$
RISE TIME	$(\tau-\tau_o \cos\theta)$	T_P
FWHM	T_P	$(\tau-\tau_o \cos\theta)$
INCIDENT PULSE ENERGY (normalized to peak power)	$\left\{ T_P - \dfrac{(\tau-\tau_o \cos\theta)}{3} \right\}$	$\left\{ (\tau-\tau_o \cos\theta) - \dfrac{T_P}{3} \right\}$

PEAK POWER $= I_P^2 Z_C$

Table 3. Incident pulse parameters for a square pulse driver air line with $\theta=0$

		SHORT LINE	LONG LINE
LOAD 1	DRIVE PULSE RELATION	$T_P > 2\tau$	$T_P \leq 2\tau$
	INCIDENT PULSE AMP (I_P)	$SI_D/2$	$(I_D T_P v_P/4)$
	RISE TIME	2τ	T_P
	FWHM	T_P	2τ
	INCIDENT PULSE ENERGY (normalized to peak power)	$\left(T_P - \dfrac{2\tau}{3}\right)$	$\left(2\tau - \dfrac{T_P}{3}\right)$
LOAD 2	DRIVE PULSE RELATION	$\tau=\tau_0$, no dependence on T_P	$\tau=\tau_0$, no dependence on T_P
	INCIDENT PULSE AMP (I_P)	$SI_D/2$	$SI_D/2$
	RISE TIME	(not applicable for square pulse driver)	
	FWHM	T_P	T_P
	INCIDENT PULSE ENERGY (normalized to peak power)	T_P	T_P

PEAK POWER $= I_P^2 Z_C$

and long if

$$T_p \approx \tau - \tau_0 \cos\theta$$

Intermediate pulse widths, namely

$$\tau - \tau_0 \cos\theta < T_p < \tau + \tau_0 \cos\theta$$

result in either "long" or "short" line responses, depending on load location. The total incident charge on one of the two loads may be noted as

$$Q_D = S\ I_D T_p/2$$

and the peak load current is directly proportional to Q_D in all cases when $\tau < \tau_0$.

The peak current is also a function of line wave velocity v_p when the line is long, and the faster the wave velocity, the higher the peak current, since the accreted charge tends to arrive faster. When $\tau < \tau_0$, the ratio of short line peak current to long line peak current in both loads is somewhat less than the ratio of line lengths, because the longer lines tend to keep somewhat more charge in the lines as a function of time.

In the limit, when $v_0 = v_p$ and $\theta = 0$, Table 3 shows that the peak line current is independent of τ in load 2 and is exactly T_p in duration regardless of line length. In load 1, the peak of the long line pulse is $I_D\ T_p\ v_p/4$ where $v_p = v_0$. Since $T_p \leqslant 2\tau = 2S/v_0$, the peak current is less than or equal to $SI_D/2$ in load 1 for the long line.

Thus, it is seen that for very long lines, significant changes in pulse amplitude and duration can be expected to occur when the line is not instantaneously illuminated, i.e., when $\theta \neq \pi/2$. In particular load 1, first illuminated, receives more energy than load 2 when both loads are matched. However, this is compensated somewhat in that the pulse duration in load 1 is longer than in load 2.

Because of the complexity of the line voltage equation (Equation 2.13), little has been said about voltage other than to recommend a numerical Fourier inverse for its computation. However, the results of Figures 36 and 37 provide some

75

interesting insights to the terminal open circuited voltage for a square pulse driver. With $Q_D = S^I_D T_P$ = the final accreted charge, the open circuit cable voltage is ultimately

$$V_{oc} = \frac{Q_D Z_C}{\tau} = \frac{S^I_D T_P}{\tau} Z_C \tag{2.61}$$

On the first reflection, the open circuited line terminal voltage is simply

$$V'_{oc} = 2i_a(t)Z_C \text{ at Load 1} \tag{2.62a}$$

$$V'_{oc} = 2i_b(t)Z_C \text{ at Load 2} \tag{2.62b}$$

where the superscript denotes the voltage due to the first incident pulse. For both loads,

$$V'_{oc} \leq V_{oc}$$

except in the case of load 2 for a long line (Figure 36f). With $\tau \geq (T_p + \tau_0 \cos\theta)$

$$\text{peak } V'_{oc} = 2 \frac{S^I_D T_P}{2(\tau - \tau_0 \cos\theta)} Z_c \geq \frac{S^I_D T_P}{\tau} Z_c = V_{oc} \tag{2.63}$$

That is to say that the peak open circuited first reflection terminal voltage at load 2 is greater than the voltage which results from Equation 2.61.

Because of reflections, this voltage peak will occur at terminal 1 on the second pulse. Since the cable is assumed lossless, the cable will ring *ad infinitum* and never settle to a quiescent V_{oc}.

It is stated without proof, that when $\theta = \pi/2$, $V_{oc} = Q_D Z_c/\tau$ is the maximum peak terminal voltage and also the peak line voltage.

SECTION 3
GENERAL MULTIWIRE TRANSMISSION LINE THEORY

3-1 BASIC EQUATIONS

A multiwire transmission line is defined as a collection of parallel conductors, all of which are separated from a reference conductor by dielectric material. For the cases of interest in this report the transmission-line is assumed to be perturbed by a current source term driven by incident ionizing radiation. In the following sections we will sketch the origin of the defining equations for a multiwire transmission line and in Appendix I, II and III, we will consider detailed solutions and the meaning of the various terms that appear in these equations.

Let us consider a length ΔX of the multiwire transmission-line consisting of N conductors and a reference conductor. Each conductor will have an inductance and a capacitance with respect to the reference conductor and with respect to every other conductor, which we denote by $\bar{L}\Delta X$ and $\bar{\bar{C}}\Delta X$, where $\bar{L}$ and $\bar{\bar{C}}$ are inductance and capacitance per unit length respectively. The voltage drop across ΔX is equal to the product of the inductance of this length of the transmission line and the time rate of change of current summed over all conductors and the reference conductor:

$$\Delta V_i = -(L_{ij})\Delta X \frac{\partial I_j}{\partial t} \quad . \tag{3.1}$$

The decrease in current across this length of line is equal to the current that is shunted across the distributed capacitance plus the current source. The change in the current is given by the capacitance multiplied by the time rate of change of the voltage plus the current source:

$$\Delta I_i = -(C_{ij})\Delta X \frac{\partial V_j}{\partial t} + (I_D)_i \Delta X \tag{3.2}$$

where $(I_D)_i$ is the current source per unit length for wire i.

In the limit $\Delta X \rightarrow 0$, these equations become

$$\frac{\partial V_i}{\partial x} = -L_{ij} \frac{\partial I_j}{\partial t} \tag{3.3}$$

$$\frac{\partial I_i}{\partial x} = -C_{ij} \frac{\partial V_j}{\partial t} + (I_D)_i \; . \tag{3.4}$$

In the remainder of this section we will adopt a matrix convention and so write the transmission line equations in the following way

$$\frac{\partial \overline{V}}{\partial X} = -\overline{\overline{L}} \frac{\partial \overline{I}}{\partial t} \tag{3.5}$$

$$\frac{\partial \overline{I}}{\partial X} = -\overline{\overline{C}} \frac{\partial \overline{V}}{\partial t} + \overline{I}_D \; . \tag{3.6}$$

The starting point of the previous derivation was the assumption that the line could be represented by a collection of segments each with a distributed capacitance and inductance along the line. A more rigorous derivation would start with Maxwell's equations appropriate to guided waves and by making the assumption that the electric and magnetic fields are both perpendicular to the direction of propogation and to each other (TEM mode) the previous set of differential equations would be obtained.

3-2 NATURE OF THREAT

In this section we derive the features of multiwire transmission line solutions which are necessary for arriving at a practical engineering method of specifying current drive levels for the multipoint, multiwire current injection technique which has been developed. As has been noted in the Section 3-1, the threat to the interface circuits is the energy arriving at the terminations due to the distributed current drivers along the cable length. The exact wave shape at the termination depends not only on the parameters of the cable (current drivers, characteristic impedance matrix, propogation velocity), but also on the termination impedances themselves. Similarly, the actual energy which is delivered to any particular load

also depends both on the cable parameters and the terminations. Thus, to ascertain the magnitude of the threat to any particular interface, it is necessary to consider how the signal arriving at that interface depends on all the other parameters of the problem. That is, a worst case approach must be developed for specifying this threat. While it is relatively easy to find upper bounds for this threat (put all current into a single termination), this naive approach can lead to excessive levels which will be above any physically realistic possibility. Instead, it has been decided to look at the multiwire interface threat in detail and extract a physically realizable worst case; that is, not just an upper bound, but a least upper bound.

It is the purpose of this section to explore the nature of interface threats due to multiconductor transmission lines driven by X-ray generated current drivers. The physically realizable worst case will be determined. An engineering prescription will be developed for specifying the current drive levels required to realize this worst case when implementing multipoint, multiwire current injection on component boxes.

The procedures for developing the prescription relies on the method of successive complication. An ideal baseline model is chosen for developing the necessary concepts. A definitive solution is presented for this model. Departures from this ideal are then discussed by successive relaxation of constraints. The same procedure is followed within the baseline model. First, the nature of the interface threat for a single-wire to shield transmission line is reviewed. Next, the simplest multiwire line which includes coupling is discussed, the two-wire to shield line. Finally, the general multiwire line is discussed, and the results related to the previous discussion. The engineering prescription then becomes apparent.

3-2.1 The Basic Model

The model chosen for the baseline investigation is that of an ideal, loss-less multiconductor transmission line which may be described by the equations of "quasi-TEM" transmission line theory. Thus, the assumptions are:

i) The propogation may be described by Equations 3.5 and 3.6.

ii) The line is combed and uniform, i.e., $\bar{\bar{C}}$ and $\bar{\bar{L}}$ are independent of X and t.

iii) The current driver I_D is uniform along the line. This corresponds to photon illumination uniform and perpendicular to the cable run.

iv) All modes of the line have the same propagation velocity v (see Appendix I). This assumption simplifies the analysis and is not far from reality. Mathematically, this requirement places a constraint on the transmission line matrices, $\bar{\bar{L}}$ and $\bar{\bar{C}}$, i.e.,

$$\bar{\bar{L}}\,\bar{\bar{C}} = \bar{\bar{C}}\,\bar{\bar{L}} = \frac{1}{v^2}\,\bar{\bar{1}}$$

(3.7)

where $\bar{\bar{1}}$ is the unit matrix.

v) For simplicity, we assume the line to be symmetrically terminated. That is, the reflection matrices for both ends are identical.

vi) Only passive resistive terminations are considered. Reactive terminations dissipate no energy and would increase the scope of the investigation significantly.

vii) All terminations are wire-to-shield only. No cross-wire terminations are considered. This corresponds to the situation of primary interest in the realistic deployment of such cables.

With the above assumptions, a closed form analytic solution of the problem may be obtained. The details of this solution may be found in Appendix II, while details of the energy deposited in the loads may be found in Appendix III. These solutions will be used extensively in the following discussion. Additionally, generalizations of the solution will be used when discussing the relaxation of some of the basic model constraints.

3-2.2 Single Wire Line

The general solutions given in Appendix II for a multiwire line of course also gives the single wire (to shield) solution. Let R be the termination resistance, $\bar{\bar{Z}}_C$ the characteristic impedance of the line, and $\eta = R/Z_C$ the impedance ratio. The reflection coefficient Γ is given by

$$\Gamma = \frac{1-\eta}{1+\eta}$$

(3.8)

and varies from -1 for a shorted termination, to +1 for an open termination. For a current driver I_D (amps/m) in an electrically short cable the current I in the load is given by

$$I(t) = -\frac{V}{2s}\,(1-\Gamma)$$

$$\sum_{n=0}^{\infty} \Gamma^{2n}\,(\Lambda Q(t-2n\tau) + \Gamma\Lambda Q\,(t-(2n+1)\tau)$$

(3.9)

where $\tau = s/v$ is the cable propagation time, v is the propagation velocity in the cable, and s is the cable length. The basic pulse i_a is given by

$$\Delta Q(t) = q(t) - q(t-\tau) \tag{3.10}$$

where

$$q(t)/s = \int_0^t I_D(t') \, dt' \tag{3.11}$$

is the basic charge transfer per unit length developed by the current driver $I_D(t)$. This is the same relation developed in Section 2-3.3 for the special case of an electrically shot cable with $r_0 = r_s$.

For the purposes of further discussion, it is assumed that the time history of the current driver I_D is a square pulse. Evaluation of the expressions for other pulse shapes will be obvious. Let T_p be the width of the square pulse, and I_D the amplitude of the pulse, as shown in Figure 38a. The charge transfer $q(t)$ ramps up to a total transfer $Q_0 = I_D T_p$ in a time T_p, as shown in Figure 38b. The basic pulse in the termination ΔQ is somewhat different depending on whether the cable is long compared to the pulse $(\tau > T_p)$. For a long cable, ΔQ ramps to a peak value $Q_0 = I_D T_p$ in a time T_p, remains at this value until τ and then ramps back to zero at a time $T_p + \tau$. For a short cable, ΔQ ramps to the smaller value of $I_D T$ in a time τ, remains at this level until T_p, and ramps back to zero at a time $T_p + \tau$. These wave forms may be seen in Figure 38c and 38d.

The important point is that the waveform $\Delta Q(t-n\tau)$, which appears in Equation 3.9, is non-zero only in the interval $nT_p \le t \le (n+1) T_p + \tau$. Outside of this interval $\Delta Q(t-n\tau)$ is zero. Thus, the successive terms in the series of Equation 3.9 appear at later and later times. Thus, the terms are easily interpreted as the successive reflections from the terminations, with the primary reflection occurring at either end, followed by propagation to the opposite end and reflection back to the termination of interest. As each pass through, the termination dissipates

81
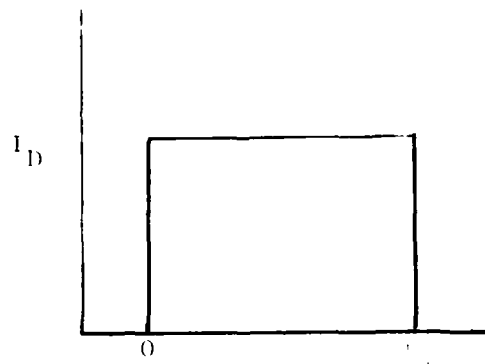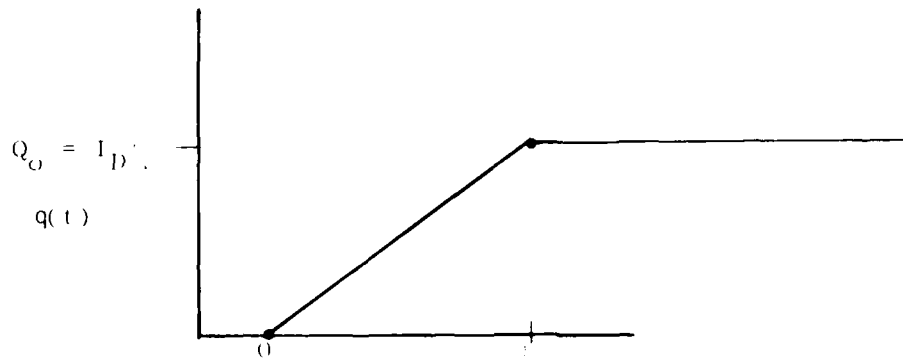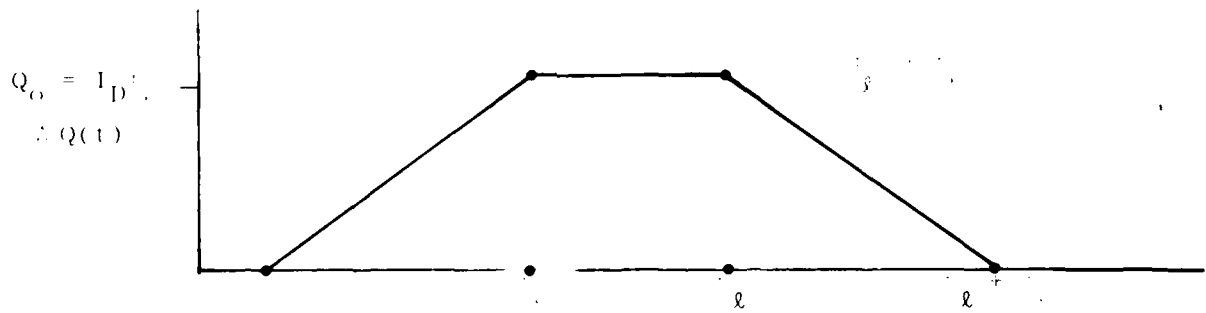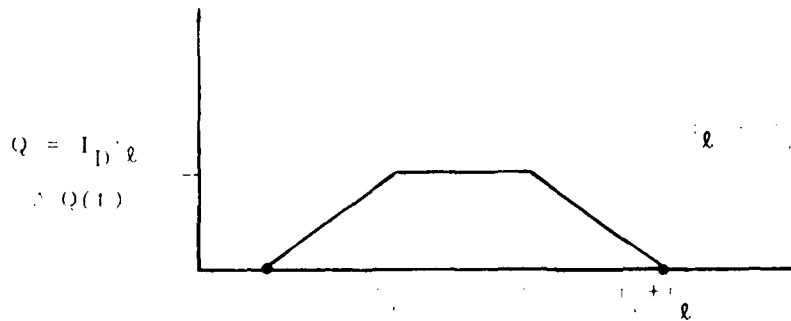
Figure 38. Square wave response

82

some of the energy of the pulse; the successive terms arrive with smaller and smaller amplitude (i.e., the pulse is multiplied by a power of ρ).

The primary pulse arriving at the termination is most easily seen by considering the special case of matched termination ($\eta=1$, $\Gamma=0$) and τ is small for any value of η, then the infinite series of Equation 3.9 reduces to

$$I(t) = -\frac{v}{2} \Delta Q(t) \tag{3.12}$$

which is the same as derived in Section 2-3.3 with $\theta=\pi/2$. Thus, the expression reproduces the well-known fact that matching terminations give rise to no reflections. The current which flows in the termination is directly obtained from the information about ΔQ previously presented. It takes on its maximum value only for $\tau > T_p$. For mismatched terminations ($\Gamma \neq 0$), the current waveform takes on a different character depending on whether there is a high mismatch ($\eta > 1$, $\Gamma < 0$) or a low mismatch ($\eta < 1$, $\Gamma > 0$). The first case has the character of an over-damped ring down of a charged capacitor, while the second case waveform has the character of an under-damped R,L,C circuit. These features of the termination waveform may be seen in Figures 39 and 40 which give the current waveforms for a moderately long cable ($\tau = T_p$) for significant high mismatch ($R = 10Z_0$) and low mismatch ($R = 0.1Z_0$).

Several other features of the solution should be noted. The load current scales directly with the source current I_0. It also scales with the phase velocity v. For long cables, the current scales as $vQ_0 = vI_0T_p$, while for short cables, it scales as $vI_D\tau = I_Ds$. The load current depends on the load resistance only through the dimensionless ratio $\eta = R/Z_0$. Finally, the time dependence of the solution in terms of a dimensionless time variable $t' = t/\tau$ depends only on the pulse length through the dimensionless ratio $\zeta = T_p/\tau$. Taken together, this means that the solution space depends only on the parameters η (equivalently Γ) and ζ, and that other solutions may be obtained by scaling. Of course, the load voltage may be obtained from the current by multiplication by R.

While load current and voltage are of some concern for semi-conductor terminations, it is recognized that many major failure mechanisms are associated with the total energy deposited in the load, and the rate at which the energy is
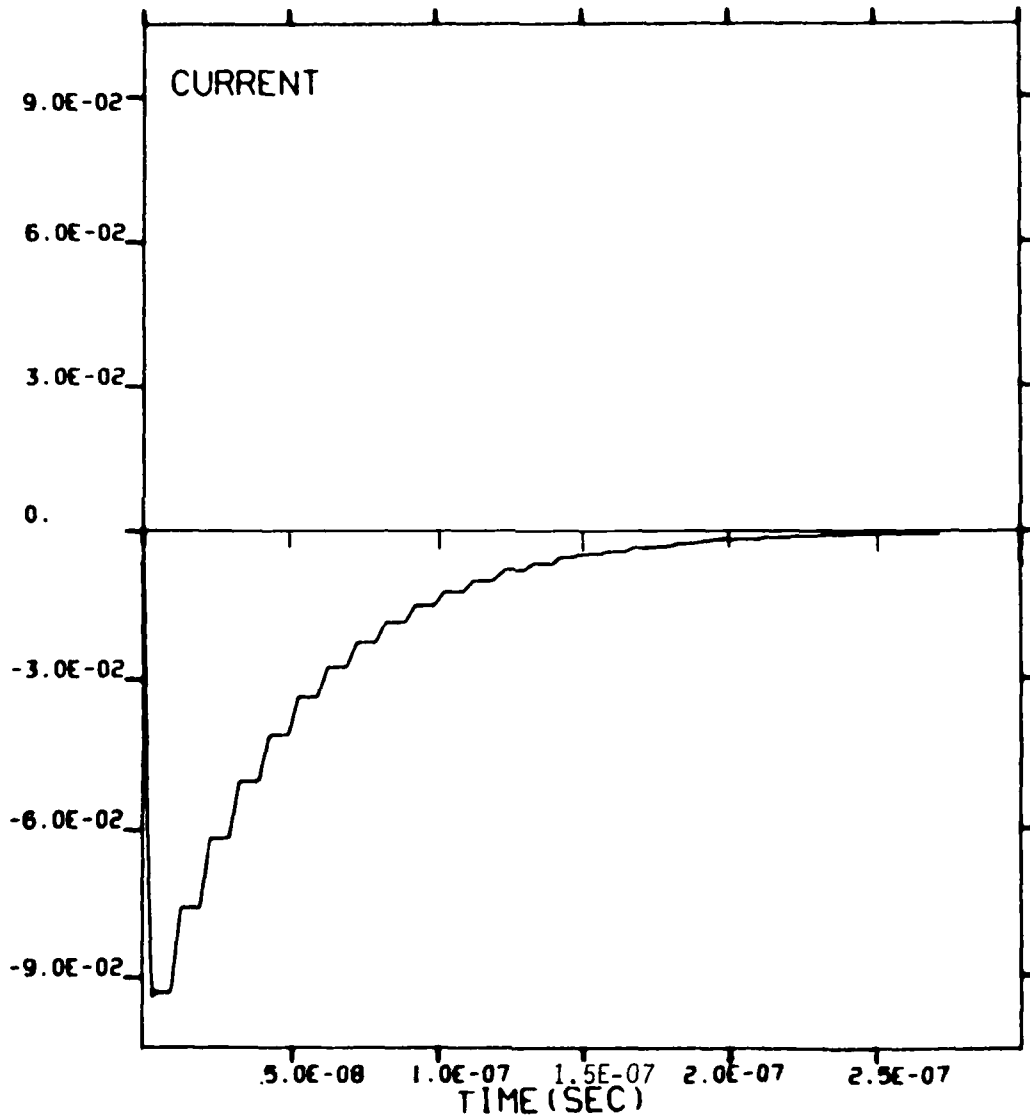
Figure 39.   Terminal response - high mismatch

84
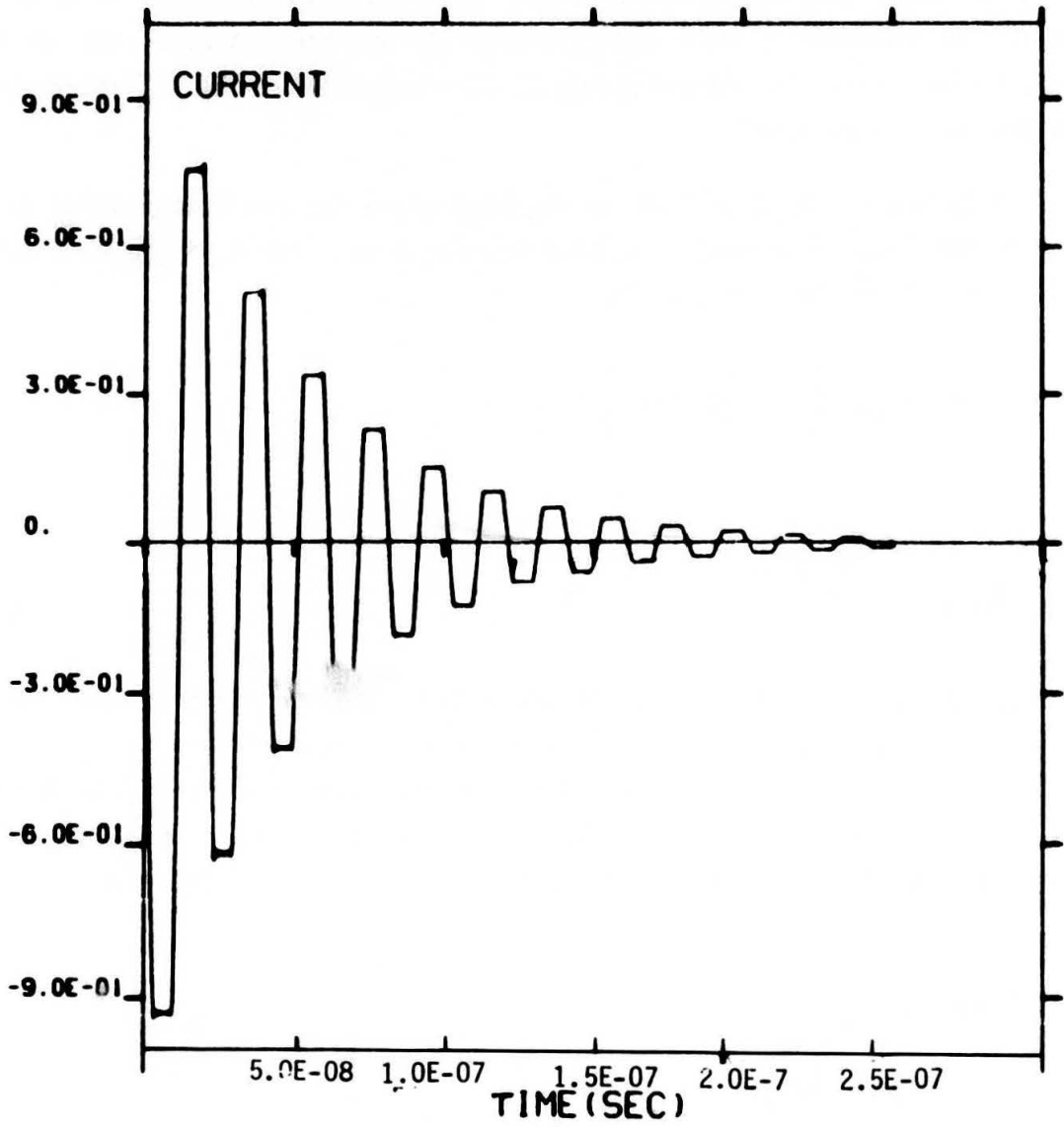
Figure 40.   Terminal response - low mismatch

85

deposited. Thus, while the current in the load reaches a maximum as the length of the cable is increased ($\frac{V}{2} I_D T_p$ for a matched load), the length of time the current flows continues to increase as the cable length increases. This implies that longer cables will deliver more energy to the load even though the peak current and voltage may be no worse than for a shorter cable. The development of worst case considerations for semi-conductor loads demands that these energy concerns be addressed. A central feature of the approach to be discussed below is a careful accounting for worst case energy capability. This criterion is taken to be of prime importance. The features of this energy capability are now discussed for the single-wire transmission line. An understanding of this capability will be central to the approach for multi-wire lines.

In Appendix III, a derivation has been given for the energy which is deposited in the loads on a multiwire transmission line. For a single wire long line ($\tau > T_p$) this expression reduces to

$$E = E_{max} \left[1 - \frac{1}{3}\zeta(1-\Gamma) \right] \tag{3.13}$$

where

$$E_{max} = \left(\frac{Q_o^2}{2C} \right) \cdot s \tag{3.14}$$

and C = capacitance per unit length. In these equations, the symbols have the same meaning as above, i.e., $\zeta = T_p/\tau$ is the characteristic time ratio, $Q_0 \geq I_D T_p$ is the charge transfer per unit length, C is the capacitance per unit length of the line, s is the line length, and Γ the reflection coefficient. Equation 3.14 may also be written in terms of the characteristic impedance of the line $Z_c = v^{-1}C^{-1}$,

$$E_{max} = \frac{s}{2v} Z_c Q_o^2$$

$$= \frac{\tau}{2} T_p^2 Z_c I_D^2 . \tag{3.15}$$

For shorter lines, ($\tau < T_p$) the expressions for the energy deposited become more complicated, as is noted in Appendix III. However, the resulting expression always gives rise to an energy less than that implied by Equation 3.13 , i.e., more and more positive terms are subtracted from this basic quantity. Furthermore, as the termination impedence becomes very large ($R \to \infty, \Gamma \to +1$), all of the expressions tend to E_{max}, no matter what the ratio of T_p to τ. For further discussion, it is therefore sufficient to consider the case $T_p < \tau$, as given be Equation 3.13 . The maximum energy available E_{max} is simply the amount of energy developed by charging up the capacitance of the cable with the total transfer Q_0. Naturally, this quantity scales linearly with the length of the cable. It is thus possible to discuss the per unit length energy capability of the cable. Note that this quantity depends not only on the magnitude of the current driver I_D (through $Q_0 = I_D T_p$) but also on the cable capacitance (or equivalently the characteristic impedence Z_c). Note that for very long cables ($\zeta << 1$), the energy delivered to the load is nearly independent of the load resistance. Shown in Figure 41 is the normalized energy E/E_{max} as a function of $\eta = R/Z_0$ for various values of ζ. Note that this quantity is a monotically increasing function of the load resistance R. Shown in Figure 42 is the same information displayed in absolute units of E which shows the increase in energy with cable length.

Not only is the total energy of importance for semi-conductor considerations, but also the energy-time history. Shown in Figure 43 are the energy time histories for three identical cables with low, matched, and high impedence terminations ($\eta=0.1$, 1, 10). The solution is for a long cable ($\tau = T_p$), so the final energies are very nearly the same. As is evident from the figure, the energy is deposited in the load much more rapidly for the matched load as compared to the mismatched loads. While no convenient analytic expression has been developed for the length of time required to deposit a fixed fraction of the energy, it is evident from the Equation 3.9 that the matched condition clearly gives rise to peak power in the load. Indeed, for very long lines, since the final deposited energy is nearly independent of the load, it is clear that the matched load represents the worst case. Indeed, the time to deposit the energy in the load is minimized by matching the line. Shown in Figure 44 is a summary of the time to deposit one half the final energy as a function of termination impedence. The deep minima for most line lengths is apparent. This plot was developed from an extensive numerical evaluation of the solution for the indicated parameter range.
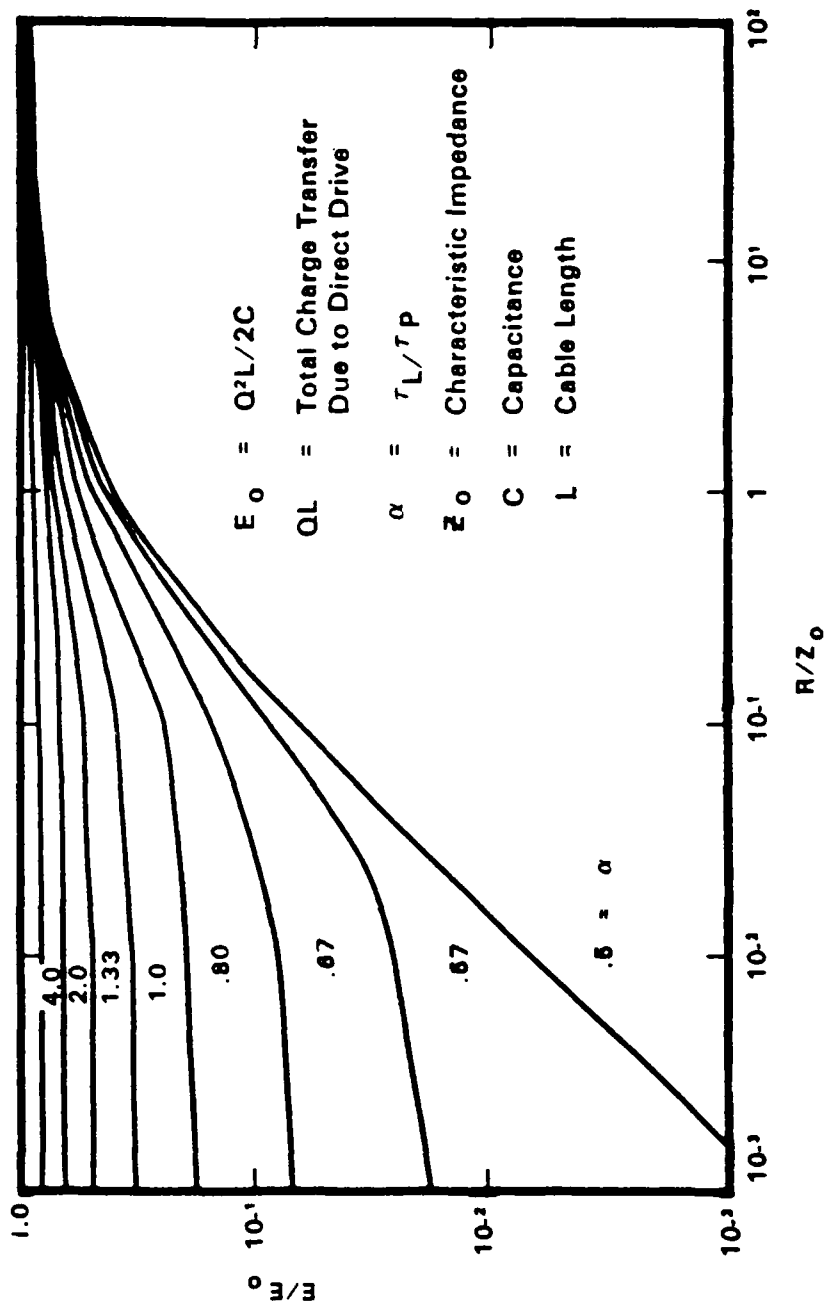
Figure 41. Normalized energy vs. R/Z_0 ($\alpha = \zeta^{-1}$)

$E_o = Q^2L/2C$

$QL = $ Total Charge Transfer Due to Direct Drive

$\alpha = \tau_L/\tau_P$

$Z_o = $ Characteristic Impedance

$C = $ Capacitance

$L = $ Cable Length
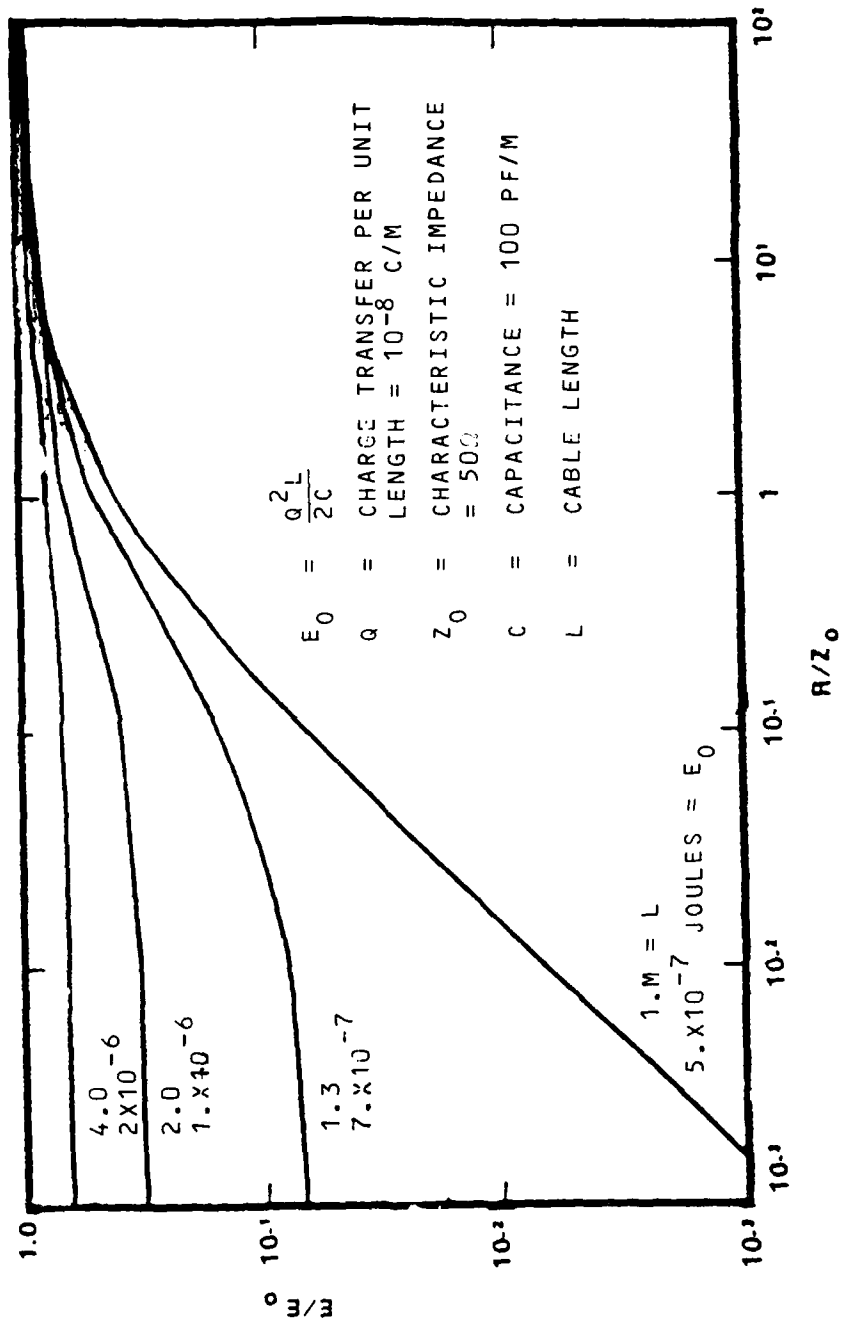
Figure 42. Energy vs. R/Z₀
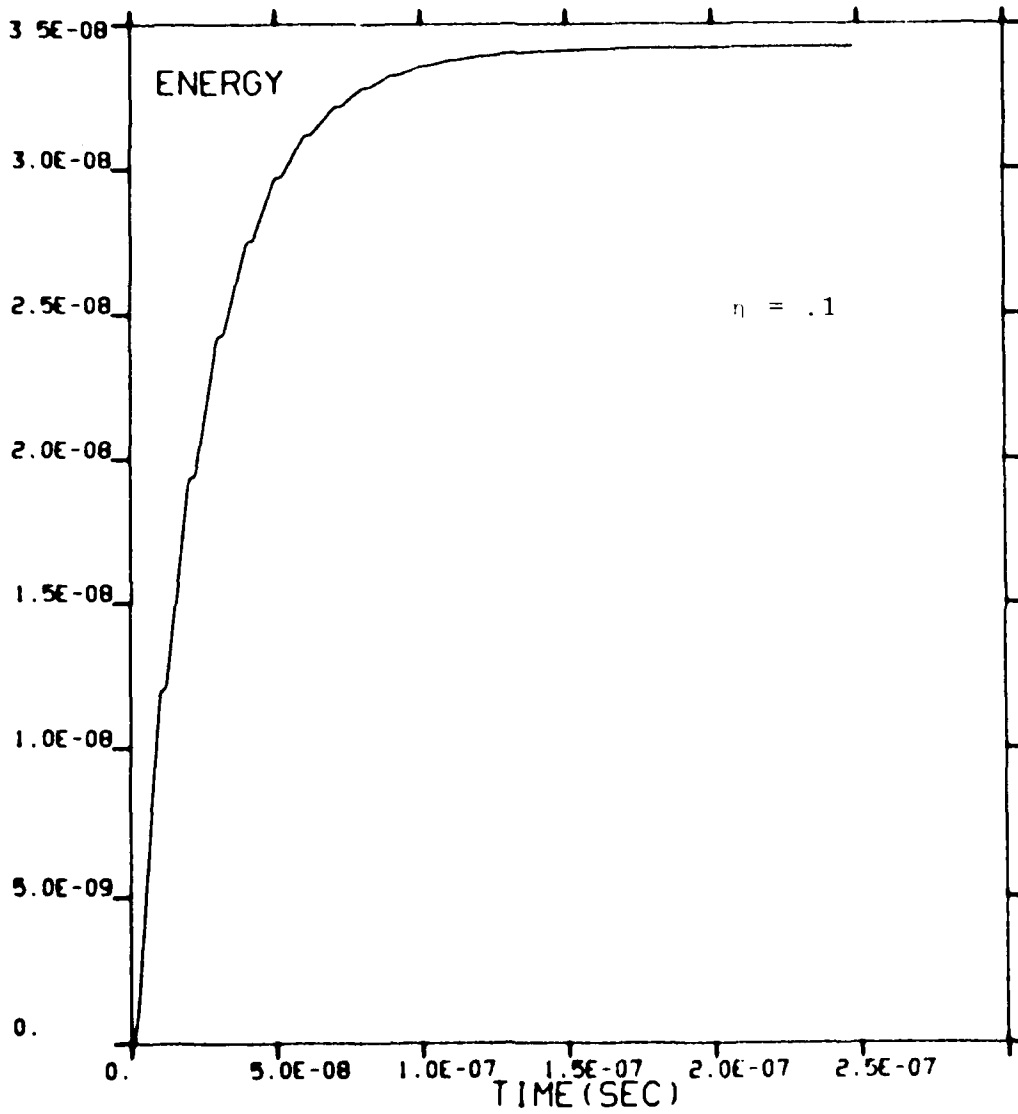
Figure 43a. Energy into load

90
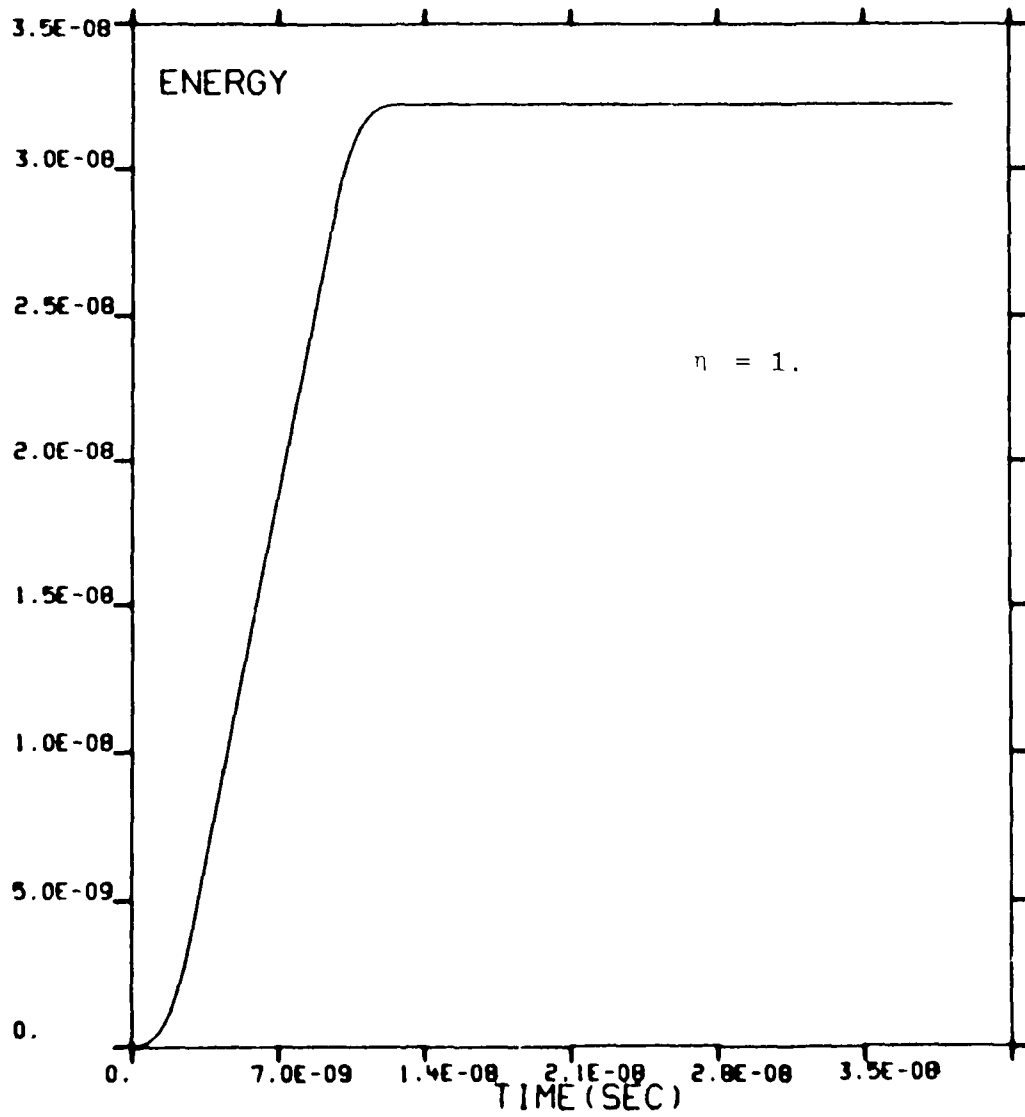
Figure 43b. Energy into load
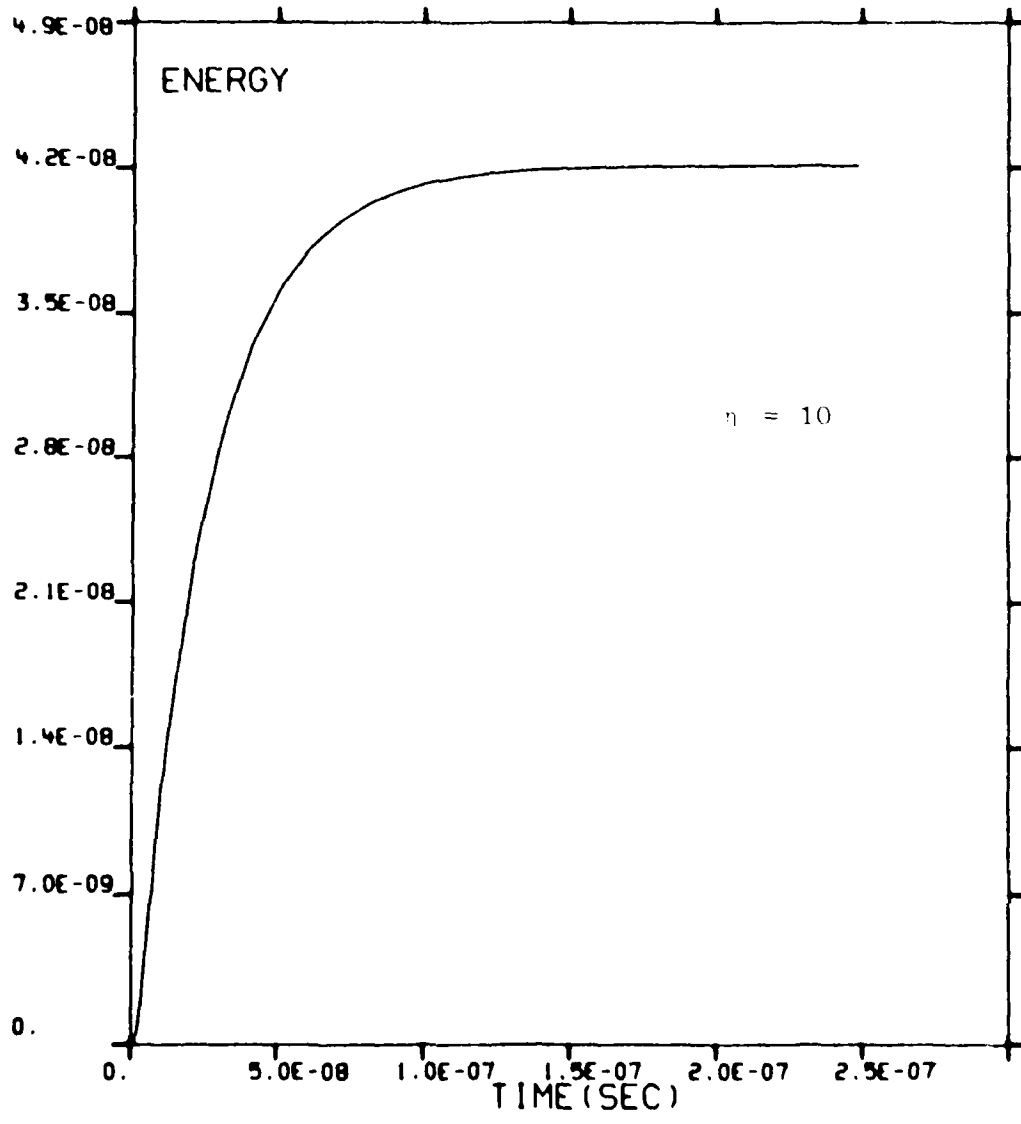
Figure 43c. Energy into load
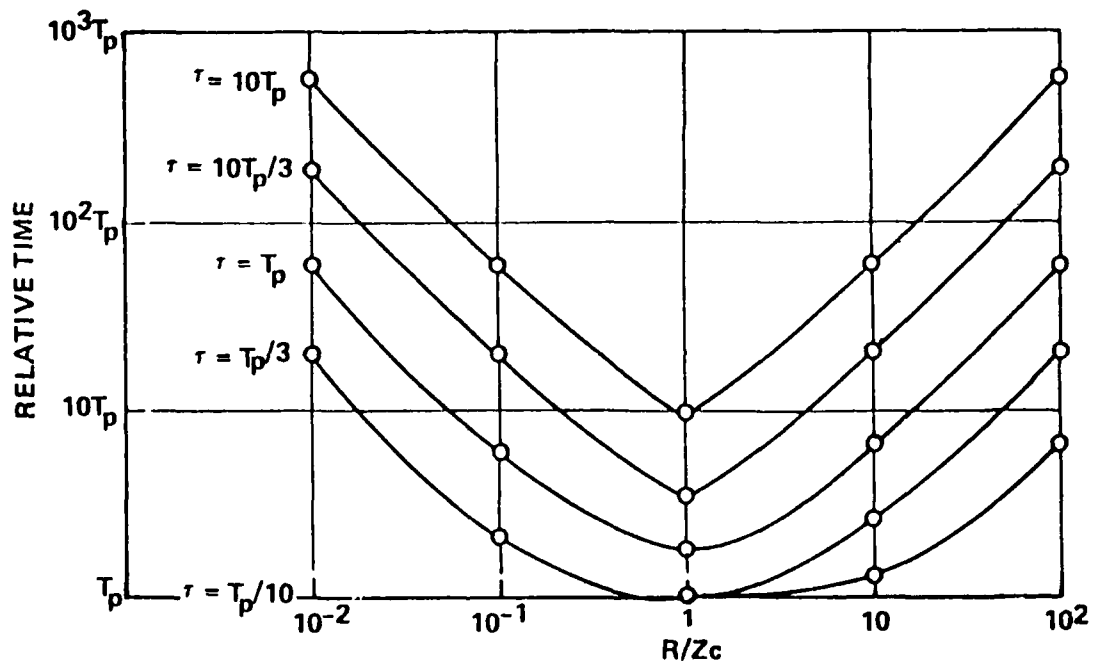
Figure 44. Time to deposit 50% of final energy into load

93

Sufficient information has now been presented about single wire solutions to proceed to the simplest multi-wire model, that of the two-wire-to-shield transmission line.

3-3 TWO WIRE ANALYSIS

It is of interest to consider, in a multi-wire bundle, how one can couple current from one wire to another. The obvious place to study such effects is the two-wire bundle. In the Appendix we have considered the analytic analysis of the two-wire bundle and have shown how the two-wire bundle reduces to single wire solutions. Such a reduction is extremely useful in terms of conceptualizing what is happening in the coupling, but the obvious way to demonstrate the coupling is to present the results of the current and energy, for example, that appear in the two wires when only one is driven. The current that flows in the un-driven wire is all coupled current. We have analyzed various two-wire bundles in order to consider various coupling effects.

The analytic solution that is presented in Appendix II assumes that there is only one propagation velocity. In general, in a multiwire bundle, there can be many propagation velocities, which are a source of coupling from one wire to another. While it is beyond the scope of this report to detail the consequences of this coupling, some calculations have been done on a two-wire bundle with two different phase velocities. The analysis seems to indicate that, particularly at low impedance termination, there can be a significant coupling effect due to the different phase velocities. The remainder of the calculations have been performed on two-wire bundles with one phase velocity. One two-wire bundle was constructed using the same capacitance matrix as the multi-phase velocity bundle and by choosing the inductance matrix in such a way as to give one phase velocity. The other two-wire bundle was constructed in such a way as to represent a seven-wire bundle where six of the seven wires are tied together. Let ℓ represent the wire of interest and

$$
\begin{aligned}
V_i &= V & i &\neq \ell \\
V_i &= V' & i &= \ell
\end{aligned}
$$

(3.16)

94

where V_i is the voltage of the ith wire with respect to the shield. The relationship between charge and voltage is again

$$Q_i = C_{ij}V_j \tag{3.17}$$

If we sum over all i, $i \neq \ell$ we have

$$\sum_{i, i \neq \ell}^{N} Q_i = \sum_{i, j, i \neq \ell} C_{ij}V_j$$

$$= \sum_{i \neq \ell}^{N} C_{i\ell}V_\ell + \sum_{i, j \neq \ell}^{N} C_{ij}V_j$$

$$= \left(\sum_{i \neq \ell}^{N} C_{i\ell} \right) V' + \left(\sum_{i, j \neq \ell}^{N} C_{ij} \right) V$$

$$\tag{3.18}$$

and

$$Q_\ell = \sum_{j=1}^{N} C_{\ell j}V_j$$

$$= C_{\ell\ell}V_\ell + \left(\sum_{j \neq \ell}^{N} C_{\ell j} \right) V \tag{3.19}$$

if we think in terms of two wires, Q_1 and Q_2 and let

$$Q_1 = Q_\ell \; , \; V_1 = V'$$

$$Q_2 = \sum_{i \neq \ell}^{N} Q_i \quad V_2 = V \tag{3.20}$$

we have

$$Q_1 = C_{11}V_1 + C_{12}V_2$$

$$Q_2 = C_{12}\,V_1 + C_{22}\,V_2 \tag{3.21}$$

where
$$C_{11} = C_{\ell\ell}$$

$$C_{12} = \sum_{j \neq \ell}^{N} C_{\ell j} = C_{21} = \sum_{j \neq \ell}^{N} C_{j\ell}$$

$$C_{22} = \sum_{i,j \neq \ell}^{N} C_{ij} \tag{3.22}$$

We have considered a seven wire bundle and picked out the wire with the largest driver so that $\ell = 3$ in the seven wire bundle.

In Figure 45 and 46 we plot the ratio of E/E_{MAX} for the bundles TW2 and TW3 respectively. In this ratio, E is the energy dissipated across each termination for the un-driven wire and E_{MAX} is the maximum energy capability across each termination for the driven wire. The quantity E/E_{MAX} is plotted as a function of R_2 for various values of R_1, where R_2 is the ratio of the termination impedance to the diagonal characteristic impedance of the un-driven wire and R_1 is the same ratio for the driven wire. These plots indicate that the coupled energy from the driven to the un-driven wire approach a maximum value of C^2 times the maximum value of the energy of the driven wire, C is the coupling factor defined in Appendix V. It is important to realize that the quantity C is always much less than one for any realizable bundle.

3-4 SEVEN WIRE ANALYSIS

The seven wire line analysis has been performed in order to demonstrate the basic tenets of the previous sections when applied to a larger bundle of wires. We have considered various distributions of seven wire drivers which are typical of groups of seven wires in a larger bundle (37 wire bundle). In these calculations we have singled out the wire in that distribution with the largest driver and varied the terminating resistance of that wire as a function of the terminating resistances of the other six wires. In Appendix VII we present the results of these calculations.

96

10^{-1}

$E/E_{MAX} = c^2$

$R_1 = 10$

$R_1 = 1$

10^{-2}

$R_1 = .1$

E/E_{MAX}

10^{-3}

10^{-4}

10^{-2} 10^{-1} 1.0 10

R_2
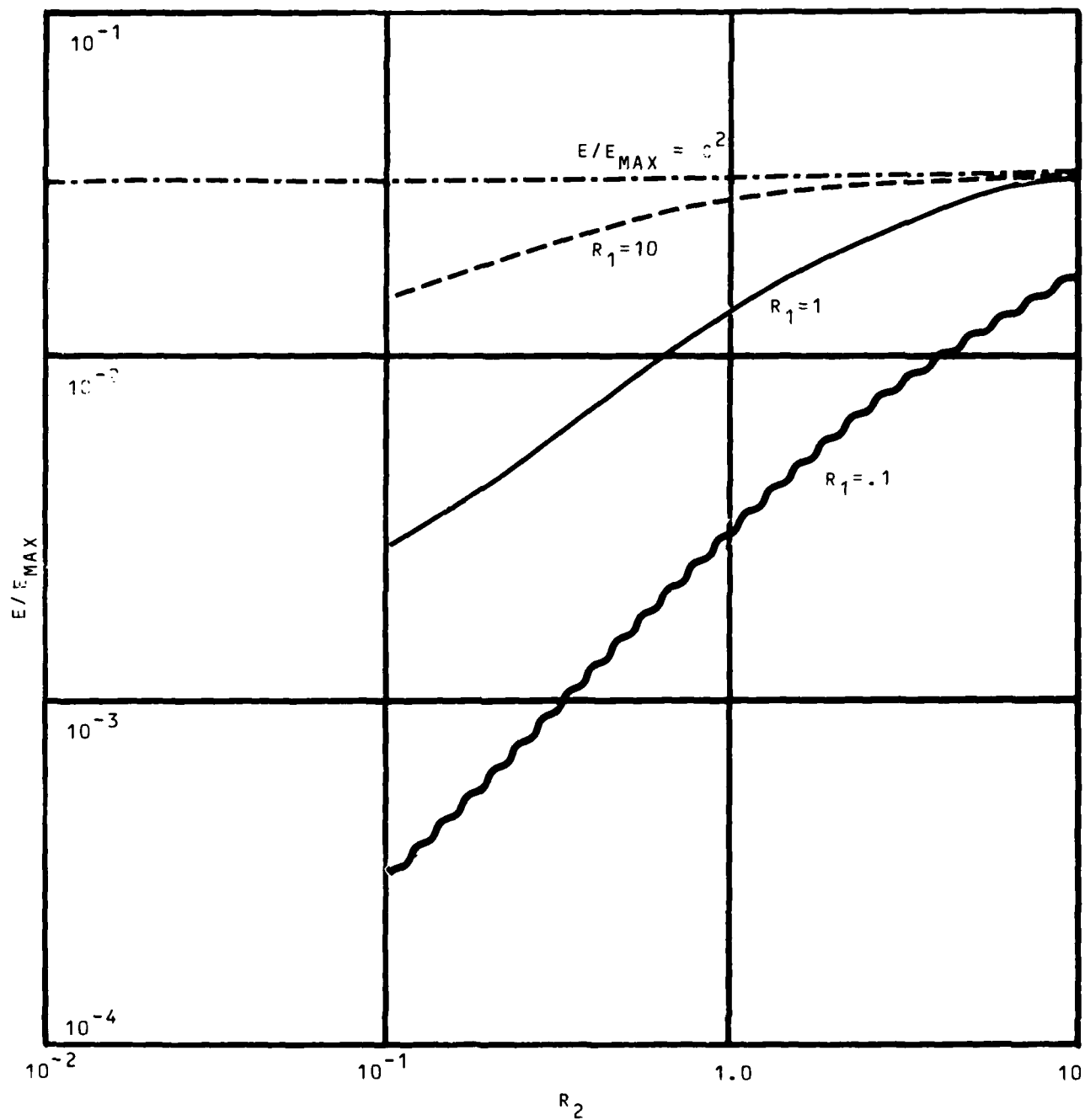
Figure 45. E/E_{max} vs. R_2 - TW2
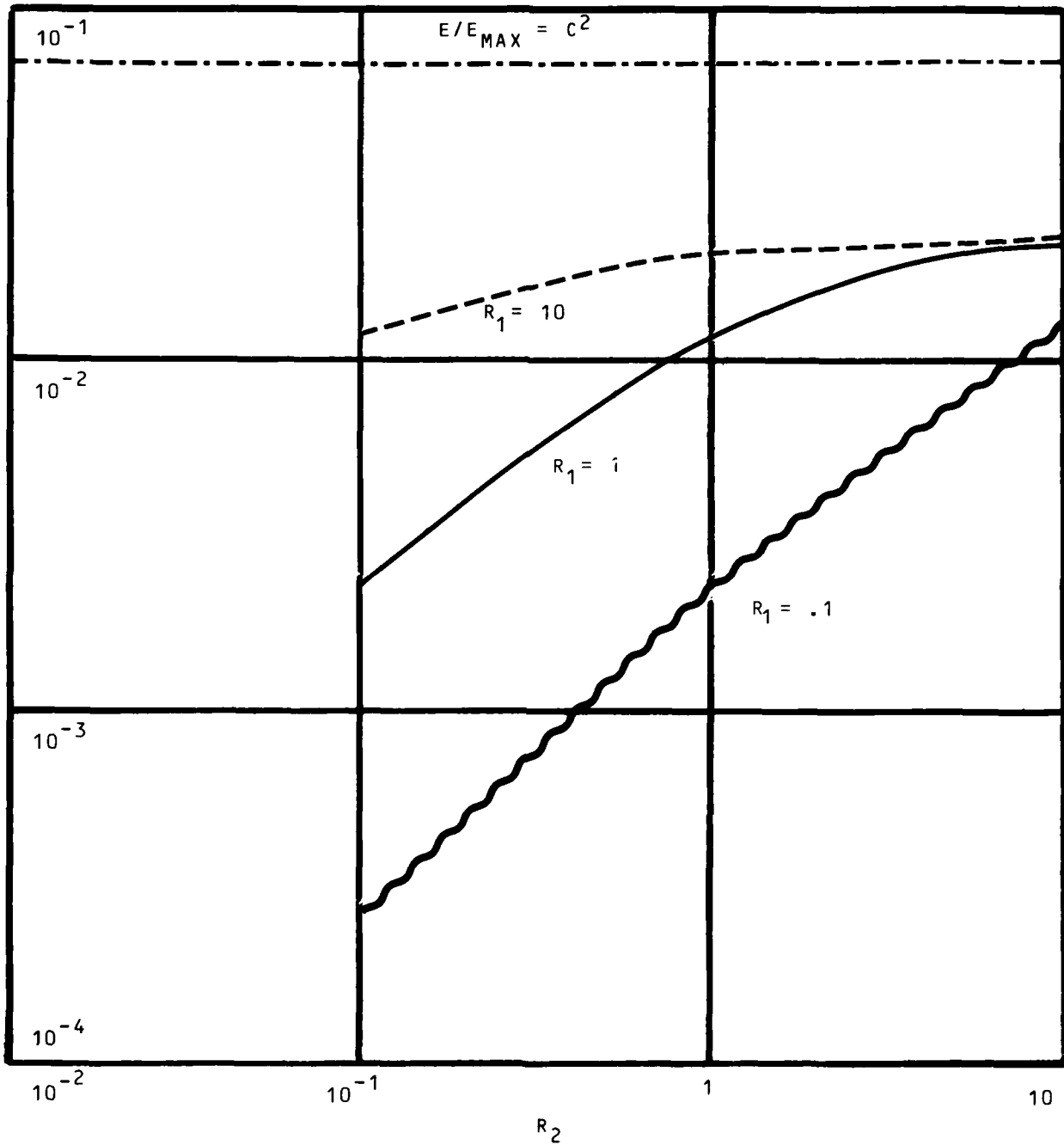
Figure 46. E/E_{max} vs. R_2 - TW3

One basic tenet of our analysis is that one can think of each wire in a multiwire bundle as a single-wire transmission-line driven by an effective drive I_D given by

$$I_D = I_\ell + \sum_{\substack{i=1 \\ i \neq \ell}}^{N} C_i |I_i|$$

(3.23)

Where I_ℓ is the driver for the wire of interest, wire ℓ, I_i are the drivers for all the other wires, and C_i are the coupling terms.

$$C_i = Z_{i\ell}/(Z_{ii}Z_{\ell\ell})^{\frac{1}{2}}$$

(3.24)

The charcteristic impedance matrix is given by $\bar{\bar{Z}}$ and N is the number of wires in the bundle. We can compute the total energy dissipated for a single-wire transmission line, E_{MAX}, driven by this effective driver using the results of Appendix III and compare with the actual energy dissipated from the numerical calculations. Shown in Figure 47-49 are the results of these calculations. The labelling convention is detailed in Appendix III. On these plots, E_{MAX} is the maximum energy capability per termination for the wire with the largest driver (including the coupling), R_1 is the ratio of the termination impedance to the diagonal element of the characteristic impedance for the wire with the largest driver, and R_2 is the same ratio for all the other wires. It is clear from these plots that E_{MAX} represents the upper limit for the energy.

3-5 LOSSY CABLE TRANSMISSION LINE

It is of interest to consider dissipative effects in evaluating the current that flows through the terminations for a cable driven by X-rays. In general, for any real cable there will be a resistance per unit length along the length of the cable due to skin depth losses and a conductance per unit length across the dielectric due to the dark conductivity of the dielectric. In the following paragraphs, we will discuss how to incorporate frequency dependent conductance and resistance into the transmission-line equations and present our solutions of these equations.

99
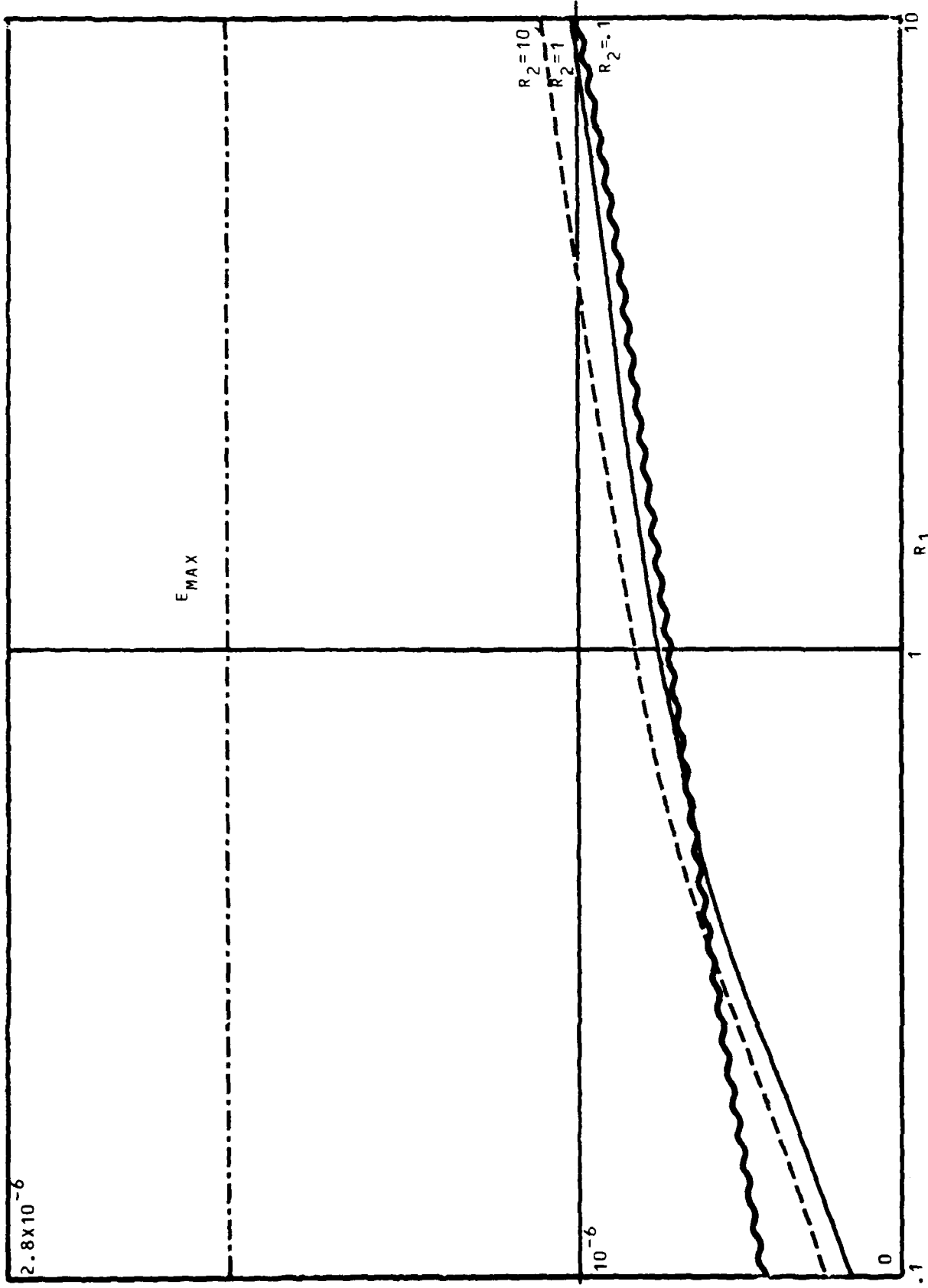
Figure 47. E(JOULES) vs. R_1 - SE)
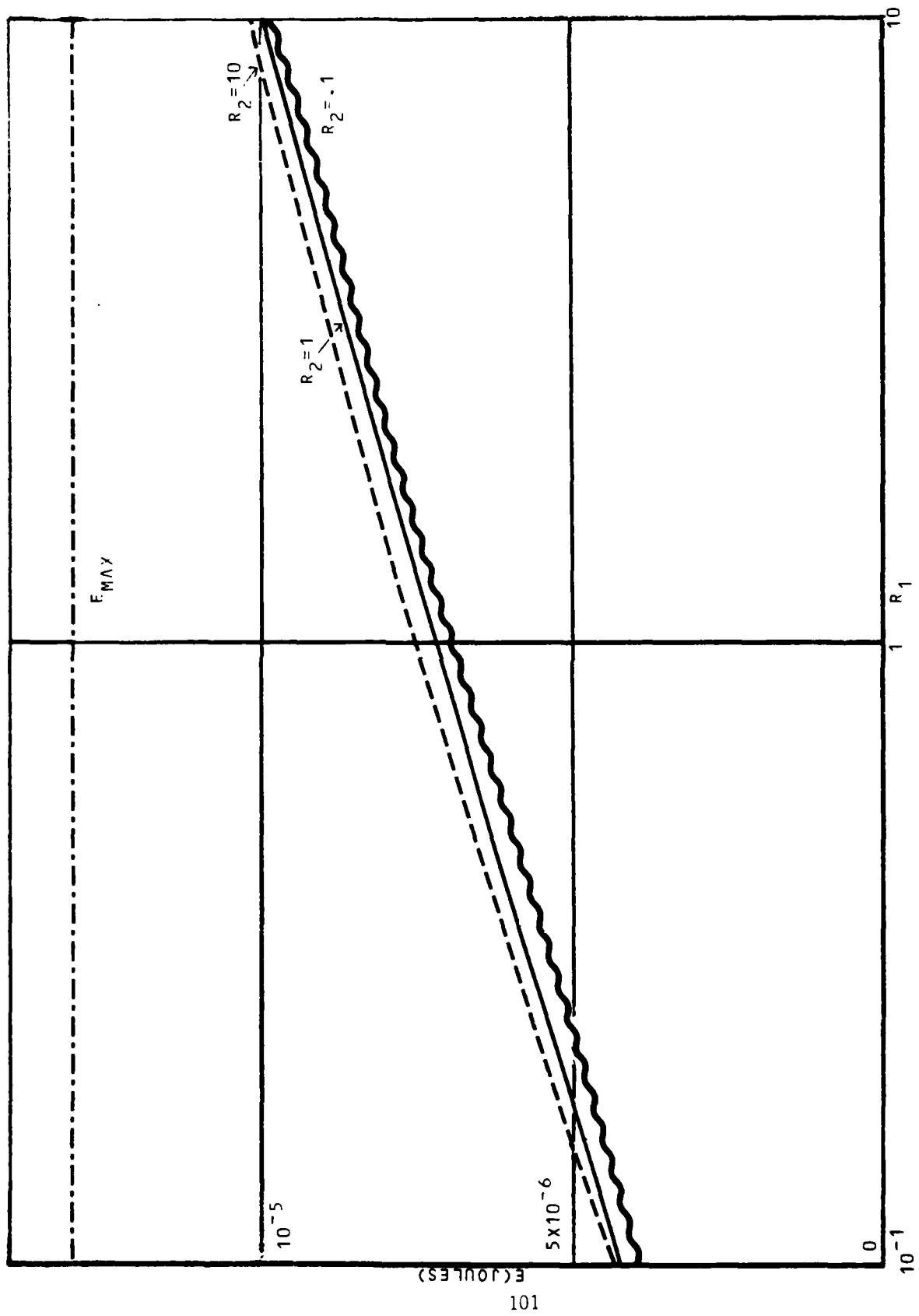
Figure 48. E(JOULES) vs. R_1 - SE2
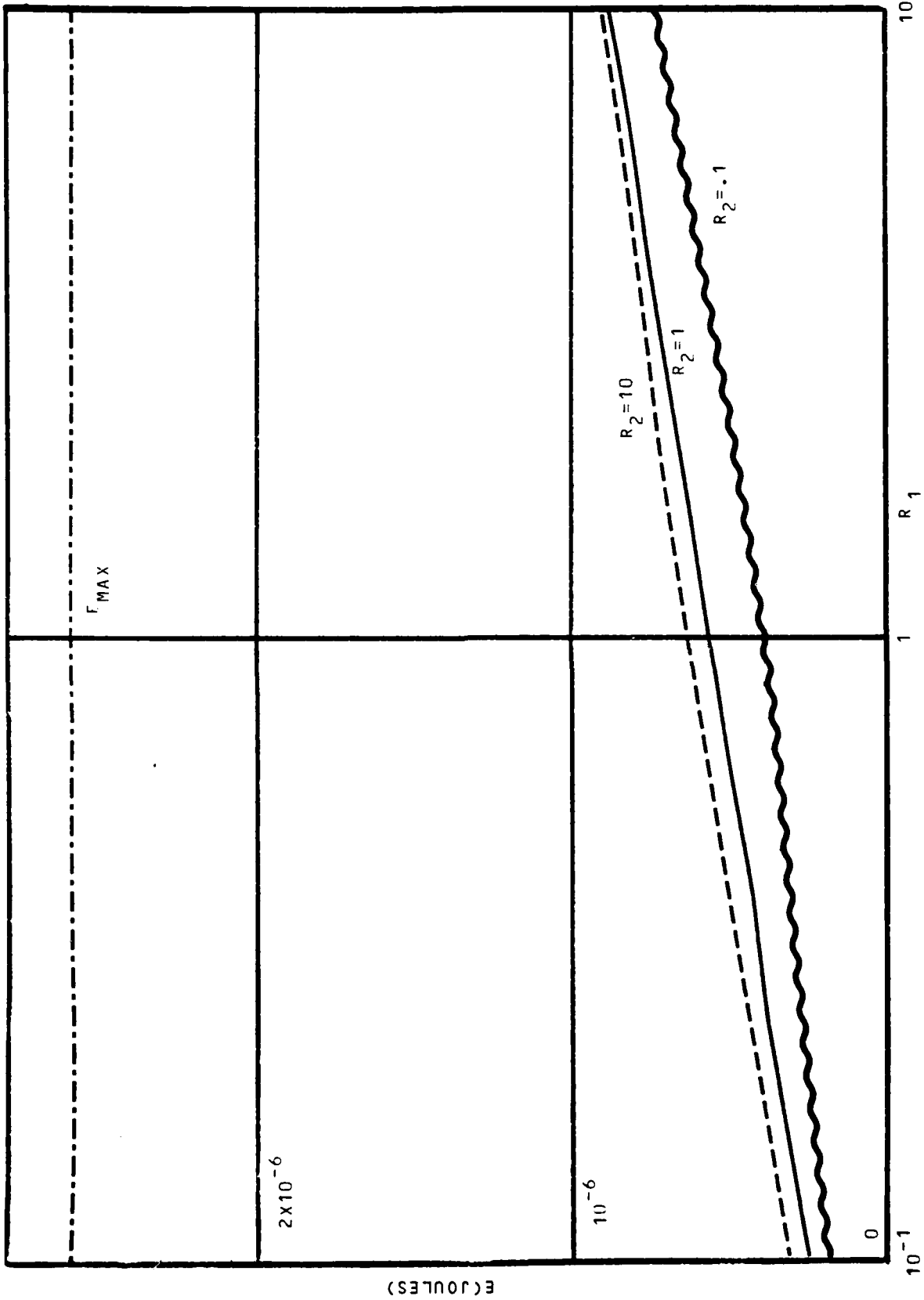
Figure 49. E(JOULES) vs. R_1 - SE 3

If we allow our cable to be lossy, the following transmissionline equations are appropriate:

$$\frac{\partial V}{\partial X} = -L\frac{\partial I}{\partial t} - RI$$

$$\frac{\partial I}{\partial X} = -C\frac{\partial V}{\partial t} - GV + I_D \quad . \tag{3.25}$$

For convenience we will limit ourselves to single-wire cables and so drop all vector notations. In these equations R is the resistance per unit length and G is the conductance per unit length. The method of solution is the same as indicated in Appendix II, and so we arrive the following fourier-transformed equations.

$$\frac{\partial \tilde{V}}{\partial X} = iwL\tilde{I} - R\tilde{I}$$

$$\frac{\partial \tilde{I}}{\partial X} = iwC\tilde{V} + \tilde{I}_D - G\tilde{V} \tag{3.26}$$

At this point, we will allow R and G to be functions of frequency, i.e.

$$R = R(W)$$
$$G = G(W) \tag{3.27}$$

Using the same assumptions as made in Appendix II we arrive at the following equations:

$$\frac{d^2\tilde{I}}{dx^2} = -k^2\tilde{I}$$

$$\frac{d^2\tilde{V}}{dx^2} = -k^2\tilde{V} + \left| iWL-R \right| \tilde{I}_D \tag{3.28}$$

where

$$k^2 = \frac{w^2}{v^2} - RG + iw(RC + GL). \tag{3.29}$$

These equations can be solved, as in Appendix II, for $\tilde{I}(w,X)$ and $\tilde{V}(w,X)$. In particular, the solution for $\tilde{I}(0,w)$ is as follows

$$\tilde{I}(o,w) = \frac{-i\tilde{I}_D(w)}{k\left[1-P_R P_L e^{2ikl}\right]} \left[\frac{Z_o}{Z_o+Z_L}\right]\left[1-p_R e^{2ikl} - \frac{2Z_o}{Z_o+Z_R} e^{ikl}\right] \tag{2.30}$$

The notation in this solution is the same as has been used previously with the following expression for Z_o, the characteristic impedance

$$Z_o = k/(wc + iG) \tag{3.31}$$

Since k and Z_o are functions of w, it is not possible to obtain directly $I(o,t)$, given by the following equation

$$I(o,t) = \frac{1}{2\pi} \int_{-\infty}^{+\infty} dw \; \tilde{I}(o,w)e^{-iwt} \tag{3.33}$$

We have performed the required integrations numerically using a fourier-transform code and will present the results of this analysis in Appendix VIII.

SECTION 4
MODEL VALIDATION

4-1 INTRODUCTION

The key to successfully developing the desired threat definition is an accurate analytical tool which can predict not only photon responses (i.e., the desired invariant current source terms) but also the desired electrical parameters required for the maximum energy analysis. Existing tools, such as the CHIC code, have been developed to provide such information. An interesting characteristic of these programs, which is associated with the physics of the direct drive phenomenon, is that the calculated electrical parameter and current driver definitions are derived from the same set of physical and material parameters contained in the subject cable. The fact that these entities are not mutually independent of one another provides a fortuitous situation which can be exploited to advantage.

Since the successful development of the maximum energy concept rests with the accuracy of such tools as the CHIC code, it is highly desirable to obtain an independent validation of the accuracy of such codes before committing extensive effort based on their utilization. Such a validation is described in this section. The interrelationship of the current driver and electrical parameter definitions provides an excellent double check on the code validation conclusions. The cable type which will be selected is also the baseline multiwire cable type which has been used as the model for the development of the multiwire analysis technique. An excellent choise for a candiate cable type is the AWG 24 (Raychem 44/0411 space wire), 37 wire foil/film (Copper/Mylar) shielded cable identical to that used in the DSCS III Spacecraft and in the DSCS III Harness Photon Test.

4-2 CABLE PARAMETER SENSITIVITY-DRIVERS

The very large parameter space associated with any possible multiwire cable configuration requires a considerable reduction if any meaningful predictive capability is to be realized. That is to say, we would like to isolate those parameters which predominantly affect the response of a multiwire cable configuration to inci-

dent ionizing radiation. In order to effect this reduction, we have employed the CHIC computer code to perform a large number of calculations in various multiwire cable configurations. The CHIC code, details of which have been presented elsewhere, [8-10] is uniquely suited to perform this analysis since it is capable of handling an arbitrary cross sectional geometry and material configuration.

For this particular cable configuration, the parameter space that is pertinent to an SGEMP analysis would include the following variables:

- Individual Wires   –   Composition, Plating, Size
- Wire Insulation   –   Composition, Thickness, Dielectric Constants, Density
- Liner   –   Composition, Thickness, Density
- Overshield   –   Composition, Plating, Thickness
- Geometric   –   Shield configuration relative to wire bundle, relative positions of wires, total number of wires in bundle.

Our approach in this sensitivity study is to consider only those variables which we feel might realistically be considered in any multi-conductor bundle. In addition, we have considered how one might reduce these variables even further for the purpose of a sensitivity study. One example of this is the assessment problem associated with multi-layered dielectrics surrounding the individual wires of the bundle, with frequency dependent dielectric constants. We have investigated the possibility of representing such a configuration with one dielectric with an effective dielectric constant. The outcome of this investigation[11] has indicated that it is perfectly adequate, for the purposes of a sensitivity study, to model a multi-layered dielectric by a single dielectric with an effective dielectric constant. Such a modeling will certainly indicate the trends in the response as a function of the various parameters. On the other hand, if one wants to pinpoint the response of a given multiwire bundle, one has to take into account the details of the multi-layered dielectric configuration. Such an analysis has been performed and it has been found that a modeling of the double layered dielectric is critical to accurately calculating the response of the multiwire bundle.[12]

106

4-2.1 Sensitivity Study

The following parameters have been considered in our sensitivity study:

- Wire Size   -   16-26 AWG
- Wire Plating   -   Sn, Ni
- Shield Composition   -   Cu, Al
- Liner Thickness   -   1,2 mil
- Angle of Incidence of Radiation
- Geometric Configuration
- Shield Configuration

4-2.1.1 Geometric and Shield Configuration

One question of interest is the dependence of the maximum response in a
bundle to the number of wires in the bundle. Shown in Figure 50 is a comparison of
a 61-wire bundle and a 7-wire bundle. The two bundles are identical, except for the
number of wires. Since the largest response is always on the wire nearest to the
shield, we do not expect there to be a significant difference in the maximum response
from a 61-wire bundle to a 7-wire bundle. In fact, our calculations indicate that
the maximum response for the 61-wire bundle is slightly smaller than the 7-wire
bundle. For this reason, we have considered the 7-wire bundle to be a canonical
configuration representing any close-packed multi-conductor bundle (see Figure 51
and have performed the majority of our computations on it. We have also considered
various packing arrangements of the wires in the bundle; the 7-wire bundle representing
hexagonal close-pack, and have found very little difference. An example of a hexa-
gonal close-pack and circular pack bundle of wires is shown in Figure 52. In addition,
we have found very little difference in the response between a circular and hexagonal
shield, and so have performed most of our calculations on a circular shield configura-
tion. An example of a hexagonal shield is shown in Figure 53.

4-2.1.2 Wire Size

We have considered four different wire radii, ranging in size from 8.0
to 25.4 mils. Shown in Figure 54 are worst case response versus wire gauge. Since
a positive response indicates that the dominant effect is wire emission, we expect
that the bundle with larger radii wires will have the larger responses, and this
is verified by the calculations.

107
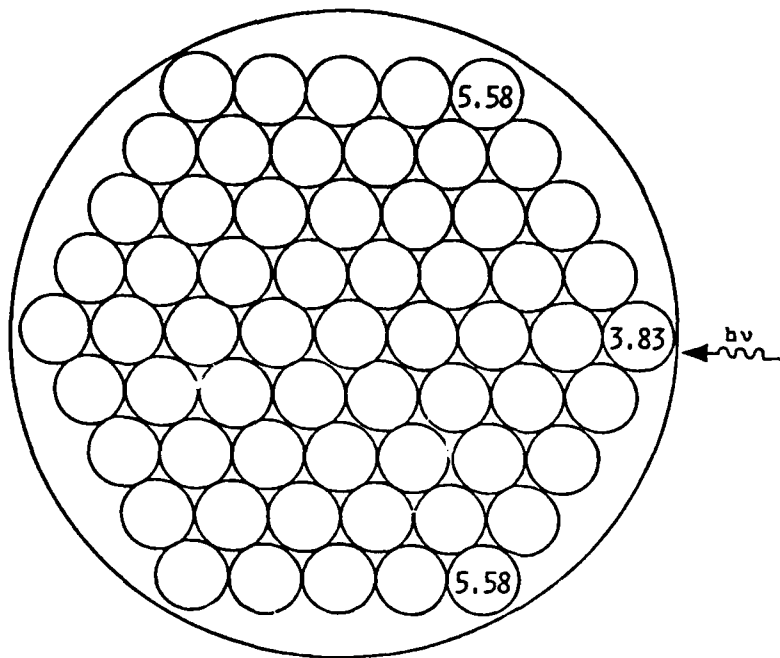
SN-PLATE
16 GAUGE
2 MIL LINER
ALUMINUM SHIELD
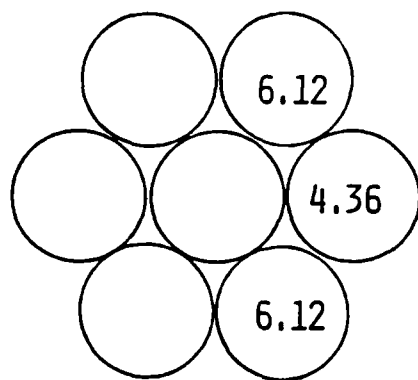
$\left[10^{-10} \text{ (COUL/CM)/(CAL/CM}^2)\right]$

SN-PLATE
16 GAUGE
2 MIL LINER
ALUMINUM SHIELD

$\left[10^{-10} \text{ (COUL/CM)/(CAL/CM}^2)\right]$

Figure 50.   Comparison of 61-wire and 7-wire bundle

SHIELD

DIELECTRIC LINER

CENTER CONDUCTOR

PRIMARY INSULATION
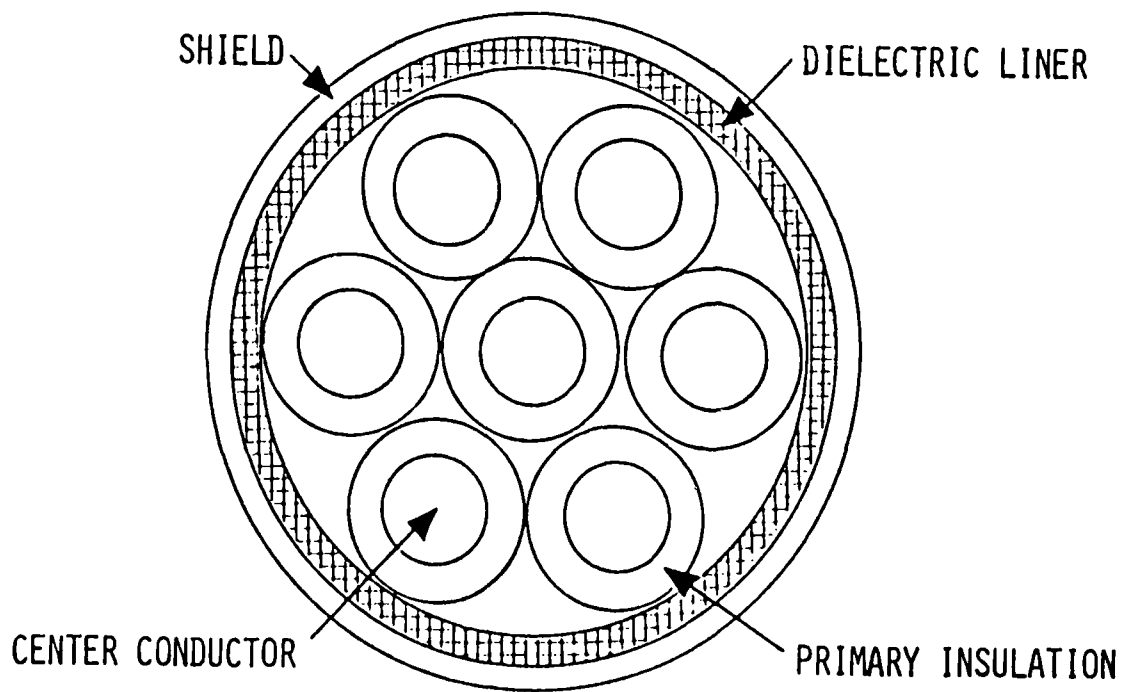
Figure 51. Geometric model used for parametric study -
hexagonal close-pack - circular shield
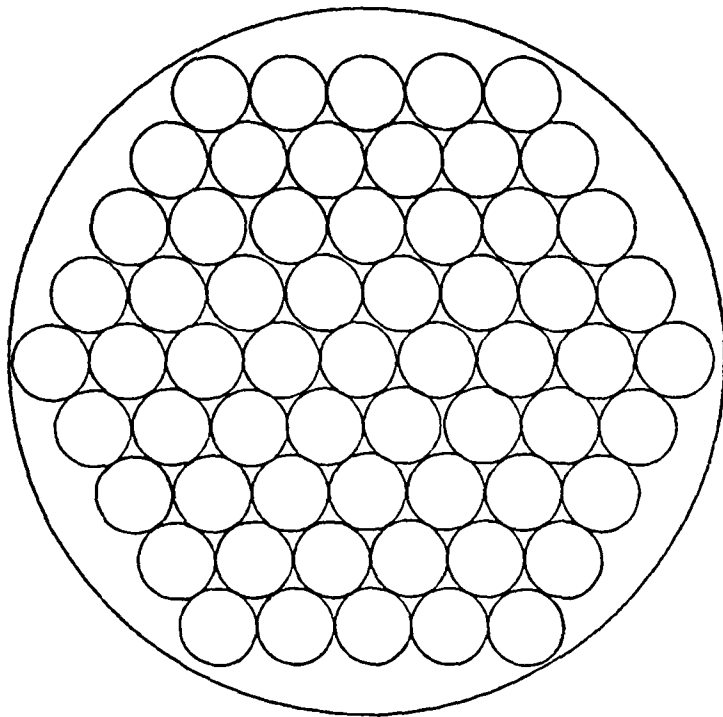
61-WIRE BUNDLE
HEXAGONAL PACK
— CIRCULAR SHIELD —
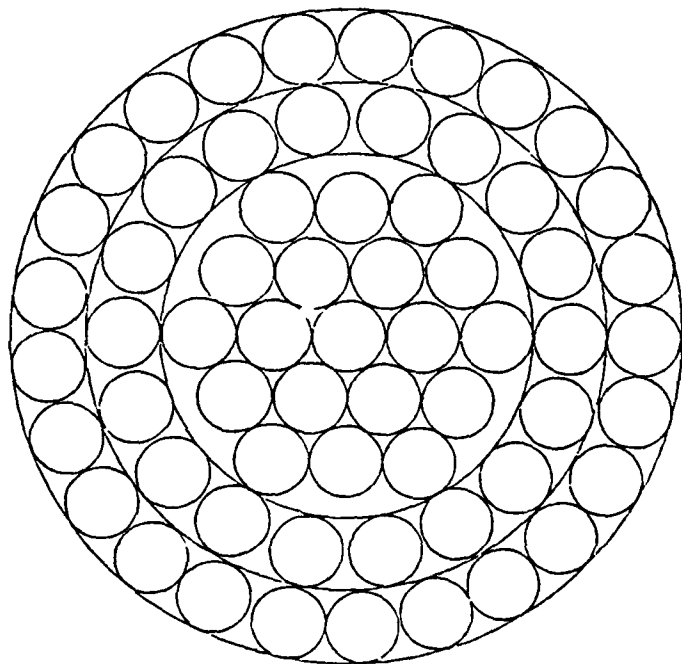
62-WIRE BUNDLE
CIRCULAR PACK
— CIRCULAR SHIELD —

Figure 52.   Comparison of hexagonal and circular pack

110
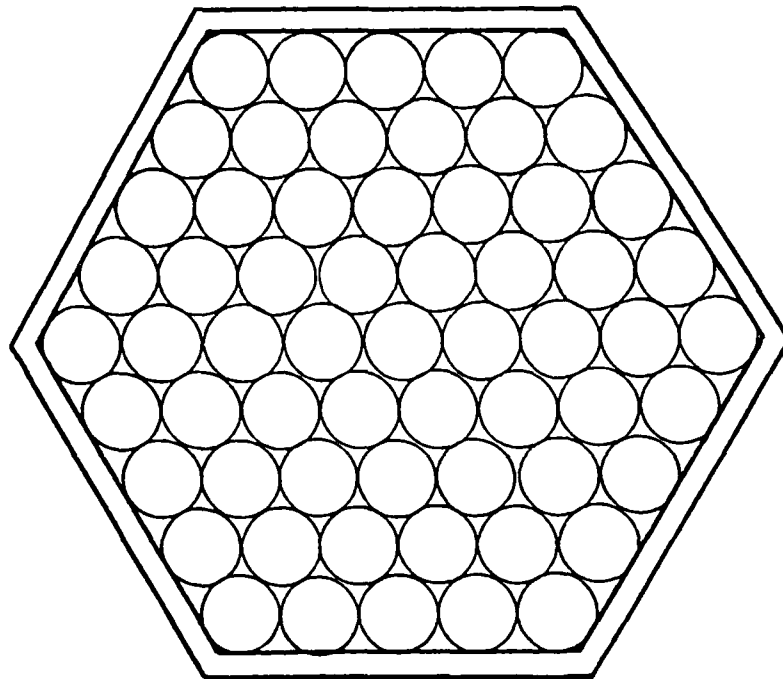
Figure 53.   61-wire bundle hexagonal pack - hexagonal shield

● Sₙ-PLATE, ALUMINUM SHIELD   AWG 16 — 25.4 MILS
○ Sₙ-PLATE, COPPER SHIELD   AWG 20 — 16.0 MILS
✕ Nᵢ-PLATE, ALUMINUM SHIELD   AWG 24 — 10.0 MILS
■ Nᵢ-PLATE, COPPER SHIELD   AWG 26 — 8.0 MILS
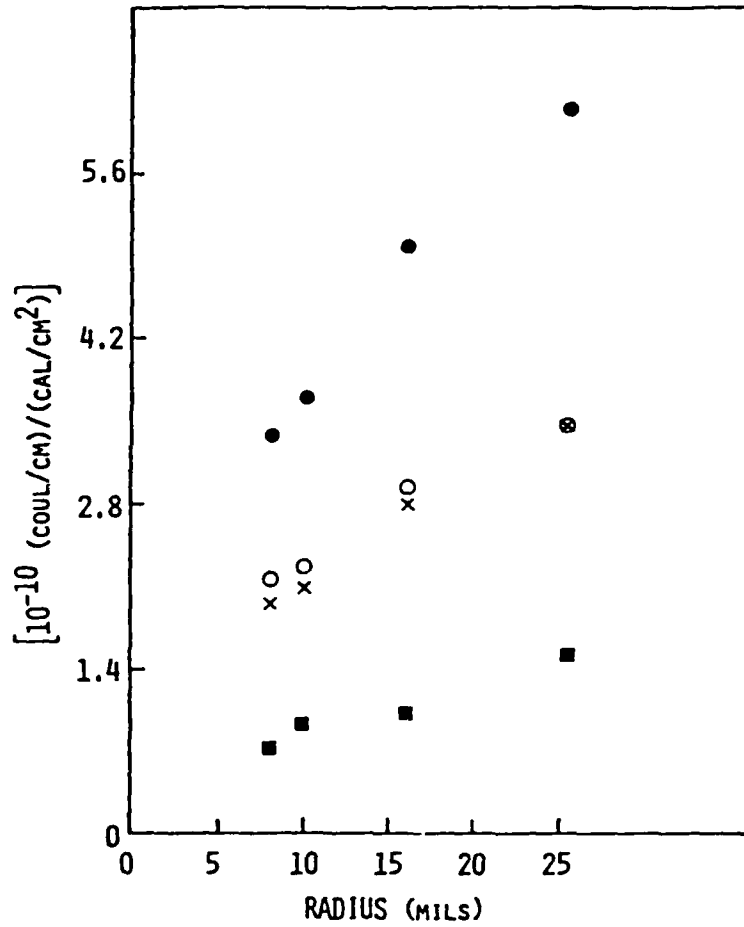
Figure 54.   Worst case response versus wire gauge - 2 mil liner

112

4-2.1.3 Wire Plating and Shield Composition

We have considered Sn and Ni wire plating and Cu and Al shield composition. Since, again, the dominant effect is wire emission, we expect the largest response to occur for that configuration which has the largest Z wire plating and the smallest Z shield composition and this is verified by the calculations, as indicated in Figure 54.

4-2.1.4 Liner Thickness

The effect of the thickness of the dielectric liner, which is bonded to the overshield, on the response of the wires in the bundle has been considered. A thinner liner would result in the shield emission being more effective, thereby reducing the worst case response for a given bundle. We have considered one and two mil liners. Shown in Figure 55 is a typical distribution of drivers for these two liners. It is clear that the response is indeed smaller when the liner is half as thick, but not significantly smaller.

4-2.1.5 Angle of Incidence of Radiation

Shown in Figure 56 are the distribution of drivers for various angles of incidence. An angle of incidence of 0° gives rise to the worst case driver.

4-2.2 Conclusions

For the purposes of comparing one bundle configuration to another, we will use as the criterion the maximum response in a given bundle. For the range of parameters considered in this study, the bundle configuration that resulted in the largest maximum response had the following parameters:

    (a) 16 AWG wire size,

    (b) Sn-plated wire,

    (c) Al shield,

    (d) 2 mil liner thickness, and

    (e) 0° angle of incidence.

The maximum response for this bundle was computed to be 6.12×10^{-10} $(coul/cm)/(cal/cm^2)$. If we take this configuration to be the baseline configuration, the following specific conclusions can be drawn from the sensitivity study:

Sn-PLATE
24 GAUGE
Aℓ SHIELD

(1 mil LINER)

$[10^{-10}$ (coul/cm)/(cal/cm^2)]

(2 mil LINER)
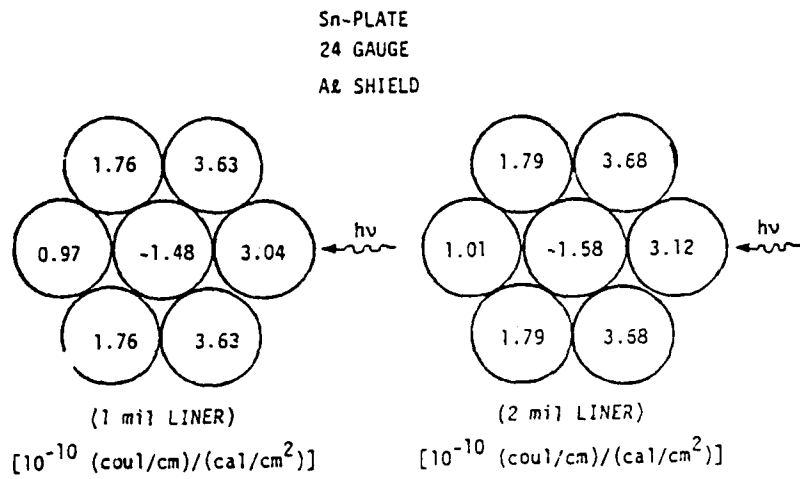
$[10^{-10}$ (coul/cm)/(cal/cm^2)]

Figure 55. 7-wire response

Sn-PLATE
16 GAUGE
ALUMINUM SHIELD
2 MIL LINER

REPEAT
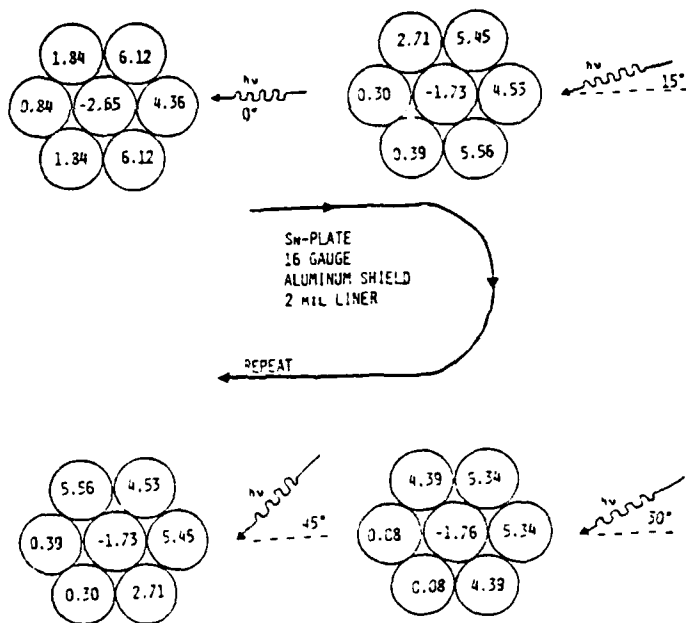
Figure 56. 7-wire response
$[10^{-10}$ coul/cm/cal/cm^2]
effect of incidence angle

114

(1) The maximum response is a monotonically increasing function
     of wire radius for all material configurations.

(2) Replacing an aluminum shield with a copper shield gives at
     least a factor of 0.64 reduction in driver from the baseline
     response.

(3) Replacing the tinned wires by Ni-plated wires, gives a factor
     of 0.58 reduction in driver from the baseline response.

(4) Replacing the tinned wires by Ni-plated wires, and replacing
     an aluminum shield by a Cu shield gives a factor of 0.26
     reduction in driver from the baseline response.

(5) For all material configurations, a small liner gives a
     slightly decreased response for the worst case driver.

(6) The angle of incidence of the radiation has only a small effect
     on the worst case driver, and 0° incident is the worst case.

These results indicate the relative insensitivity of a multi-conductor
bundle to realistic variations in the parameter space. In general, if we take the
maximum response as an indicator, the maximum variation is less than a factor of
ten. Although this analysis has mainly been carried out for one typical blackbody
spectrum, our calculations have also indicated that the response increases with
blackbody temperature, a result consistent with the absence of gaps between all
conductor-dielectric interfaces.

4-3 MODEL DRIVERS

This section will present the results of a complete analysis of the elec-
trical parameters and current drivers associated with 7 and 37 foil/film multiwire
cables. This analysis has been performed using the CHIC code, det.ils of which
have been considered elsewhere.[8] The CHIC code has the capability, not only
of calculating the current sources associated with Photon Direct Drive SGEMP, but
also all the parameters which electrically identify a given multiwire cable. The
electrical parameters can be conveniently represented in matrix form and are completely
analogous to the capacitance and inductance of a coaxial cable.

4-3.1 Foil/Film Multiwire Cable - Specification

We will be considering a 7 and 37 wire bundle in this section. These two
bundles are identical, except for the difference in the number of wires. Each multi-
wire cable consists of N individually unshielded wires within a single foil/film
overshield. In this section, we will specify completely the geometrical and material
configuration which has been used in these calculations.

115

4-3.1.1 Individual Wires

The individual wires are Raychem AWG #24 space wire which consists of pure tin coated, copper wire covered by a combination cross-linked, extruded poly-alkene and cross-linked, extruded polyvinyldene fluoride dielectric (Kynar). The extrusion process used for the Raychem space wire is such that there are no gaps between the dielectric and the conductor. Shown in Figure 57 is a model of the Raychem space wire with appropriate labels. Table 4 is a table of the corresponding parameters associated with the Raychem space wire which serves as inputs to the CHIC code.

4-3.1.2 Foil/Film Overshield

The foil/film overshield consists of a Sun Chemical #1132 film-foil laminate made of an electro deposited Copper foil on a polyester (Mylar) film. Figure 58 is a model of the overshield with appropriate labels and Table 5 is a table of the associated parameters which also serve as inputs to the CHIC code.

4-3.1.3 Geometric Model

We have assumed in these calculations that the individual wires in the multiwire bundle are hexagonally close-packed and that the overshield is circular. Shown in Figures 59 and 60 are the geometric models assumed in the calculations along with the labeling of the individual wires in the bundle. This labeling convention will be used throughout this section, both in the definition of the capacitance and inductance matrices and in the current drivers.

4-3.2 Incident Spectrum

The current drivers have been computed using the PIMBS-1A spectrum shown in Figure 61. We have assumed a 20 mil Mylar and 1 mil Al window between the photon source and the multi-wire cable, and will present all current drivers normalized to 1 cal/cm^2 incident on the cable overshield.

4-3.3 Electrical Parameter Definition of a Multiwire Bundle

There are two capacitive matrices which are relevant to multiwire bundles of N wires. One, which we will call Maxwell's capacitance coefficients, is defined by the following matrix equation:[6]

$$Q_i = \sum_{j=1}^{N} C_{ij} V_j \quad , \quad i = 1, \ldots, N$$

116
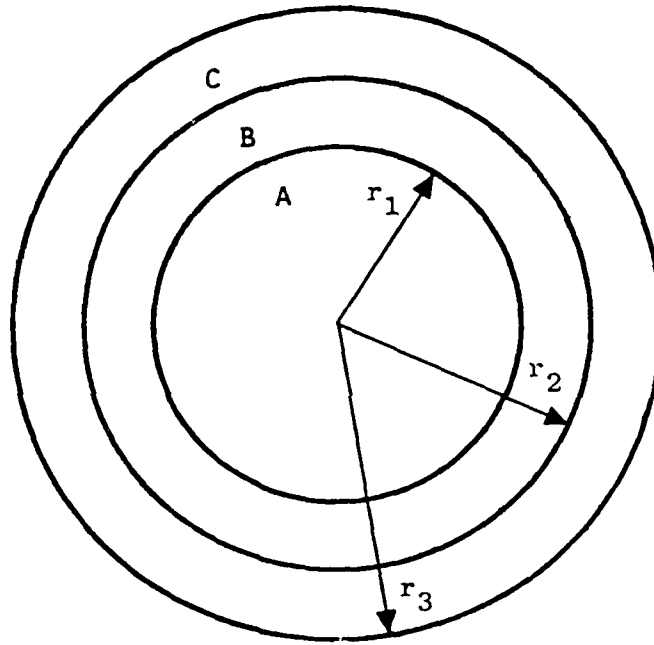
Figure 57. RAYCHEM space wire #24 AWG

Table 4. Parameters associated with RAYCHEM space wire # 24 AWG

MATERIAL	RADIUS (mils)	DENSITY (gm/cm^3)	RELATIVE DIELECTRIC CONSTANT
A (TIN COATED COPPER)	r_1 = 13.0	8.96	——
B (POLYALKENE)	r_2 = 16.5	1.08	2.25
C (KYNAR)	r_3 = 19.5	1.73	7.0
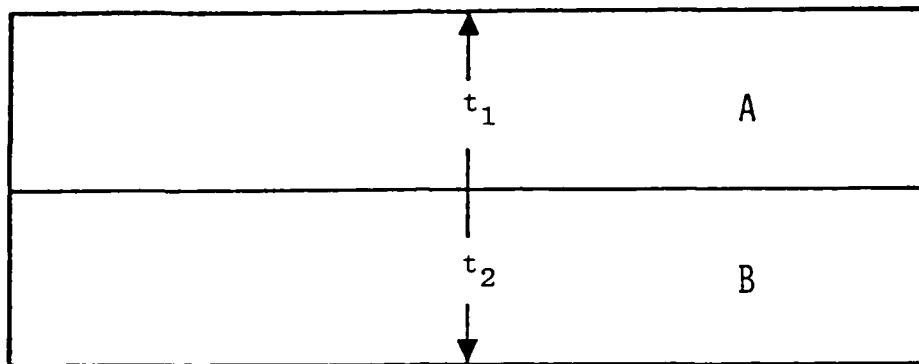
Figure 58.   Foil/film overshield

Table 5.   Parameters associated foil/film overshield

MATERIAL	THICKNESS (MILS)	DENSITY (GM/CM^3)	DIELECTRIC CONSTANT
A (COPPER FOIL)	t_1 = 0.7	8.96	---
B (MYLAR)	t_2 = 0.92	1.35	2.9
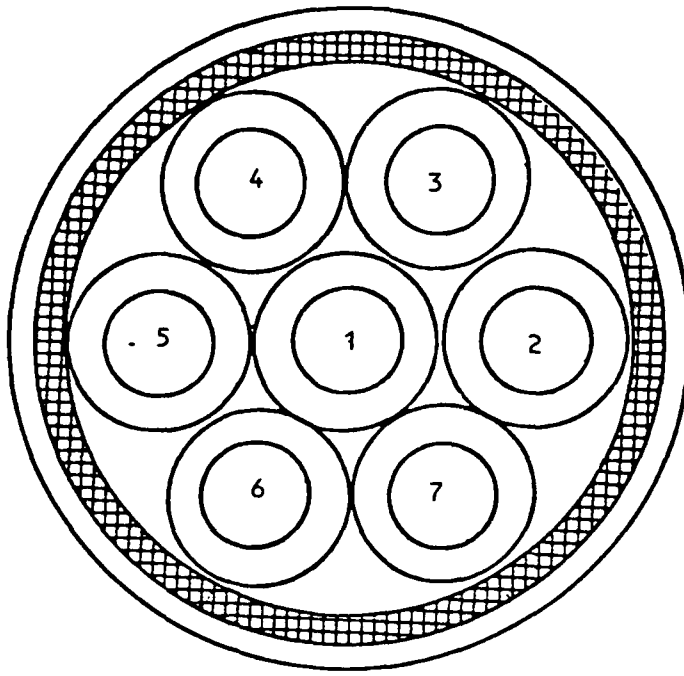
Figure 59.   7-wire multiwire bundle with labelling convention
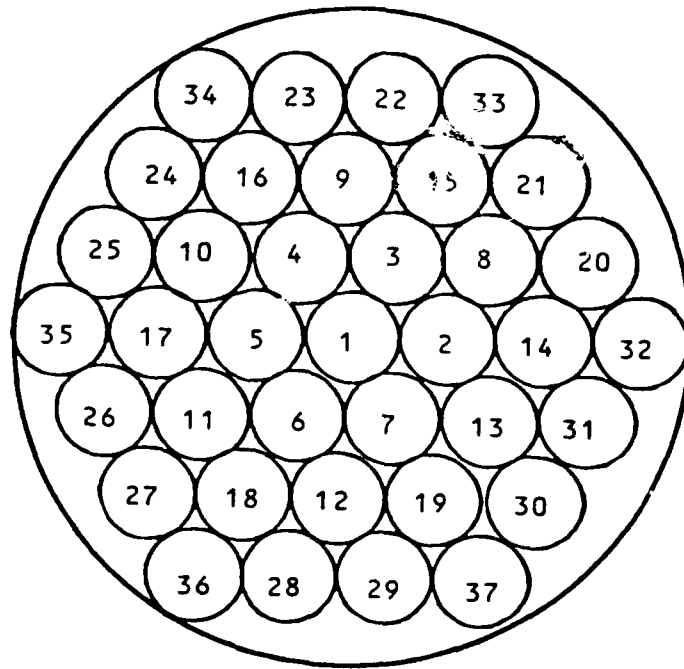
Figure 60.   37-wire multiwire bundle with labelling convention
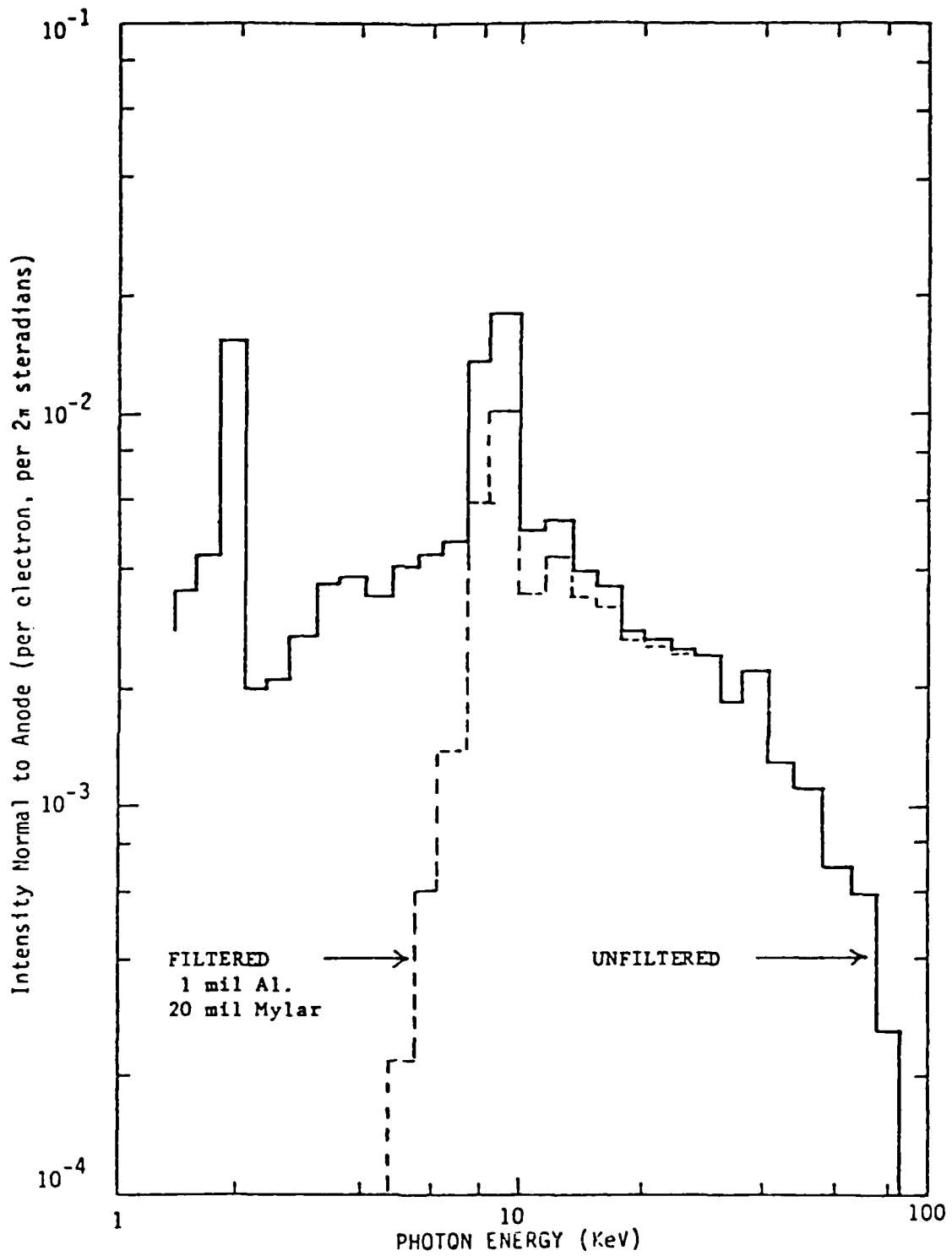
Figure 61. Sandyl calculation of PIMBS spectrum incident on cables

where Q_i is the charge on the ith conductor, V_j is the voltage of the jth conductor with respect to the shield, and C_{ij} are Maxwell's capacitance coefficients. C_{ij} is the ratio of the charge induced on the ith conductor to the potential on the jth conductor when all other conductors are at zero potential. An alternative capacitance matrix which can be determined from C_{ij} will be labeled $(C_M)_{ij}$. In this definition, $(C_M)_{ii}$ is the ratio of the charge on the ith conductor to the potential on the ith conductor when all other conductors have no charge. $(C_M)_{ij}$ ($i \neq j$) is the ratio of the charge on the ith conductor to the potential difference $(V_j - V_i)$ when all other conductors have no charge.

The inductance matrix is determined by computing the capacitance matrix C_{ij}^0 of the identical multiwire bundle without dielectric. The inductance matrix L_{ij} is determined by the following equation:

$$L_{ij} = \frac{(C^0)_{ij}^{-1}}{C^2}$$

where C is the speed of light in vacuum.

The propagation matrix $(\gamma^2)_{ij}$ is determined once L_{ij} and C_{ij} are known and is defined by the following equation:

$$(\gamma^2)_{ij} = \sum_{k=1}^{N} L_{ik} C_{kj} \quad .$$

This matrix is, in general, not diagonal; but when brought to diagonal form $(\gamma^2)_{ij}^D$; the diagonal elements are related to the multiwire phase velocities V_i by the following equation:

$$V_i = \left((\gamma^2)_{ii}^D \right)^{-1/2} \quad .$$

A knowledge of L_{ij} and C_{ij} can also be used to determine the characteristic impedance matrix Z_{ij} of a multiwire bundle which can best be represented symbolically as:

$$\bar{\bar{Z}} = \sqrt{\bar{\bar{L}}/\bar{\bar{C}}}$$

where $\bar{\bar{Z}}$, $\bar{\bar{L}}$, and $\bar{\bar{C}}$ are the impedance, inductance, and capacitance matrices, respectively.

121

4-3.3.1 Electrical Parameter Results

In this section, we present the complete 7-wire results and a limited amount of 37-wire results. In Tables 6-10 are given the complete set of parameters for the seven wire bundle. In Tables 11-15 are given the diagonal elements of all the matrices for the 37-wire bundle.

4-3.4 Fall-Off of Capacitance Matrix

For a given wire, i, in a multiwire bundle, we do not calculate all of the elements of the capacitance matrix C_{ij}, j=1, 2, ..., N, but only those elements which correspond to wires that are nearest to wire i. This is justified in light of the fact that C_{ij} is very small for wire j far away from wire i, and is, therefore, for the purposes of any calculation zero. To justify this assumption, we have computed C_{1j}, j=1, ..., N, for the 37-wire bundle. Shown in Table 16 are the results of this calculation.

4-3.5 Current Driver Results

Using the geometrical and material configuration described in Section 4-3.1 and the x-ray spectrum described in Section 4-3.2, we have computed the current drivers for the 7- and 37-multiwire bundles. The results are indicated in Figure 62 and Tables 17 and 18. The largest driver for the 7-wire bundle is #3 with a driver of $+4.14 \times 10^{-10}$ coul/cm/cal/cm^2. The largest negative driver for the 37-wire bundle is #14 with a driver of -1.27×10^{-10} coul/cm/cal/cm^2.

4-3.6 Comparison to Experiment

It is of interest, once the model drivers and associated electrical parameters have been computed, to compare results with actual multiwire bundles. The particular quantities that have been measured are the Norton equivalent current drivers for a 37-wire bundle and various capacitance, wire to shield and wire to wire, for that bundle. When comparing theory and experiment, however, it is important to keep in mind the fact that the geometrical model assumes a close-packed configuration whereas there is a certain tendency for the wires to move around in the actual bundle. It is difficult to make a detailed comparison wire by wire for this reason. Our model predictions always have the wire with the largest driver at the outer edge of bundle with the peak $\sim 4 \times 10^{-10}$ coul/cm/cal/cm^2, and the experimental results give the largest driver $\sim 6 \times 10^{-10}$ coul/cm/cal/cm^2. The wire

122

Table 6. Capacitance matrix $\bar{\bar{C}}$ (pf/m) for 7-wire bundle

248.08	-31.86	-31.86	-31.86	-31.86	-31.86	-31.86
-31.86	225.76	-37.83	-0.55	-0.08	-0.55	-37.83
-31.86	-37.83	225.76	-37.83	-0.55	-0.08	-0.55
-31.86	-0.55	-37.83	225.76	-37.83	-0.55	-0.08
-31.86	-0.08	-0.55	-37.83	225.76	-37.83	-0.55
-31.86	-0.55	-0.08	-0.55	-37.83	225.76	-37.83
-31.86	-37.83	-0.55	-0.08	-0.55	-37.83	225.76

Table 7. Capacitance matrix $\bar{\bar{C}}_M$ (pf/m) for 7-wire bundle

207.19	130.10	130.10	130.10	130.10	130.10	130.10
130.10	203.05	128.63	110.01	107.64	110.01	128.63
130.10	128.63	203.05	128.63	110.01	107.64	110.01
130.10	110.01	128.63	203.05	128.63	110.01	107.64
130.10	107.64	110.01	128.63	203.05	128.63	110.01
130.10	110.01	107.64	110.01	128.63	203.05	128.63
130.10	128.63	110.01	107.64	110.01	128.63	203.05

Table 8. Inductance matrix L (nH/m) for 7-wire bundle

187.72	40.58	40.58	40.58	40.58	40.58	40.58
40.58	152.11	31.79	12.71	10.05	12.71	31.79
40.58	31.79	152.11	31.79	12.71	10.05	12.71
40.58	12.71	31.79	152.11	31.79	12.71	10.05
40.58	10.05	12.71	31.79	152.11	31.79	12.71
40.58	12.71	10.05	12.71	31.79	152.11	31.79
40.58	31.79	12.71	10.05	12.71	31.79	152.11

Table 9. Propagation matrix $\overline{\overline{\gamma}}^2$ ($10^{-20}(m/s)^{-2}$) for 7-wire bundle

3881.29	6.25	6.25	6.25	6.25	6.25	6.25
206.46	3063.77	-37.46	-9.88	-3.27	-9.88	-37.46
206.46	-37.46	3063.77	-37.46	-9.88	-3.27	-9.88
206.46	-9.88	-37.46	3063.77	-37.46	-9.88	-3.27
206.46	-3.27	-9.88	-37.46	3063.77	-37.46	-9.88
206.46	-9.88	-3.27	-9.88	-37.46	3063.77	-37.46
206.46	-37.46	-9.88	-3.27	-9.88	-37.46	3063.77

Table 10. Phase velocities (e-values $\overline{V}$ (10^8 m/s) for 7-wire bundle

1.61

1.84

1.80

1.80

1.79

1.81

1.79

Table 11. Diagonal capacitance matrix
$\bar{\bar{C}}$ (pf/m) of a 37-wire bundle

$c(1,1)$	=	247.29
$c(2,2)$	=	205.90
$c(3,8)$	=	207.34
$c(14,14)$	=	208.74
$c(20,20)$	=	182.27
$c(32,32)$	=	243.35

Table 12. Diagonal capacitance matrix
$\bar{\bar{C}}_M$ (pf/m) of a 37-wire bundle

$c_M(1,1)$	=	167.93
$c_M(2,2)$	=	123.96
$c_M(8,8)$	=	119.63
$c_M(14,14)$	=	124.19
$c_M(20,20)$	=	124.90
$c_M(32,32)$	=	196.33

Table 13. Diagonal inductance matrix
$\bar{\bar{L}}$ (nH/MO) of a 37-wire bundle

$\bar{L}(1,1)$	=	224.23
$\bar{L}(2,2)$	=	242.37
$\bar{L}(8,9)$	=	236.03
$\bar{L}(14,14)$	=	233.71
$\bar{L}(20,20)$	=	217.83
$\bar{L}(32,32)$	=	160.25

Table 14. Diagonal propagation matrix
$\bar{\bar{\gamma}}^2$ (10^{-18} (m/s)$^{-2}$) of a 37-wire bundle

$\bar{\bar{\gamma}}^2(1,1)$	=	39.58
$\bar{\bar{\gamma}}^2(2,2)$	=	31.99
$\bar{\bar{\gamma}}^2(8,8)$	=	31.15
$\bar{\bar{\gamma}}^2(14,14)$	=	31.75
$\bar{\bar{\gamma}}^2(20,20)$	=	29.14
$\bar{\bar{\gamma}}^2(32,32)$	=	32.89

Table 15. Phase velocity V_i (10^8 m/s) of a 37-wire bundle

V_1	=	1.59	V_{20}	=	1.77
V_2	=	2.11	V_{21}	=	1.76
V_3	=	1.88	V_{22}	=	1.77
V_4	=	1.78	V_{23}	=	1.78
V_5	=	1.97	V_{24}	=	1.76
V_6	=	1.84	V_{25}	=	1.78
V_7	=	1.85	V_{26}	=	1.76
V_8	=	1.79	V_{27}	=	1.77
V_9	=	1.97	V_{28}	=	1.77
V_{10}	=	1.84	V_{29}	=	1.77
V_{11}	=	1.83	V_{30}	=	1.76
V_{12}	=	1.85	V_{31}	=	1.75
V_{13}	=	1.85	V_{32}	=	1.77
V_{14}	=	1.75	V_{33}	=	1.75
V_{15}	=	1.79	V_{34}	=	1.75
V_{16}	=	1.76	V_{35}	=	1.76
V_{17}	=	1.77	V_{36}	=	1.74
V_{18}	=	1.77	V_{37}	=	1.76
V_{19}	=	1.77			

Table 16. Capacitance of wire 1 with respect to all wires
37-wire bundle

$$
\begin{array}{lcl}
C(1,1) & = & 247.29 \ \text{pf/m} \\[2ex]
C(1,2) & = & -30.99 \ \text{pf/m} \\[2ex]
C(1,8) & = & -1.61 \times 10^{-1} \ \text{pf/m} \\[2ex]
C(1,14) & = & -4.66 \times 10^{-3} \ \text{pf/m} \\[2ex]
C(1,20) & = & -4.49 \times 10^{-5} \ \text{pf/m} \\[2ex]
C(1,32) & = & -3.27 \times 10^{-6} \ \text{pf/m}
\end{array}
$$

Table 17. 7-wire current drivers

WIRE		CURRENT DRIVER $(coul/cm/cal/cm^2)$
1	=	-1.60×10^{-11}
2	=	2.64×10^{-10}
3	=	4.14×10^{-10}
4	=	6.39×10^{-11}
5	=	5.41×10^{-11}
6	=	6.39×10^{-11}
7	=	4.14×10^{-10}

10^{-10} $(coul/cm/cal/cm^2)$
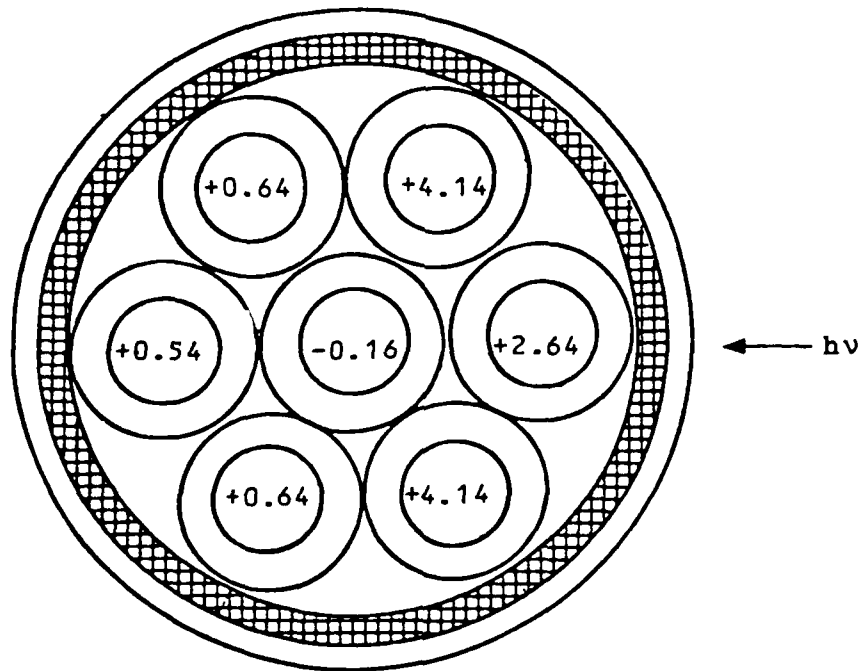
Figure 62. 7-wire current drivers

Table 18. 37-wire current drivers

WIRE #		CURRENT DRIVER $(coul/cm/cal/cm^2)$
1	=	6.48×10^{-11}
2	=	-4.69×10^{-11}
3	=	-1.34×10^{-11}
4	=	-8.15×10^{-12}
5	=	-2.72×10^{-11}
6	=	-8.15×10^{-12}
7	=	-1.34×10^{-11}
8	=	-7.18×10^{-11}
9	=	-9.26×10^{-12}
10	=	-1.62×10^{-13}
11	=	-1.62×10^{-13}
12	=	-9.26×10^{-12}
13	=	-7.18×10^{-11}
14	=	-1.27×10^{-10}
15	=	-5.40×10^{-11}
16	=	1.78×10^{-12}
17	=	-1.38×10^{-11}
18	=	1.78×10^{-12}
19	=	-5.40×10^{-11}
20	=	1.32×10^{-10}
21	=	1.37×10^{-10}
22	=	-1.98×10^{-11}
23	=	-3.15×10^{-12}
24	=	9.26×10^{-12}
25	=	9.38×10^{-12}
26	=	9.38×10^{-12}
27	=	9.26×10^{-12}
28	=	-3.15×10^{-12}
29	=	-1.98×10^{-11}
30	=	1.37×10^{-10}
31	=	1.32×10^{-10}
32	=	2.67×10^{-10}
33	=	4.19×10^{-10}
34	=	2.65×10^{-11}
35	=	5.53×10^{-11}
36	=	2.65×10^{-11}
37	=	4.19×10^{-10}

with the largest driver tends to be on the outside of the bundle in such a way that there is a separation between it and the nearest neighbors. We believe, therefore, that the difference between the model predictions and the experimental data are due to the fact that the wires are, in fact, not totally close packed. The model drivers range from -1.27×10^{-10} to $+4.2 \times 10^{-10}$ coul/cm/cal/cm^2. Another way to compare theory and experiment is to compare the bulk current drivers defined as the algebraic sum for the bundle. The model predicts a bulk current $I_\beta \sim 4.2 \times 10^{-9}$. The difference between the model predictions and the experimental data can more vividly be seen by the two histograms plotted in Figure 63 and 64. In the model, there are more negative drivers in the interior of the bundle due to the close packing of the wires. This is what gives rise to a smaller bulk current.

Measurements have been made of the capacitance matrix of a 37-wire bundle, and it is of interest to compare these results with the model predictions. It is important to note that whatever is the reason for differences between the model and the data as far as the current drivers are concerned can also be responsible for difference in the capacitance matrix. We can think of the capacitance matrix as defining the geometry and dielectric properties of the bundle. Table 19 is a comparison of the experimental data of various elements of the capacitance matrix $\bar{\bar{C}}_M$ and the corresponding model prediction. In all cases the data are somewhat smaller than the model. The difference is consistent with the fact that the wires are not as close packed as the model assumes.
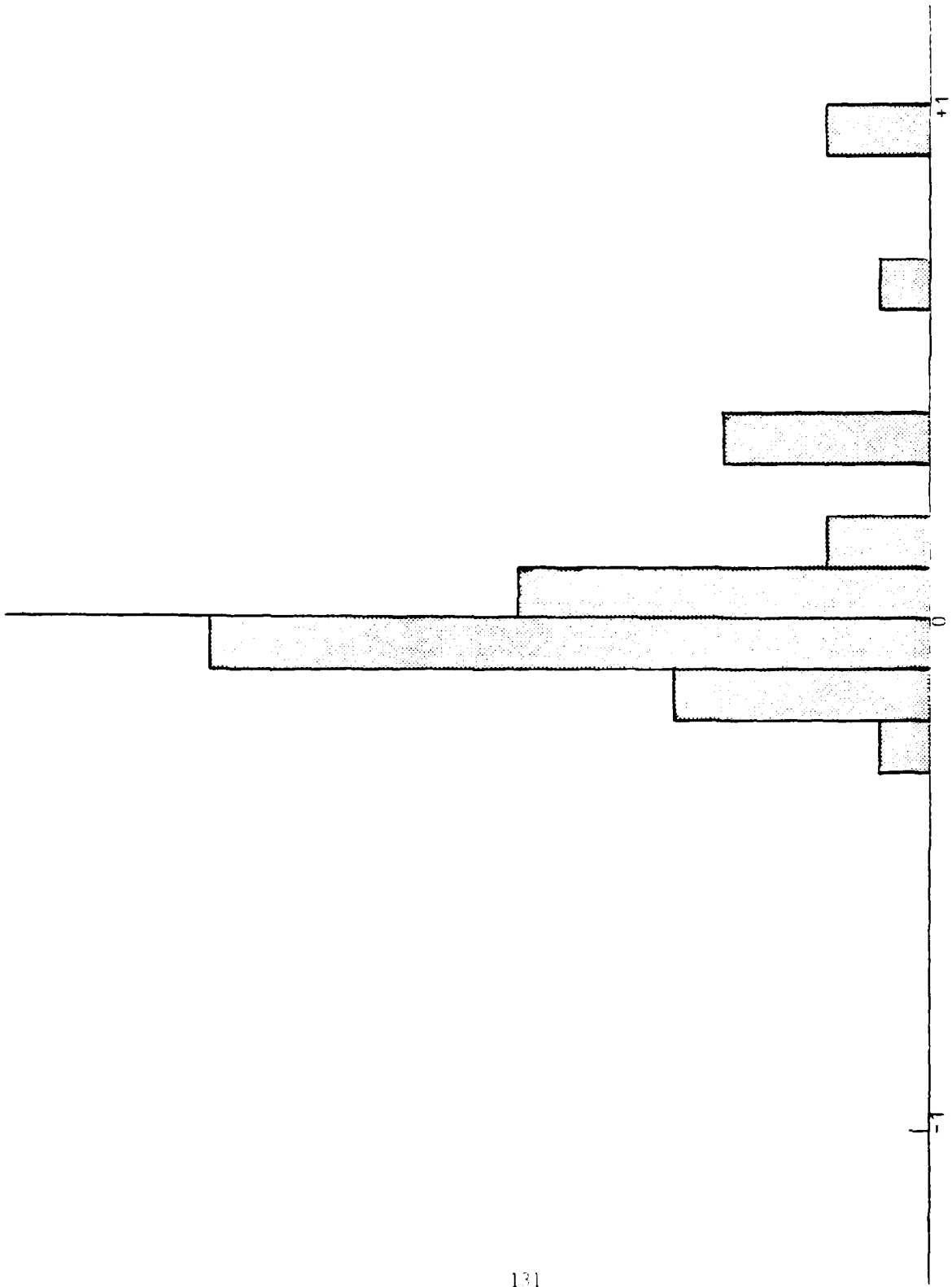
Figure 63. 37-wire model – histogram of normalized distribution
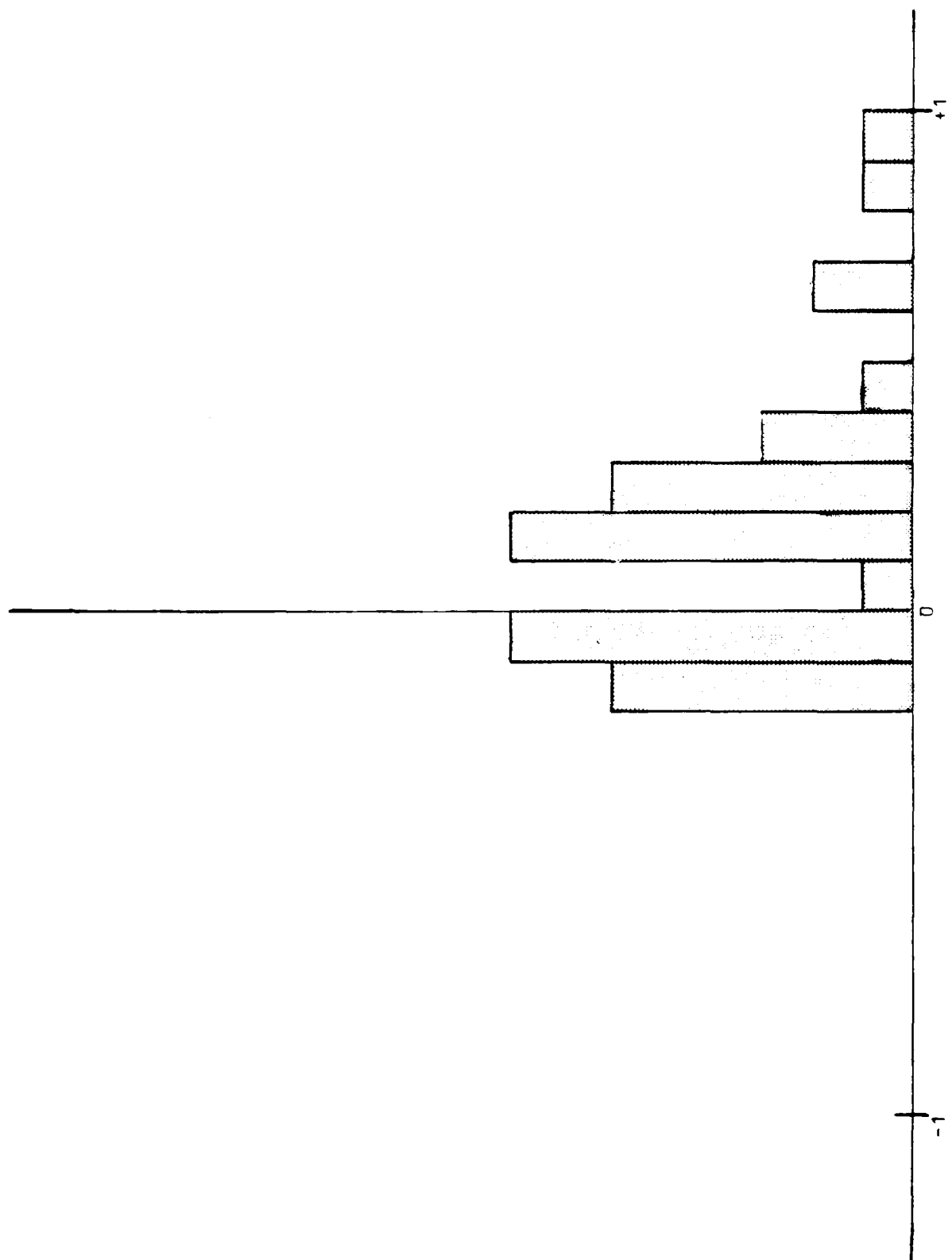
Figure 64. 37-wire data - histogram of normalized distribution

Table 19. Comparison of capacitance matrix elements – model and experiment

WIRE TO SHIELD			WIRE TO WIRE		
CAPACITANCE (PF/M)	MODEL	EXP. DATA	CAPACITANCE (PF/M)	MODEL	EXP. DATA
C(1,1)	168	90	C(1,2)	112	86
C(2,2)	124	90	C(2,3)	106	85
C(3,3)	124	89	C(3,4)	106	85
C(4,4)	124	90	C(4,5)	106	85
C(5,5)	124	89	C(5,6)	106	85
C(6,6)	124	90	C(6,7)	106	86
C(7,7)	124	90	C(7,8)	78	67
C(8,8)	120	95	C(8,9)	81	65
C(9,9)	119	95	C(9,10)	81	65
C(10,10)	119	96	C(10,11)	81	65
C(11,11)	119	95	C(11,12)	81	65
C(12,12)	119	96	C(12,13)	81	65
C(13,13)	119	96	C(13,14)	106	83
C(14,14)	125	91	C(14,15)	80	64
C(15,15)	124	90	C(15,16)	80	63
C(16,16)	124	90	C(16,17)	80	64
C(17,17)	124	91	C(17,18)	80	64
C(18,18)	124	91	C(18,19)	80	64
C(19,19)	124	96	C(19,20)	70	60
C(20,20)	124	108	C(20,21)	103	84
C(21,21)	124	110	C(21,22)	79	68
C(22,22)	125	107	C(22,23)	103	86
C(23,23)	124	112	C(23,24)	79	68
C(24,24)	125	110	C(24,25)	103	86
C(25,25)	124	112	C(25,26)	79	69
C(26,26)	125	108	C(26,27)	103	86
C(27,27)	124	109	C(27,28)	79	68
C(28,28)	125	108	C(28,29)	103	86
C(29,29)	124	113	C(29,30)	79	69
C(30,30)	125	111	C(30,31)	103	86
C(31,31)	125	115	C(31,32)	111	87
C(32,32)	196	113	C(32,33)	105	65
C(33,33)	196	109	C(33,34)	105	63
C(34,34)	196	113	C(34,35)	105	65
C(35,35)	196	112	C(35,36)	105	65
C(36,36)	196	111	C(36,37)	105	65
C(37,37)	196	115	C(34,37)	100	63
			C(33,36)	100	61
			C(32,35)	100	62
			C(1,32)	99	60
			C(1,33)	99	60
			C(1,34)	99	60
			C(1,35)	99	60
			C(1,36)	99	60
			C(1,37)	112	60

SECTION 5
CIT DESIGN AND DEVELOPMENT

5-1 INTRODUCTION

The ground characteristic of the photon direct drive threat has been shown in Sections 2 and 3 to be one of a large differential mode, wire-to-shield transmission line type electrical surge. This type of threat produces a unique energy-time, transmission line controlled waveshape at electronic interfaces and, it is to this threat profile that satellite electronics are hardened. Hence, the primary requirement imposed on any candidate C.I.T. technique is that it provides a meaningful SGEMP hardness verification test with respect to correctly simulating the electrical energy-time nature of the SGEMP threat. There are, however, a number of additional design constraints which are imposed at the satellite system program level which impact the specific method and configuration that can be used to meet the C.I.T. specification. These constraints are both of a practical nature as well as those associated with actual spacecraft hardware. Specifically, the C.I.T. must be compatible with the SGEMP hardening designs employed in actual satellite systems, it must be of a low risk approach which provides individual, positive control of currents delivered to each pin, and finally, be practical for user test evaluation.

An additional requirement is associated with the correct electrical parameter definition of the maximum SGEMP energy threat which exists in a cable bundle, since it is these parameters which must be used in a meaningful hardness verification test. Furthermore, the maximum energy capability of a particular wire is not only controlled by the magnitude of the wire's current source term but is also controlled by the wire-to-shield characteristic impedance.

The situation is further complicated by the fact that since satellite cables are comprised of many unshielded wires enclosed by a common bundle shield, significant interwire coupling occurs which alters the equivalent electrical parameters of the transmission line type threat.

From a threat specification standpoint, one could adopt an approach based on defining the maximum threat posed to the component box pins in terms of the total cable core current and some nominal or worst case characteristic impedance.

134

This is an extemely conservative approach which is unrealistic but mathematically representative of an upper limit. This approach, however, is completely intolerable from a satellite system standpoint since is represents a significant hardware impact design solution to providing adequate hardening against a realistic threat level.

5-2 DESIGN CONSIDERATIONS

Since the SGEMP threat in present day, design hardened, satellite system is associated with photon direct drive effects in electrical cables, the foundation for the overall hardening designs for component boxes is based upon the energy-time, transmission line nature of the direct drive threat. However, since system weight, power, cost and reliability are of utmost concern, these hardening designs, by necessity, are of a hardware efficient nature for both new and existing design component boxes. Thus, SGEMP hardening is implemented on a "specifically where required" basis rather than legislated on an "across the board" basis.

Since the severity of the SGEMP threat is controlled by energy-time transmission line characteristics and specific wire length, hardening requirements are imposed based on actual cable lengths in the satellite system for each interface circuit as well as the quantitatively defineable electrical loads, not only at the circuit of concern, but at the interfacing circuit at the opposite end of the wire. In many cases, for example, the presence of a particular low impedance electrical load or the addition of a single zener diode at one end of a short-to-medium length wire is sufficient to provide protection to the interfacing circuits at both ends of the line. For longer length lines, SGEMP hardening is implemented at both ends of the line consistent with the line length of the transmission line type threat. Hence, many interface circuits in a component box are only SGEMP hardened when all their respective interface component boxes are electrically connected.

An additional design consideration is associated with the physical nature of the electrical systems (cables and connectors) in actual satellites. Satellite cables are unlike re-entry vehicle cables in that they are not generally straight, two connector cables. Instead, satellite cables are typically complex configurations comprised of large bundles of upwards of hundreds of unshielded wires contained within a common bundle shield with numerous branches and connector breakouts, with high density (large number of pins) connectors used for component box interfaces. Furthermore, the wiring in these cables consists of wires with short total lengths (low

135

threat level wires which require minimal SGEMP hardening of their respective inter-
face circuits) in a common bundle with wires of long total lengths (high threat
level wires which require extensive interface circuit hardening).

The consequence of these design aspects is that an SGEMP simulation tech-
nique must provide high simulation fidelity of the energy-time transmission line
nature of the SGEMP threat for multipin, simultaneous drive of component boxes. It
also must be capable of correctly driving a component box whose SGEMP protection is
contained in numerous other component boxes which are not in the test setup during
individual component box testing. Furthermore, the technique must be capable of
simultaneously driving some pins at high levels and others at low levels to accom-
modate various distributions of long and short wire threats at the same connector
interface. This latter requirement also has a significant impact on the risk potential
associated with any potential simulation technique.

Since the SGEMP hardness verification test is typically performed in line
at the latter portion of the total qualification cycle (generally before thermal-
vacuum qualification), a low risk simulation approach is required to avoid inadver-
tent overstress levels which could cause spacecraft equipment failures and impact
system integration and, possibly, flight schedules. In view of the typical SGEMP
hardening designs employed in satellite systems, one cannot generally afford the
luxury of overdriving some pins at higher levels in order to assure that the minimum
required test levels are properly established in all pins. As such, the simulation
method must also be capable of providing individual positive control of each of the
currents delivered to each of the interface pins to eliminate high current (or voltage)
hazards to both the equipment as well as the operating personnel. An obvious addition-
al requirement, which is more practically oriented for user test evaluation, is that
the simulation methods be capable of being configured into portable, in-house hard-
ware readily adaptable to correctly interfacing (both electrically and mechanically)
with actual satellite component boxes and their associated ground test equipments.

5-3 CIT DESIGN

The detailed design requirements were based on the design constraints
described in the previous section. In order to achieve the desired electrical simula-
tion the design and development of the test techniques were accomplished in the
following five subsystems elements.

1) A central source term generator to reproduce the desired invariant current driver waveshape to drive a practical multiport current source.

2) A set of cable delays from the central generator to the multiport current source to provide time-phased photon source term simulation.

3) Discrete current source injection into a controlled characteristic impedance (Z_0) test cable for each pin under test to provide simulation of the distributed source term nature of the threat.

4) Multiple cable line drive capability in order to simultaneously drive the number of pins which corresponds to the maximum number in the cable bundle which could realistically be at maximum threat conditions.

5) Provide a range of termination impedances and drive levels for the test injection cable to simulate those corresponding to the realistic maximum threat when considering realistic maximum multiwire coupling effects in the actual multiwire cable which is connected to the component box being tested.

The central direct drive source term generator provides a large amplitude current pulse which has the same time waveshape as the actual photon pulse. This is the unit which reproduces the basic invariant current driver waveshape and is the heart of the C.I.T. technique. The multiport currents source and time phasing cables provide the correct distribution of the invariant current driver waveshape to the pins of the component box to complete the simulation.

A significant element in the development of the C.I.T. approach was the proper technique to distribute the source term generator to a multiwire, controlled impedance network for correct simulation. This distribution depends on the specific wire placement in each cable manufactured. Hence, each pin on the component box must be evaluated for maximum threat in order to ensure that the complete interface is survivable no matter what manufacturing variations occur in the production satellites. This evaluation must be performed keeping in mind that the hardened level of each pin corresponds to the actual wire length in the system and that the indiscriminate injection of current into a high characteristic impedance wire could produce an overstress condition.

The approach for distributing the source terms which was more preferred from a practical and simulation aspect was to simultaneously test the desired number of signal lines at maximum threat levels using controlled characteristic impedance

137

values and current amplitude values corresponding to maximum threat conditions. Hence, each pin should be driven by its own controlled impedance pulse generator interface at maximum wire-to-shield threat levels when considering realistic worst case multiwire coupling effects. Multiwire transmission line analyses is required in this approach for the proper definition of such effects and for the development of user oriented simplified techniques to readily define realistic test parameters to use for maximum threat testing of any specific cable design and configuration.

A simplified diagram of the multipin C.I.T. method and equipment which was developed is shown in Figure 65. This method is essentially a group of "N" transmission lines driven by "S" current sources. Line-to-line isolation diodes are provided as shown to prevent interwire bias loading and to prevent loading of the injection test cable by the multiport current source. A bipolar, central source term generator is formed by the voltage pulse across the two output resistors. The multiport current source is formed by the drive resistors in series with the isolation diodes which are driven by the voltage pulse across the output resistors of the central source term generator. Photon time phasing simulation is accomplished, quite simply, by driving each section of the line through different lengths of coaxial cable.

The pulser consists of the current pulse generator, various load impedances and test cables. The basic schematic for the C.I.T. Pulser is shown in Figure 66. A test cable impedance of 36 ohms was used as a result of an analysis which indicated that the average wire-to-shield characteristic impedance on typical DSCS III cables was 36 ohms. The remaining variables, such as, cable length and termination impedance was specified by the particular component, or connector under test. Simulation of the distributed current source was achieved by using the pulser to inject the 36 ohm test cable once per meter. A typical test setup shown in Figure 67 used test cable lengths of 1/2 meter between the I/F adaptor of the box under test and the pulser, 1 meter between current injection points and 1/2 meter between the last current injection point and the termination load. A Tektronix CT-2 current probe was used to measure the current delivered into the box under test. When opening all outputs of the pulse generator are either connected to a test cable or connected to a short.

Typical design capability of this C.I.T. equipment is shown below when using a 10 amp per meter drive level.
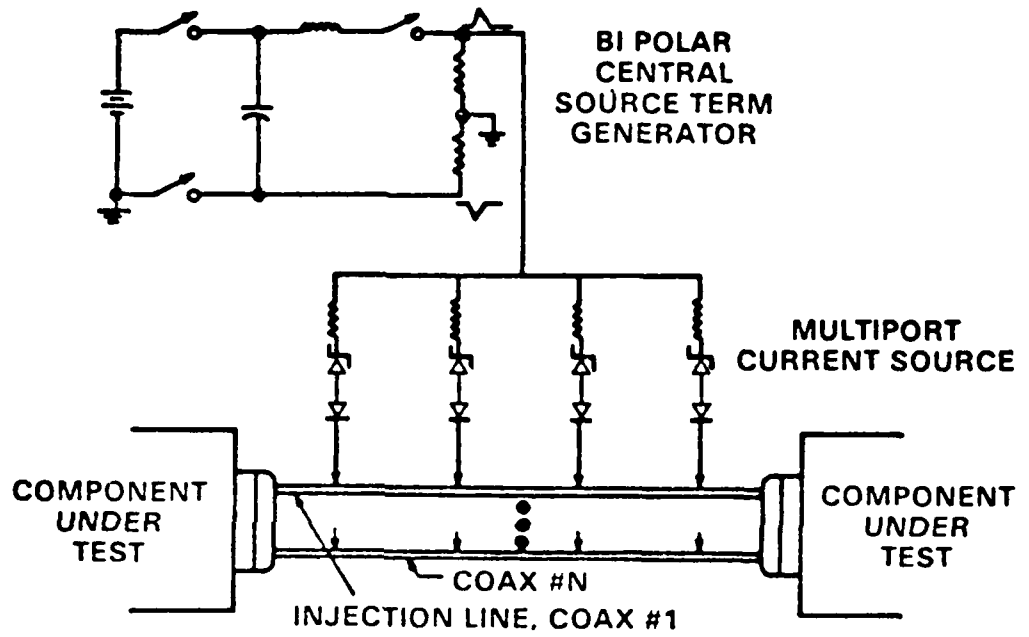
Figure 65.   Simplified schematic diagram of the multipin C.I.T.
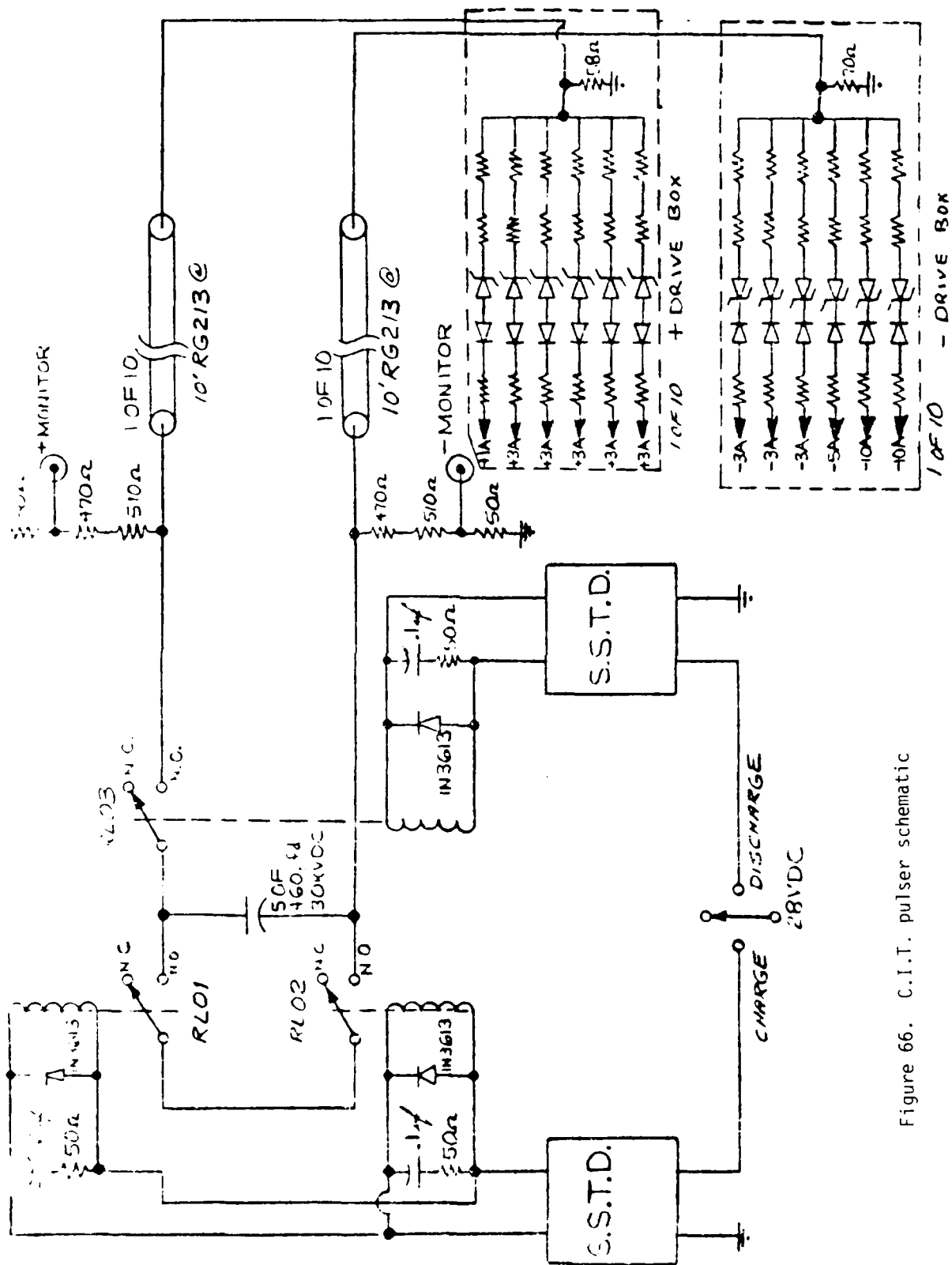
Figure 66. C.I.T. pulser schematic
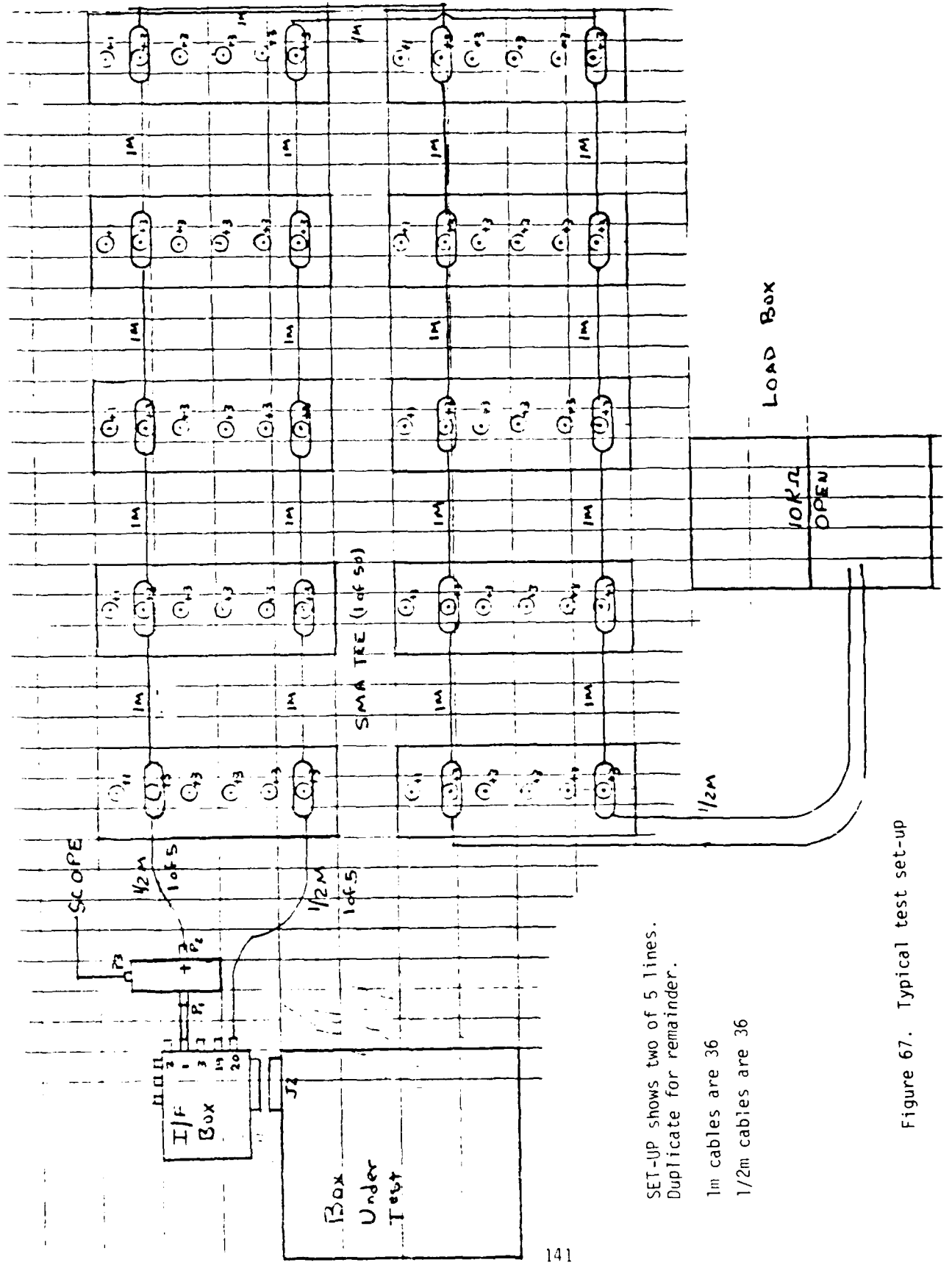
SET-UP shows two of 5 lines.
Duplicate for remainder.

1m cables are 36

1/2m cables are 36

Figure 67. Typical test set-up

Pulse Generator Charge:	20 kV
Pulse Shaping Resistor:	10 Ω
1 Driver Max:	10 Amp/Meter
Cable Impedance:	50 Ω

Cable Length: (τ/τ_p)	Absolute Maximum Number of Wires Which can be Driven
0.17	120
0.5	60
1.7	40

Figure 68 shows the overall layout of the C.I.T. equipment which was designed. Figure 69 shows an overall view of the attached pulser hardware that was subsequently developed based upon this design. This hardware was then used to test actual spacecraft boxes to demonstrate the application and utility of the test techniques and pulser hardware. The results of these tests are given in the Final Technical Report, Task 2 of this Program (Reference 13).

Typical pulse current waveshapes resulting from the simulated SGEMP response of numerous cable lengths and which are delivered to a large range of component box pin impedances by the C.I.T. method are described here are shown in Figure 70. The component box pin impedances "R" are expressed in terms of the impedance relative to the wire-to-shield characteristic impedance (Z_c) of the cable response being simulated. The cable electrical length threat τ being simulated is expressed in terms of the cable propagation time compared to the full width-half maximum (FWHM) of the photon pulse being simulated. The time-per-division "t_D" and the amperes-per-division "I_D" of the oscilloscope traces are expressed in time relative to one another. Each of the amplitudes and waveshapes shown are in excellent agreement with those which are predicted by analytical codes.
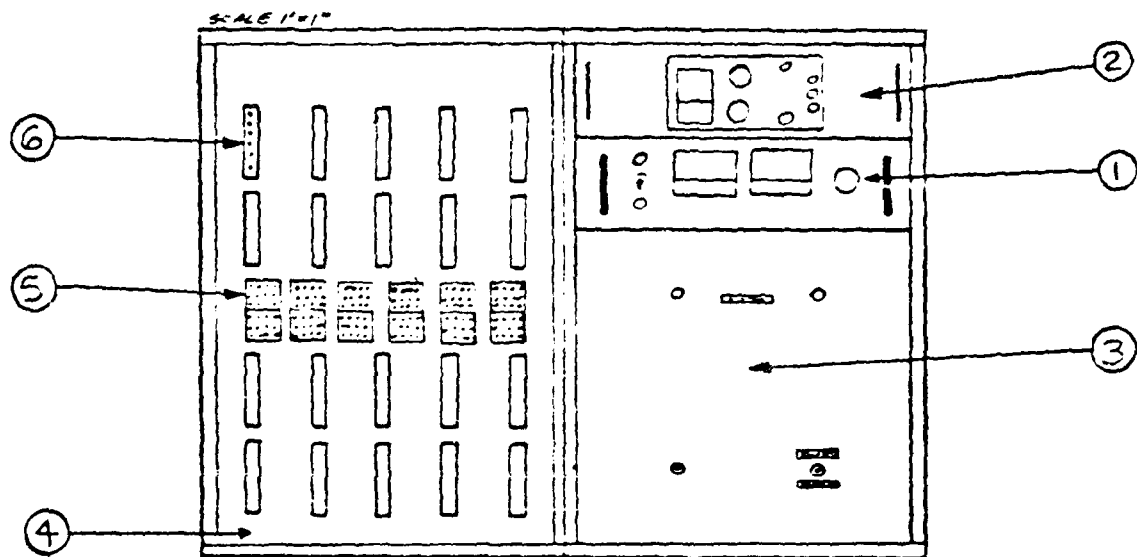
CENTRAL SGEMP SOURCE TERM GENERATOR

ITEM #	DESCRIPTION
1	HVDC POWER SUPPLY
2	LVDC POWER SUPPLY
3	CONTROL PANEL
4	FRONT PANEL
5	LOAD BOX
6	DRIVE BOX

Figure 68. Pulser layout
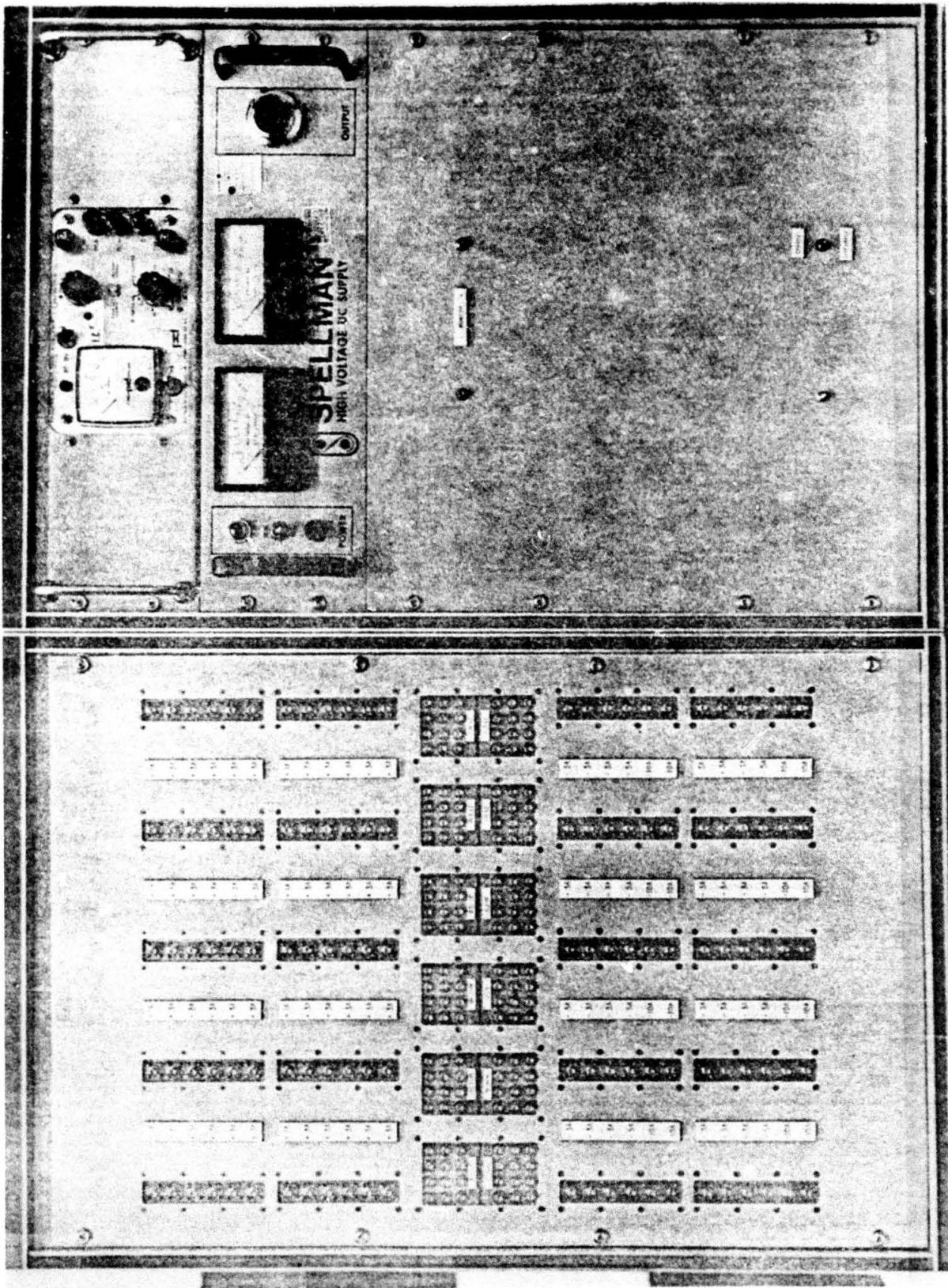
Figure 69. Overall front view of the C.I.T. equipment

144
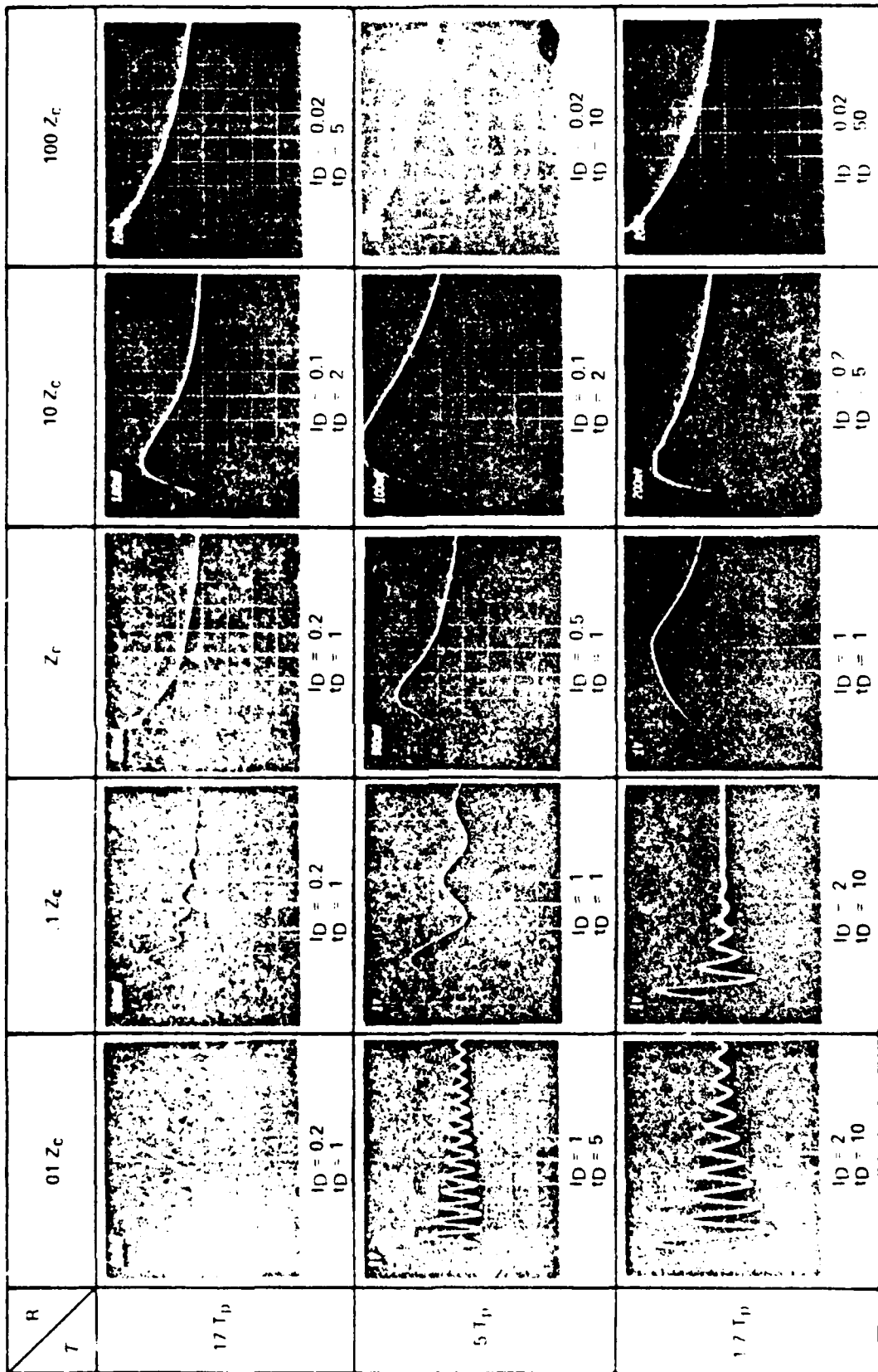
Figure 70. Typical interface pin waveshapes produced by the C.I.T. method

SECTION 6
CONCLUSION

The need for this analysis, design and development effort is rooted in the requirement for a safe and reliable simulation test method to verify satellite electrical system operation in a nuclear X-ray environment. A number of fundamental transmission line response equations have been developed, progressing from the simple two-wire case to the multiwire cable, which provide useful tools for analyzing cable response in radiation, including the case where the radiation propagates along the length of the cable. Numerical and graphic results are provided.

For the multiwire bundle the current driver description has been reduced to an effective single wire transmission line with an effective current driver. Using this effective current driver the worst case current and energy into an interface is developed as a function of line length and termination impedance.

The current injection test method which has been designed and described here represents what is felt to be an optimum approach for performing a meaningful multipin C.I.T. on electronic component boxes. The photon direct drive simulation has been accomplished within the overall satellite program level constraints of actual electronic equipment.

The major objectives of developing simplified analytical and experimental techniques for simulation of the photon direct drive threat to satellite electronics has been met in three areas.

1. The photon/electrical response of multiwire cables has been determined with respect to their SGEMP direct drive sources, transmission line parameters and realistic multiwire coupling.

2. The electrical test requirements for component box current injection testing have been defined with respect to the SGEMP electrical energy distribution in multiwire cables and injection current level and characteristic impedance of this threat.

146

3. Direct drive current injection test simulation has been performed using the designed C.I.T. pulser on electrically active component boxes to achieve a proper simulation of threat, at low risk, while being compatible with actual hardened satellite electronics and practical for user test performances.

REFERENCES

1. Schelkunoff, S. A.: Electromagnetic Waves; Van Nostrand Co., 1943.

2. King, R. W. P.: Transmission Line Theory; McGraw-Hill, 1955.

3. Weeks, W. L.: Electromagnetic Theory for Engineering Applications; Wiley & Sons, 1964.

4. Carlin, H. J. and Giordano, A. B.: Network Theory; Prentice-Hall, 1964.

5. Tasca, D. M., Beers, B. L., Klisch, J. A., and Tigner, J. E.: Interface Threat Analysis and Current Injection Testing for Direct Drive SGEMP in Multiwire Cables; IEEE Transactions on Nuclear Science, Vol. NS-26, No. 6, Dec. 1979, pp. 4918-4926.

6. Frankel, S.: Cable and Multiconductor Transmission Line Analysis, HDL-TR-091-1, 1974.

7. Ramo, S., Whinnery, J. R., and Van Duter, T.: Fields and Waves in Communication Electronics, Wiley & Sons, 1967.

8. Chadsey, W. L., Beers, B. L., Pine, V. W., and Wilson, C. W.: IEEE Trans. Nuc. Sci., NS-23, 1933, 1976.

9. Beers, B. L.: IEEE Trans. Nuc. Sci., NS-24, 2429, 1977.

10. Chadsey, W. L.: "POEM", AFCRL Technical Report, No. TR-75-0324, 1975.

11. Beers, B. L., Tigner, J. E., and Tasca, D. M.: IEEE Trans. Nuc. Sci., NS-25

12. Tasca, D. M., Raylman, E. T., Beers, B. L., and Tigner, J. E.: IEEE Trans. Nuc. Sci., NS-25, 1382, 1978.

13. Tasca, D. M., Klisch, J. S.: Design and Development of a Multipin SGEMP Current Injection Test Technique, Final Technical Report, Task 2, Contract No. DNA 001-78-C-0251, 1982.

Appendix I

PROPERTIES OF THE TRANSMISSION-LINE MATRICES

There are two matrices which uniquely determine the electrical properties of a multiwire bundle. These matrices are the capacitance matrix $\overline{\overline{C}}$ and the inductance matrix $\overline{\overline{L}}$. The elements of the capacitance matrix $\overline{\overline{C}}$, also called Maxwell's capacitance coefficients, are defined by the following matrix equation

$$Q_i = \sum_j C_{ij} V_j \qquad (I-1)$$

where Q_i is the charge on the i'th conductor, V_j is the voltage of the j'th conductor with respect to the shield and C_{ij} are Maxwell's capacitance coefficients. C_{ij} is the ratio of the charge induced on the i'th conductor to the potential on the j'th conductor when all other conductors are at zero potential. The capacitance matrix has the following properties:

a) $\overline{\overline{C}}$ is symmetric

b) The diagonal elements are all greater than or equal to zero.

c) The off-diagonal elements are all less than or equal to zero.

d) $\sum_{j=1}^{N} C_{ij} \geq 0$ for every i.

These properties can all be proven from the defining relationship, Equation (I-1), and from the basic principles of electrostatics.

The inductance matrix $\bar{\bar{L}}$ is defined in a way analogous to the capacitance matrix

$$L_{ij} = \frac{\phi_{ij}}{I_j \Delta X} \tag{I-2}$$

In this equation L_{ij} is the inductance coefficient, ϕ_{ij} is the magnetic flux linking the i'th conductor and the shield when there is a current I_j flowing through the j'th conductor and no current flowing through any other conductor, and ΔX is a short section of length. This equation merely states that the inductance coefficient L_{ij} is equal to the *flux linking the i'th conductor* per unit length of cable per unit current flowing in the j'th conductor. The inductance matrix has the following properties:

a) $\bar{\bar{L}}$ is symmetric.

b) All elements are greater than or equal to zero.

The propagation matrix $\bar{\bar{\gamma^2}}$ is defined by the following equation

$$\bar{\bar{\gamma^2}} = \bar{\bar{C}} \cdot \bar{\bar{L}} \tag{I-3}$$

This matrix is, in general, not diagonal; but when brought to the diagonal form by the appropriate

150

transformation matrix, the diagonal elements are related
to the multiwire phase velocities. If we denote the
diagonal form of the propagation matrix as $\overline{\overline{\gamma_D^2}}$ and the
multiwire phase velocities as $\overline{V}$, then we have

$$V_i = \left[\left(\gamma_D^2 \right)_{ii} \right]^{-1/2} \qquad (I-4)$$

Although, in general, the multiwire phase velocities can
all be different, there are important circumstances in
which they are all the same. In particular, if there is
a uniform dielectric surrounding all the wires in the
multiwire bundle, there is only one phase velocity asso-
ciated with this bundle and it will be found that the
propagation matrix $\overline{\overline{\gamma^2}}$ is diagonal with only one diagonal
element γ^2. The phase velocity V for this bundle is,
therefore,

$$V = \frac{1}{\gamma} \qquad (I-5)$$

and we have

$$\overline{\overline{L}} \, \overline{\overline{C}} = \overline{\overline{C}} \, \overline{\overline{L}} = \frac{1}{V^2} \overline{\overline{I}} \qquad (I-6)$$

where $\overline{\overline{I}}$ is the identity matrix.

Since the inductance matrix does not depend on
the dielectric properties of the multiwire cable, but
only on the relative positions of conductors, $\overline{\overline{L}}$ is the
same for a given multiwire cable with or without any
dielectric. If we know the capacitance matrix $\overline{\overline{C^o}}$ of

our multiwire cable <u>without</u> dielectric, we can use the fact that there is only one phase velocity for this cable V=C, the speed of light, and the relationship

$$\overline{\overline{L}} \ \overline{\overline{C^\bullet}} = \overline{\overline{C^\circ}} \ \overline{\overline{L}} = \frac{1}{C^2} \ \overline{\overline{I}}$$

$$\overline{\overline{L}} = \frac{\overline{\overline{(C^\circ)^{-1}}}}{C^2} \qquad\qquad (I-7)$$

to determine the inductance matrix of our multiwire cable.

The characteristic impedance matrix $\overline{\overline{Z}}_O$ of a multiwire cable is determined once $\overline{\overline{L}}$ and $\overline{\overline{C}}$ are known by the following relation

$$\overline{\overline{Z}}_O = (\overline{\overline{C^{-1} \ \overline{\overline{L}}}})^{1/2}$$

$$= \overline{\overline{C^{-1}}}(\overline{\overline{C}} \ \overline{\overline{L}})^{1/2} = \overline{\overline{C^{-1}}}(\overline{\overline{\gamma^2}})^{1/2} \qquad\qquad (I-8)$$

In general, if $\overline{\overline{\gamma^2}}$ is not a diagonal matrix, but can be brought to the diagonal form $\overline{\overline{\gamma_D^2}}$ by the transformation matrix $\overline{\overline{T}}$, we have

$$\overline{\overline{\gamma_D^2}} = \overline{\overline{T^{-1}}} \ \overline{\overline{\gamma^2}} \ \overline{\overline{T}} \qquad\qquad (I-9)$$

and, therefore,

$$\overline{\overline{Z}}_O = \overline{\overline{C^{-1}}} \ \overline{\overline{T}} \ \overline{\overline{\gamma_D}} \ \overline{\overline{T^{-1}}} \qquad\qquad (I-10)$$

152

For the special case when there is only one phase velocity V, we have

$$\bar{\bar{Z}}_o = \frac{\overline{\overline{C^{-1}}}}{V} \tag{I-11}$$

RELATION TO MEASURABLE QUANTITIES

From the results of the preceding section, it is clear that a complete description of the electrical properties of a multiwire bundle is obtained once the capacitance matrix $\bar{\bar{C}}$ and $\overline{\overline{C^\sigma}}$ is computed. As part of the computer code CHIC, these matrices are calculated and all other relevant parameters are computed. It is important to note that a knowledge of $\bar{\bar{C}}$ and $\overline{\overline{C^\sigma}}$ entails complete information about the electrical properties of a multiwire bundle, and, therefore, any particular measurement made of capacitances and inductances can be compared with the theoretical results by appropriate manipulation.

It is usually more convenient, when making a capacitance measurement, to relate charge to the potential difference between two conductors. If one performs such an exercise on a multiwire bundle one obtains a capacitance matrix $\bar{\bar{C}}_M$ which is different from the one considered in the previous sections. In the following paragraph we will indicate how one obtains $\bar{\bar{C}}_M$ by appropriate manipulation of $\bar{\bar{C}}$.

The defining relation for $\overline{\overline{C}}$ is again

$$\overline{Q} = \overline{\overline{C}}\,\overline{V} \tag{I-12}$$

We can invert this relation and solve for $\overline{V}$

$$\overline{V} = \overline{\overline{C^{-1}}}\,\overline{Q} \tag{I-13}$$

If we specify the potential on wire i as V, let the charge of wire i be Q and at the same time let all of the other wires float so that $Q_j = 0$ for $i \neq j$, we have

$$V = (C^{-1})_{ii} Q \tag{I-14}$$

We can write this relation in the following way

$$Q = \frac{1}{(C^{-1})_{ii}} V$$

$$= (C_M)_{ii} V \tag{I-15}$$

This relation defines the diagonal elements of C_M

$$(C_M)_{ii} = \frac{1}{(C^{-1})_{ii}} \tag{I-16}$$

The off-diagonal elements of $\overline{\overline{C_M}}$ are determined by the following prescription

$$Q_j = -Q_i = Q$$

$$Q_k = 0, \ k \neq i,j \tag{I-17}$$

154

With this assumption, we can expand Equation (I-14) for i and j

$$V_j = (C^{-1})_{jj} Q - (C^{-1})_{ji} Q$$

$$V_i = (C^{-1})_{ij} Q - (C^{-1})_{ii} Q \qquad (I-18)$$

So that

$$V_j - V_i = \left((C^{-1})_{jj} + (C^{-1})_{ii} - (C^{-1})_{ji} - (C^{-1})_{ij} \right) Q \qquad (I-19)$$

Re-writing, we have

$$Q = (C_M)_{ij} \, \Delta V$$

$$(C_M)_{ij} = \frac{1}{(C^{-1})_{ii} + (C^{-1})_{jj} - 2(C^{-1})_{ij}}$$

$$\Delta V = V_j - V_i \qquad (I-20)$$

The manipulations outlined above result in a capacitance matrix $\overline{\overline{C_M}}$, the elements of which can be conveniently measured. In this definition of $\overline{\overline{C_M}}$, $(C_M)_{ii}$ is the ratio of the charge on the i'th conductor to the potential on the i'th conductor when all other conductors have no charge. $(C_M)_{ij}$ (i≠j) is the ratio of the charge on the i'th conductor to the potential difference $V_j - V_i$ when all other conductors k(k≠i,j) have no charge.

Appendix II

SOLUTION OF TRANSMISSION-LINE EQUATIONS

In this appendix we will discuss the solution to the T-L equations as presented in the main body of the text. In order to arrive at the exact solution we have made the following assumptions:

1) There is only one propagation velocity, V.

2) $\overline{I}_D$ is uniform along the multiwire bundle (normal X-ray incidence).

3) Resistive terminations.

The equations to be solved are:

$$\frac{\partial \overline{V}}{\partial X} = -\overline{\overline{L}} \frac{\partial \overline{I}}{\partial t}$$

$$\frac{\partial \overline{I}}{\partial X} = -\overline{\overline{C}} \frac{\partial \overline{V}}{\partial t} + \overline{I}_D \qquad (II-1)$$

together with the boundary conditions

$$\overline{I}(X, t=0) = \overline{V}(X, t=0) = \overline{0}$$

$$\overline{V}(X=0, t) = -\overline{\overline{Z}}_L \overline{I}(X=0, t)$$

$$\overline{V}(X=\ell, t) = \overline{\overline{Z}}_R \overline{I}(X=\ell, t) \qquad (II-2)$$

where $\overline{\overline{Z}}_L(\overline{\overline{Z}}_R)$ is the termination impedance matrix on the left (right) end of the cable of length .

The method of solution is to take the fourier transform of the two equations using the following convention

$$\tilde{\overline{I}}(X,w) = \int_0^\infty dt \ \overline{I}(X,t)e^{iwt}$$

$$\tilde{\overline{V}}(X,w) = \int_0^\infty dt \ \overline{V}(X,t)e^{iwt}$$

$$\tilde{\overline{I}}_D(w) = \int_0^\infty dt \ \overline{I}_D(t)e^{iwt} \tag{II-3}$$

The fourier transformed version of these two equations are

$$\frac{\partial \tilde{\overline{V}}}{\partial X} = iw\overline{\overline{L}} \ \tilde{\overline{I}}$$

$$\frac{\partial \tilde{\overline{I}}}{\partial X} = iw\overline{\overline{C}} \ \tilde{\overline{V}} + \tilde{\overline{I}}_D \tag{II-4}$$

We can take the second derivative of each of these equations with respect to X, noting by assumption 1 that $\overline{\overline{C}} \ \overline{\overline{L}} = \overline{\overline{L}} \ \overline{\overline{C}} = \frac{1}{V^2} \ \overline{\overline{I}}$ and by assumption 2 that $\frac{\partial \tilde{\overline{I}}_D}{\partial X} = 0$, and arrive at the following two equations

158

$$\frac{\partial^2 \overset{\sim}{\overline{I}}}{\partial X^2} + k^2 \overset{\sim}{\overline{I}} = 0$$

$$\frac{\partial^2 \overset{\sim}{\overline{V}}}{\partial X^2} + k^2 \overset{\sim}{\overline{V}} = iw\overline{\overline{L}} \; \overset{\sim}{\overline{I}}_D \tag{II-5}$$

where

$$k^2 = \frac{w^2}{V^2} \tag{II-6}$$

The solution of these two equations is straightforward

$$\overset{\sim}{\overline{V}} = e^{ikX} \overline{V}_+ + e^{-ikX} \overline{V}_- + \frac{i\overline{\overline{Z}}_0 \overset{\sim}{\overline{I}}_D}{k}$$

$$\overset{\sim}{\overline{I}} = e^{ikX} \overline{I}_+ + e^{-ikX} \overline{I}_- \tag{II-7}$$

where

$$\overline{\overline{Z}}_0 = \frac{k(\overline{\overline{C^{-1}}})}{V}$$

$$\overline{V}_+ = \overline{\overline{Z}}_0 \; \overline{I}_+$$

$$\overline{V}_- = \overline{\overline{Z}}_0 \; \overline{I}_-$$

$$\overline{I}_+ = (\overline{\overline{I}} - \overline{\overline{P}}_R \overline{\overline{P}}_L e^{2ik\ell})^{-1} x \left[(\overline{\overline{Z}}_0 + \overline{\overline{Z}}_L)^{-1} - \overline{\overline{P}}_L (\overline{\overline{Z}}_0 + \overline{\overline{Z}}_R)^{-1} e^{ik\ell} \right] x$$

$$\left[-\frac{i\overline{\overline{Z}}_0 \overset{\sim}{\overline{I}}_D}{k} \right]$$

$$\overline{I}_- = -(\overline{\overline{I}}-\overline{\overline{P}}_R\overline{\overline{P}}_L e^{2ik\ell})^{-1}\left[(\overline{\overline{Z}}_0+\overline{\overline{Z}}_R)^{-1} - \overline{\overline{P}}_R(\overline{\overline{Z}}_0+\overline{\overline{Z}}_L)^{-1}e^{iL\ell}\right]x$$

$$e^{ik\ell}\left[-\frac{i\overline{\overline{Z}}_0\tilde{\overline{I}}_D}{k}\right]$$

$$\overline{\overline{P}}_R = (\overline{\overline{Z}}_0 + \overline{\overline{Z}}_R)^{-1}\ (\overline{\overline{Z}}_0 - \overline{\overline{Z}}_R)$$

$$\overline{\overline{P}}_L = (\overline{\overline{Z}}_0 + \overline{\overline{Z}}_L)^{-1}\ (\overline{\overline{Z}}_0 - \overline{\overline{Z}}_L) \qquad (II-8)$$

The solution for $\tilde{\overline{I}}$ at X=0 is simply

$$\tilde{\overline{I}}(X=0,w) = \overline{I}_+ + I_-$$

$$= \left\{(\overline{\overline{I}}-\overline{\overline{P}}_L)\left[1-\overline{\overline{P}}_R\overline{\overline{P}}_L e^{2ik\ell}\right]^{-1}\left[\overline{\overline{P}}_R(\overline{\overline{Z}}_0+\overline{\overline{Z}}_L)^{-1}e^{2ik\ell}\right.\right.$$

$$\left.\left.+ (\overline{\overline{Z}}_0+\overline{\overline{Z}}_R)^{-1}e^{ik\ell}\right] - (\overline{\overline{Z}}_0+\overline{\overline{Z}}_L)^{-1}\right\}\left[\frac{i\overline{\overline{Z}}_0\tilde{\overline{I}}_D}{k}\right] \quad (II-9)$$

We can take the inverse fourier transform of this equation, according to the following definition

$$\overline{I}(X,t) = \frac{1}{2\pi}\int_{-\infty}^{+\infty} dw\ \tilde{\overline{I}}(X,w)e^{-iwt}$$

$$\widetilde{V}(X,t) = \frac{1}{2\pi}\int_{-\infty}^{+\infty} dw\ \tilde{\overline{V}}(X,w)e^{-iwt}$$

$$\overline{I}_D(t) = \frac{1}{2\pi}\int_{-\infty}^{+\infty} dw\ \tilde{\overline{I}}_D(w)e^{-iwt} \qquad (II-10)$$

160

The analysis of the fourier-transform of Equation (II-9) is made intelligible by the following observations. Let $\overline{Q}(t)$ be the total charge deposited at time t due to the Norton equivalent driver $\overline{I}_D$

$$\overline{Q}(t) = \int_0^t \overline{I}_D(t')dt' \qquad (II-11)$$

Using Equation (II-10) we can write

$$\overline{Q}(t) = \frac{1}{2\pi} \int_0^t dt' \int_{-\infty}^{+\infty} dw\ \tilde{\overline{I}}_D(w)e^{-iwt}$$

$$= \frac{1}{2\pi} \int_{-\infty}^{+\infty} dw\ \frac{i\tilde{\overline{I}}_D(w)e^{-iwt}}{w} \qquad (II-12)$$

So that we have

$$\frac{1}{2\pi} \int_{-\infty}^{+\infty} dw\ e^{-iwt}\ \frac{i\overline{\overline{Z}}_0\tilde{\overline{I}}_D}{k} = V\ \overline{\overline{Z}}_0\ \overline{Q}(t) \qquad (II-13)$$

In addition we have

$$(1-\overline{\overline{P}}_R\overline{\overline{P}}_L e^{2ik\ell})^{-1} = \sum_{n=0}^{\infty} (\overline{\overline{P}}_R\overline{\overline{P}}_L)^n e^{i2nk\ell} \qquad (II-14)$$

So that

$$\tilde{\bar{I}}(0,w) = \left\{ (\bar{\bar{1}}-\bar{\bar{P}}_L)\left[\sum_{n=0}^{\infty} (\bar{\bar{P}}_R\bar{\bar{P}}_L)^n e^{i2nk\ell} \right] \right.$$

$$\left[\bar{\bar{P}}_R(\bar{\bar{Z}}_0+\bar{\bar{Z}}_L)^{-1}e^{2ik\ell} + (\bar{\bar{Z}}_0+\bar{\bar{Z}}_R)^{-1}e^{ik\ell} \right]$$

$$\left. - (\bar{\bar{Z}}_0+\bar{\bar{Z}}_L)^{-1}\right\} \left[\frac{i\bar{Z}_0\tilde{\bar{I}}_D}{k} \right] \tag{II-15}$$

If we take the fourier-transform of this equation, using Equation (II-10), we have

$$\bar{I}(0,t) = -\frac{V}{2} (\bar{\bar{1}} + \bar{\bar{P}}_L) \times$$

$$\sum_{n=0}^{\infty} (\bar{\bar{P}}_R\bar{\bar{P}}_L)^n \left\{ \delta Q(t-2n\tau_\ell) - \bar{\bar{P}}_R \delta Q(t-(2n+1)\tau_\ell) \right\} \tag{II-16}$$

where

$$\delta\bar{Q}(t) = \bar{Q}(t) - Q(t-\tau_\ell)$$

$$\tau_\ell = \ell/V \tag{II-17}$$

as the final solution for the current that flows at X=0 as a function of time.

Appendix III

ENERGY THEOREM

An important consequence of the properties of the T-L equations as presented in the main body of the text and in the preceding Appendix is the presence of an energy theorem. The total energy density for a multiwire bundle is defined by the following equation

$$\mu = \frac{1}{2} \left\{ (\overline{V}, \overline{\overline{C}} \, \overline{V}) + (\overline{I}, \overline{\overline{L}} \, \overline{I}) \right\} \qquad (III\text{-}1)$$

where the inner product of two vectors $\overline{A}$ and $\overline{B}$ is denoted by the symbol $(\overline{A}, \overline{B})$. If we take the partial derivative of μ with respect to t and X and use the T-L equations, Equation (II-1) to simplify, we can write a Poynting equation for μ

$$\frac{\partial \mu}{\partial t} + \frac{\partial S}{\partial X} = (\overline{I}_D, \overline{V}) \qquad (III\text{-}2)$$

where S is the energy flux (Poynting Vector) and is defined

$$S = (\overline{I}, \overline{V}) \qquad (III\text{-}3)$$

and the source term is $(\overline{I}_D, \overline{V})$. The energy which is transported to the loads is generated by the source term, which is directly related to the Norton Equivalent drivers $\overline{I}_D$.

163

If we integrate Equation (II-2) over the
length of the cable ℓ, we obtain an expression for
the total energy in the multiwire cable E

$$\frac{dE}{dt} + \left\{ \left(\overline{I}(\ell),\ \overline{V}(0) \right) - \left(\overline{I}(0),\ \overline{V}(0) \right) \right\}$$

$$= \int_0^\ell (\overline{I}_D,\ \overline{V})\ dx \qquad\qquad (III-4)$$

If we again assume, as we did in Appendix II, that $\overline{I}_D$ is
independent of X, then the right-hand side of the
previous equation can be written

$$\int_0^\ell dx\ (\overline{I}_D,\ \overline{V}) = \ell(\overline{I}_D,\ \langle \overline{V} \rangle) \qquad\qquad (III-5)$$

where $\langle \overline{V} \rangle$ is the average voltage

$$\langle \overline{V} \rangle = \frac{1}{\ell} \int_0^\ell \overline{V}\ dx$$

The quantity, therefore, in Equation (III-5) represents
the total power source and the total available energy is

$$\mathcal{E} = \ell \int_0^\infty (\overline{I}_D,\ \langle \overline{V} \rangle)\ dt \qquad\qquad (III-6)$$

We can, again, use the T-L equations to get an expression
for $\langle \overline{V} \rangle$.

164

$$\frac{\partial}{\partial t} \langle \overline{V} \rangle = \overline{\overline{C^{-1}}} \, \overline{I}_D - \frac{\overline{\overline{C^{-1}}}}{\ell} \left(\overline{I}(\ell) - \overline{I}(0) \right) \tag{III-7}$$

This equation, together with the relationship between current driver and charge

$$\overline{I}_D = \frac{d}{dt} \overline{Q} \tag{III-8}$$

allows us to rewrite the total available energy as

$$\mathcal{E} = \int_0^\infty dt \left\{ \left(\overline{Q}, \overline{\overline{C^{-1}}} \, \overline{I}(\ell) \right) - \left(\overline{Q}, \overline{\overline{C^{-1}}} \, \overline{I}(0) \right) \right\}$$

$$- \frac{\ell}{2} \left(\overline{Q}_D, \overline{\overline{C^{-1}}} \, \overline{Q}_D \right) \tag{III-9}$$

where $\overline{Q}_D$ is the total charge transfer in the multiwire cable

$$\overline{Q}_D = \int_0^\infty \overline{I}_D \, dt \tag{III-10}$$

To arrive at the expression in Equation (III-9) for $\mathcal{E}$, we have assumed that at t=∞, $\overline{V}(\infty) = \overline{0}$.

Since the expression for $\mathcal{E}$ in Equation (III-9) represents the total energy that can be dissipated across all terminations in a multiwire bundle, it is of interest to cast this equation into a more useable form. It is immediately obvious that the energy is not a constant of

the motion, since it depends on the solution $\overline{I}(\ell)$, $\overline{I}(0)$, which is associated with the fact that the Poynting equation, Equation (III-3) has a current source term. We can, however, arrive at a usable expression for $\mathcal{E}$, since we have an analytic solution for the current $\overline{I}$ that flows across the terminations, as presented in Appendix II. For convenience in this derivation, we will assume that the terminations are symmetric, i.e.

$$\overline{\overline{P}}_L = \overline{\overline{P}}_R = \overline{\overline{P}} \tag{III-11}$$

The solution for the current at X=0 is, therefore

$$\overline{I}(0,t) = -\frac{V}{2}(\overline{\overline{I}} + \overline{\overline{P}})$$

$$\sum_{n=0}^{\infty}(\overline{\overline{P}})^{2n}\left[\delta\overline{Q}(t-2n\tau_\ell) - \overline{\overline{P}}\ \delta\overline{Q}(t-(2n+1)\tau_\ell)\right] \tag{III-12}$$

For the case of symmetric terminations, we have

$$\overline{I}(\ell) = -\overline{I}(0) \tag{III-13}$$

So that

$$\mathcal{E} = -2\int_0^\infty dt\left(\overline{Q},\ \overline{\overline{C^{-1}}}\ \overline{I}(0)\right)$$

$$-\frac{\ell}{2}(\overline{Q}_D,\ \overline{\overline{C^{-1}}}\ \overline{Q}_D) \tag{III-14}$$

166

In addition, we will assume that the waveform f(t) for the current driver $\overline{I}_D$ is a square wave of width τ_p, so that

$$\overline{I}_D(t) = \overline{I}_0\ f(t)$$

$$\overline{Q}(t) = \overline{I}_0 t \qquad 0 \leq t \leq \tau_p$$

and
$$= \overline{I}_0 \tau_p \qquad t \geq \tau_p$$

$$\overline{Q}_D = \overline{I}_0 \tau_p \qquad\qquad\qquad \text{(III-15)}$$

where $\overline{I}_0$ is the peak driver in a/m. The other time of interest is the propagation time, τ_ℓ where

$$\tau_\ell = \ell/V \qquad\qquad\qquad\qquad \text{(III-16)}$$

In order to obtain an expression for $\mathcal{E}$ from Equation (III-14) we must assume a particular value for the ratio

$$\zeta = \tau_p/\tau_\ell \qquad\qquad\qquad\qquad \text{(III-17)}$$

Since we are interested in obtaining an expression for $\mathcal{E}$ the maximum energy that can be dissipated, it is natural to look at the particular values of ζ that correspond to long cables, i.e.

$$0 \leq \zeta \leq 1 \qquad\qquad\qquad\qquad \text{(III-18)}$$

If we assume the range of ζ as given above, and substitute the expression for $\overline{I}(0)$ into Equation (III-14),

using Equation (III-15) we can perform the integrations over time and sum the infinite series. The result is a closed form expression for the total energy that can be dissipated across all terminations

$$\mathcal{E}/\mathcal{E}_{MAX} = 1 - \frac{1}{3}\zeta(1 + \langle \overline{\overline{p}} \rangle) \qquad \text{(III-19)}$$

where

$$\mathcal{E}_{MAX} = \frac{1}{2}\left(\overline{Q}_D, \ \overline{\overline{C^{-1}}} \ \overline{Q}_D\right) \cdot \ell$$

$$\langle \overline{\overline{p}}{}^n \rangle = \frac{\left(\overline{Q}_D, \ \overline{\overline{C^{-1}}} \ \overline{\overline{p}}{}^n \ \overline{Q}_D\right)}{\left(\overline{Q}_D, \ \overline{\overline{C^{-1}}} \ \overline{Q}_D\right)} \qquad \text{(III-20)}$$

This result is valid in the range

$$0 \le \zeta \le 1 \qquad \text{(III-21)}$$

In general, the solution for $\mathcal{E}$ is different in other ranges of ζ, getting more complicated as ζ gets larger. The result for the range

$$1 \le \zeta \le 2 \qquad \text{(III-22)}$$

can be written

$$\mathcal{E}/\mathcal{E}_{MAX} = 1 - \left[f\left(1 + 2\langle \overline{p} \rangle + \langle \overline{p}{}^2 \rangle\right) \right.$$

$$\left. - \frac{1}{3}\zeta\left(\langle \overline{p} \rangle + \langle \overline{p}{}^2 \rangle\right)\right] \quad 1 \le \zeta \le 2 \qquad \text{(III-23)}$$

where

$$f = 1 - \zeta^{-1} + \frac{1}{3} \zeta^{-2} \qquad \text{(III-24)}$$

Appendix IV

MULTIWIRE TERMINATION IMPEDANCE
MATRIX AND REFLECTION COEFFICIENT

The solutions to the T-L equations presented previously, both for the current and energy into the loads, depend on the terminations through the impedance matrix $\bar{\bar{Z}}$ or, alternatively, on the reflection coefficient $\bar{\bar{p}}$ which is a function of $\bar{\bar{Z}}$. In this appendix we will consider the relationship between $\bar{\bar{Z}}$ and physical resistance and, also, what the reflection coefficient $\bar{p}$ looks like for the various possible terminations.

IV.1   *IMPEDANCE MATRIX*

The boundary conditions for an n+1 bundle of wires terminated at the left (right) end with a termination impedance matrix $\bar{\bar{Z}}_L$ ($\bar{\bar{Z}}_R$) is:

$$\bar{V}(0,t) = -\bar{\bar{Z}}_L \ \bar{I}(0,t)$$

$$\bar{V}(\ell,t) = \bar{\bar{Z}}_R \ I(\ell,t) \qquad (IV-1)$$

If we consider the left side of the transmission line, we can write:

$$\bar{I}(0,t) = (\overline{\overline{Z_L^{-1}}}) \ \bar{V}(0,t) \qquad (IV-2)$$

171

If we denote the current (voltage) at X=0 in wire i by I_i, (V_i) we have

$$I_i = \sum_{j=1}^{N} (Z_L^{-1})_{ij} V_j \qquad (IV-3)$$

This current will divide depending upon the physical resistances that it sees. If we denote these physical resistances by R_{ij} j=1, n, where R_{ii} is the resistance from i to ground and R_{ij}, j=1, n (i≠j) are the resistances from i to all the other wires in the bundle, then we have

$$I_i = \sum_{\substack{j=1 \\ i \neq j}}^{N} \frac{V_i - V_j}{R_{ij}} + \frac{V_i}{R_{ii}} \qquad (IV-4)$$

Equating these two expressions for I_i, we have

$$\sum_{\substack{j=1 \\ i \neq j}}^{N} \frac{V_i - V_j}{R_{ij}} + \frac{V_i}{R_{ii}} = \sum_{j=1}^{N} (Z_L^{-1})_{ij} V_j \qquad (IV-5)$$

Rearranging these terms we have

$$\left[\sum_{\substack{j=1 \\ i \neq j}}^{N} \frac{1}{R_{ij}} + \frac{1}{R_{ii}} - (Z_L^{-1})_{ii} \right] V_i$$

$$- \sum_{\substack{j=1 \\ i \neq j}}^{N} \left[\frac{1}{R_{ij}} + (Z_L^{-1})_{ij} \right] V_j = 0 \qquad (IV-6)$$

172

These equations imply

$$(Z_L^{-1})_{ii} = \sum_{\substack{j=1 \\ i \neq j}}^{N} \frac{1}{R_{ij}} + \frac{1}{R_{ii}}$$

$$(Z_L^{-1})_{ij} = - \frac{1}{R_{ij}} \qquad i \neq j \qquad \text{(IV-7)}$$

We can rewrite the first equation using the second equation and we obtain

$$(Z_L^{-1})_{ii} = \sum_{\substack{j=1 \\ i \neq j}}^{N} - (Z_L^{-1})_{ij} + \frac{1}{R_{ii}} \qquad \text{(IV-8)}$$

which implies

$$\frac{1}{R_{ii}} = (Z_L^{-1})_{ii} + \sum_{\substack{j=1 \\ i \neq j}}^{N} (Z_L^{-1})_{ij}$$

$$= \sum_{j=1}^{N} (Z_L^{-1})_{ij} \qquad \text{(IV-9)}$$

And so we obtain the following two equations

$$R_{ij} = - \frac{1}{(Z_L^{-1})_{ij}} \qquad i \neq j$$

$$R_{ii} = \frac{1}{\sum_{j=1}^{N} (Z_L^{-1})_{ij}} \qquad \text{(IV-10)}$$

If we desire to characteristically terminate the multi-wire cable, we can use the above two equations to determine the appropriate physical resistances. If we desire to determine what termination matrix $\bar{\bar{Z}}_L$ to use corresponding to a given set of physical resistances R_{ij}, we can use Equation (IV-7). These can be written as:

$$(Z_L^{-1})_{ii} = \sum_{j=1}^{N} \frac{1}{R_{ij}}$$

$$(Z_L^{-1})_{ij} = -\frac{1}{R_{ij}} \qquad i \neq j \qquad\qquad (IV-11)$$

IV.2   EXAMPLES — TWO WIRE

In this section we will consider some particular examples of the results indicated in the previous paragraph. Let us consider a TSP with the following capacitance $\bar{\bar{C}}$, inductance $\bar{\bar{L}}$ and characteristic impedance matrix $\bar{\bar{Z}}_0$:

$$\bar{\bar{C}} = \begin{pmatrix} 207. & -36. \\ -36. & 207. \end{pmatrix} \text{pf/m}$$

$$\bar{\bar{L}} = \begin{pmatrix} 223. & 11.0 \\ 11. & 223. \end{pmatrix} \text{nH/m}$$

$$\bar{\bar{Z}}_0 = \begin{pmatrix} 33.3 & 3.73 \\ 3.73 & 33.3 \end{pmatrix} \Omega \qquad\qquad (IV-12)$$

CASE 1:   CHARACTERISTIC TERMINATION

If we desire to terminate the TSP character-
istically, we can use Equation (IV-10) to determine the
appropriate physical resistances.   The inverse of the
characteristic impedance matrix $\overline{\overline{Z}}_L$ is given by:

$$\overline{\overline{Z}}_0^{-1} = \begin{pmatrix} 3.04 \times 10^{-2} & - & 3.41 \times 10^{-3} \\ - & 3.41 \times 10^{-3} & 3.04 \times 10^{-2} \end{pmatrix} \Lambda^{-1} \qquad \text{(IV-13)}$$

and the physical resistance matrix $\overline{\overline{R}}$ is:

$$\overline{\overline{R}} = \begin{pmatrix} 32.9 & 293.6 \\ 293.6 & 32.9 \end{pmatrix} \Lambda \qquad \text{(IV-14)}$$

The reflection coefficient $\overline{\overline{p}}$ when the cable is charac-
teristically terminated is given by:

$$\overline{\overline{p}} = \overline{\overline{0}}$$

$$= \begin{pmatrix} 0 & 0 \\ 0 & 0 \end{pmatrix} \qquad \text{(IV-15)}$$

CASE 2:   WIRE-TO-SHIELD TERMINATION

If we desire to terminate the TSP only wire-to-
shield with $R_{12}=R_{21}=\infty$, corresponding to no wire-to-wire
termination, we can set $R_{12}=R_{21}=\infty$ in Equation (IV-11) to
determine the appropriate $\overline{\overline{Z}}_L$ matrix:

$$(Z_L^{-1})_{11} = \frac{1}{R_{11}}$$

$$(Z_L^{-1})_{22} = \frac{1}{R_{22}}$$

$$(Z_L^{-1})_{12} = (Z_L^{-1})_{21} = 0 \qquad (IV-16)$$

which implies:

$$\overline{\overline{Z}}_L = \begin{pmatrix} R_{11} & 0 \\ 0 & R_{22} \end{pmatrix} \Omega \qquad (IV-17)$$

For this case, therefore, the diagonal elements of Z_L are identical to the physical resistances R_{11}, R_{22}.

If we write the characteristic impedance matrix in the following way

$$Z_0 = \begin{pmatrix} Z_1 & Z \\ Z & Z_2 \end{pmatrix} \qquad (IV-18)$$

then $\overline{\overline{p}}$ can be written:

$$\overline{\overline{p}} = \frac{1}{D} \begin{pmatrix} (Z_1-R_1)(Z_2+R_2)-Z^2 & 2ZR_2 \\ 2ZR_1 & (Z_1+R_1)(Z_2-R_2)-Z^2 \end{pmatrix}$$

$$D = (Z_1+R_1)(Z_2+R_2)-Z^2 \qquad (IV-19)$$

It is important to note from the above expression for $\overline{\overline{p}}$ that whenever the two wires are terminated wire-to-shield only, $\overline{\overline{p}}$ can never be diagonal for any finite value of R_1 and R_2.

CASE 3:   SHORT-CIRCUIT WIRE-TO-WIRE

If we desire to determine the appropriate $\overline{\overline{Z}}$ when the two wires of the TSP are tied together and terminated with one resistance to ground we can set:

$$R_{12} = R_{21} = 0$$

$$R_{11} = R_{22} = R \qquad (IV-20)$$

This corresponds to:

$$Z_L = \frac{R}{2} \begin{pmatrix} 1 & 1 \\ 1 & 1 \end{pmatrix} \qquad (IV-21)$$

The reflection coefficient is:

$$\overline{\overline{p}} = \frac{1}{D} \begin{pmatrix} (Z_1-R)(Z_2+R)-Z^2 & 2ZR \\ 2ZR & (Z_1+R)(Z_2-R)-Z^2 \end{pmatrix}$$

$$D = (Z_1+R)(Z_2+R)-Z^2 \qquad (IV-22)$$

177

CASE 4:   GENERAL EXPRESSION — TSP

For the general situation of any combination of physical resistances we can write down the appropriate termination matrix $\overline{\overline{Z}}_L$.

$$\overline{\overline{R}} = \begin{pmatrix} R_{11} & R_{12} \\ R_{21} & R_{22} \end{pmatrix}$$

$$\overline{\overline{Z}}_L = \frac{1}{R_{12}R_{21}+R_{11}R_{21}+R_{22}R_{12}} \begin{pmatrix} (R_{22}+R_{21})(R_{11}R_{12}) & R_{12}R_{11}R_{22} \\ R_{21}R_{11}R_{22} & (R_{12}+R_{11})(R_{21}R_{22}) \end{pmatrix} \quad \text{(IV-23)}$$

Appendix V

TWO WIRE SOLUTIONS

V.1   CURRENT

The termination dependence of both the current and energy in a multiwire bundle can be conveniently represented by the dimensionless matrix $\bar{\bar{p}}$ defined as

$$\bar{\bar{p}} = (\bar{\bar{Z}}_0 + \bar{\bar{Z}})^{-1} (\bar{\bar{Z}}_0 - \bar{\bar{Z}}) \qquad (V-1)$$

The exact solution for the current given in Equation (II-16) indicates that the fact that $\bar{\bar{p}}$ is, in general, a non-diagonal matrix distinguishes a multiwire bundle from a single wire transmission line. Since the characteristic impedance matrix $\bar{\bar{Z}}_0$ can never be diagonal for any physically reasonable multiwire bundle, $\bar{\bar{p}}$ can never be diagonal for any finite value of the terminations. It is possible, however, to make a transformation which diagonalizes $\bar{\bar{p}}$, and which allows the solution for a multiwire bundle to be written in terms of single wire solutions. While this procedure, in principle, can be done for any number of wires, in practice, the algebra becomes rather tedious for n>2. In the following paragraph we will sketch this procedure for a two-wire bundle.

The characteristic impedance matrix is defined

$$\bar{\bar{Z}}_0 = \begin{pmatrix} z_1 & z \\ z & z_2 \end{pmatrix} \qquad (V-2)$$

and the termination impedance matrix is defined

$$\overline{\overline{Z}} = \begin{pmatrix} R_1 & 0 \\ 0 & R_2 \end{pmatrix} \qquad (V-3)$$

where we will only consider terminations wire-to-shield, and R and R are the physical resistances wire-to-shield. The reflection coefficient can be written

$$\overline{\overline{p}} = \frac{1}{\Delta} \begin{pmatrix} (Z_1-R_1)(Z_2+R_2)-Z^2 & 2ZR_2 \\ 2ZR_1 & (Z_1+R_1)(Z_2-R_2)-Z^2 \end{pmatrix} \qquad (V-4)$$

where

$$\Delta = (Z_1+R_1)(Z_2+R_2)-Z^2$$

The e-values of $\overline{\overline{p}}$ can be found directly

$$\lambda_2^1 = \frac{\left(1-r_1 r_2-C^2\right) \pm \left((r_1-r_2)^2+4C^2 r_1 r_2\right)^{1/2}}{(1+r_1)(1+r_2)-C^2} \qquad (V-5)$$

where

$$r_1 = R_1/Z_1$$

$$r_2 = R_2/Z_2$$

$$C = Z/(Z_1 Z_2)^{1/2} \qquad (V-6)$$

The e-vectors corresponding to these e-values can also
be obtained directly

$$
\hat{n}_2^1 = \left(
\begin{array}{c}
\left| (\beta \pm \alpha)/(1+\iota)\beta \pm (1-\zeta)\alpha \right|^{1/2} \\
\pm \left| \zeta(\beta \mp \alpha)/(1+\zeta)\beta \pm (1-\zeta)\alpha \right|^{1/2}
\end{array}
\right)
\tag{V-7}
$$

where

$$
\alpha = R_1 Z_2 - R_2 Z_1
$$

$$
\beta = (\alpha^2 + 4Z^2 R_1 R_2)^{1/2}
$$

$$
\zeta = R_1/R_2
\tag{V-8}
$$

The quantity C is a measure of the wire-to-
wire coupling. It is easily seen that the solution
reduces to two independent uncoupled transmission
lines when C is zero. From general properties of the
impedance matrix, it may be shown that the maximum
value of C is unity.

Once the e-values and e-vectors have been
determined, it is straightforward to construct the
transformation matrix $\overline{\overline{T}}$. If we denote $\hat{e}_1$ and $\hat{e}_2$ as
the unit vectors in the original basis, which can be
written as

$$
\hat{e}_1 = \begin{pmatrix} 1 \\ 0 \end{pmatrix}
$$

$$
\hat{e}_2 = \begin{pmatrix} 0 \\ 1 \end{pmatrix}
\tag{V-9}
$$

We can write

$$\begin{pmatrix} \hat{n}_1 \\ \hat{n}_2 \end{pmatrix} = \overline{\overline{T}} \begin{pmatrix} \hat{e}_1 \\ \hat{e}_2 \end{pmatrix} \tag{V-10}$$

where

$$\overline{\overline{T}} = \begin{pmatrix} \left(\dfrac{\beta+\alpha}{(1+\zeta)(\beta)+(1-\zeta)\alpha} \right)^{1/2} & \left(\dfrac{\zeta(\beta-\alpha)}{(1+\zeta)\beta+(1-\zeta)\alpha} \right)^{1/2} \\[4ex] \left(\dfrac{\beta-\alpha}{(1+\zeta)\beta-(1-\zeta)\alpha} \right)^{1/2} & -\left(\dfrac{\zeta(\beta+\alpha)}{(1+\zeta)\beta-(1-\zeta)\alpha} \right)^{1/2} \end{pmatrix}$$

In order to write the solution for the current in wire one and two it is necessary to obtain $(\overline{\overline{T}})^{-1}$ which we can write:

$$\begin{pmatrix} \hat{e}_1 \\ \hat{e}_2 \end{pmatrix} = (\overline{\overline{T}})^{-1} \begin{pmatrix} \hat{n}_1 \\ \hat{n}_2 \end{pmatrix} \tag{V-11}$$

where

$$(\overline{\overline{T}})^{-1} = \begin{pmatrix} \left(\dfrac{D}{4\,\zeta\beta^2} \right)^{1/2} T_{22} & \left(\dfrac{D}{4\,\zeta\beta^2} \right)^{1/2} T_{12} \\[4ex] \left(\dfrac{D}{4\,\zeta\beta^2} \right)^{1/2} T_{21} & -\left(\dfrac{D}{4\,\zeta\beta^2} \right)^{1/2} T_{11} \end{pmatrix}$$

and

$$D = (1+\zeta)^2\beta^2 - (1-\zeta)^2\alpha^2$$

$$\overline{\overline{T}} = \begin{pmatrix} T_{11} & T_{12} \\ T_{21} & T_{22} \end{pmatrix} \tag{V-12}$$

In order to understand wire-to-wire coupling in a multiwire transmission line, it is of interest to drive one wire and look at the current that flows in the other wire. The analysis that we have just developed allows us to accomplish this. Let $\overline{X}$ denote the basic current driver

$$\overline{X} = X_i \hat{e}_i \tag{V-13}$$

From the previous section we have

$$\hat{e}_i = (T^{-1})_{ij} \hat{n}_j$$

So that

$$\overline{X} = X_i (T^{-1})_{ij} \hat{n}_j \tag{V-14}$$

The current that flows in both lines can then be written

$$I_\ell = X_i(T^{-1})_{ij} I(\lambda_j) A_{j\ell} \tag{V-15}$$

where $I(\lambda_j)$ is the single wire solution for the e-value λ_j. For the special case that we drive only wire two, we have

$$X_1 = 0$$

$$X_2 = 1 \qquad\qquad\qquad\qquad (V-16)$$

and the solution for the current in wire one and two can be written:

$$I_1 = \left(\frac{\beta^2 - \alpha^2}{4\zeta\beta^2}\right)^{1/2} \left\{ I(\lambda_1) - I(\lambda_2) \right\}$$

$$I_2 = \left(\frac{\beta-\alpha}{2\beta}\right) I(\lambda_1) + \left(\frac{\zeta+\alpha}{2\zeta}\right) I(\lambda_2) \qquad (V-17)$$

where $I(\lambda_2^1)$ are the single wire solutions with reflection coefficient λ_2^1.

V.2 ENERGY

Once the current in both lines is written in terms of single wire solutions, it is of interest to compute the energy dissipated across the terminations. Our main interest in this analysis is the calculation of the energy dissipated across termination one when wire two is driven, since all of this energy represents coupled energy. The current that flows in wire one can be written

$$I_1 = \frac{ZR_2}{\left[\left(R_1Z_2 - R_2Z_1\right)^2 + 4Z^2 R_1 R_2\right]^{1/2}} \left\{ I(\lambda_1) - I(\lambda_2) \right\} \quad \text{(V-18)}$$

and the energy is

$$E_1 = R_1 \Lambda_1^2 \left[\int_0^\infty dt \left[I(\lambda_1)^2 + I(\lambda_2)^2 - 2I(\lambda_1)I(\lambda_2) \right] \right]$$

where

$$\Lambda = \frac{ZR_2}{\left[\left(R_1Z_2 - R_2Z_1\right)^2 + 4Z^2 R_1 R_2\right]^{1/2}} \quad \text{(V-19)}$$

If we assume a square wave driver, we can perform these integrations as has been done in previous sections. In particular, if we take the long line limit which corresponds to

$$\zeta = \tau_p / \tau_\ell \quad <<1 \quad \text{(V-20)}$$

We arrive at the following expression for E_1:

$$E_1 = E_2^{\text{MAX}} \left\{ \left[\frac{1}{2} \frac{r_1 r_2^2 c^2}{(\dot{r}_1 - r_2)^2 + 4c^2 r_1 r_2} \right] \times \left[\frac{1+\lambda_1}{1-\lambda_1} + \frac{1+\lambda_2}{1-\lambda_2} \right. \right.$$

$$\left. \left. - 2 \frac{(1+\lambda_1)(1+\lambda_2)}{(1-\lambda_1\lambda_2)} \right] \right\} \quad \text{(V-21)}$$

Where E_2^{MAX} is the maximum energy capability of wire 2
and is given by

$$E_2^{MAX} = \frac{1}{2}(VZ_2)Q_D^2 \ell \tag{V-22}$$

From these expressions, one can show that the coupled
current and energy tend to zero as the termination
resistance on line 2 goes to zero (shorted) and
increases as the termination resistance is increased.
If line 2 is opened, the current on line 1 simply
appears as if line 1 were being directly driven with
an effective source term of C times the line 2 source
term. In particular, all the energy capability of
line 2 is not coupled into line 1. The final voltage
on the second line is not zero, and leads to capaci-
tive energy storage of a portion of the energy capa-
bility of this line.

Appendix VI

TWO-WIRE CALCULATIONS

We have considered a number of two-wire cables. Each cable is labeled by the designation TWI where I=1,2,3. The following parameters distinguish each cable from one another.

TW1

$$\bar{\bar{C}} = \begin{pmatrix} 207. & -36.0 \\ -36.0 & 207. \end{pmatrix} \text{ pf/m}$$

$$\bar{\bar{L}} = \begin{pmatrix} 223. & 11. \\ 11. & 223. \end{pmatrix} \text{ nH/m}$$

$$\bar{\bar{Z}}_c \begin{pmatrix} 33.3 & 3.73 \\ 3.73 & 33.3 \end{pmatrix} \text{ ohms}$$

TW2

$$\bar{\bar{C}} = \begin{pmatrix} 207. & -36. \\ -36. & 207. \end{pmatrix} \text{ pf/m}$$

$$\bar{\bar{L}} = \begin{pmatrix} 55.4 & 9.6 \\ 9.6 & 55.4 \end{pmatrix} \text{ nh/m}$$

$$\bar{\bar{Z}}_c = \begin{pmatrix} 16.6 & 2.9 \\ 2.9 & 16.6 \end{pmatrix} \text{ ohms}$$

<u>TW3</u>

$$\bar{\bar{C}} = \begin{pmatrix} 226. & -109. \\ -109. & 751. \end{pmatrix} \quad \text{pf/m}$$

$$\bar{\bar{L}} = \begin{pmatrix} 53. & 8. \\ 8. & 16. \end{pmatrix} \quad \text{nH/m}$$

$$\bar{\bar{Z}}_C = \begin{pmatrix} 15.9 & 23.5 \\ 23.5 & 4.8 \end{pmatrix} \quad \text{ohms}$$

In the following pages we will present the results of the calculations. The cable designated TW1 is the two-wire cable which has two phase velocities whereas cables 1 and 3 each have one phase velocity. Each plot presented is labeled by a header which indicates the parameters used. In the following Tables we indicate the definition of these headers. For cables TW1 and TW2 the current drivers were as follows

$$I_D = \begin{pmatrix} 1 \\ 0 \end{pmatrix}$$

and for TW3 the current drivers were

$$I_D = \begin{pmatrix} 0 \\ 1 \end{pmatrix}$$

TABLE VI.1

TW1

$$\overline{\overline{Z}} = \begin{pmatrix} 33.3 & 0 \\ 0 & 33.3 \end{pmatrix} \text{ ohms}$$

$\overline{\overline{R}}$ = termination impedance matrix (ohms) (symmetric termination)

τ_p = pulse width (square wave) (ns)

L = length of cable (meter)

$\overline{\overline{R}}$	τ_p	L	Header
.1Z	3	.3	TW1R11T1L1
.1Z	3	3.	TW1R11T1L2
.1Z	3	30.	TW1R11T1L3
.1Z	30	.3	TW1R11T2L1
.1Z	30	3.	TW1R11T2L2
.1Z	30	30.	TW1R11T2L3
.1Z	300	.3	TW1R11T3L1
.1Z	300	3.	TW1R11T3L1
.1Z	300	30.	TW1R11T3L3
Z	3	.3	TW1R22T1L1
Z	3	3.	TW1R22T1L2
Z	3	30.	TW1R22T1L3
Z	30	.3	TW1R22T2L1
Z	30	3.	TW1R22T2L2
Z	30	30.	TW1R22T2L3

TABLE VI.1 (Continued)

$\overline{\overline{R}}$		τ_p	L	Header
	Z	300	.3	TW1R22T3L1
	Z	300	3.	TW1R22T3L2
	Z	300	30.	TW1R22T3L3
10	Z	3	.3	TW1R33T1L1
10	Z	3	3.	TW1R33T1L2
10	Z	3	30.	TW1R33T1L3
10	Z	30	.3	TW1R33T2L1
10	Z	30	3.	TW1R33T2L2
10	Z	30	30.	TW1R33T2L3
10	Z	300	.3	TW1R33T3L1
10	Z	300	3.	TW1R33T3L2
10	Z	300	30.	TW1R33T3L3

TABLE VI.2

<u>TW2</u>

$$\bar{\bar{Z}} = \begin{pmatrix} 16.6 & 0 \\ 0 & 16.6 \end{pmatrix}; \quad Z_1 \begin{pmatrix} 16.6 & 0 \\ 0 & 0 \end{pmatrix}$$

$$Z_2 \begin{pmatrix} 0 & 0 \\ 0 & 16.6 \end{pmatrix}$$

$\bar{\bar{R}}$ = termination impedance matrix (ohms) (symmetric termination)

τ_p = pulse width (square wave) (ns)

L = length of cable (meter)

$\bar{\bar{R}}$	τ_p	L	Header
.1Z	3	.3	TW2R11T1L1
.1Z	3	3.	TW2R11T1L2
.1Z	3	30.	TW2R11T1L3
.1Z	30	.3	TW2R11T2L1
.1Z	30	3.	TW2R11T2L2
.1Z	30	30.	TW2R11T2L3
.1Z	300	.3	TW2R11T3L1
.1Z	300	3.	TW2R11T3L2
.1Z	300	30.	TW2R11T3L3
Z	3	.3	TW2R22T1L1
Z	3	3.	TW2R22T1L2
Z	3	30.	TW2R22T1L3
Z	30	.3	TW2R22T2L1
Z	30	3.	TW2R22T2L2
Z	30	30.	TW2R22T2L3

TABLE VI.2 (Continued)

$\bar{\bar{R}}$	τ_p	L	Header
Z	300	.3	TW2R22T3L1
Z	300	3.	TW2R22T3L2
Z	300	30.	TW2R22T3L3
10 Z	3	.3	TW2R33T1L1
10 Z	3	3.	TW2R33T1L2
10 Z	3	30.	TW2R33T1L3
10 Z	30	.3	TW2R33T2L1
10 Z	30	3.	TW2R33T2L2
10 Z	30	30.	TW2R33T2L3
10 Z	300	.3	TW2R33T3L1
10 Z	300	3.	TW2R33T3L2
10 Z	300	30.	TW2R33T3L3
$.1Z_1 + Z_2$	3	3	TW2R12T1L2
$.1Z_1 + 10Z_2$	3	3	TW2R13T1L2
$Z_1 + .1Z_2$	3	3	TW2R21T1L2
$Z_1 + 10Z_2$	3	3	TW2R23T1L2
$10Z_1 + .1Z_2$	3	3	TW2R31T1L2
$10Z_1 + Z_2$	3	3	TW2R32T1L2

TABLE VI.3

__TW3__

$$\bar{\bar{Z}} = \begin{pmatrix} 16. & 0 \\ 0 & 5. \end{pmatrix} \quad \bar{\bar{Z}}_1 = \begin{pmatrix} 16. & 0 \\ 0 & 0 \end{pmatrix} \quad \bar{\bar{Z}}_2 = \begin{pmatrix} 0 & 0 \\ 0 & 5. \end{pmatrix}$$

$\bar{\bar{R}}$ = termination impedance matrix (ohms) (symmetric termination)

τ_p = pulse width (square wave) (ns)

L = length of cable (meters)

$\bar{\bar{R}}$	τ_p	L	Header
$.1Z$	3	3	TW3R11T1L2
Z	3	3	TW3R22T1L2
$10 \quad Z$	3	3	TW3R33T1L2
$.1Z_1 + Z_2$	3	3	TW3R12T1L2
$.1Z_1 + 10Z_2$	3	3	TW3R13T1L2
$Z_1 + .1Z_2$	3	3	TW3R21T1L2
$Z_1 + 10Z_2$	3	3	TW3R23T1L2
$10Z_1 + .1Z_2$	3	3	TW3R31T1L2
$10Z_1 + Z_2$	3	3	TW3R32T1L2

Appendix VII

SEVEN-WIRE CALCULATIONS

We have considered various distributions of drivers for the seven wire bundle discussed in Section V. These distributions represent typical groups of seven wires in the thirty-seven wire bundle also discussed in Section V. The propagation time and pulse width were chosen such that

$$\tau_p = \tau_\ell = 17\text{ns}$$

which corresponds to a length of cable equal to $\sim$3m. Three different distributions of drivers were considered SE1, SE2, SE3 according to the following

$$\underline{\text{SE1}} - I_D(1) = \begin{pmatrix} - .5 \\ +1.0 \\ + .5 \\ - .3 \\ - .2 \\ - .3 \\ + .5 \end{pmatrix}$$

$$\underline{\text{SE2}} - I_D(2) = \begin{pmatrix} - .1 \\ + .3 \\ +1.0 \\ - .05 \\ - .02 \\ - .03 \\ - .20 \end{pmatrix}$$

$$\underline{SE3} - I_D(3) = \begin{pmatrix} +1.0 \\ - .7 \\ - .2 \\ - .1 \\ - .4 \\ - .1 \\ - .2 \end{pmatrix}$$

Each plot is labeled by a header. The definition of the header for each plot is given in Table (VII.1)-(VII.3).

TABLE VII.1

SE1

$$\bar{\bar{Z}} \quad = \quad \begin{pmatrix} 30.1 \\ & 27.4 & & & & & \bar{0} \\ & & 27.4 \\ & & & 27.4 \\ & & & & 27.4 \\ & \bar{0} & & & & 27.4 \\ & & & & & & 27.4 \end{pmatrix}$$

$$\bar{\bar{Z}}_1 \quad = \quad \begin{pmatrix} 0 \\ & 27.4 & & & & & \bar{\bar{0}} \\ & & 0 \\ & & & 0 \\ & & & & 0 \\ & \bar{\bar{0}} & & & & 0 \\ & & & & & & 0 \end{pmatrix}$$

$$\bar{Z}_2 \quad = \quad \begin{pmatrix} 30.1 \\ & 0 & & & & \bar{\bar{0}} \\ & & 27.4 \\ & & & 27.4 \\ & & & & 27.4 \\ & \bar{\bar{0}} & & & & 27.4 \\ & & & & & & 27.4 \end{pmatrix}$$

TABLE VII.1 (Continued)

$\overline{\overline{R}}$ = termination impedance matrix (ohms) (symmetric termination)

τ_p = pulse width (square wave) (ns)

L = length of cable (meter)

$\overline{\overline{R}}$	τ_p	L	Header
$.1Z$	17	3	SE1R11T1L1
Z	17	3	SE1R22T1L1
$10\ Z$	17	3	SE1R33T1L1
$.1Z_1+Z_2$	17	3	SE1R12T1L1
$.1Z_1+10Z_2$	17	3	SE1R13T1L1
$Z_1+.1Z_2$	17	3	SE1R21T1L1
Z_1+10Z_2	17	3	SE1R23T1L1
$10Z_1+.1Z_2$	17	3	SE1R31T1L1
$10Z_1+Z_2$	17	3	SE1R32T1L1

TABLE VII.2

SE2

$$\overline{\overline{Z}} = \begin{pmatrix} 30.1 & & & & & & \\ & 27.4 & & & & \overline{\overline{0}} & \\ & & 27.4 & & & & \\ & & & 27.4 & & & \\ & & & & 27.4 & & \\ & \overline{\overline{0}} & & & & 27.4 & \\ & & & & & & 27.4 \end{pmatrix}$$

$$\overline{\overline{Z}}_1 = \begin{pmatrix} 0 & & & & & & \\ & 0 & & & & \overline{\overline{0}} & \\ & & 27.4 & & & & \\ & & & 0 & & & \\ & & & & 0 & & \\ & \overline{\overline{0}} & & & & 0 & \\ & & & & & & 0 \end{pmatrix}$$

$$\overline{\overline{Z}}_2 = \begin{pmatrix} 30.1 & & & & & & \\ & 27.4 & & & & \overline{\overline{0}} & \\ & & 0 & & & & \\ & & & 27.4 & & & \\ & & & & 27.4 & & \\ & \overline{\overline{0}} & & & & 27.4 & \\ & & & & & & 27.4 \end{pmatrix}$$

TABLE VII.2 (Continued)

$\overline{\overline{R}}$ = termination impedance matrix (ohms) (symmetric termination)

τ_p = pulse width (square wave) (ns)

$\overline{\overline{L}}$ = length of cable (meter)

$\overline{\overline{R}}$	τ_p	L	Header
$.1Z$	17	3	SE2R11T1L1
Z	17	3	SE2R22T1L1
$10 \ Z$	17	3	SE2R33T1L1
$.1Z_1 + Z_2$	17	3	SE2R12T1L1
$.1Z_1 + 10Z_2$	17	3	SE2R13T1L1
$Z_1 + .1Z_2$	17	3	SE2R21T1L1
$Z_1 + 10Z_2$	17	3	SE2R23T1L1
$10Z_1 + .1Z_2$	17	3	SE2R31T1L1
$10Z_1 + Z_2$	17	3	SE2R32T1L1

TABLE VII.3

<u>SE3</u>

$$\bar{\bar{Z}} = \begin{pmatrix} 30.1 & & & & & & \\ & 27.4 & & & & & \bar{\bar{0}} \\ & & 27.4 & & & & \\ & & & 27.4 & & & \\ & & & & 27.4 & & \\ & \bar{\bar{0}} & & & & 27.4 & \\ & & & & & & 27.4 \end{pmatrix}$$

$$\bar{\bar{Z}}_1 = \begin{pmatrix} 30.1 & & & & & & \\ & 0 & & & & & \bar{\bar{0}} \\ & & 0 & & & & \\ & & & 0 & & & \\ & & & & 0 & & \\ & \bar{\bar{0}} & & & & 0 & \\ & & & & & & 0 \end{pmatrix}$$

$$\bar{\bar{Z}}_2 = \begin{pmatrix} 0 & & & & & & \\ & 27.4 & & & & & \bar{\bar{0}} \\ & & 27.4 & & & & \\ & & & 27.4 & & & \\ & & & & 27.4 & & \\ & \bar{\bar{0}} & & & & 27.4 & \\ & & & & & & 27.4 \end{pmatrix}$$

201

TABLE VII.3 (Continued)

$\overline{\overline{R}}$ = termination impedance matrix (ohms) (symmetric termination)

τ_p = pulse width (square wave) (ns)

$\overline{\overline{L}}$ = length of cable (meter)

$\overline{\overline{R}}$	τ_p	L	Header
$.1Z$	17	3	SE3R11T1L1
Z	17	3	SE3R22T1L1
$10 \quad Z$	17	3	SE3R33T1L1
$.1Z_1 + Z_2$	17	3	SE3R12T1L1
$.1Z_1 + 10Z_2$	17	3	SE3R13T1L1
$Z_1 + .1Z_2$	17	3	SE3R21T1L1
$Z_1 + 10Z_2$	17	3	SE3R22T1L1
$10Z_1 + .1Z_2$	17	3	SE3R31T1L1
$10Z_1 + Z_2$	17	3	SE3R32T1L1

Appendix VIII

LOSSY CABLE CALCULATIONS

The effects of loss have been considered for the following cable:

RG - 316

C = 95 pf/m

L = 237.5 nH/m

ϵ = 2.05

In the following pages we will list the results of the calculations. Each plot is labeled by a header to identify it. In Table (VIII.1) is indicated the definition of the header. In the first two plots are indicated R(W) and G(W) as is used in all the calculations and the remainder of the plots indicate the results of the calculations.

TABLE VIII.1

R   =   termination impedance (ohms) (symmetric termination)

τ_p =   pulse width (square wave) (ns)

L   =   length of cable (meters)

R	τ_p	L	Header
.5	3	.3	ON1R1T1L11
.5	3	3.	ON1R1T1L21
.5	3	30.	ON1R1T1L31
.5	30	.3	ON1R1T2L11
.5	30	3.	ON1R1T2L21
.5	30	30.	ON1R1T2L31
.5	300	.3	ON1R1T3L11
.5	300	3.	ON1R1T3L21
.5	300	30.	ON1R1T3L31
50	3	.3	ON1R2T1L11
50	3	3.	ON1R2T1L21
50	3	30.	ON1R2T1L31
50	30	.3	ON1R2T2L11
50	30	3.	ON1R2T2L21
50	30	30.	ON1R2T2L31
50	300	.3	ON1R2T3L11
50	300	3.	ON1R2T3L21
50	300	30.	ON1R2T3L31
5000	3	.3	ON1R3T1L11
5000	3	3.	ON1R3T1L21
5000	3	30.	ON1R3T1L31

TABLE VIII.1 (Continued)

R	τ_p	L	Header
5000	30	.3	ON1R3T2L11
5000	30	3.	ON1R3T2L21
5000	30	30.	ON1R3T2L31
5000	300	.3	ON1R3T3L11
5000	300	3.	ON1R3T3L21
5000	300	30.	ON1R3T3L31

LIST OF TERMS

SGEMP	System Generated Electromagnetic Pulse
DSCS III	Defense Satellite Communications System, Phase III
C.I.T.	Current Injection Test
L/C	Inductive/Capacitance
TL	Transmission Line
Z	Impedance
Z_c	Characteristic line impedance
Z_x	Load impedance at position x
$i_0(x,+)$	point current source
Γ	reflection coefficient
γ	line propagation constant
$v(x)$	line voltage at position x
θ	angle of incidence of photon to cable
Q	total charge accreted on open circuited line
I_D	Current Driver
s,l	line length
z	distance of line from its end
$I_1,(I_2)$	contribution to current from all source left (right) point of z
I_L	Load Current
T_p	pulse width (square wave)
V_{oc}	open circuit voltage

DISTRIBUTION LIST

DEPARTMENT OF DEFENSE

Defense Communications Agency
    ATTN: DWSE-E, B. Hoff

Defense Communications Engineer Center
    ATTN: Code R401, T. Ellington

Defense Intelligence Agency
    ATTN: DB-4C, Rsch, Phys Vuln Br

Defense Nuclear Agency
 2 cy ATTN: RAEV
 4 cy ATTN: TITL

Defense Technical Information Center
12 cy ATTN: DD

Field Command
DNA Det 1
Lawrence Livermore Lab
    ATTN: FC-1

Field Command
DNA Det 2
Los Alamos National Lab/DST
    ATTN: MS-635 FC-2

Field Command
Defense Nuclear Agency
    ATTN: FCTXE
    ATTN: FCPR
    ATTN: FCTO
    ATTN: FCLMC, H. Putnam
    ATTN: FCTT, W. Summa
    ATTN: FCTP
    ATTN: FCTT, G. Ganong

Field Command Test Directorate
    ATTN: FCTC

Joint Chiefs of Staff
    ATTN: C3S, Evaluation Office, HD00
    ATTN: GD10, J-5 Nuc & Chem Div

Joint Strat Tgt Planning Staff
    ATTN: JLTW-2
    ATTN: JLA, Threat Applications Div

National Communications System
    ATTN: NCS-TS

Under Secy of Def for Rsch & Engrg
    ATTN: Strategic & Space Sys (OS)
    ATTN: AE

DEPARTMENT OF THE ARMY

BMD Advanced Technology Center
    ATTN: ATC-O

BMD Systems Command
    ATTN: BDMSC-H

Deputy Chief of Staff for Rsch Dev & Acq
    ATTN: DAMA-CSS-N

DEPARTMENT OF THE ARMY (Continued)

Harry Diamond Laboratories
    ATTN: DELHD-NW-RH, R. Gilbert
    ATTN: DELHD-TA-L

US Army Communications Sys Agency
    ATTN: CCM-AD-LB

US Army Foreign Science & Tech Ctr
    ATTN: DRXST-IS-1

USA Missile Command
    ATTN: Documents Section

DEPARTMENT OF THE NAVY

Naval Electronic Systems Command
    ATTN: PME-106
    ATTN: PME-106-1

Naval Research Laboratory
    ATTN: Code 6707, K. Whitney
    ATTN: Code 4720, J. Davis
    ATTN: Code 6701

Naval Surface Weapons Center
    ATTN: Code F31

Strategic Systems Project Office
    ATTN: NSP

DEPARTMENT OF THE AIR FORCE

Air Force Geophysics Laboratory
    ATTN: PH, C. Pike

Air Force Weapons Laboratory
    ATTN: NTN
    ATTN: SUL
    ATTN: NT, Col Bloemker
 2 cy ATTN: NTYC

Air University Library
    ATTN: AUL-LSE

Ballistic Missile Office
    ATTN: SYDT
    ATTN: ENMG
    ATTN: ENSN

Deputy Chief of Staff
Research, Development, & Acq
    ATTN: AFRDQI
    ATTN: AFRDS, Space Sys & C3 Dir
    ATTN: AFRD-M

Office of Space Systems
    ATTN: Director

Rome Air Development Center
    ATTN: ESR/ET, E. Burke

207

DEPARTMENT OF THE AIR FORCE (Continued)

Space Division
    ATTN: XR
    ATTN: YDE
    ATTN: YEZ
    ATTN: YGJ
    ATTN: YKD
    ATTN: YKF
    ATTN: YKM
2 cy ATTN: YNV
    ATTN: YO

Strategic Air Command
    ATTN: XPFS
    ATTN: NRI-STINFO Library

OTHER GOVERNMENT AGENCIES

Central Intelligence Agency
    ATTN: OSWR/STD/MTB, A. Padgett

Department of Commerce
National Oceanic & Atmospheric Admin
    ATTN: F. Fehsenfeld

NASA
    ATTN: Library
    ATTN: C. Purvis
    ATTN: N. Stevens

DEPARTMENT OF ENERGY CONTRACTORS

University of California
Lawrence Livermore National Lab
    ATTN: Technical Info Dept Library

Los Alamos National Laboratory
    ATTN: Reports Library

Sandia National Lab
    ATTN: Tech Lib 3141
    ATTN: Org 9336, D. Allen

Sandia National Labs, Livermore
    ATTN: T. Dellin

DEPARTMENT OF DEFENSE CONTRACTORS

Aerospace Corp
    ATTN: Library
    ATTN: P. Hansen
    ATTN: V. Josephson

AVCO Systems Division
    ATTN: Library A830

Beers Associates, Inc
4 cy ATTN: B. Beers

Computer Sciences Corp
    ATTN: A. Schiff

Dikewood
    ATTN: Technical Library

Dikewood Corporation
    ATTN: K. Lee

DEPARTMENT OF DEFENSE CONTRACTORS (Continued)

Effects Technology, Inc
    ATTN: A. Hunt

EG&G Wash Analytical Svcs Ctr, Inc
    ATTN: Library

Ford Aerospace & Communications Corp
    ATTN: A. Lewis

General Electric Co
    ATTN: J. Peden
4 cy ATTN: H. O'Donnell
4 cy ATTN: D. Tasca
4 cy ATTN: J. Tigner

Hughes Aircraft Co
    ATTN: Technical Library

Hughes Aircraft Co
    ATTN: E. Smith, MS V347
    ATTN: W. Scott, S32/C332
    ATTN: A. Narevsky S32/C332

IRT Corp
    ATTN: N. Rudie
    ATTN: B. Williams
    ATTN: Library

JAYCOR
    ATTN: W. Radaski

JAYCOR
    ATTN: Library
    ATTN: E. Wenaas

JAYCOR
    ATTN: R. Sullivan

JAYCOR
    ATTN: R. Poll

JAYCOR
    ATTN: M. Bell

Johns Hopkins University
    ATTN: P. Partridge

Kaman Sciences Corp
    ATTN: W. Rich
    ATTN: Library
    ATTN: N. Beauchamp
    ATTN: D. Osborn

Kaman Tempo
    ATTN: W. McNamara
    ATTN: DASIAC

Lockheed Missiles & Space Co, Inc
    ATTN: L. Chase

Lockheed Missiles & Space Co, Inc
    ATTN: Dept 85-85

Martin Marietta Corp
    ATTN: J. Caselese
    ATTN: B. Broulik

Martin Marietta Denver Aerospace
    ATTN: D. Tehielan

McDonnell Douglas Corp
    ATTN: R. Kloster
    ATTN: R. Andrews

McDonnell Douglas Corp
    ATTN: S. Schneider

Mission Research Corp
    ATTN: R. Stettner
    ATTN: C. Longmire
    ATTN: M. Scheibe

Mission Research Corp
    ATTN: B. Goplen

Mission Research Corp, San Diego
    ATTN: Library

Mission Research Corporation
    ATTN: W. Ware

Pacific-Sierra Research Corp
    ATTN: L. Schlessinger
    ATTN: H. Brode, Chairman SAGE

Rockwell International Corp
    ATTN: Library

R&D Associates
    ATTN: C. Rogers
    ATTN: S. Siegel
    ATTN: Technical Information Center

S-CUBED
    ATTN: Library
    ATTN: A. Wilson

Science Applications, Inc
    ATTN: W. Chadsey

Science Applications, Inc
    ATTN: D. Woodward
    ATTN: K. Sites

Spire Corp
    ATTN: R. Little

SRI International
    ATTN: Library

Teledyne Brown Engineering
    ATTN: I. Ford

TRW Electronics & Defense Sector
    ATTN: C. Woller
    ATTN: D. Clement
    ATTN: Technical Information Center